BASIC STUDY OF SCANNING AUGER ELECTRON MICROSCOPY

FOR SURFACE ANALYSIS

1980

Shingo Ichimura

BASIC STUDY OF SCANNING AUGER ELECTRON MICROSCOPY

FOR SURFACE ANALYSIS

（表面分析に対する走査型オージェ電子顕微鏡法の基礎的研究）

Shingo Ichimura

Department of Applied Physics

Osaka University

December, 1980

Preface and Acknowledgement

The analytical potential of Auger electron spectroscopy (AES) has increased considerably over the last few years. The growing interest of research and industrial laboratories in surface studies has stimulated the rapid development of quantitative Auger electron spectroscopy and also of the high spatial resolution measurement by AES.

The scanning Auger electron microscope (SAEM), which is one of the most powerful tools for surface analysis, has been in development since the early 1970's. Although the SAEM satisfies the requirement of high spatial resolution to a considerable extent, it is still open to further improvement.

In the present work, basic problems in the scanning Auger electron microscopy were studied, especially, in terms of both high spatial resolution and quantitative analysis measurement. For this purpose, signal detection and processing systems for high spatial resolution measurement were devised and a simulation program to accomplish quantitative analysis by AES was also developed.

The present paper is comprised of 5 chapters. As an introduction to the present work, Chapter 1 describes the general background of AES and development of scanning Auger electron microscopy. The present status of the quantitative analysis by AES is also described in this chapter.

Chapter 2 deals with various approaches to attain high resolution and accuracy in scanning Auger electron microscopy. Auger signal detection and processing techniques are examined

and improved.

Chapter 3 discusses the theoretical treatment of quantitative analysis by AES. Monte Carlo simulation programs developed for the purpose of quantitative analysis are described, and the backscattering correction factor in AES is calculated for a number of pure elements, compounds and alloys.

Chapter 4 compares the contribution of backscattered electrons to Auger signal excitation between the present calculated results and experiment.

Chapter 5 presents applications of the scanning Auger electron microscopy to fundamental problems of surface analysis with high spatial resolution. The basic study of electron beam damage during surface analysis with a scanning Auger electron microscope is also described in this chapter.

All the results are summarized in the Summary.

Research for the present thesis was carried out under the direction of Professor H. Hashimoto of the Department of Applied Physics, Osaka University.

The author wishes to express his thanks to Professor H. Hashimoto for the encouragement and stimulus during the course of the research. Thanks are also due to Professors T. Suzuki and S. Fujita of Department of Applied Physics for their critical suggestions, and to Professors A. Mitsuishi and S. Minami of Department of Applied Physics for the critical reading and important suggestions.

To associate Professor R. Shimizu, I am intimately grateful for his invaluable suggestions and systematic discussion of both experiments and theory throughout the present work. I would also like to express thanks to the staff members of the Hashimoto Laboratory, Dr. K. Ueda for initiating me into the field of AES, to Mr. H. Endoh for his advices for computer programming, and to Mr. E. Fukada for photography.

I am very grateful to Mr. K. Goto of Nagoya Institute of Technology and Dr. C. LeGressus of CEN-Sacley for critical discussions and helpful suggestions provided through the cooperative researches (described in Chapters 2 and 5, respectively). Thanks are also due to Dr. Y. Yamazaki of Tokyo Institute of Technology for his advice and stimulating discussions especially on the calculation of elastic scattering cross-sections and to Dr. T. Uchida of Department of Applied Physics for helpful suggestions on electronics.

Several critical suggestions on elementary excitation processes by Professor T. Ichinokawa of Waseda University and on AES quantitation by Dr. C.J. Powell of NBS have been very helpful.

My sincere gratitude is due to Associate Professors T. Ikuta and T. Koshikawa of Osaka Electro-Communication University for invaluable advices on signal processing systems and critical suggestions, and also to Drs. Y. Ogata and T. Matsukawa of Mitsubishi Electric Corp. for their advices and supports in preparing samples. My intimate thanks are also due to Mr. A. Mogami of JEOL Co. for useful suggestions and various supports in the instrumentation, and to Dr. N. Saeki of Minolta Co. for his advices and encouragement.

I am also thankful to my colleague Mr. M. Aratama (now Kawasaki Steel Corp.) for his assistance in the development of Motne Carlo calculation program and to all other members of the Hashimoto Laboratory who supported the present work.

Finally, the skillful typing of Miss. K. Nishiyama and Mrs. M. Masuda, my syster, should be gratefully acknowledged.

CONTENTS

Chap. 1 Present Status of Surface Analysis by Scanning Auger Electron Microscopy

1-1 Introduction

Scanning Auger electron microscopy is one of the most powerful techniques for surface research. This technique enables the surface characterization as well as the surface topography of a local area of submicron region and its rapid progress has been stimulated by an increasing necessity of surface analysis with high spatial resolution in various practical fields including semiconductor device technology. Furthermore, Auger electron spectroscopy (AES) is, at present, nearest to the goal of quantitative surface analysis.

In the scanning Auger electron microscopy, kilovolt electrons ($\sim$10 kV) are used as a primary beam, which is focused on a sample surface as finely as possible in order to assure high spatial resolution in the surface analysis, and the current density at the surface often reaches so high as even to ~ 10 A/cm^2. The scanning Auger electron microscopy, therefore, reveals a quite new aspect in electron-specimen interaction than does the conventional AES which uses a rather low primary accelerating voltage (below 3 kV) and low current density (10^{-4} A/cm$^2 \sim 10^{-3}$ A/cm^2).

The electron-specimen interaction is schematically shown in Figure 1-1. Primary electrons strongly interact with electrons and atoms in a specimen either elastically or inelastically. Some of them lose their whole kinetic energies in the specimen and finally come to rest, which are detected as absorbed current. The rest of

them come out from the specimen and are called backscattered electrons. Besides those primary electrons, the electron penetration is associated with generation of secondary electrons. Those backscattered (and secondary) electrons with high energy contribute to another excitation of Auger electrons as well as the primary electrons. This additional contribution is called the backscattering effect and the correction of the backscattering effect, which is often called backscattering correction, is of most practical importance in accomplishing quantitative analysis by AES.

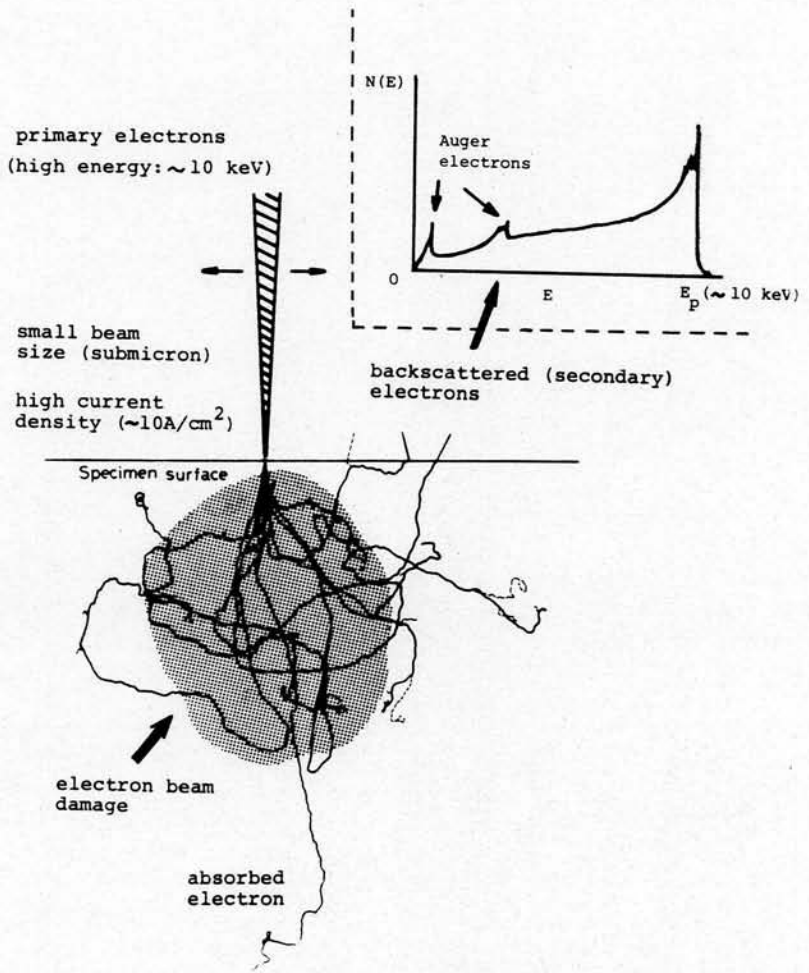

Fig. 1-1 A schema of electron-specimen interaction in scanning Auger electron microscopy.

Experimental studies of the backscattering correction published so far have been limited to a few specific samples due to the difficulty in distinguishing Auger electrons generated by backscattered electrons from those by primary electrons. Theoretical approaches for the estimation of the correction factor proposed so far also have some difficulties which cause considerable inaccuracy, resulting from the treatment of scattering processes of low energy (several hundreds-eV ~ several keV) electrons.

High energy primary electrons with high current density, on the other hand, cause damage on the specimen. They dissociate the surface compositions, and desorb the surface element. The damage during AES has attracted much attention in recent years.
The damage under such high energy and high current density as that in the scanning Auger electron microscopy, however, has not been well studied as yet.

The present paper is aimed at studying basic problems in the scanning Auger electron microscopy for establishing quantitative analysis as well as more comprehensive surface characterization with high accuracy.

From the view point of quantitative analysis,

i) the estimation of backscattering correction is inevitable, and this can be achieved theoretically by introducing an exact treatment of scattering processes of low energy electrons in a specimen.

From the view point of a more comprehensive surface analysis, on the other hand,

ii) improvement of the Auger signal detection system ensures high spatial resolution spectroscopy, leading to the reduction of the damage by shortening the signal acquisition and processing time.

iii) A fundamental study is highly required as to irradiation of primary electrons with such a high energy and high current density. This enables the scanning Auger electron microscopy to be more a powerful technique for surface micro analysis.

1-2. Present status of scanning Auger electron microscopy

1-2-1. Principles and features of AES

A) Principle of Auger electron ejection

The scanning Auger electron microscopy utilizes Auger electrons as the signal for surface study as well as AES.

The Auger electron was first detected by Auger (1925) during the observation of X-ray with the Willson chamber. The principle of Auger electron ejection is shown schematically in Fig. 1-2, where a lower-shell (denoted by U) is assumed to be ionized.

An atom in an excited state decays through one of the channels as

1. radiative transition,
2. Auger transition,

and

3. Coster-Kronig transition (if energetically possible).

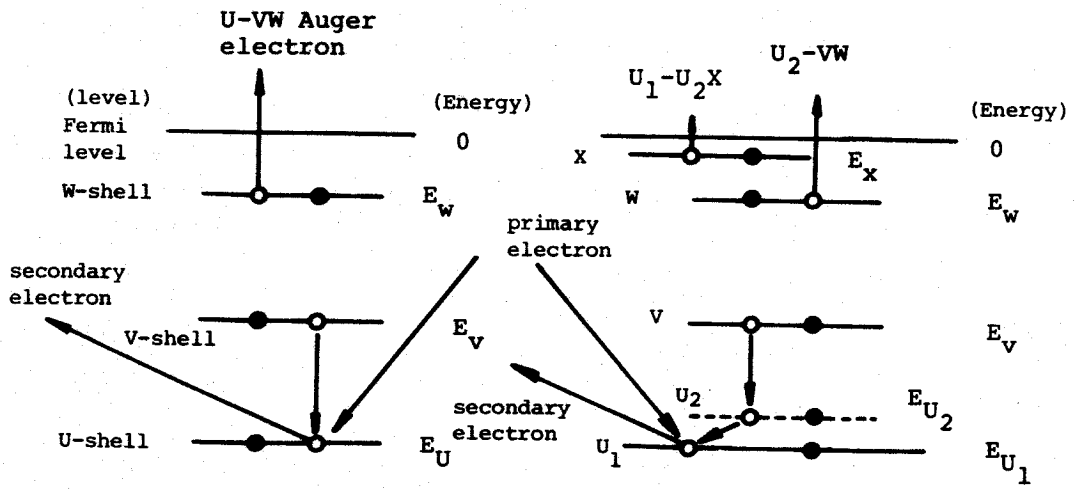

Fig. 1-2 A schema for the principle of Auger electron ejection. Right hand side shows the Auger electron ejection after the Coster-Kronig transition.

In the case of the first, the excess energy due to the de-excitation transition from an outer-shell (V-shell) to the inner-shell is emitted as a photon (X-ray), while in the second case, it is transferred to another electron which is ejected from an outer-shell (W-shell). After the Auger electron ejection, the atom is in the excited state that V- and W-shells are doubly ionized instead of the initial U-shell excited state. So, the ejected electron is called U-VW (or UVW) Auger electron.

The last channel means the filling of a primary vacancy by an electron from the same major atomic shell (having the same principal quantum number), which was first explained by Coster and Kronig (1935). Therefore, it can occur only when the excess energy is large enough to eject an outer-most shell electron. The transition leads to another Auger electron ejection (see Fig. 1-2) as it is clearly seen in the Auger-photoelectron coincidence measurements in copper (Haak et al. 1978), so it has much importance in quantitative discussion by AES. (See Section 1-3).

The kinetic energy of the UVW-Auger electron is expressed by

$$Euvw = Eu - Ev - Ew', \qquad (1\text{-}1)$$

where Eu and Ev are the first ionization energy of the U- and V-shell, respectively. Ew', on the other hand, represents the ionization energy of the W-shell under the condition that the atom is already ionized in an inner-shell. The energy is uniquely determined as a function of Z, the atomic number of the element, so we can easily identify the element by the energy analysis of ejected electrons.

B) Escape depth

Usually, Auger electrons which have a kinetic energy of between a few tens of eV and 2000 eV are used for the identification of

an element. These electrons strongly interact with electrons and nuclei in a specimen and lose their energy while escaping from the surface. So Auger electron which are excited at the inner part of a specimen cannot be detected.

The escape depth of Auger electrons. which corresponds to the inelastic mean free path of each Auger electron, is shown in Fig. 1-3. As is seen in the figure, the detection depth by AES is about 3 Å~30 Å, so AES is a surface sensitive technique.

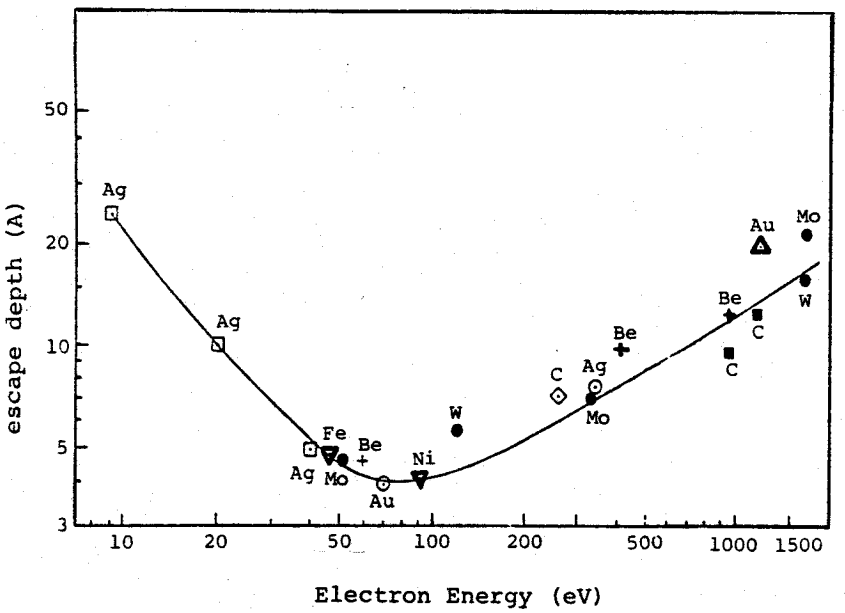

Fig. 1-3 Escape depth of Auger electrons.
(Palmberg 1973)

C) Transition probability

The probability of Auger electron ejection (Auger yield a) after an inner shell excitation has been studied both theoretically and experimentally. The yield has an opposite meaning of ω, the fluorescence yield, so

$$a = 1 - \omega \quad . \tag{1-2}$$

The Auger transition probability is calculated by (Burhop 1952),

$$\nu_{UVW} = \frac{2\cdot\pi}{\hbar}\cdot\left|\int\int \chi^{*}_{\infty}(\vec{r}_1)\cdot\psi^{*}_{U}(\vec{r}_2)\cdot\frac{e^2}{|\vec{r}_1-\vec{r}_2|}\cdot\chi_W(\vec{r}_1)\cdot\psi_V(\vec{r}_2)\cdot d\vec{r}_1\cdot d\vec{r}_2\right|^2 , \tag{1-3}$$

where χ_W and ψ_V represent the initial single-electron wave function, while χ_∞ and ψ_ν represent those of the final state. The equation (1-3) corresponds to the transition

$$\chi_W \longrightarrow \chi_\infty \quad , \qquad \psi_V \longrightarrow \psi_U \quad ,$$

while the transition corresponding to the exchange interaction is also taken into account in exact calculation. Many calculations of the transition probability were reviewed in detail by Bambynek et al. (1972).

The fluorescence yield ω is shown in Fig. 1-4, and strong Z dependency (Z^4 dependency) (Chattarji 1976) can be seen. So the Auger yield is close to unity at low Z, which makes AES a suitable technique for light element electrons. AES is also useful for heavy elements since a becomes larger for the outer-shell of heavy elements.

D) Application of AES to surface measurement

The applicability of AES to surface study was first pointed out by Lander (1953). He attributed the fine structures in the energy spectra of secondary electrons to Auger electrons, and estimated that Auger electrons from an outer surface layer of ten atoms thick would be observed. AES, however, had not been a powerful technique for surface study due to the large background until

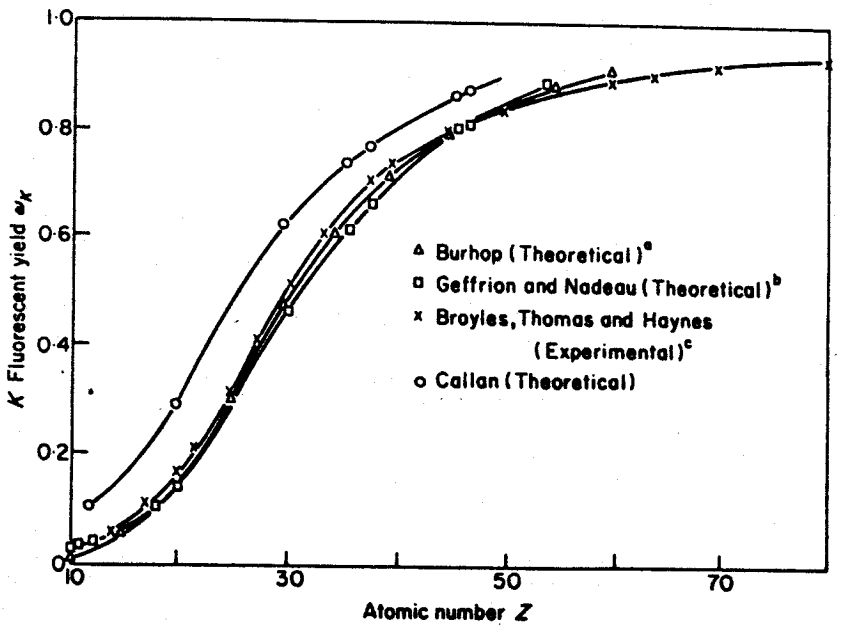

Fig. 1-4 K-shell fluorescence yield as a function of atomic number (Callan 1961)

Harris (1968) first succeeded in obtaining a derivative mode spectra using phase sensitive detection technique (see Section 2-2). The derivative mode spectra can stress small peaks and humps on the energy distribution which correspond to Auger electrons, which could be well applied in LEED (low energy electron diffraction) apparatus (Weber and Peria 1967). Thus, AES immediately became a popular technique in many fields of research and applications in industry where chemical composition of surface was of importance. Furthermore it enabled in-depth analysis using an ion gun system which sputtered away the sample surface layer by layer.

Its characteristic features are 1) non-destructive as compared to SIMS (secondary ion mass spectroscopy), and 2) high spatial resolution spectroscopy as compared to XPS (X-ray photoelectron spectroscopy), UPS (ultraviolet photoelectron spectroscopy) and

SIMS, too. Moreover, AES gives information about transition probability if valence electrons take part in the Auger transition, which have been extensively studied as described below.

The spectrum corresponding to XVV transition (V denotes a valence state) can be expressed by a convolution integral of a valence band density of state ($\rho(E)$) as shown first by Lander (1953),

$$N(E_x-2E)\sim\begin{cases}\int_0^{E} \rho(E-\Delta E)\cdot\rho(E+\Delta E)\cdot d(\Delta E) & (0\leq E\leq\frac{E_1}{2})\\ \int_0^{E_1-E} \rho(E-\Delta E)\cdot\rho(E+\Delta E)\cdot d(\Delta E) & (\frac{E_1}{2}\leq E\leq E_1)\end{cases}, \qquad (1\text{-}4)$$

where Ex and E_1 denote the energy level of the inner-shell (X-shell) and the bottom of the valence band, respectively. All those are measured from the Fermi-level. (Therefore, the energy width of the valence band equals to E_1). Strictly the $\rho(E)$ should be considered as the product of the state density and the square root of the spatial integrated square of the transition matrix element. Through the comparison of the N(E) between experiment (which is obtained by the deconvolution of the spectrum) and theory, an energy variation of the transition probability is examined. (Powell 1973, Feibelman et al. 1976). Moreover, the effect of the final hole in the valence state is also studied through comparison with theory (Houston et al. 1977, Smith and Levenson 1977, Feibelman and McGuire 1977).

This study will lead AES to further applicability of surface measurement.

1-2-2. Scanning Auger electron microscopy

A) Instrumentation

The combination of Auger electron detection systems with conventional scanning electron microprobe system which is called scanning Auger electron microscope (SAEM) has been attempted since the early stage of the application of AES for surface qualitative analysis. Use of the scanning electron microprobe allows for intimate insight into close relationship between surface topography and surface chemistry, and this strongly supports the utilization of AES as a surface analytical tool much more than other surface sensitive techniques, for instance, XPS, UPS, etc.

The first success of the attempt was reported by MacDonald and his co-workers in the beginning of 1970's (MacDonald 1970, MacDonald and Waldrop 1971). They obtained the Auger electron images (the distribution of an element on a specimen surface) of Fe and Cu, which are shown in Fig. 1-5. Their SAEM needed a rather long processing time of ~1.7 hour with the primary beam current of 2.5×10^{-8}A to visualize the image using a laboratory digital computer. It is not satisfactory and the vacuum conditions (in the order of $10^{-7} \sim 10^{-8}$ Torr) were not high enough for AES.

A schematic diagram of an SAEM in the present wider use is shown in Fig. 1-6. Primary electrons (~10 keV) are finely focused by a magnetic lens system (condenser lens and objective lens) onto a specimen. Auger and secondary electrons excited by primary electrons are energy-analyzed by a cylindrical mirror analyzer (CMA) which is equipped in most SAEM because of its high sensitivity. The output signal of the CMA is fed to a X-Y recorder to obtain an Auger spectrum in the case of point analysis relating to the surface morphology of a specimen. Otherwise it fed to a brightness modulation circuit of a cathode ray tube to obtain an

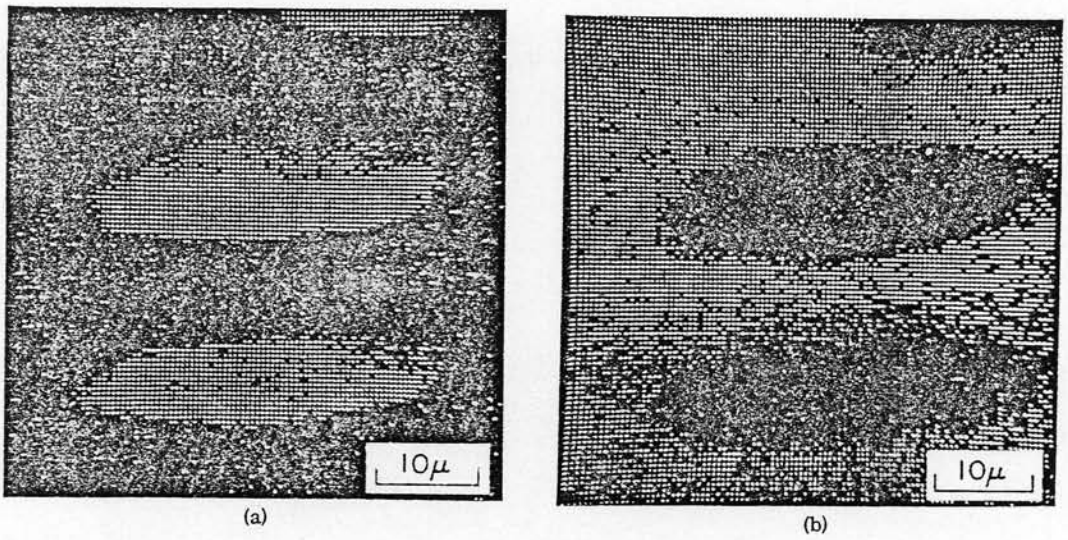

Fig. 1-5 Auger electron images observed for the first time by McDonald and Waldrop (1971):
(a) Fe Auger image, (b) Cu Auger image.

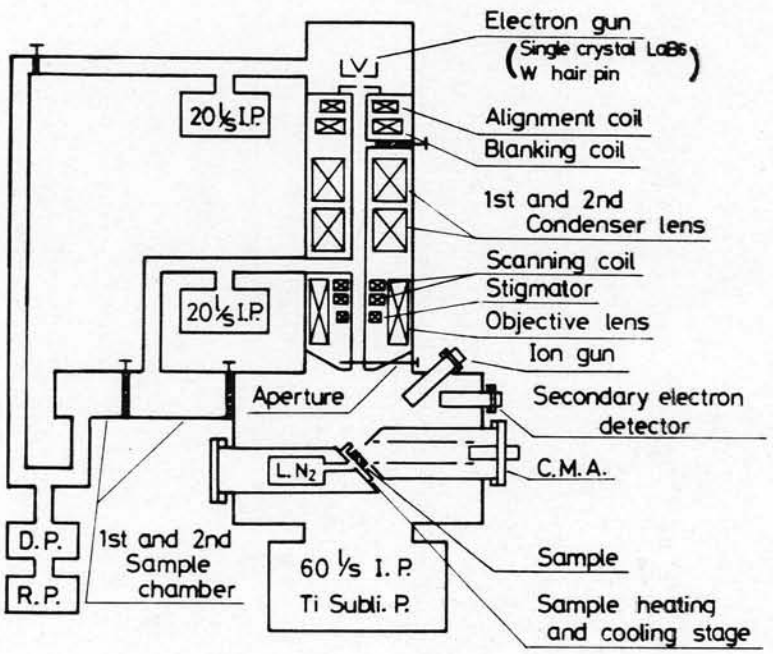

Fig. 1-6 A schema of a scanning Auger electron microscope.

Auger electron image. In the latter case, primary electrons are scanned synchronously with CRT using a scanning coil.

An example of the energy spectrum obtained with an SAEM with a CMA is shown in Fig. 1-7. Primary electrons lose their energy through inelastic scattering with electrons and nuclei in the specimen, and they either come out from the surface (backscattered electrons) or are absorbed in the specimen losing their whole kinetic energy (absorbed electrons). Some excited electrons are also ejected from the surface (secondary electrons). Those secondary and backscattered electrons distribute continuously forming an energy distribution as shown in the figure, which is often conventionally called energy distribution of backscattered electrons even though it includes the secondary electrons. A peak in the high energy region is due to the characteristic feature of the CMA, that is, due to

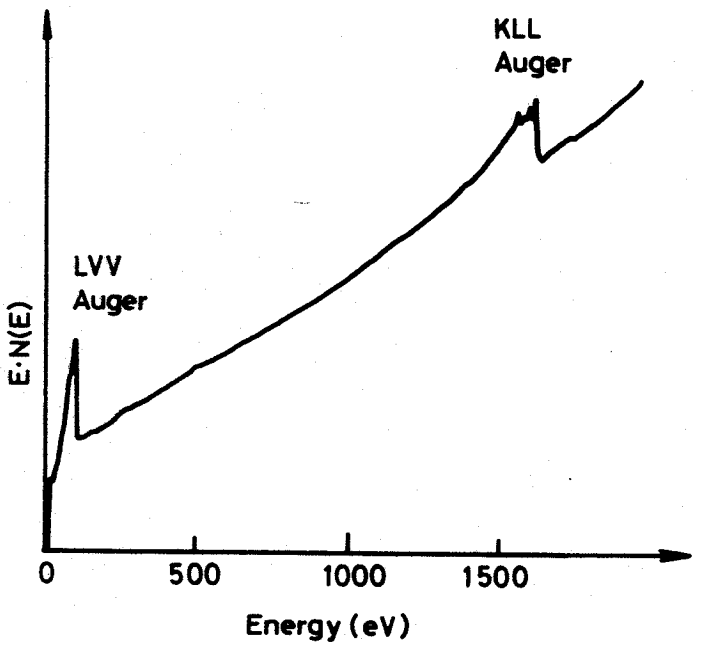

Fig. 1-7 Auger electron spectrum of Si measured with a scanning Auger electron microscope. (Ep= 10 keV)

the constant energy resolution ($\Delta E/E$ = K: constant)

Auger electrons appear as a small peak on the distribution (see Fig. 1-7). In the scanning Auger electron microscopy the signal to background ratio is much higher than that in conventional AES, and this leads to a more prominent appearance of Auger peaks in the spectrum. This is due to the fact that the backgroud reduces almost inversely in proportion to the primary energy (since total secondary electron yield remains nearly constant) while the Auger signals do not show such a rapid change with an incident energy.

Auger electrons must be well distinguished from the background in order to get an Auger image in which the brightness corresponds to the concentration of an element. It is also required to draw out quantitative information from the Auger spectrum.

B) Methods for background subtraction

Many methods for background subtraction have been studied (Sickafus 1971, Grant et al. 1973, Staib and Kirschner 1974, Springer et al. 1975, Martin 1975) some of which are discussed as follows;

(1) Method by derivative mode spectra

The energy spectrum from a specimen has fine structures other than Auger spectra in high (nearly elastically scattered) and low (true secondary) energy regions. The use of high energy primary electrons in scanning Auger electron microscopy leads to a relatively low influence of the feature in high energy region. Auger electrons, in such a case, can be approximately considered to exist on a linear background. So the energy spectrum can be represented as

$$KE \cdot N(E) = KE \cdot A(E) + KE \cdot B(E) \qquad (1\text{-}5)$$

$$KE \cdot B(E) = CE + D \qquad (1\text{-}6)$$

(K,C, and D are constants)

Here KE denotes the window width of the CMA, and A(E) and B(E) are energy distrubutions of Auger and backscattered electrons, respectively. The derivative of the equation becomes,

$$\frac{d(KE \cdot N(E))}{dE} = KE \cdot \frac{dA(E)}{dE} + K \cdot A(E) + C \qquad (1\text{-}7)$$

If A(E) has a Gaussian distribution and the peak to peak height in a derivative spectrum is measured, the height h_{p-p} is (see Fig. 1-8)

$$h_{p-p} = 2KE \cdot \left(\frac{dA(E)}{dE}\right)_{E=E_\sigma} , \qquad (1\text{-}8)$$

where the backgroung is eliminated.

The derivative Auger spectrum was first measured by Harris (1968) using phase sensitive detection systems (see Section 2-2). Since then it has been used often in AES probably because it can stress small peaks and humps in energy spectrum (which correspond to Auger signals). Since the energy width of Auger electrons associated with inner-shell (K-shell) excitation is narrow (~1 eV: Chen et al. 1980), the method seems to be quite useful for the background subtraction of high energy Auger electrons.

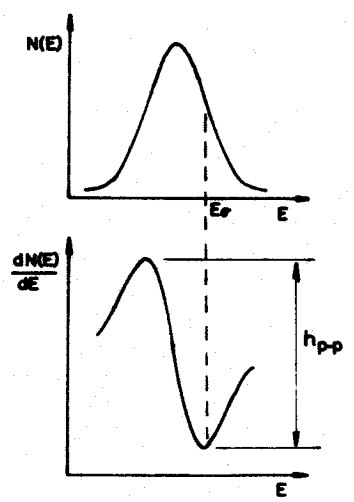

Fig. 1-8
A schema for the derivative mode detection of the Auger spectrum.

As for low energy Auger electrons which are excited from valence states, the subtraction by the derivative method have some difficulties due to the so-called 'chemical effect' (Palmberg 1972).

(2) dynamic background subtraction

Grant et al. (1973, 1974a,b,c) proposed the dynamic background subtraction method which means successive differentiation and integration to remove the background. The theoretical basis for this operation was explored by Houston (1974), and assumes that background function B(E) has a Taylor series representation with a large radius of convergence. Therefore, the characteristic function A(E) is represented by

$$A(E) = R_n(E,\alpha) \tag{1-9}$$

where

$$R_n(E,\alpha) = \underbrace{\int_\alpha^E \cdots\cdots \int}_{n} dE' \cdots\cdots dE'' \; H^{(n)}(E'') \tag{1-10}$$

$$H(E) = A(E) + B(E) \quad , \quad H^{(n)}(E) = \frac{d^n H(E)}{dE^n} \tag{1-11}$$

This method largely overcomes the problem accompanied by shape changes in dN(E)/dE mode detection (Grant et al. 1973).

(3) Method of functional representation of the background

Staib and Kirschner (1974) proposed to use the Spline polynomial fitting for 1) structureless background distribution whose first and second derivatives are continuous and derivable, assuming 2) the pure background exists between two separate Auger lines. Then, the n-1 third order polinomials

$$B_k(x) = a_k(x-x_k)^3 + b_k(x-x_k)^2 + c_k(x-x_k) + d_k \qquad (k=1, \cdots, n-1) \qquad (1\text{-}12)$$

(a_k, b_k, c_k, and d_k are constants)

are assigned to the sets of data points (x_k, y_k), and an approximating function for the background is

$$B(x) = \begin{cases} B_1(x) & x < x_1 \\ B_k(x) & x_k \leq x < x_{k+1} \\ B_{n-1}(x) & x_{n-1} \leq x \end{cases} \qquad (1\text{-}13)$$

This method seems to be one of the most effective approaches.

From the view point of the application to a scanning Auger image, the above methods except for the derivative one needs long data processing time to be practically used though they are useful in conventional AES. Usually, an Auger electron image is taken within several hundreds seconds for reasons such as damage reduction, primary current stability, and so on. Picture elements per frame are 256 x 256 or more, so Auger signals from a picture element should be subtracted the background within several milli-seconds. Thus, the derivative method using phase sensitive detection technique has been used leaving, however, the room for further improvement (see Section 2-2). For this improvement, square wave modulation technique by Springer et al. (1975) is most useful (see Section 2-2).

As to the subtraction of inelastically scattered Auger electrons, the iterative method by Martin (1975) is most useful.

1-2-3. Approaches to attain high spatial resolution surface analysis

The spatial resolution obtained in the Auger analysis is mainly

determined by the probe size of the primary beam which gives a reasonable signal to noise ratio. In the case of point Auger analysis, the signal to noise ratio (S/N) is estimated by

$$S/N = \frac{N_A}{\sigma_B} \quad , \qquad (1\text{-}14)$$

where N_A denotes an Auger signal intensity and σ_B, the fluctuation of background signals (see Fig. 1-9). N_A is given by the following equation,

$$N_A = \gamma I_p \cdot \frac{\Omega}{4\pi} \quad . \qquad (1\text{-}15)$$

Here I_p and Ω represent primary beam current and detection solid angle of the analyzer, respectively, while γ denotes the Auger electron yield by a primary electron. The valus γ is estimated

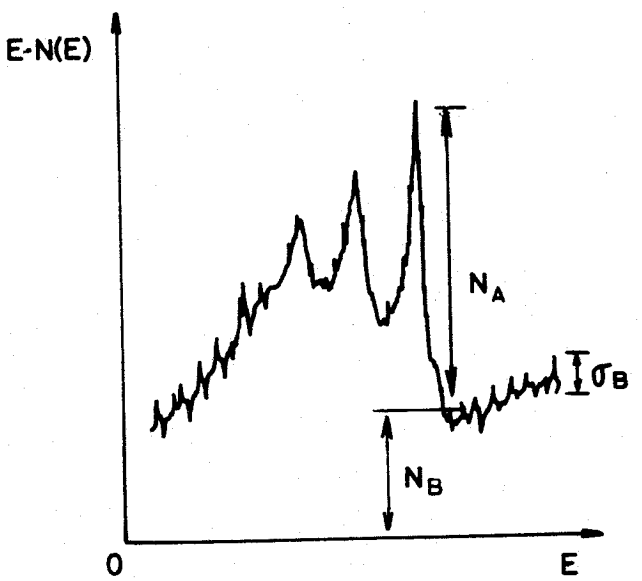

Fig. 1-9 A schema for signal and noise in Auger signal detection

about $10^{-4} \sim 10^{-5}$ (Bishop and Riviere 1969, also see Section 3-6). Primary beam current is represented as a function of electron beam size d by (Booker 1970)

$$I_p = (\frac{d}{2})^2 \cdot \pi j_0 = (\frac{d}{2})^2 \cdot \pi B \pi \alpha^2 \qquad (1\text{-}16)$$

Here, j_0 denotes the current density of the primary beam, and it is given by the brightness B of an electron source and α, beam divergence on the specimen. Therefore, high spatial resolution in scanning Auger electron microscopy has been accomplished by A) the use of electron sources with high brightness, B) the improvement of the S/N ratio by effectively subtracting the background. They are discussed as follows;

A) Use of electron source with high brightness

Various electron sources for high resolution Auger spectroscopy have been studied by Christou (1976). He obtained Au Auger images with various electron sources and concluded that the field emission source gave the highest resolution at a primary beam current of below 10^{-9} A, while LaB_6 source was superior to field emission source and also to conventional W-hairpin cathode at the region of primary beam current above 1×10^{-8} A. The result is shown in Fig. 1-10.

Some trials for the application of the field emission electron gun for high spatial resolution Auger spectroscopy have been reported (Pocker and Haas 1975, Todd et al. 1975), and the spatial resolution of 30 mm in an Auger image (Venables et al. 1976) is probably the highest resolution reported, to the author's knowledge, at the present time. They obtained Ag Auger map with primary beam current of $\sim 1 \times 10^{-8}$ A, primary beam voltage of 30 kV and a frame time of 500 sec.

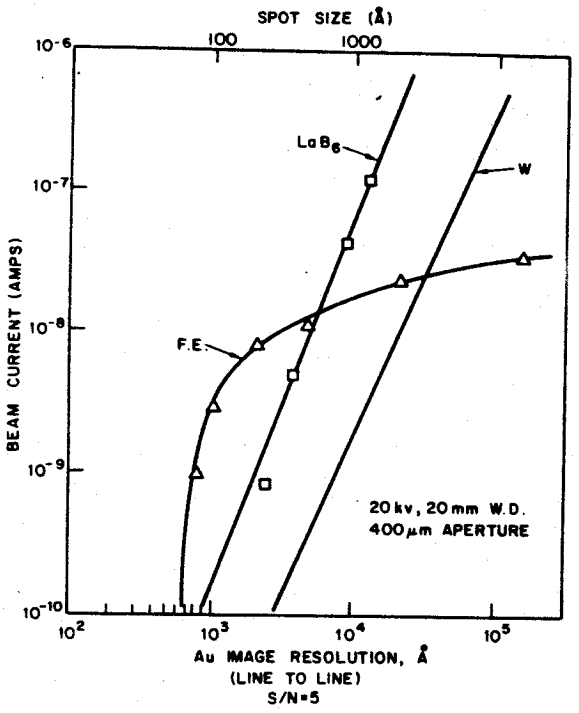

Fig. 1-10 Comparison of various electron sources. (Christou 1976)

The main problem which occurs in the application of the field emission source exists in electron beam instability. It is well known that the gas adsorption onto the emitter tip and residual gas ion sputtering of the emitter tip brings about instability of emission current causing serious trouble particularly in accomplishing quantitative analysis with high accuracy. To overcome this difficulty the following techniques have been proposed, and used;

1) signal averaging over repetitive traces (Pocker and Haas 1975),
2) digital referencing method which uses the primary beam current intensity as the gate pulse of the analyzer (Todd et al. 1975),
3) a rationing technique which uses the ratio of Auger-signal to the background as a signal (Janssen et al. 1977a).

Compared to the field emission type electron gun, LaB_6 cathode has a high current-stability and seems to be most favorable for scanning Auger electron microscopy. (See Section 2-5).

B) Improvement of the S/N ratio

In an SAEM, Auger and secondary electrons are amplified by an electron multiplier after passing through the CMA. Then, the gain fluctuation of the electron multiplier affects σ_B, so σ_B is represented by (Shockley and Pierce 1938)

$$\sigma_B = \sqrt{(N_B - \overline{N_B})^2}$$

$$= \sqrt{\overline{n_B}\,\overline{(\delta-\bar{\delta})^2} + (\bar{\delta})^2\,\overline{(n_B-\overline{n_B})^2}} \qquad (1\text{-}17)$$

Here n_B and N_B denote the number of secondary electrons before and after amplification by the multiplier, respectively. δ denotes the gain of the multiplier, and the over-bar in the equation denotes the mean value of each physical quantity. So the signal to noise ratio is given by

$$\frac{S}{N} = \frac{\overline{n_A}\cdot\bar{\delta}}{\sqrt{\overline{n_B}\cdot\overline{(\delta-\bar{\delta})^2} + (\bar{\delta})^2\cdot\overline{(n_B-\overline{n_B})^2}}} \qquad (1\text{-}18)$$

where n_A denotes the number of Auger electrons before amplification.

The pulse counting method can cancel out the gain fluctuation of the amplifier ($\delta=\bar{\delta}$), so it leads to the improvement of the signal to noise ratio. This method was applied to an SAEM which had a digital data acquisition system with considerable success in attaining high spatial resolution microscopy (Browning et al. 1977a,b) This method seems to be effective for low primary beam current (10^{-9}A or less). However, for fast observation of an Auger image with a little higher primary beam current ($\sim 10^{-8}$A), the method has a

problem in the maximum counting rate of the mutiplier, and also in the problem of background subtraction.

Another data processing system using conventional current mode detection which is more useful for this purpose has been developed by the author (see Section 2-4).

1-2-4. Discussion about resolution limit

The theoretical limit of spatial resolution of the Auger analysis has been discussed. The spatial resolution of several tens of Å is obtained with a scanning electron microscope (SEM). So much attention has been paid to the possibility of such a high resolution spectroscopy with the SAEM.

Almost all of the discussions (Christou 1976, Kirschner 1977, Shimizu et al. 1977a, 1978a, El Gomatti and Prutton 1978, Janssen and Venables 1978) concern the effect of the backscattered electrons, that is, whether the spread causes deterioration of spatial resolution or not. Christou concluded through his experiment about Au Auger image that the limit of the spatial resolution is ten times the probe diameter and attributed his results to the effect of backscattered electrons. El Gomatti and Prutton, on the contrary, concluded that spatial resolution is dominated by the size of the primary beam. Spatial distributions of the Auger signal generation calculated by them using the Mont Carlo simulation approach show a δ-function like feature at the spot of the electron beam incidence which was surrounded by a broad region due to backscattered electrons. A more detailed discussion on this problem was done by the author using the Monte Carlo calculation for Al (see Section 3-6).

El Gomatti and Prutton also estimated the spatial effect of

backscattering for the case of a step-like distribution of an element using the response function obtained by the Monte Carlo calculation. They concluded that the spatial resolution which is estimated as the spacing between 25% and 75% of the maximum is 200 Å for an incident beam with 100 Å diameter (for Cu). Similar estimations (in more strict spacing) have been tried by Kirschner for Al and Au, and Janssen and Venables for Ag. Shimizu et al. (1978a) have revealed an edge effect for Al on Si, inherent to AES of steplike sample and clarified it theoretically using the Monte Carlo calculation.

1-2-5. Problems associated with the application of SAEM to surface measurement.

The SAEM developed so far allows us to study the material surface with a short processing time (in a few minutes), under high vacuum (10^{-9}~10^{-10} Torr), and high spatial resolution (Gerlach and MacDonald 1976, Mogami and Sekine 1976, Venables et al. 1976, Ishida Y. et al. 1976). Actually it has been applied to various surface problems of either physical or practical importance such as grain boundary diffusion (Ishida T. et al. 1976, Janssen et al. 1977 b) and device deterioration due to surface migration (Inoue et al. 1976). The high spatial resolution surface characterization, however, is associated with electron beam damage due to the high current density of primary electrons incurring serious problems as mentioned below.

Electron beam damage under low primary energy and low current density has been studied in relation to compositional change during the irradiation. (For SiO_2, Thomas 1974, Menyhard and Gergely 1977, Le Gressus et al. 1977, Carriere and Lang 1977, Schwidtal 1978). Electron beam damage under high primary energy

(10 keV 15 keV) but at low exposure was also studied with an electron microprobe. (Borom and Hanneman 1967 , Sigsbee and Wilson 1973). Electron beam damage under such a high current density and high primary energy as an SAEM, however, has yet to be well studied. Mogami and Sekine (1978) investigated the damage for Si plate specimen with an SAEM and found that Si LVV-Auger peak and secondary electron emission abruptly change even for 1 sec. irradiation. They proposed to use beam brightness modulation (BBM) method instead of the conventional Auger signal detection technique in order to minimize the beam damage. This method is based on the use of chopping of primary beam and the chopping frequency is used as a reference signal of phase sensitive detection. So it gives a N(E) mode spectra, and effective power transfered to the specimen by primary electrons becomes half that of the SAEM with the usual signal detection method. The damage observation by an SAEM in respect to the surface topography as well as the surface composition is also studied (see Section 5-4).

1-3 Present status of quantitative analysis by AES

1-3-1. Physical basis for quantitative approach

a) Model equation for Auger signal intensity

In AES, signals (Auger electrons) are generated in electron-specimen interaction, and the basic process of the excitation is, in principle, the same as in electron probe microanalysis (EPMA). The following simple equation has been used by several authors (Biship and Riviere 1969, Palmberg 1976, Powell 1977, Holloway 1977) to describe the signal intensity for UVW Auger transition of i-th element, $I_i(E_i, UVW)$.

$$I_i(E_i, UVW) = X_i \cdot I_p(E_p) \cdot N \cdot \sigma_i(E_p, E_u) \gamma_i(Z,U) \nu_i(UVW) \times R_i(E_p, E_u) \lambda_i(E_i) T(E_i) G, \quad (1\text{-}19)$$

where X_i is the concentration of the i-th element ($0 \leq X_i \leq 1$ = 100%) and other symbols denote physical quantities as follows;

$I_p(E_p)$: Primary beam current with the primary energy E_p

N : atom density of the materials (bulk)

$\sigma_i(E_p, E_u)$: the ionization cross-section for U-shell (its binding energy E_u) of the i-th element

$\gamma_i(Z,U)$: the correction factor for the additional ionization of the U-shell of the i-th element due to Auger and Coster-Kronig transitions that can occur after ionization of electrons in other level Z.

$\nu_i(UVW)$: the probablity that an atom ionized in the U-level will decay through the UVW Auger transition.

$R_i(E_p,E_u)$: correction factor for the additional ionization of electrons in the level U due to backscattered electrons.

$\lambda_i(E_i)$: the inelastic mean free path in the sample for electrons of kinetic energy E_i.

$T(E_i)$: the transmission function of the analyzer for electrons of kinetic energy E_i.

G : the geometrical factor concerning the collection efficiency of Auger electrons.

Note that the above is based on the following assumptions :

(i) The element, i, to be analyzed is distributed uniformly parallel to the surface and also in depth from the surface.

(ii) Inelastic scattering events that an Auger electron undergoes in a target occur in a random process and the absorption effect effect of the Auger electron during the travelling path, s, is simply represented with the inelastic mean free path λ by $\exp(-s/\lambda)$.

(iii) The number of electrons with kinetic energy E is uniform within the escape depth of Auger electrons. This is quite reasonable since the escape depth of Auger electrons is less than several tens of Å while the electrons with energy E spread over a depth corresponding to the range of primary electrons, two or three orders of magnitude larger than the escape depth.

These physical quantities must be well studied before the AES can be accomodated to quantitative analysis. This is, how-

ever, not easy since those are represented as functions of many variables. Moreover, the dependence of some parameters (for example, $\lambda_i(E_i)$, $R_i(E_p,E_u)$, etc.) on the composition of a material which is often referred to as 'matrix effects' (Chang 1974, 1975) makes the relation between I_i and x_i very intricate.

Powell (1977) checked the validity and utility of the model equation (1-19) and the data for each physical quantity that had been available. He estimated the signal intensity of KLL and LVV Auger signals of Al using the equation (1-19) and compared the ratio of the two Auger signals (I_{LVV}/I_{KLL}) with the value obtained by experiment, which is shown in Table 1-1. The results, although the comparison of calculation and experiment was carried out only for 2 keV of primary electron energy due to the lack of data for R, show an excellent agreement. Therefore, the model equation seems to be valid and useful for the quantitative approach by AES.

Table 1-1 Comparison of measured and computed relative yields of KLL and LVV Auger electrons of Al. (Powell 1977)

E_o (keV)	$\frac{I_{LVV}}{I_{KLL}}$ (measured)	$\frac{I_{LVV}}{I_{KLL}}$ (computed)
2	12.6±0.4	13.7
3	4.6±0.2	--
4	2.8±0.2	--
5	2.2±0.1	--

B) Practical formalism for quantification.

Formalism relating Auger signal intensities measured to those for bulk reference standards has been presented in the past by several authors in analogy to quantitative correction in EPMA. (Heinlich et al. 1976). The following equation can be obtained using equation (1-19).

$$\frac{I_i}{I_i^s} = \frac{X_i \cdot N \cdot \sigma_i(E_p,E_u)\gamma_i(Z,U)\nu_i(UVW)R_i(E_p,E_u)\lambda_i(E_i)}{C_i^s\, N_i^s\, \sigma_i^s(E_p,E_u)\gamma_i^s(Z,U)\nu_i^s(UVW)R_i^s(E_p,E_u)\lambda_i^s(E_i)} \quad , \qquad (1\text{-}20)$$

where superscript s denotes physical quantities for the reference standard of i-th element. One can further put the equation (1-20), as convincing assumptions, to

$$X_i = \frac{I_i}{I_i^s} \times \frac{C_i^s\, N_i^s\, R_i^s(E_p,E_u)\lambda_i^s(E_i)}{N \cdot R_i(E_p,E_u)\lambda_i(E_i)} \quad , \qquad (1\text{-}21)$$

where C_i^s is the concentration of i-th element in references standard. Therefore the concentration can be estimated if N, R and λ are known with the ratio I_i/I_i^s experimentally obtained.

Another formalism was proposed by Chang (1974). In this case an Auger signal intensity ratio of reference standard with an arbitrarily chosen standard, i.e.,

$$\alpha_i = I_a^s/I_i^s \qquad (1\text{-}22)$$

is used. I_a^s denotes the Auger signal intensity of an arbitrarily chosen (e.g., Ag) standard. The factor α is called "inverse Auger sensitivity factor". Then, using equation (1-21) and (1-22) we obtain

$$X_i = \frac{\alpha_i \, I_i \, C_i^s \, N_i^s \, R_i^s(E_p,E_u) \lambda_i^s(E_i)}{I_a^s \, N \, R_i(E_p,E_u) \lambda_i(E_i)} = \frac{I_a}{I_a^s} \beta_i \qquad (1\text{-}23)$$

Here, β_i is represented by

$$\beta_i = \alpha_i \times \frac{C_i^s \, N_i^s \, R_i^s(E_p,E_u) \lambda_i^s(E_i)}{N \, R_i(E_p,E_u) \lambda_i(E_i)} \qquad (1\text{-}24)$$

and it denotes 'inverse Auger sensitivity factor' taking into account the 'matrix effects'. Equation (1-23), then, becomes,

$$X_i = \frac{\beta_i \, I_i}{\sum_j \beta_j \, I_j} \qquad (1\text{-}25)$$

(for all elements)

which indicates that the signal intensity of the reference standard does not need to be recorded if once β_i is obtained. Of course, the signal intensity must be measured under the same experimental conditions. Both of the methods need precise knowledge about R and λ. As to the binary and ternary alloys, Hall et al. (1977a, b, 1979) proposed the use of relative sensitivity factors through the investigation of matrix dependent parameters. Their formulations are as follows; the concentration of an element in a binary alloy AB can be expressed with relative sensitivity factor P_{rel} by the equation,

$$X_A = \frac{I_A}{I_A + I_B \, P_{rel}} \qquad (1\text{-}26)$$

Here P_{rel} is a factor which is necessary to correct the different Auger yield of A and B in an composition, which can be written explicitly by

$$P_{rel} = \frac{I_A}{I_B} = \frac{f(X_A)}{f(X_B)} \quad (1\text{-}27)$$

where

$$X_A f(X_A) = \frac{I_A}{I_A^\circ} \quad (1\text{-}28\text{-}a)$$

$$X_B f(X_B) = \frac{I_B}{I_B^\circ} \quad (1\text{-}28\text{-}b)$$

I_A° and I_B° are the signal intensity of pure A and B element, respectively. Though the matrix sensitive factor $f(X_A)$ and $f(X_B)$ strongly depend on the value of X_A and X_B, the ratio shown in equation (1-27) can be considered to be constant for many sets of binary alloys. Their results are shown in Table 1-2 with standard deviations. (Here, P^S_{rel} is the relative sensitivity factor after sputtering, and it is related with P_{rel} by $P^S_{rel} = R \cdot P_{rel}$, where R denotes the ratio of sputtering yield of A and B). As can be seen in the Table 1-2, the standard deviation is small especially for binary alloys of Ni-Cr and Ta-Si. It is probably because of the similarity of the atomic number effect in the former alloy and of the closeness of the Auger excitation energy in the latter.

Table 1-2 Relative sensitivity factors for binary alloys. (Hall et al. 1977a)

Element pair A–B	Peaks used (eV)		AES system	Sputter ion voltage (kV)	Primary electron voltage (kV)	Number of points	Concentration range		P^S_{rel} (A, B)	Std. dev. on P^S_{rel}	Std. dev. P^S_{rel} (%)
	E_A	E_B					$C_{A_{min}}$	$C_{A_{max}}$			
Fe–Cr	703	529	M	2	5	12	0.01	0.989	0.66	0.19	29
Fe–Cr	703	529	C	1	5	11	0.01	0.972	0.91	0.23	25
Ni–Cr	845	529	M	2	5	5	0.35	0.78	0.45	0.05	10
Ni–Cr	845	529	C	1	5	5	0.35	0.78	0.62	0.06	9
Ag–Cu	356	920	B + F	1.5	1.7	6	0.05	0.80	4.5	1.0	22
Ta–Si	1680	1619	M	1	3	4	0.09	0.94	0.90	0.07	8
Au–Cu	2024	920	C	1	5	11	0.04	0.97	0.184	0.06	33
N–Ti	381	418	M	2	5	6	0.06	0.55	1.20	0.17	14
O–Ti	510	418	M	2	4	6	0.04	0.26	1.53	0.14	9

1-3-2 Physical quantities for quantitative correction

A) Inelastic mean free path of Auger electrons

The inelastic mean free path of an electron, which is often used as a measure of the depth detected by AES, has been studied both in theory and experiment. Seah and Dench (1979) have compiled about 350 experimental results for the inelastic mean free path, and proposed empirical formulae for elements, inorganic compounds, organic compounds and adsorbed gases which are most useful for quantitative estimation by AES. Their results were given through the least square fit to the relation,

$$\lambda = \frac{A}{E^2} + BE^{1/2} \quad , \tag{1-29}$$

where E denotes the kinetic energy of an (Auger) electron above the Fermi level in eV. The E^{-2} dependency in the low energy region was also shown by the simple estimation by Sze et al (1964). For high energy electrons (above 150 eV), Penn (1976) has obtained the following formula for free-electron-like materials,

$$\lambda = \frac{E}{a(\ln E + b)} \quad , \tag{1-30}$$

which shows $E^{0.77}$ dependency in the middle energy range instead of the empirical value of 0.5. The resultant empirical formulae are,

i) for elements

$$\lambda_m = \frac{538}{E^2} + 0.41(aE)^{1/2} \quad \text{(monolayers)}, \tag{1-31-a}$$

where a is the monolayer thickness in nanometers,

ii) for inorganic compounds

$$\lambda_m = \frac{2170}{E^2} + 0.72 \cdot (aE)^{1/2} \quad \text{(monolayers)} \quad , \qquad \text{(1-31-b)}$$

iii) for organic compounds

$$\lambda_d = \frac{49}{E^2} + 0.11 \cdot E^{1/2} \qquad (\text{mg cm}^{-2}) \qquad \text{(1-31-c)}$$

In this case the path in mass thickness unit gives the least square fit.

The comparison of the empirical formula with the experimental results (for element) is shown in Fig. 1-11. Seah and Dench have also discussed the interatomic difference of the inelastic mean free path, which is also useful for the estimation of matrix sensitive sensitivity factor β.

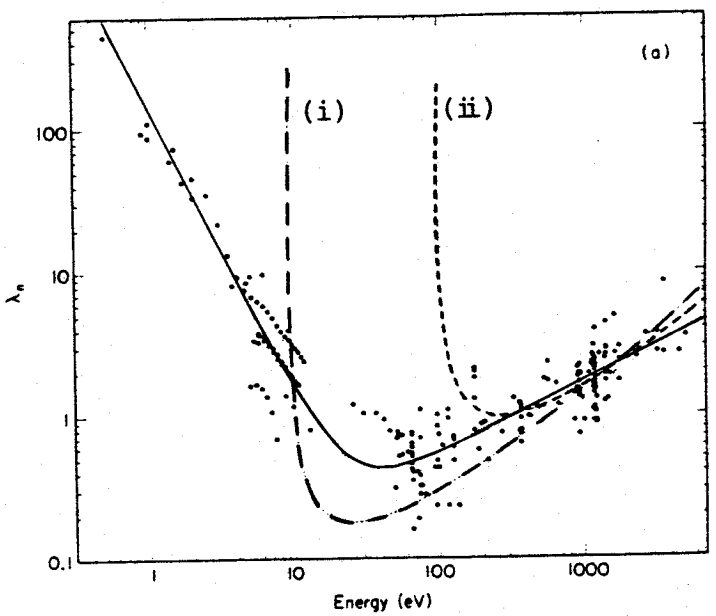

Fig. 1-11 Inelastic mean free path of electrons in nanometers (λ_n):
solid line; least square fit by Seah and Dench (1979)
i); Penn's calculation (1976)
ii); least square fit above 150 eV (Seah and Dench 1979)

B) Backscattering factor

The correction factor $R(E_p,E_u)$ for additional ionization due to backscattered electrons can be represented by

$$R(E_p,E_u) = 1 + \frac{\int_\Omega \int_{E_u}^{E_p} \sec\theta \frac{d^2\eta}{dE\, d\Omega} \sigma(E,E_u)\, dE\, d\Omega}{\sec\psi\ \sigma(E_p,E_u)} \qquad (1\text{-}32)$$

Here $\frac{d^2\eta}{dE\, d\Omega}$ denotes the energy- and angular distribution of backscattered electrons, while the incident angle ψ of primary electrons and ejection angle θ of backscattered electrons are measured from the surface normal. The second term of the right hand side of equation (1-32) represents a ratio of Auger signal intensity excited by backscattered electrons with that by primary electrons.

i) Experimental determination of R

Experimental determination of R is very scarce.

Usually, following equation

$$\int_\Omega \sec\theta \frac{d^2\eta}{dE\, d\Omega} d\Omega = \overline{\sec\theta} \frac{d\eta}{dE} \qquad (1\text{-}33)$$

($\overline{\sec\theta}$: mean ejection angle)

was assumed in the experimental estimation of R, and a theoretical expression for the ionization cross section was used with experimentally obtained energy distributions. (Gerlach and DuCharme, 1972). Smith and Gallon (1974), on the other hand, obtained both the ionization cross-section formula as well as the backscattering factor by an iteration method as follows; Auger signal intensity

$$I_A = I_p \sec\psi\ \sigma(E_p,E_u) + I_p \overline{\sec\theta} \int_{E_u}^{Ep} \sigma(E,E_u) \frac{d\eta}{dE} dE \qquad (1\text{-}34)$$

is measured for different primary energies and those are used as the first approximation for $\sigma(E, E_u)$. Then, the second term of

equation (1-25) was calculated using the measured energy distribution of backscattered electrons, and the cross-section was modified taking into account the contribution of the second term. The procedure was repeated until consistent results were obtained. Their results for the backscattering factor seem to be reliable since the ionization cross-section agrees reasonably well with theory. Moreover, as the theoretical ionization cross-section formula has yet to be well studied especially for outer shells of high atomic number (Powell 1976), the method explored by them is very useful.

Another experimental method for the estimation of R was reported by Goto et al (1975). Applying the evaporation technqiue, they estimated the Auger signal intensity of Be on Cu due only to primary electrons by the extrapolation, so called the δ-η method. Their method can be applied to other materials on the condition that the uniform film of an element can be obtained by vacuum evaporation.

The backscattering factors which are obtained experimentally up to this time are compiled by Jablonski (1979a) which is shown in Tab. 1-3.

ii) Theoretical estimation of R

Theoretical estimation of the backscattering factor has been attempted by the Monte Carlo simulation method as an extension of quantitative correction in EPMA since Bishop and Riviere (1969). Recently, Jablonski (1979b) calculated it for K-shell excitation of C, Mg, Al, and Si. Since the screened Rutherford cross-section,

$$\frac{d\sigma}{d\theta} = \frac{Z^2 e^2}{4E^2 (1-\cos\theta + 2\beta)^2} \quad , \qquad (1\text{-}35)$$

(β : screening parameter)

is used for describing elastic scattering in the simulation, this method is liable to considerable errors for heavy elements and relatively low excitation energies.

Table 1-3 Experimental backscattering factors in AES (Jablonski 1979a)

Element	Atomic number	Auger electron energy[a] (eV)	Primary energy (eV)	Reduced energy	Experimental method	Backscattering factor
Be	4	104	800		Goto *et al.*	1.1
			1000			1.2
			1500			1.2
			2000			1.25
C	6	272		2	Gallon	1.11[b]
				3		1.15[b]
				4		1.18±0.03[b]
				5		1.21[b]
Si	14	120–510 C, N, O, P, S, Cl on Si single crystals		3.33–10	Meyer and Vrakking	1.2±0.1
Si	14	510 O on Si(100)		1.88	Meyer and Vrakking	1.26±0.10
				2.82		1.30±0.10
				4.69		1.32±0.10
		152 S on Si(100)		4.55		1.51±0.10
				12.20		1.62±0.10
Si	14	92		3	Gallon	1.32[b]
				4		1.38[b]
				5		1.42[b]
				6		1.47[b]
				7		1.51[b]
				8		1.55[b]
				9		1.58[b]
				10		1.60[b]
Ge	32	120–510 C, N, O, P, S, Cl on Ge single crystals		3.33–10	Meyer and Vrakking	1.3±0.1
Se	34	99		2	Gallon	1.27[b]
				3		1.38[b]
				4		1.46[b]
				5		1.53[b]
				6		1.59[b]
Ag	47	351, 356		2	Gallon	1.34[b]
				3		1.45[b]
				4		1.51[b]
				5		1.55[b]
Gd	64	138		3	Gallon	1.53[b]
				4		1.66[b]
				5		1.82[b]
W	74	272 C on W(100)		1.06	Gerlach and DuCharme	1.06[d]
				1.41		1.20[d]
				1.76		1.26[d]
				2.46		1.34[d]
				3.52		1.36[d]
				4.23		1.40[d]
				5.29		1.52[d]
Au	79	69		1.5[c]	Gallon	1.28[b]
				2[c]		1.52[b]
				3[c]		1.77[b]
				4[c]		1.88±0.05[b]
Au	79	69	2000		Gallon	1.94±0.08

[a] Energies reported in *Handbook of Auger Electron Spectroscopy*
[b] Values taken from the plot.
[c] Scaled using the ionization energy of the N_{45} shell, i.e. 350 eV.
[d] The relation between the parameter γ_B of Gerlach and DuCharme and r given by Eqn (12) has the form $r \doteq 1 + 2\gamma_B$.

C) Ionization cross-section formula

As is seen in equation (1-32), a precise knowledge of ionization cross section is inevitable to perform accurate quantitative correction. Although theoretical expressions of ionization cross-section have been reported, we do not have, at the moment, comprehensive theoretical equations which cover all the inner-shell electrons of different energy levels except for K-shell and L-shell electron excitations of specific element. The ionization cross-section formulae are reviewed in detail by Powell (1976).

Among those theoretical ionization cross-sections, the excitation function derived by Gryzinski (1965) describes to some extent the energy loss of penetrating electrons due to inner-shell electron excitations. The formula is described in Section 3-3. Other typical theoretical expressions used in practical calculations are as follows;

i) Worthington and Tomlin (1956)

$$\sigma(E_p) = \frac{6.51 \times 10^{-14}\, n}{E_p\, E_u} \cdot b \cdot \ln\frac{4E_p}{B} \quad , \qquad (cm^2 \cdot eV^2) \qquad (1\text{-}36)$$

and

$$B = [1.65 + 2.35(1-\frac{E_p}{E_u})]\, E_u$$

$$b = \begin{cases} 0.35 & \text{for K-shell electrons} \\ 0.25 & \text{fro L-shell electrons} \end{cases}$$

ii) Fabre de la Ripelle (1949)

$$\sigma_K(E_p) = \frac{1.302 \times 10^{-13}\, \ln(E_p/E_K)}{E_K^2\, k(E_p/E_K + x_K)} \qquad (cm^2 \cdot eV^2) \qquad (1\text{-}37)$$

iii) Bethe (1930)

$$L(E_p) = \frac{6.51 \times 10^{-14}}{E_p \cdot E_u} \cdot Z_L \; b_L \cdot \ln\left(C_L \cdot \frac{E_p}{E_L}\right) \quad (cm^2 \cdot eV^2), \qquad (1\text{-}38)$$

where

$b_L = 0.55$ and $C_L = 1$.

The ionization cross-sections given by these formula is shown in Fig. 1-12 as a function of E_p/E_c (Ec : critical ionization energy), where the values are normalized at $E_p/E_c = 3$. As seen in the figure, the cross-section steeply increases from $E_p/E_c=1$ reaching to the maximum value at about $E_p/E_c=3$, then it gradually decreases. Formulae in ii) and iii) are used in the estimation of intensity ratio of KLL and LVV Auger signals from Al by Powell (1977) (see Section 1-3-1).

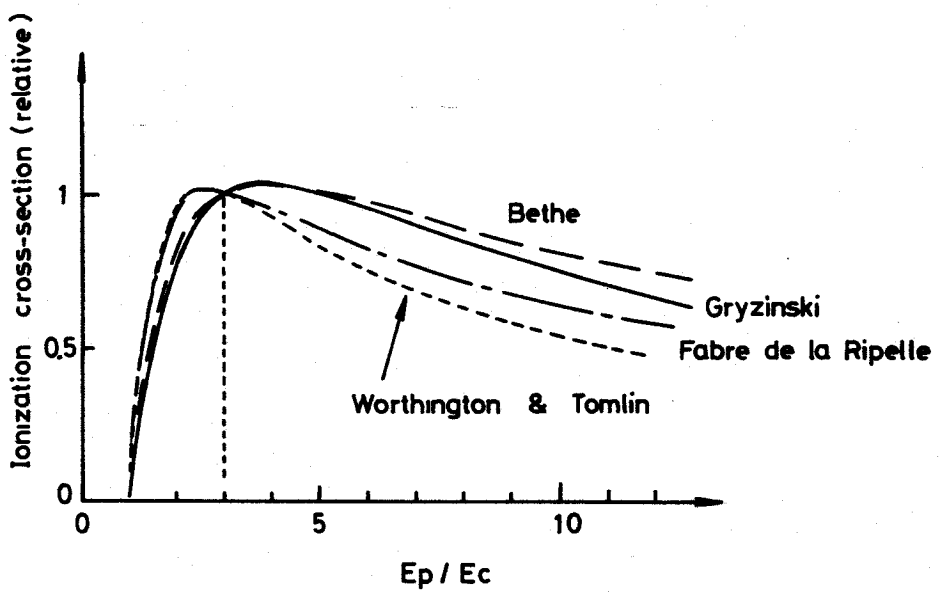

Fig. 1-12 Comparison of the theoretical ionization cross-sections as a function of over-voltage ratio (Ep/Ec). All the results are normalized at Ep/Ec = 3.

1-4 Conclusions

The present status of high spatial resolution surface analysis by scanning Auger electron microscopy and the status of quantitative analysis by AES were described in this chapter.

A description of the general aspect of AES, i.e., the principles of the Auger process and the features of AES as a technique for surface study, was followed by a description of various approaches for improvement of the spatial resolution of surface analysis by AES. These are,

1) to reduce the electron beam size by use of a high brightness electron source,

and

2) to improve the signal to noise ratio by the effective Auger signal detection.

Those approaches have succeeded in obtaining high spatial resolution of submicrons in the surface analysis.

AES under such a high spatial resolution, however, has another problem, i.e., electron beam damage, due to high density and high energy of primary electrons. Some attempts to reduce the damage were described in this chapter, and the possibility of reducing it by improving the Auger signal detection method was also pointed out.

Next, the present status of quantitative analysis was described. Some practical approaches to the quantitative analysis by AES were introduced. Many problems which are often called 'matrix effect' and make quantitative analysis difficult were also discussed. Through out the discussion, the necessity of precise knowledge about the backscattering correction factor

was stressed. Some experimental and theoretical attempts to obtain the factor were described. The necessity and possibility of estimating it by theoretical calculations with a more exact treatment of electron scattering in a specimen was also suggested.

Chap. 2 Approaches to High Spatial Resolution Measurement with SAEM

2-1 Introduction

With the development of SAEM, requirements for local surface analysis have been increasing especially in fields of semiconductor technology and metallurgy, where the size of objects for analysis is in the order of microns to submicrons (Inoue et al. 1976, MacDonald et al. 1977, Janssen et al. 1977b).

To obtain high resolution images with an SAEM, the primary electron beam must be focused as finely as possible, the same as an SEM, but at the cost of primary beam current. In SAEM, however, we need a rather large primary current as compared to an SEM since the excitation probability of an Auger electron by a primary electron is very small (typically in the order of $\sim 10^{-5}$) (Bishop and Riviere 1969). So Auger signals must be detected efficiently to assure a reasonable signal to noise ratio under conditions of fine measurements.

This chapter describes some newly developed practical attempts for obtaining Auger images with high spatial resolution, especially in the range of submicrons, using conventional SAEM.

First, in Section 2-2, a modulation technique which is often used in phase sensitive detection is examined and improved. Instead of sinusoidal wave modulation, which has been most commonly used in AES since Harris (1968) adopted it, the square wave modulation technique was developed and applied to AES with considerable success to improve the signal to noise ratio in an Auger image.

For wider practical use in SAEM this square wave modulation technique has been successfully combined with the digital scanning systems of a commercial type SAEM, JEOL JAMP-3.

The synchronization of signal modulation with the scanning of Auger images has also improved the degradation of Auger images by moire which will be discussed in Section 2-3.

In Section 2-4, digital systems which were designed for Auger signal processing are described in detail. That is, in Section 2-4-1, the signal processing system for 'real time' observation of an Auger image was devised and its usefulness was confirmed by comparing the Auger image with those obtained by the ordinary system. It should be mentioned that the synchronization and the new system for Auger mapping were developed in cooperative research with Mr. K. Goto.

In parallel with these researches, another digital system based on the use of a micro-computer was devised particularly to attain accurate and high energy-resolution measurement of Auger spectra. The design and performance of the new system are described in Section 2-4-2.

Finally, in Section 2-5, an approach to high spatial resolution measurement in the SAEM by use of the LaB_6 cathode is described. The single crystal LaB_6 cathode developed by Shimizu et al. (1975a,b, 1977b) as a conventional electron probe instrument was applied to attain high spatial resolution scanning Auger electron microscopy with JAMP-3.

2-2 Signal modulation technique in AES and square wave modulation technique as newly applied for SAEM

2-2-1 Principle of sinusoidal wave modulation technique and its disadvatage

Since Harris (1968) pointed out that the derivative of the energy distribution provides a more sensitive means of detecting Auger electrons, sinusoidal modulation techniques have been commonly used in AES. Figure 2-1 shows the schematic diagram for measuring Auger signals with a cylindrical mirror analyzer (CMA) in its derivative mode spectra, dN(E)/dE.

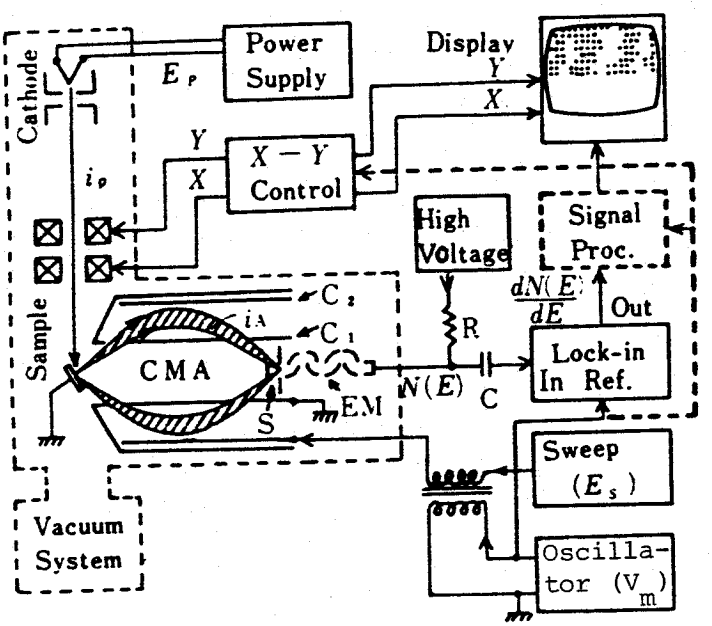

Fig. 2-1
A schematic diagram for Auger signal detection with CMA

Secondary electrons are energy-analyzed by the CMA and those which have an energy E corresponding to the deflection voltage V of the CMA are passed through the exit slit and detected. If a small modulation signal $\Delta V=V_m \sin\omega t$, where V_m denotes the modulation amplitude, is superimposed on the deflecting voltage, the

number of detected secondary electrons can be described by the following equation using Taylor series expansions,

$$N(E+\Delta E) = N(E) + \frac{dN(E)}{dE}\cdot E_m \sin\omega t + \frac{1}{2}\cdot\frac{d^2N(E)}{dE^2}\cdot E_m^2 \sin^2\omega t + \frac{1}{3!}\cdot\frac{d^3N(E)}{dE^3}\cdot E_m^3 \sin^3\omega t + \text{-----} \quad . \qquad (2\text{-}1)$$

Here, E_m ($=CV_m$: C is a constant) is the amplitude in energy corresponding to V_m and ω the modulation frequency. The various powers of the sine function are then converted to harmonics through the use of trigonometric identities and the coefficient of the first and second harmonics are (Taylor 1969)

$$\text{first harmonic} = E_m\cdot\frac{dN(E)}{dE} + \frac{E_m^3}{8}\cdot\frac{d^3N(E)}{dE^3} + \frac{E_m^5}{192}\cdot\frac{d^5N(E)}{dE^5} + \text{---} \quad , \qquad (2\text{-}2)$$

$$\text{second harmonic} = \frac{E_m^2}{4}\cdot\frac{d^2N(E)}{dE^2} + \frac{E_m^4}{48}\cdot\frac{d^4N(E)}{dE^4} + \frac{E_m^6}{1536}\cdot\frac{d^6N(E)}{dE^6} + \text{----} \quad . \qquad (2\text{-}3)$$

It is clear from equation (2-2) that the second and the following term in the equation make little contribution to the first harmonic in the case of small modulation amplitude. Therefore, using the phase sensitive detection system (lock-in amplifier in Fig. 2-1) with reference frequency of ω, we can detect signals corresponding only to the derivative of the energy distributions.

The dN(E)/dE mode spectra have their merits in emphasizing

small changes (peaks and hamps) in the energy distributions of secondary electrons which just correspond to Auger signals. In this detection mode, however, the modulation amplitude V_m must be small to assure that the first harmonic of the collected signals is equivalent to the second term in equation 2-1, i.e., the derivative of N(E). The distortion of detected signals from the derivative of energy distributions with large modulation amplitude was discussed in detail by Taylor (1969) in relation to Auger peak width. He estimated percentage deviation below proportionality between fundamental (first harmonic) signal and modulation amplitude assuming that the Auger peak has a Gaussian distribution. The result showed that the deviation comes up to ∿9% even in the case that 2Em/FWHM (full width at half maximum) equals 0.5. Thus, the modulation amplitude must be set small in order to assure a linear relation between detected signals by a lock-in amplifier and dN(E)/dE at the cost of signal to noise ratio.

Another probelm of measuring Auger spectra in dN(E)/dE mode becomes serious in the use of quantitative analysis by AES. The derivative mode spectra are sensitive to the deformation of Auger peak shape which are often observed in valence band spectra. Therefore the peak height of Auger peaks in the derivative mode cannot be simply related to the concentration of each element which is discussed in detail in the Chapter 1.

2-2-2 Square wave modulation technique as newly applied to SAEM

Compared to the dN(E)/dE mode spectra discussed in the

previous section, N(E) mode spectra of Auger electrons provide some improvement in the signal to noise ratio (Grant et al. 1973, Houston 1974). This mode of spectra can be obtained by direct recording of collected signals passing through the CMA without any modulation, or by modulating primary beam intensity to utilize phase sensitive detection technique (Seah 1972).

The N(E) mode operation, however, inherently has a problem in subtracting the background level of the Auger electron spectrum. Grant and his coworkers (Grant et al. 1973, 1974a, b, c, Houston 1974a, b) could overcome this difficulty successfully by adoption of the dynamic background subtraction method which involves the multiple differentiation followed by the multiple integration of some experimental variable. It is clear that this method needs so much time that it cannot be easily applied to SAEM where 'real-time' data processing is required.

It has been recently reported that using the square wave modulation technique instead of the conventional sinusoidal one called tailored modulation technique would overcome problems mentioned above (Springer et al. 1975, Grant et al. 1976, Springer and Pocker 1977). This new technique has merits for both the N(E) and dN(E)/dE mode operations leading to substantial improvement in AES.

The principle of this modulation technique is shown schematically in Fig. 2-2 where an Auger signal is superimposed on the secondary electron energy distribution, i.e., background which is assumed to be linear for simplicity. On the condition that the modulation amplitude V_m is adequately chosen so that it is at least larger than a (see Fig. 2-2), we can obtain the signal

output V_{out} which is in principle equal to the peak height, i.e., $N(E_A)-B(E_B)$. This is true, of course, only in the case that the frequency characteristic of the lock-in amplifier is broadband, that is, all the harmonics are passed with the same amplification. This method also gives the dN(E)/dE mode spectra (strictly speaking, the difference spectra of N(E)) only using a small modulation amplitude.

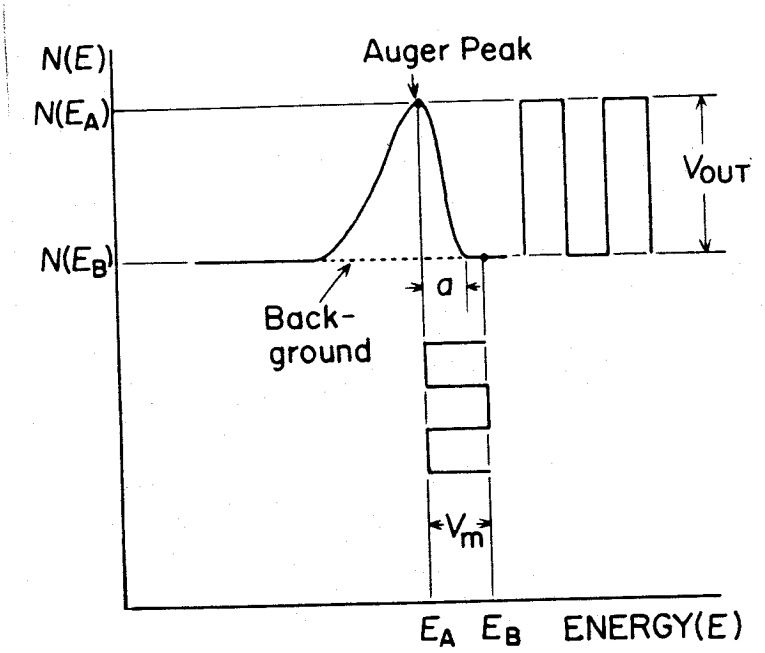

Fig. 2-2 Schematic illustration of square wave modulation. V_m; amplitude of modulation, E_A; maximum Auger peak energy, a; energy width between the maximum Auger peak and higher energy side of the Auger peak.

The features of this method are clearly shown in Fig. 2-3 where Ag-Auger spectra are recorded by these two modulation techniques. With small modulation amplitude both methods give

nearly the same spectra, but the peak to peak height of the Auger spectrum by the square wave method (solid lines) is larger than that by the sinusoidal one (dotted lines). It is obvious comparing the characteristics of the two methods that the ratio of the peak to peak heights obtained by these methods $(\text{P-P heights})_{\text{square}}/(\text{P-P heights})_{\text{sinusoidal}}$ comes up to $\pi/2$ in ideal conditions. Using large modulation amplitude the difference between two methods becomes clear. The spectra obtained by the square wave modulation show fine structures (double peaks) clearly while the spectra were deteriorated in the sinusoidal wave modulation.

Therefore, if output signals of the lock-in amplifier obtained by the square wave modulation technique with large modulation amplitude are used in an SAEM, we can get a Auger-map of an element whose brightness directly corresponds to the 'peak height' of the

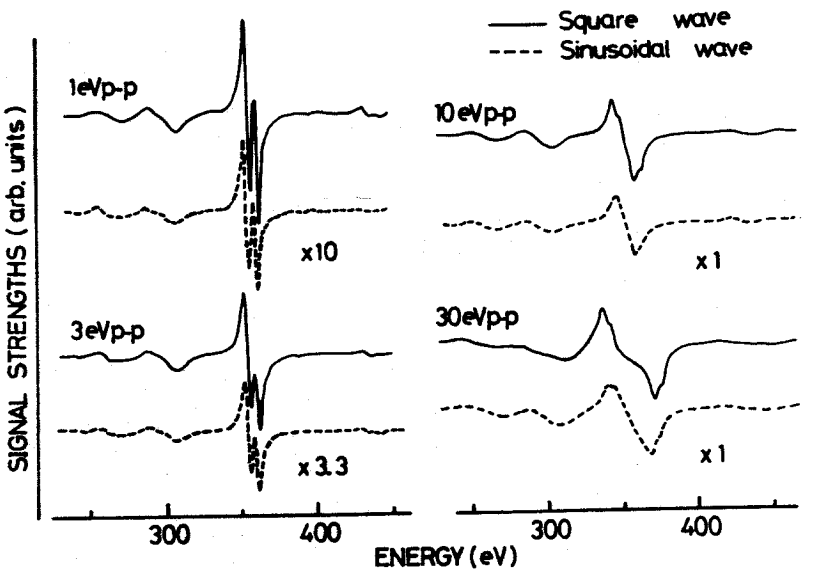

Fig. 2-3 Ag Auger spectra in dN(E)/dE mode obtained for an Ag-Cu alloy:
solid lines ; square wave modulation
dashed lines; sinusoidal wave modulation

Auger signal and the background is automatically eliminated on each surface point of analysis. Moreover the method can be expected to gives a higher signal to noise ratio in an Auger image than that by the ordinary method.

So the present technique was applied to a commercial type SAEM, JAMP-3, to confirm its usefulness through the direct comparison of Auger images of a silver-copper alloy for soldering. The result is shown in Fig. 2-4.

Figures 2-4(a) and (b) are the Cu(LMM) Auger electron images and each photograph was taken and processed under the same condition except for the modulation waveform. The modulation frequency was $\sim$3 kHz and the scanning speed, 400 seconds per frame. The time constant of the lock-in amplifier, Brookdeal 9402 whose frequency characteristic is broadband, was 1 msec. The primary beam current was $\sim 3 \times 10^{-8}$ A at 10 keV. These photographs show that the present technique (Fig. 2-4(a)) allows us to obtain the higher contrast scanning Auger electron images (high signal to noise ratio). The Ag(MNN) Auger electron image using this technique and the absorbed electron image of the same area are also shown in Fig. 2(c) and (d), respectively, and the former is in good contrast with (a). These figures show that the Auger images shown here have a submicron spatial resolution.

This technique will be easily extended to such a case that energy positions of the Auger signal peaks of different elements are close to each other and obtain the Auger images using the signal of each element. Therefore, it is ascertained that the square wave modulation technique is also as effective in SAEM as in AES.

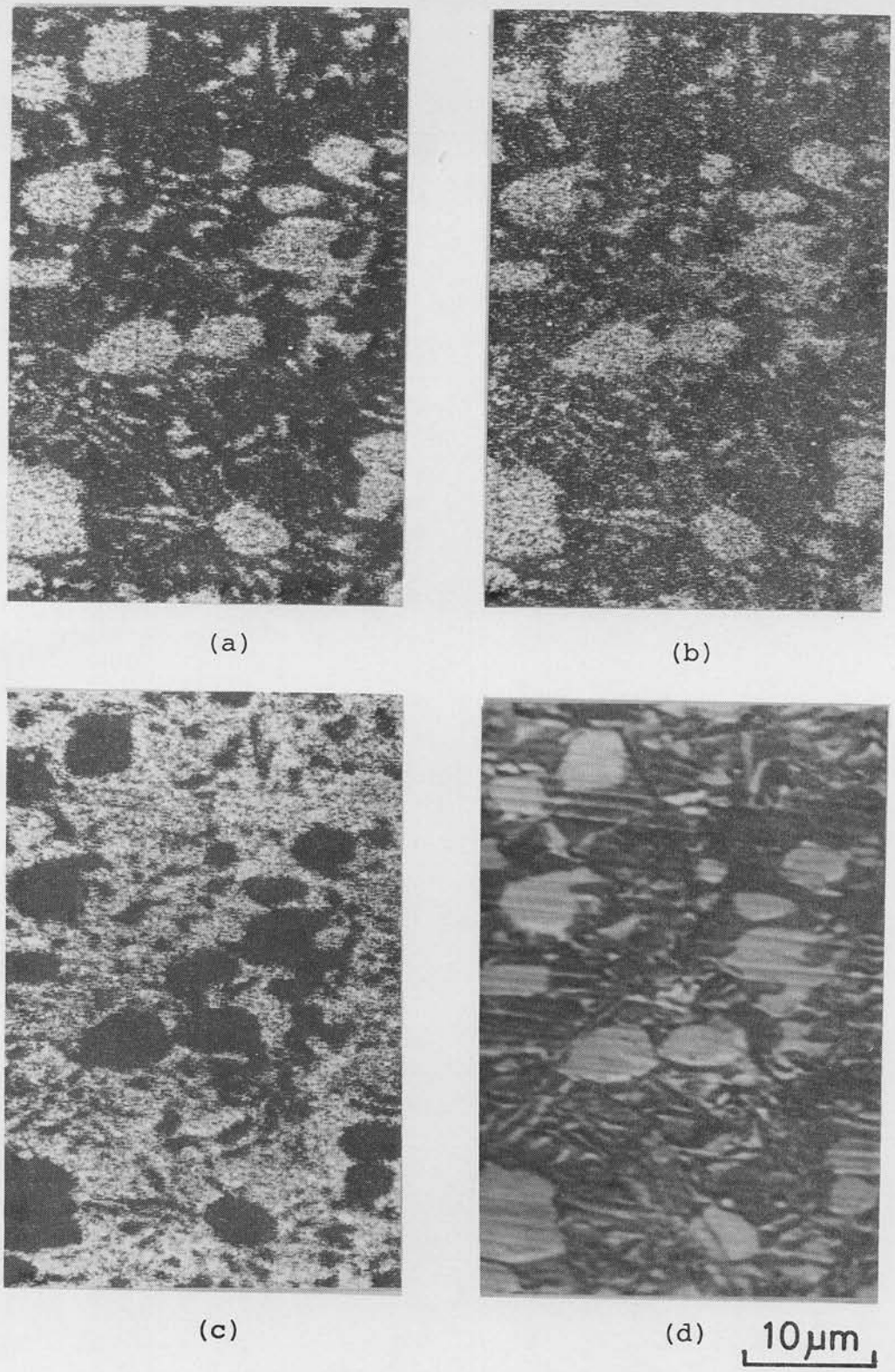

Fig. 2-4 Scanning Auger electron images ((a), (b), and (c)) and an absorbed electron image ((d)) of an Ag-Cu soldering alloy. (a) and (b) are Cu-signal (920 eV) images obtained by square and sinusoidal wave modulation, respectively, (c) is the Ag-signal (350 eV) one by square wave modulation. Modulation voltages are 30 eV_{p-p}.

2-3 Synchronization of signal modulation with electron beam scanning

Although the square wave modulation technique mentioned in the previous section has merits of both the background subtraction and high efficiency of Auger signal detection, one problem is still left. That is, it may lead to distortion of the Auger image when the modulation and scanning frequencies are comparable, i.e., the number of picture elements scanned per seconds and the modulation signal can interfere to results in a moiré image.

The mechanism of the degradation by moiré in an Auger image is shown schematically in Fig. 2-5(a), where the deflecting voltage is assumed to be modulated by a frequency of f (modulation amplitude is V_m). It is also assumed that the same amount of an element exists at analyzing points denoted by x_{n-1} (time period of electron beam scanning at the point is $t_{n-1} \leq t < t_n$) and x_n ($t_n \leq t < t_{n+1}$). The output signal of a CMA is also shown schematically in the right hand part of the figure. In the case that the modulation and the electron beam scanning are not synchronized, it is clear from the figure that the detected signal at the point of x_{n-1} is different from that at x_n (The detected signal corresponds to the difference between the shaded part and the white part in the figure). Therefore, this results in another variation of Auger image contrast in addition to that by the surface concentration.

An example of this moire image is shown in Fig. 2-5 (b) where

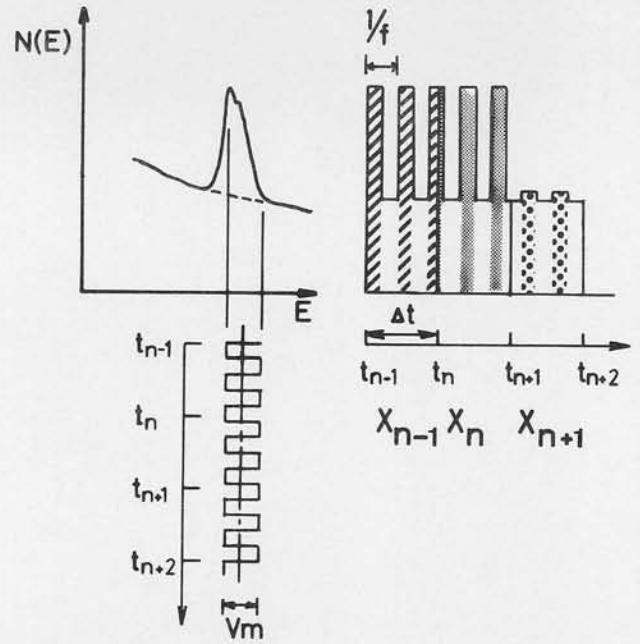

(a)

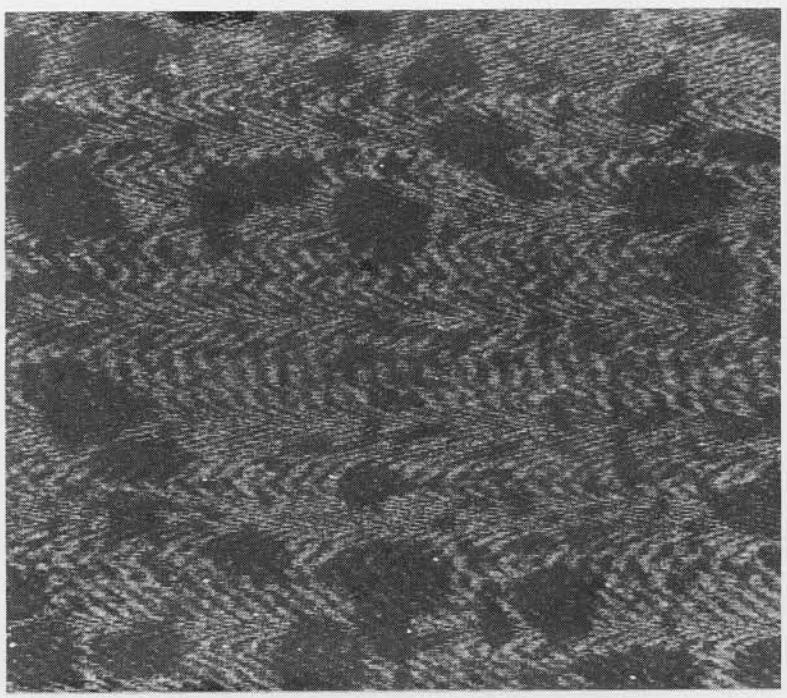

(b) 10 μm

Fig. 2-5 Principle and an example of moire image.
(a); schematic illustration of signal modification by moire
(b); Ag-Auger (350 eV) image deteriorated by moire (primary electron energy 10 keV, primary current $\sim 3 \times 10^{-8}$ A, and 30 eV_{p-p} modulation)

the overall quality of Ag Auger image is degraded. The moire can be changed with different modulation frequency and the number of stripes of the pattern roughly agrees with calculation. It should be mentioned that the SAEM used in this experiment is isolated from 60 Hz line frequency and other noise sources.

The phenomenon is not a problem when the modulation frequency differs by order of magnitude from the scanning rate, but it seems to be a severe restriction for electronic circuit considering the scanning speed of the SAEM.

To overcome this difficulty, synchronization of modulation with electron beam scanning was attempted (Goto et al. 1979). In the SAEM used here, a digital scan design is fortunately available which allows us to use the clock pulse of the image scan as the signal for CMA modulation. The circuit for the present purpose is shown in Fig. 2-6. The original clock pulse is fed to the digital scanning control circuits (X and Y) for the image display and to the modulation circuit, so that they are simultaneously driven from the same source. In the modulation, the original clock frequency, 360 kHz, is counted down by the two binary counter ICs(7493) by a factor 2^7 (128) to be 2.8 kHz. This frequency was chosen considering the characteristics of an isolation transformer. This frequency corresponds to four modulation pulses for one element of the SAEM image if we choose image elements of 512 x 512 for a frame and 400s per frame for the scanning speed. The resulting pulse height is adjusted by variable resistor VR and is then amplified to a desired amplitude for the CMA through the isolation transformer. The SAEM image of Ag-Cu soldering alloy obtained by using this circuit is shown in Fig.

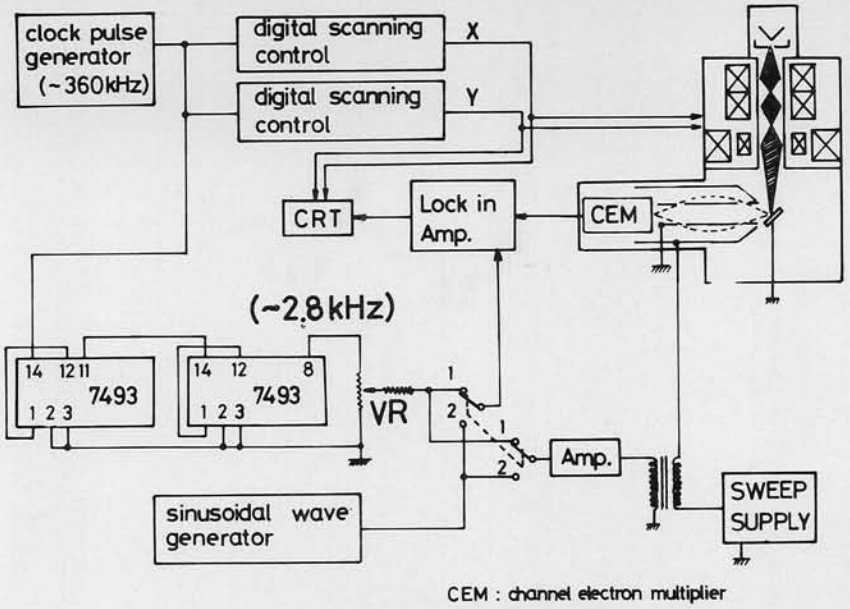

Fig. 2-6 A circuit for synchronous modulation with digital scanning systems (X,Y). Two binary counter ICs (7493), which count down the original 360 kHz to 2.8 kHz, are used to obtain a synchronized square wave.

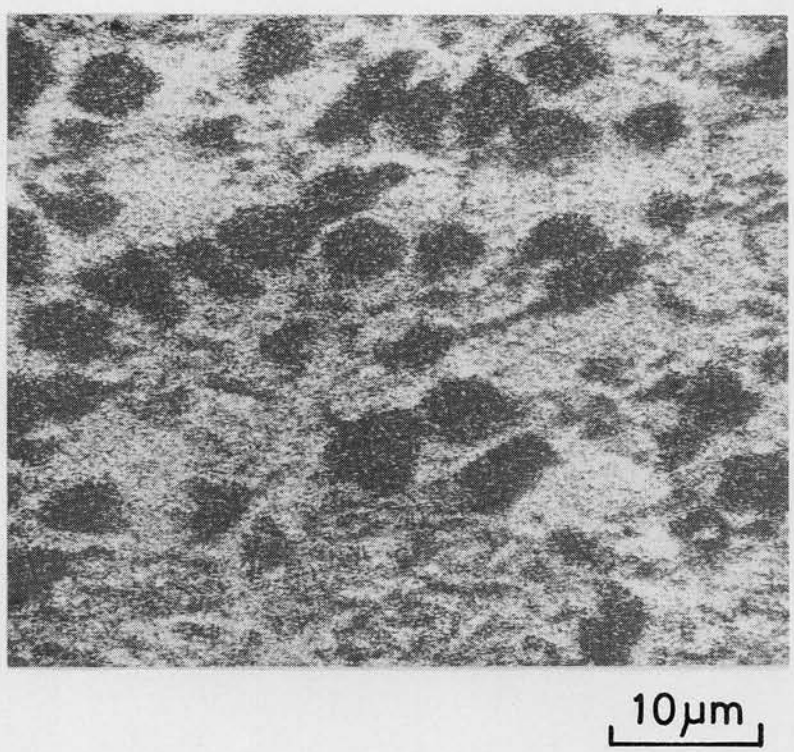

Fig. 2-7 Ag (350 eV) Auger image obtained by synchronized square wave modulation technique. Primary electron energy 10 keV, primary current $\sim 3 \times 10^{-8}$ A. Image elements 512 x 512 points, and frame time 400 sec.

2-7. The SAEM images have been taken under the following conditions. primary energy of 10 keV, primary current of $\sim 3 \times 10^{-8}$ A, amplitude of modulation 10 eV_{p-p}, time constant of lock-in amplifier of 1 ms, and image elements of 512 x 512 for a frame.

Comparing this picture with that shown in Fig. 2-5(b), it is clear that the degradation of Auger image by moiré is much improved and that synchronous modulation associated with the square wave technique allows for the use of any modulation frequency. This technique, therefore, enables the operation of SAEM in the optimum condition determined from capacitive couplings and other design characteristic of the detector electronics, leading to more flexible analysis for various types of sample and research programs with an SAEM.

2-4 Applications of digital control systems to SAEM

2-4-1 Real time signal processing in an Auger image.

The new modulation technique and the synchronization of modulation mentioned in the previous section have provided considerable improvement in an Auger image. However, the noises in the Auger signal have been processed only by photographic integration on film with photographic equipment and by the time constant of the lock-in amplifier. It is true that we can have an Auger image with enough signal to noise ratio by the use of a large time constant, but at the cost of spatial resolution. That is, the integrated signal at one point of analysis shall affect the signal which should be detected at the next and following points due to the delay characteristic of integration circuits in the lock-in amplifier.

The signal integration adoped by MacDonald and Waldrop (1971) which is mentioned in Section 1-2 is very useful. The technique, however, needs such a long time for signal acquisition that we cannot get an Auger image by 'real time' processing. The counting method by Browning et al. (1977a,b) is one such type of system that would meet the requirement of 'real time' data processing, but because of its N(E) mode its use is fairly limited to the ranges of lower signal intensity in order to avoid satulation (due to counting capability) of the channeltron used.

Therefore, the signal processing technique is still open to further improvement and the technique combined with the previous ones (in 2-2 and 2-3) seems to be most desirable.

Hence a new signal processing system for Auger electron mapping was approached (Goto et al. 1980) and the schematic illustration of the characteristic and electronic circuit for this are shown Fig. 2-8 and Fig. 2-9, respectively.

In figure 2-8, it is assumed that an element exists at a point denoted by x_n and the output signal of the CMA is phase sensitively detected by a lock-in amplifier with a small time constant compared to the dwelling time at each point. (The signal modulation at the CMA is, of course, synchronized with electron beam scanning.) Therefore, the output signal from the lock-in amplifier which has a relatively large noise steeply rises up at $t = t_n$ and falls down at $t = t_{n+1}$. The signal from the lock-in amplifier is then converted to the digital one and counted throughout the dwelling time. The final value of the counter at the time $t = t_{n+1}$ which corresponds to the shaded portion of

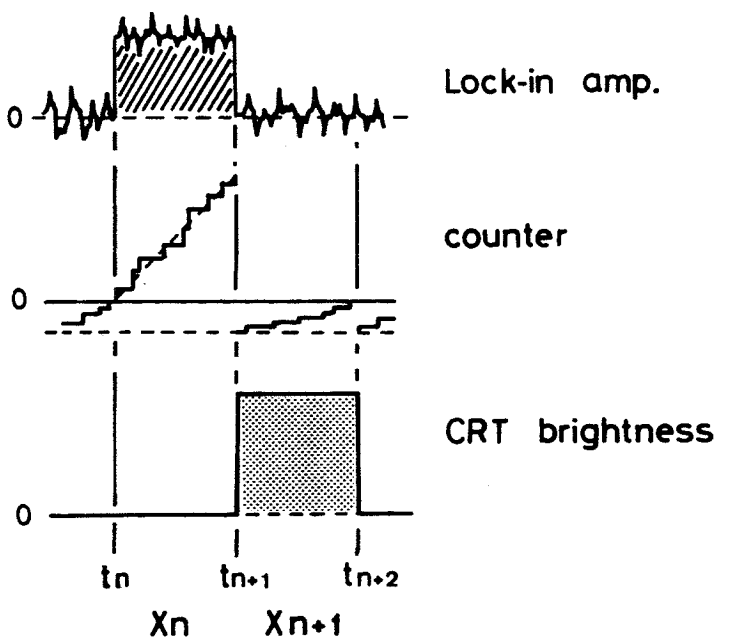

Fig. 2-8 Schematic illustration of the characteristic of the new processing system.

the output signal of the lock-in amplifier is latched and the brightness of a CRT is modulated by the amount during the next time period of $t_{n+1} \leq t < t_{n+2}$. Thus, the present system gives an Auger image without any reduction of spatial resolution due to signal processing.

As can be seen in Fig. 2-9, the signal from the lock-in amplifier is first amplified to a suitable level considering the intensity of the signal under ordinary operating conditions of the SAEM and the characteristic of a voltage to frequency converter (V/F) A-8400 used in the system. Since A-8400 is sensitive for only the positive polarity range, the input signal of the V/F is properly biased at half of the input dynamic range. Therefore, the negative signal due to the noise in the negative side (no signal input is assumed to be zero level) is also converted to the digital pulses which act to setoff noise in the positive side (see also Fig. 2-8) This results in an Auger image

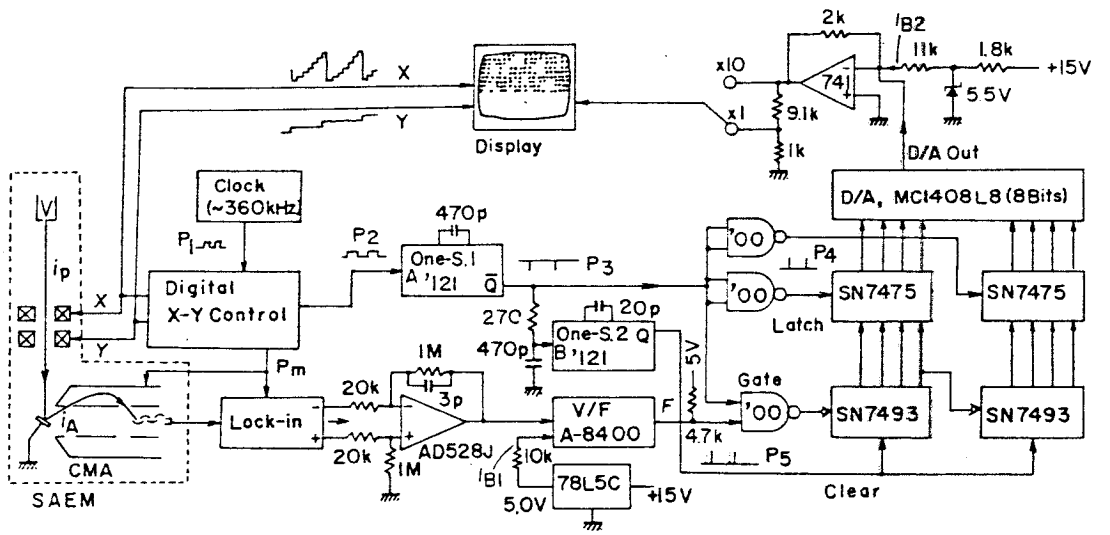

Fig. 2-9 Schematic diagram of SAEM and circuits for digital integrator. (R; in ohms, C; in farads)

with an improved signal to noise ratio as compared to an image obtained by an ordinary system with a small time constant.

All the counters (SN 7493), latches (SN 7475) and gates (SN 7400) are controlled by the clock pulse of the SAEM, JAMP-3, through the one-shot (SN 74121) for pulse shaping.

The usefulness of the present system was confirmed by comparing the Auger image with that obtained by the ordinary system, as is shown in Fig. 2-10.

They are Ag Auger images of Ag-Cu soldering alloy, where the primary energy and current of the SAEM for the observation were 10 keV and $\sim 3 \times 10^{-8}$ A, respectively. The picture elements were 256 x 256 and the frame time was 190 sec., so the dwelling time for each point was 2.7 msec. Figure 2-10(a) was taken using a conventional method with a time constant of 3 msec., while Fig. 2-10(b) was taken using the present system. The time constant of the lock-in amplifier was chosen to 0.1 msec. in the latter, which was short enough compared to the dwelling time to assure a steep change of the signal. It is also mentioned that the time which is required for the 'latch' and 'clear' (less than 1 μsec) of the signal is also short enough as compared to the dwelling time.

Comparing the image shown in Fig. 2-10 (a) with the image (shown in Fig. 2-10 (b)) by the present system, a considerable improvement in the spatial resolution can easily be seen.

Therefore, it is ascertained that the present system is very useful for signal processing in the Auger image.

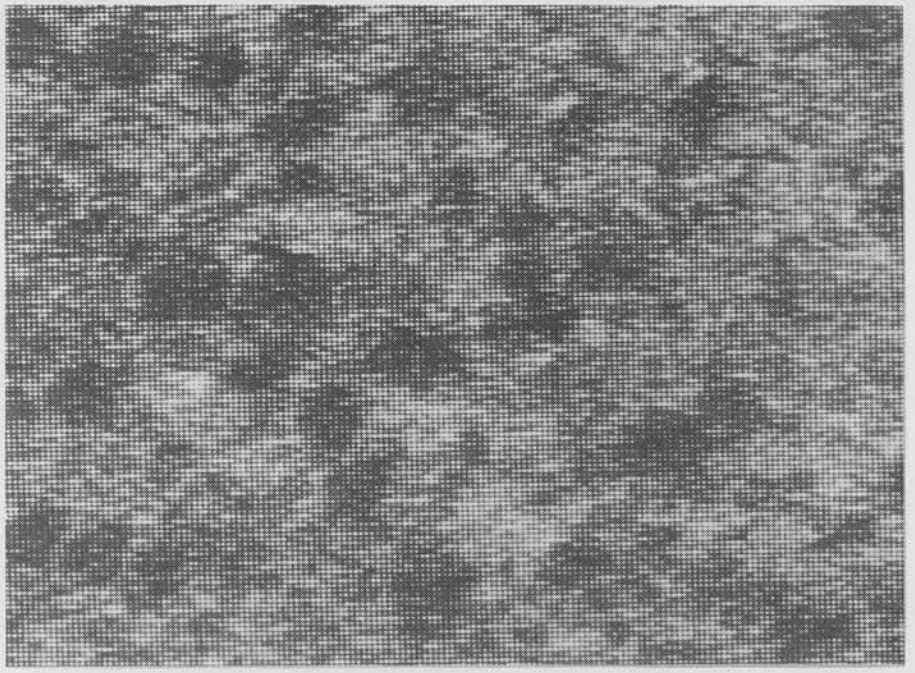

(a)

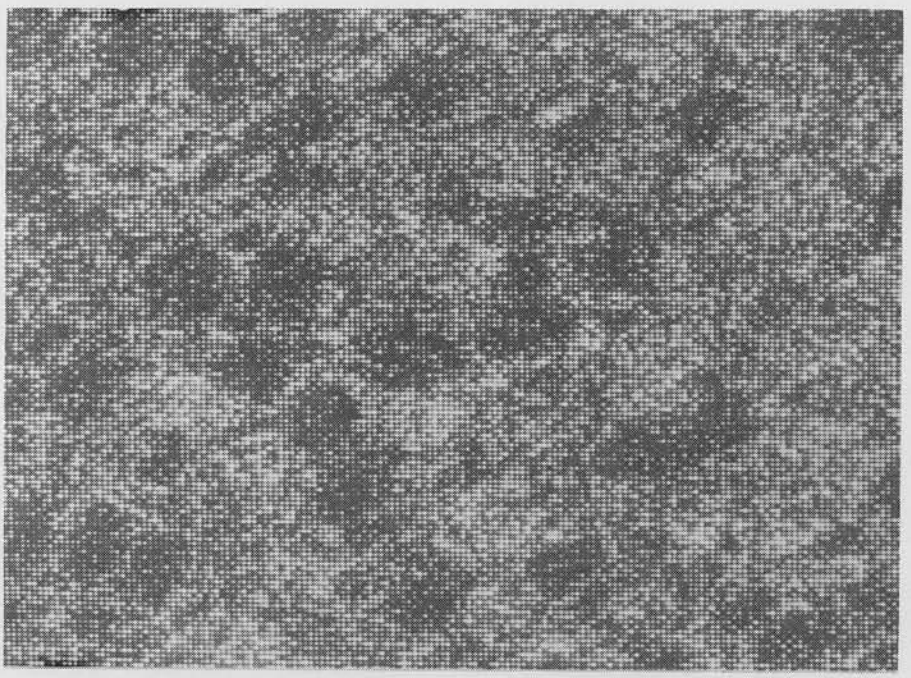

(b)

10μm

Fig. 2-10. Ag-Auger (350 eV) images of Au-Cu soldering alloy.
(a); Auger image obtained with relatively large time constant of the lock-in amp. (ordinary system)
(b); Auger image obtained with the present system with small time constant (0.1 msec.).
Both images were obtained under conditions of 10 keV, $\sim 3 \times 10^{-8}$ A, and 10 eV_{p-p} modulation. Dwelling time for one picture element was 2.7 msec. (190 sec./frame)

2-4-2 Applications of a micro-computer to SAEM

In the application of an SAEM to surface analysis, observation of Auger images has been substantially improved by the system described in the previous section (2-4-1). Another requirement for the surface analysis with an SAEM is the precise measurement of Auger signals at a local area of a specimen (point analysis). The accurate determination of Auger signal intensities is very important especially for quantitative analysis by AES.

It is true that the detected signals have a high signal to noise ratio due to the use of a large time constant of the lock-in amplifier, but at the cost of the energy resolution instead of the spatial resolution in an Auger image. Therefore the Auger signal has to be measured with a small time constant spending a relatively long time for signal acquisition. For this purpose, it seems desirable to measure the Auger spectrum in repetition since it will compensate such signal variations as those resulting from instability inherent to the measurement.

Hence the signal processing system for the JAMP-3 has been devised and constructed using a micro-computer, the Commodore CBM 3032, as the main control system.

The function of the new system is shown schematically in Fig. 2-11 in comparison with the ordinary system. Thick lines in the figure represent the sequence of signals controlled by the CBM 3032, while thin lines represent the operation through which the JAMP-3 has been processed by the work described in the previous sections. In addition to the function described above, i.e., the function of accurate measurement, another function of the control of electron beam scanning by the CBM 3032 is intended for fur-

ther sophisticated studies with the JAMP-3. The electronic circuit of the interface to the CBM3032 is shown in Appendix I.

Procedures for Auger signal detections using the system are briefly described as follows : (detailed explanations about the functions of the interface are also described in the Appendix I)

1) A deflection energy is first applied to the CMA from the CBM 3032 through a versatile interface adaptor MCS 6522, a 12 bit D/A (digital to analog) converter, and a programmable power supply, KEPCO 2000B.

2) At the energy, Auger signals are converted to digital pulses by the V/F (see also Fig. 2-9) and counted by a counter (2 byte) of the MCS 6522 during a sampling time.

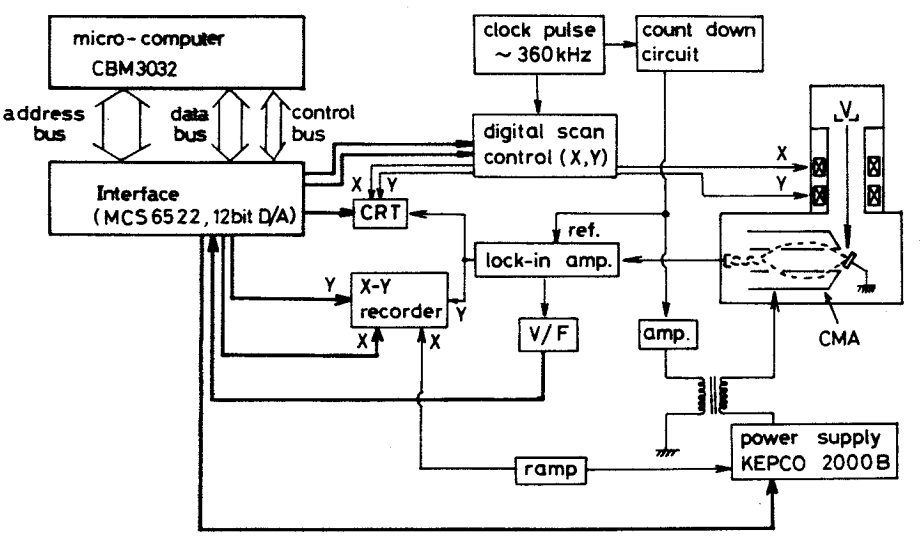

Fig. 2-11 Schema of the signal sequence controlled by a micro-computer

3) The MCS 6522 has a timer, so the sampling time can be designated voluntarily by the initial programming. The time constant of the lock-in amplifier is chosen to be shorter than the sampling time.

4) Counted signals are stored at corresponding memories (in 3 bytes) in the CBM 3032.

5) Then, the energy corresponding to the next step is applied to the CMA and procedures described in 2) - 4) are repeated. Energy steps are designated at the initial programming.

6) After Auger signal detection at all energy steps, the same procedures from 1) to 5) are repeated. The number of repetitions is also designated initially.

All the procedures described above are programmed in the CBM 3032 by the machine language, so the time required for the measurement is roughly given by (the number of steps) x (sampling time) x (the number of repetition). The measured Auger spectrum is recorded by the X-Y recorder.

An Auger spectrum obtained with the new system is shown in Fig. 2-12 in comparison with the spectra obtained with the ordinary system. Those are the Auger spectra of Ag contaminated with carbon and oxygen (as received), and they were obtained under the conditions of E_p = 10 keV and $I_p \sim 5 \times 10^{-7}$ A. The modulation amplitude is 5 eV_{p-p} and the frequency, ∿2.8 kHz.

Two spectra in Fig. 2-12(a) are obtained using the ordinary system with a large time constant of 1 sec. The upper spectrum is obtained with a relatively low sweep rate (1.2 eV) while the lower spectrum is obtained with a high sweep rate (6 eV/sec). It is clear

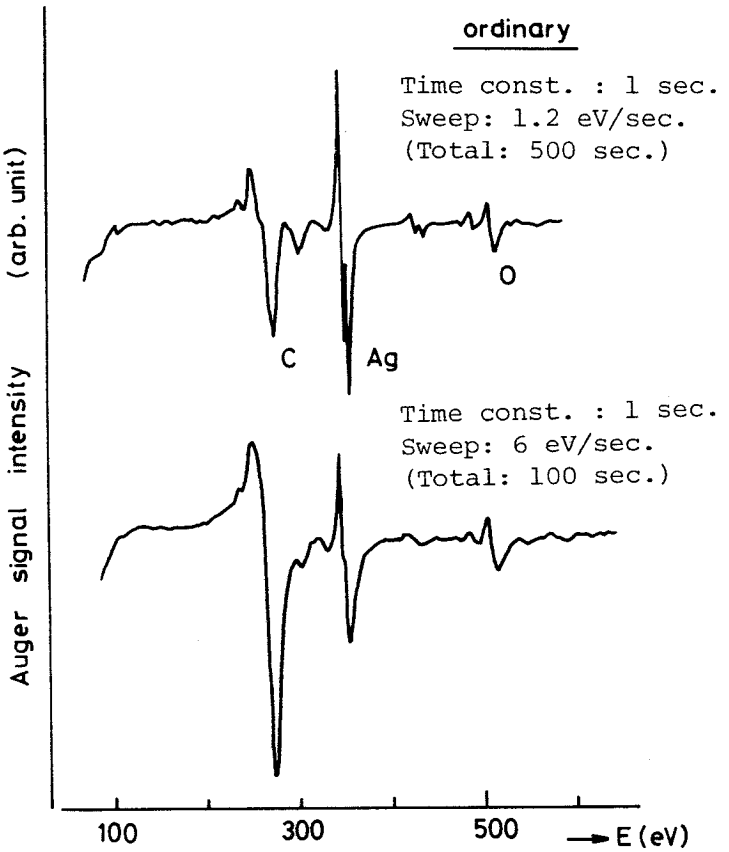

(a)

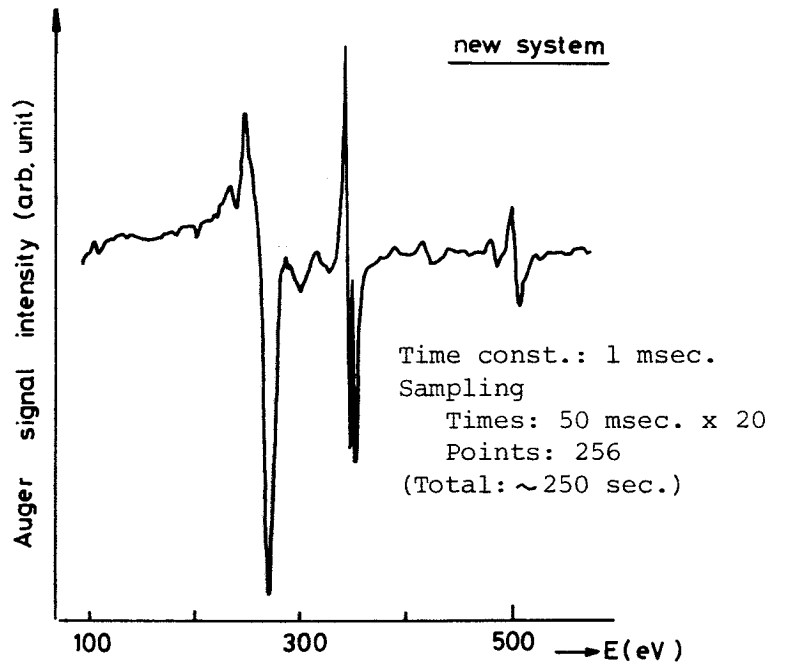

(b)

Fig. 2-12 Auger spectra obtained with the ordinary ((a)) and new ((b)) system. All the spectra were obtained under conditions of E_p= 10 keV and $I_p \simeq 5 \times 10^{-7}$A.

that the large time constant results in the degradation of the energy resolution especially in the case of high speed measurement, i.e., high sweep rate. (See the Auger spectra of Ag).

On the other hand, the spectrum shown in Fig. 2-12(b), which is obtained with the new system, has enough energy resolution without affecting the signal to noise ratio. The time constant of the lock-in amplifier was 1 msec and the total time required for the measurement was 250 sec. It is about half the time required for the measruement of the spectrum shown in the upper part of Fig. 2-12(a).

Therefore, it is ascertained that the new system is very useful for the measurement of Auger signals accurately (in high signal to noise ratio) without deteriorating the energy resolution. The system can also accomodate the measurement under primary current of $10^{-9} \sim 10^{-10}$ A, with the data smoothing procedure (Savitzky and Golay 1964) if necessary.

2-5 Application of LaB_6 single crystal cathode to SAEM

Another approach for measurement with high spatial resolution in the SAEM is to use a high brightness cathode. As mentioned in Section 1-2, the primary beam current is given by the equation (1-16), which is transformed to

$$d = \frac{2}{\pi \cdot \alpha}\sqrt{I_p} \cdot \sqrt{B} \qquad (2\text{-}4)$$

Since the signal to noise ratio in an Auger image as well as in an Auger spectrum is mainly determined by the amount of the primary beam current, and that the spatial resolution in the surface analysis is determined by the electron beam size, equation (2-4) indicates that spatial resolution will be improved as the sqaure root of the beam brightness.

Single crystal LaB_6 cathode for electron probe instruments has been investigated by several workers (Lafferty 1951, Broers 1969, Vogel 1970, Shimizu et al. 1975a, b, 1977b), and found to be most suitable as a cathode since it gives high emission current and stable performance in long service life.

In this experiemnt, a single crystal LaB_6 cathode was used to examine its applicability to an conventional SAEM. An electron gun assembly of Vogel type was used since it has an advantage of ensuring high mechanical stability of the position of the cathode during the long run operation.

The picture and cut away drawing of the electron-gun assembly are shown in Fig.2-13, which was designed considering a direct plug-in replacement for a W-hairpin cathode.

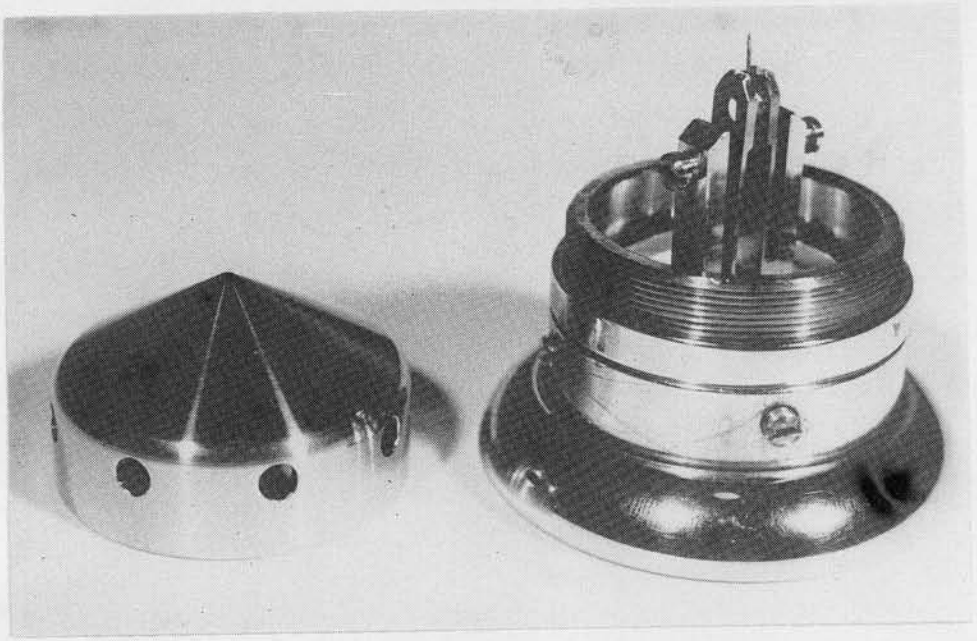

(a)

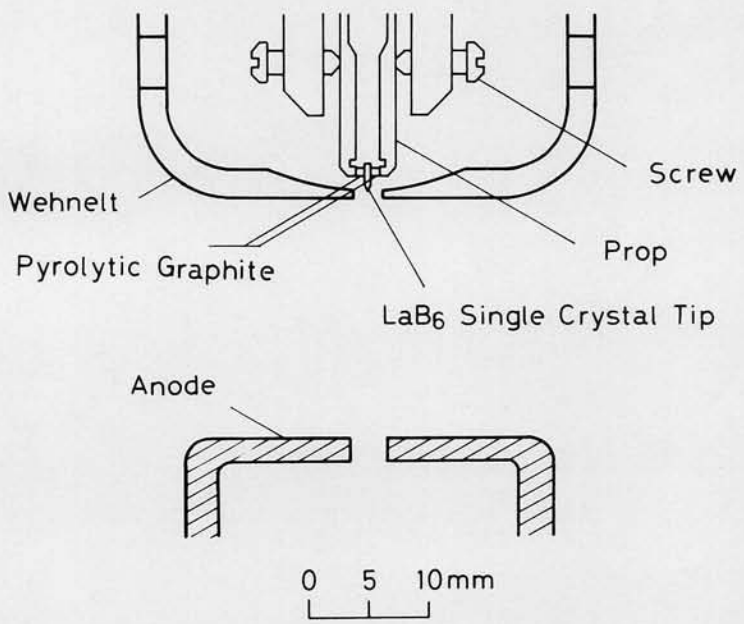

(b)

Fig.2-13. Picture ((a)) and cut away drawing ((b)) of the electron-gun assembly with single crystal LaB_6 tip.

The usefulness of the single crystal LaB_6 cathode was examined through direct comparison of absorbed- and Auger-electron images with those obtained by the ordinary W-hairpin cathode. The results are shown in Fig. 2-14.

Figure 2-14(a) and (b) are absorbed electron images of Au-Cu soldering alloy, while Fig. 2-14 (c) and (d) are Ag-Auger images of the sample. The figures (a) and (c) are obtained using the ordinary W-hairpin cathode, and (b) and (d) are obtained using the LaB_6 cathode. All figures were taken and processed under the same experimental conditions, i.e., E_p = 10 keV, $I_p \simeq 3 \times 10^{-8}$ A, and 400 sec./frame.

As can be seen in the figure, the single crystal LaB_6 cathode shows the fine structures of the sample. These results, therefore, lead us to conclude that the single crystal LaB_6 cathode is very useful for attaining high spatial resolution measurement with the SAEM.

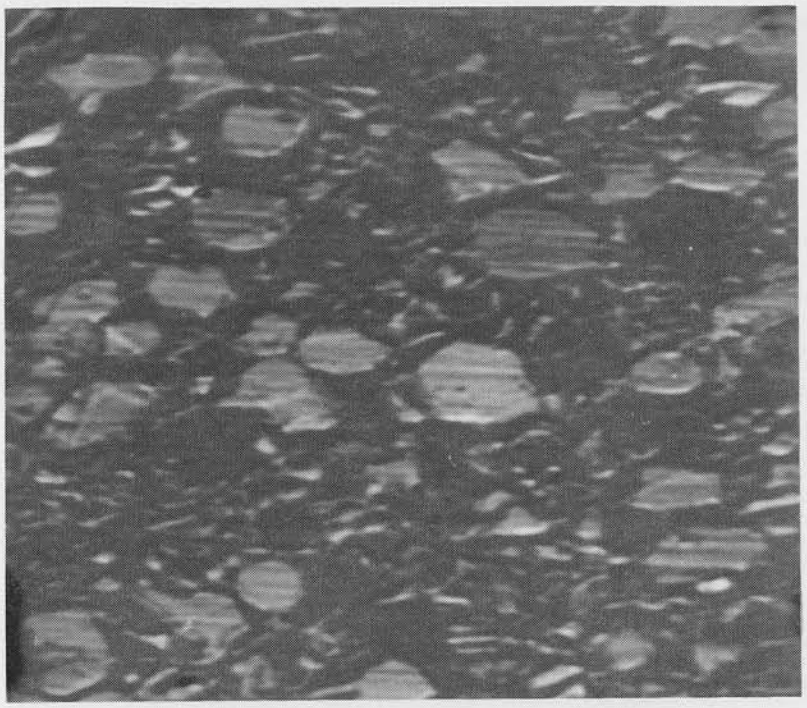

(a)

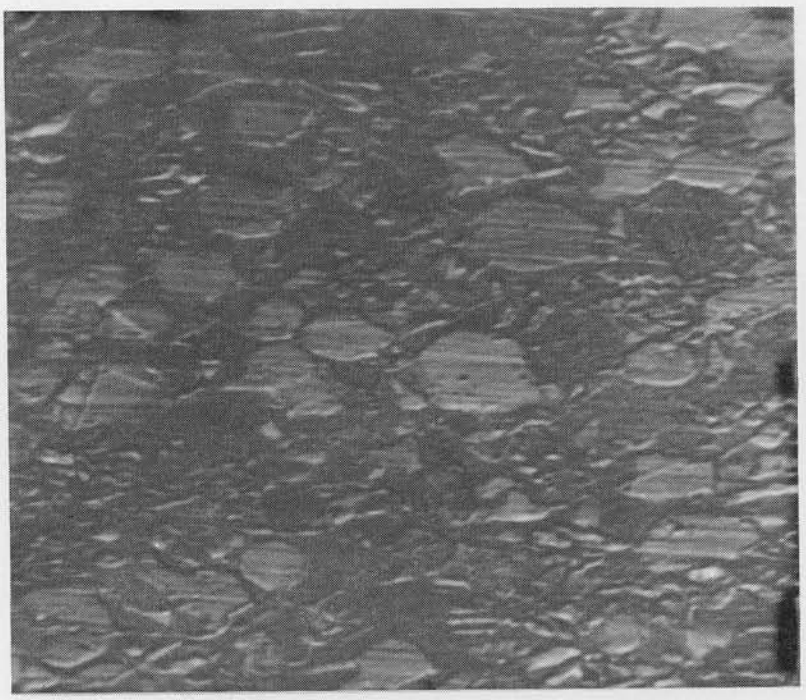

(b)

10 μm

Fig. 2-14. Absorbed electron images of Ag-Cu soldering alloy obtained with (a)W-hairpin and (b)LaB_6 cathode. Primary electron energy is 10 keV, and the current 3×10^{-8}A.

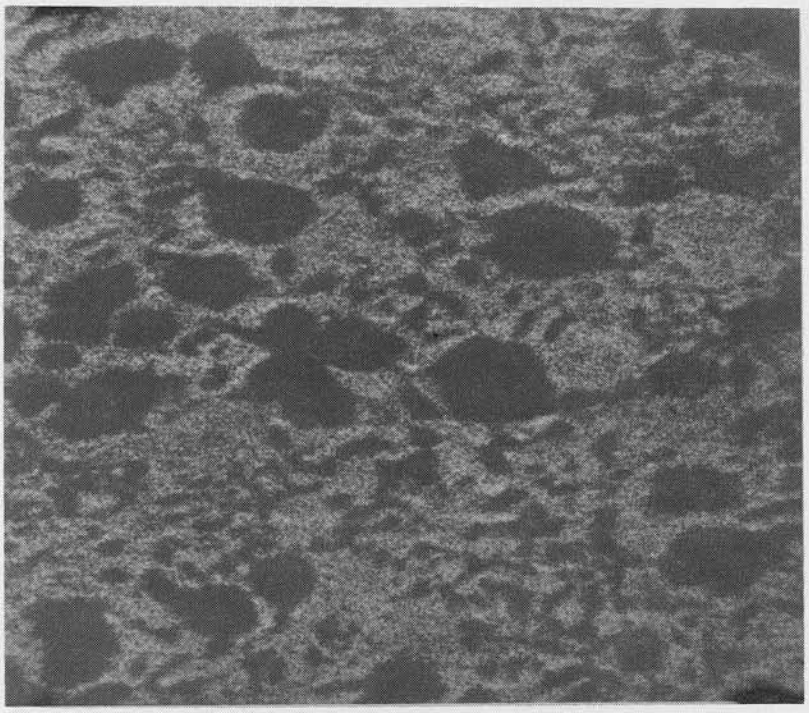

(c)

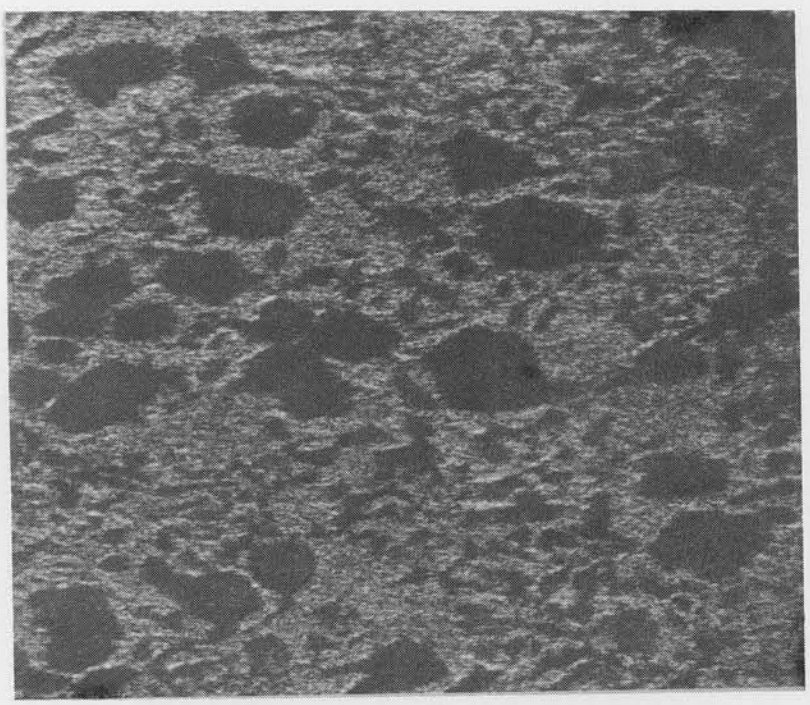

(d) 10 μm

Fig. 2-14. Ag-Auger (350 eV) image of Ag-Cu soldering alloy obtained with (c)W-hairpin and (d) LaB_6 cathode. Both images were taken and processed under the same conditions of E_p= 10 keV, I_p 3 x 10^{-8}A, 30 eV_{p-p} modulation, and 400 sec./frame.

2-6 Conclusions

In this chapter some practical approaches for improving the spatial resolution and also the energy resolution in the scanning Auger electron microscopy were described.

The square wave modulation technique has the merits of both background subtraction and signal detection corresponding to the Auger peak height, and can easily be applied to the SAEM improving signal to noise ratio in an Auger image. Moreover this modulation technique was easily combined with the digital systems for electron beam scanning and can improve the degradation of the Auger image by moire.

Further approaches for high spatial resolution measurement by an SAEM were accomplished successfully by the developments of digital integrator of Auger signals and electron gun with LaB_6 single crystal cathode equipped instead of W-hairpin.

It has been confirmed in experiment that Auger signal detection by the digital integrator is very useful especially in 'real-time' signal processing.

For the measurement of high accuracy with relatively long processing time in the SAEM, another digital system using a microcomputer was also developed for the SAEM, and this has enabled with substantial improvement in the energy resolution of the Auger spectrum.

These techniques and the signal acquisition procedure developed in the present studies have assured higher spatial resolution measurement in scanning Auger electron microscopy.

Chap. 3 Application of Monte Carlo Calculation to AES
- Approach to quantitative analysis -

3-1 Introduction

This chapter describes the application of the Monte Carlo calculation to quantitative analysis by AES. AES as a quantitative analytical technique requires a simple formula relating the Auger electron current collected by the analyzer to the concentration of an element in the surface region. The physical formalism involves, basically, a knowledge of the inelastic mean free path (IMFP) of Auger electrons and a knowledge of some measure accounting for the influence of backscattered electrons on the Auger electron yield besides accurate measurement of Auger electron current. The latter aspect is associated with Auger electrons produced by backscattered electrons ejected by primary electrons. This backscattering contribution is probably the most basic factor for accomplishing accurate quantitative AES analysis. The IMFP is concerned with absorption of Auger-electrons produced by the primary and backscattered electrons in a target. The accuracy of the final quantitative result for the composition of the surface atom layer depends directly on accuracy, with which the IMFP is known.

Concerning the IMFP, theoretical studies including a semi-empirical formulation have clarified the general quantitative tendency of the IMFP below 1 keV for pure elements. Furthermore the experimental determination based on currently about 350 measurements of IMFPs in different materials allows for empirical formulae of

the IMFPs for various types of target materials, elements, inorganic compound, organic compound and absorbed gas (Seah and Dench 1979), which are most useful for practical quantitative AES analysis.

The backscattering effect, however, has yet to be studied in more detail in both theory and experiment before the backscattering correction can accomodate to the quantitative analysis for practical use. In experiment, few systematic investigations have been reported so far for the backscattered electrons in an energy range below a few keV (Sternglass 1954, Koshikawa 1973) and the backscattering effect has been deduced from the results for kV electrons which were obtained in rather low vacuum ($\sim 10^{-6}$ Torr) evacuated with oil diffusion pump (Kanter 1957, Wittry 1966, Bishop 1966, Colby 1968). The effect of surface contamination was, therefore, significant and, thus, caused considerable errors, e.g., particularly in a low energy region. In theory, on the other hand, an extension of Monte Carlo calculations based on the use of the Rutherford scattering formula and Bethe's stopping power equation, which has widely been used for quantitative electron microprobe analysis with considerable success, was attempted for the correction of the backscattering effect.

In AES, however, the excitation energy of Auger electrons is usually lower than 2 keV and both the Rutherford scattering formula and Bethe's stopping power equation are no longer applicable in such a low energy region for describing electron penetration associated with Auger electron generation, particularly, for heavy elements (Krefting and Reimer, 1976). Hence the more accurate differential cross section for elastic scattering is required.

In this respect, although the differential cross sections

for elastic scattering by an accurate calculation have been published for electrons either below 1.5 keV (Fink and Yates 1970a, 1970b, Fink and Ingram 1972) or above a few tens of keV for the electron polarization study (Kessler 1976), the cross-sections for the energy region between 1.5 keV and a few tens of keV, which is often used in conventional AES and scanning Auger electron microscopy, has yet, to our knowledge to be well studied.

Therefore, elastic scattering cross-sections were obtained by partial wave expansion method (p.w.e.m.), which is described in Section 3-2. The treatment of inelastic scattering in the Monte Carlo simulation will be discussed in Section 3-3. The direct simulation approach (Shimizu et el. 1976, Green and Leckey 1976) which treats all the individual inelastic scattering processes statistically can be applied with accuracy and confidence only to a few materials since it requires detailed knowledge about individual inelastic processes. Similar problems occur for the approach which uses the dielectric function to describe other excitations than inner-shell electron excitations (Ganachaud and Cailler 1979). Krefting and Reimer's approach (Krefting and Reimer 1976), then, is used since it can be easily applied to any polyatomic materials being researched. Further discussions on inelastic scattering and precise representation of the simulation model are also presented in Section 3-4. The calculation of backscattering factors and others will be presented in Section 3-5.

Finally, in Section 3-6, application of the Monte Carlo calculation to a fundamental problem in the SAEM, i.e., the spatial resolution limit for AES with the SAEM, is described. The resolution limit has attracted much attention and discussed

by several workers (Christou 1976, Kirschner 1977, El Gomati and Prutton 1978, Janssen and Venables 1978) as mentioned in Section 1-2. Particularly the effect of the backscattered electrons to spatial resolution in AES, i.e., whether the spatial distribution of backscattered electrons deteriorates the resolution or not, has yet to be fully understood. So, the spatial resolution of Auger signal generation for KLL- and LVV-Auger electrons of Al is calculated using the Monte Carlo simulation and shows that the spatial resolution in AES is mainly determined by the beam size of primary electrons. A rough estimation about the resolution limit in an Auger image is also described in the section.

3-2. Calculation of elastic scattering cross-sections by partial wave expansion method

3-2-1. Partial wave expansion method using Dirac equation

According to the relativistic treatment by Dirac, the wave function ψ can be represented by the four components (ψ_1, ψ_2, ψ_3, ψ_4) which satisfy the following equations in a central field of force (Mott and Massey 1965),

$$\begin{cases} (W-V+1)\psi_1 + (p_1-ip_2)\psi_4 + p_3\psi_3 = 0 & (3\text{-}1\text{-}a) \\ (W-V+1)\psi_2 + (p_1+ip_2)\psi_3 - p_3\psi_4 = 0 & (3\text{-}1\text{-}b) \\ (W-V-1)\psi_3 + (p_1-ip_2)\psi_2 + p_3\psi_1 = 0 & (3\text{-}1\text{-}c) \\ (W-V-1)\psi_4 + (p_1+ip_2)\psi_1 - p_3\psi_2 = 0 & (3\text{-}1\text{-}d) \end{cases}$$

Here, W denotes the total energy measured in units of mc^2, V the atomic potential energy, and

$$p_1 = -i\hbar\frac{\partial}{\partial x} \quad , \quad p_2 = -i\hbar\frac{\partial}{\partial y} \quad , \quad p_3 = -i\hbar\frac{\partial}{\partial z} \quad , \qquad (3\text{-}2)$$

respectively. The system of units in so-called natural unit, in which $c = m = \hbar = 1$, where c is the light velocity, m the electron rest mass and $\hbar$ the Planck's constant divided by 2π ($\hbar = \frac{h}{2\pi}$).

The necessity of treating the electron atom scattering relativistically even in the non-relativistic energy region of incident electrons is well discussed by Yamazaki(1977b). That is, in short, the electrons passing through near a nucleus may be accelerated to near light velocity, which in turn necessitates relativistic correction of the electron mass as a distance function between the electron and nucleus.

As the asymptotic form of these four components are related with one another, it suffices to treat only the lower two component of the four (Mott and Massey 1965) in electron scattering problems. The asymptotic forms of the scattering state, therefore, are described as follows,

$$\psi = \begin{pmatrix} \psi_3 \\ \psi_4 \end{pmatrix} \sim \begin{pmatrix} e^{ikr} + r^{-1} \cdot e^{ikr} \cdot f_1(\theta,\phi) \\ r^{-1} \cdot e^{ikr} \cdot g_1(\theta,\phi) \end{pmatrix}, \qquad (3\text{-}3)$$

for incident electrons of parallel spin state with respect to Z-axis (incident direction), and

$$\psi = \begin{pmatrix} \psi_3 \\ \psi_4 \end{pmatrix} \sim \begin{pmatrix} r^{-1}\, e^{ikr}\, g_2(\theta,\phi) \\ e^{ikr} + r^{-1}\, e^{ikr}\, f_2(\theta,\phi) \end{pmatrix}, \qquad (3\text{-}4)$$

for those of anti-parallel spin state. Here f and g are called direct and spin-flip scattering amplitude, respectively.

These scattering amplitudes can be obtained using the solutions of equations (3-1) given by Darwin (1928). The solutions are,

$$\begin{aligned} \psi_3 &= (\ell+1) G_\ell P_\ell(\cos\theta) \ , \quad \psi_4 = -G_\ell P_\ell^1(\cos\theta) \cdot e^{i\phi} \\ \psi_3 &= \ell\, G_{-\ell-1} P_\ell(\cos\theta) \ , \quad \psi_4 = G_{-\ell-1} P_\ell^1(\cos\theta) \cdot e^{i\phi} \end{aligned} \qquad (3\text{-}5)$$

for parallel spin state, and

$$\psi_3 = G_\ell P_\ell^1(\cos\theta)\cdot e^{-i\phi} \quad , \quad \psi_4 = (\ell+1) G_\ell P_\ell(\cos\theta)$$
$$\psi_3 = -G_{-\ell-1} P^1(\cos\theta) e^{-i\phi} \quad , \psi_4 = \ell\, G_{-\ell-1} P_\ell(\cos\theta) \qquad (3\text{-}6)$$

for anti-parallel spin state, where $P(\cos\theta)$ and $P^1(\cos\theta)$ are Legendre and associated Legendre function, respectively. G_ℓ is a solution of the simultaneous equations

$$\begin{cases} (W-V+1)F_\ell + \dfrac{dG_\ell}{dr} - \dfrac{\ell}{r} G_\ell = 0 & (3\text{-}7\text{-a}) \\ (W-V-1)G_\ell - \dfrac{dF_\ell}{dr} - \dfrac{\ell+2}{r} F_\ell = 0 & (3\text{-}7\text{-b}) \end{cases} ,$$

and $G_{-\ell-1}$ is a solution of a similar pair of equations with $-\ell-1$ in place of ℓ. By elimination of the function F_ℓ from equation (3-7-a) and (3-7-b) we have

$$\frac{d^2G_\ell}{dr^2} + \left(\frac{2}{r} - \frac{\alpha'}{\alpha}\right)\frac{dG_\ell}{dr} + \left\{\alpha\beta - \frac{\ell(\ell+1)}{r^2} + \frac{\ell}{r}\cdot\frac{\alpha'}{\alpha}\right\}G_\ell = 0 \quad , \qquad (3\text{-}8)$$

where

$$\alpha = (W-V+1) \quad , \quad \beta = (W-V-1) \quad , \quad \alpha' = \frac{d\alpha}{dr}$$

For $r \to \infty$, equation (3-8) reduces to

$$\frac{d^2G_\ell}{dr^2} + \frac{2}{r}\cdot\frac{dG_\ell}{dr} + \left(K^2 - \frac{\ell(\ell+1)}{r^2}\right)G_\ell = 0 \quad , \qquad (3\text{-}9)$$

where $K^2 = W^2 - 1$. Since this differential equation is that of spherical Bessel function, the solution may be represented in the asymptotic form as follows;

$$G_\ell \xrightarrow[r\to\infty]{} j_\ell(Kr)\cdot\cos\eta_\ell - n_\ell(Kr)\cdot\sin\eta_\ell$$
$$\sim \frac{1}{Kr}\cdot\sin(Kr - \frac{\ell}{2}\pi + \eta_\ell) \quad , \tag{3-10}$$

where j_ℓ and n_ℓ are spherical Bessel and spherical Neumann functions. As $G_{-\ell-1}$ also satisfies the similar differential equation, the asymptotic form for it is

$$G_{-\ell-1} \xrightarrow[r\to\infty]{} \frac{1}{Kr}\sin(Kr - \frac{\ell}{2}\pi + \eta_{-\ell-1}) \quad . \tag{3-11}$$

Here η_ℓ and $\eta_{-\ell-1}$ are called phase shift.

By combining the solutions (3-5) in the following way, therefore, we obtain functions ψ_3 and ψ_4 having the asymptotic forms (3-3):

$$\psi_3 = \sum_{\ell=0}^{\infty} \{(\ell+1)\, e^{i\eta_\ell}\cdot G_\ell + \ell e^{i\eta_{-\ell-1}}\cdot G_{-\ell-1}\} i^\ell P_\ell(\cos\theta) \quad ,$$
$$\psi_4 = \sum_{\ell=1}^{\infty} \{-e^{i\eta_\ell}\cdot G_\ell + e^{i\eta_{-\ell-1}}\cdot G_{-\ell-1}\} i^\ell P_\ell^1(\cos\theta)\, e^{i\phi} \quad . \tag{3-12}$$

Here, the Rayleigh's formula,

$$e^{iKz} = \sum_{\ell=0}^{\infty} (2\ell+1) i^\ell j_\ell(Kr) P_\ell(\cos\theta) \tag{3-13}$$

is taken into account. From these we have

$$f_1(\theta,\phi) = \frac{1}{2iK}\sum_{\ell=0}^{\infty}\{(\ell+1)(e^{2i\eta_\ell} - 1) + \ell(e^{2i\eta_{-\ell-1}} - 1)\}P_\ell(\cos\theta) \quad , \tag{3-14-a}$$

$$g_1(\theta,\phi) = \frac{1}{2iK}\sum_{\ell=1}^{\infty}\{-e^{2i\eta_\ell} + e^{2i\eta_{-\ell-1}}\}P_\ell^1(\cos\theta)\ e^{i\phi} \quad . \tag{3-14-b}$$

For the case of incident electrons with anti-parallel spin we find, by a similar procedure, that

$$f_2(\theta,\phi) = f_1(\theta,\phi) \left(= f(\theta)\right) \quad , \tag{3-15}$$

and that

$$g_2(\theta,\phi) = -\ g(\theta)\ e^{-i\phi} \quad , \tag{3-16-a}$$

where

$$g_1(\theta,\phi) = g(\theta)\ e^{i\phi} \quad . \tag{3-16-b}$$

Therefore the scattering cross-section for unpolarized electrons can be obtained by the equation,

$$\sigma\ (\theta) = \left|f(\theta)\right|^2 + \left|g(\theta)\right|^2 \quad . \tag{3-17}$$

3-2-2. Numerical calculation procedure

Since the scattering amplitudes are expressed as a function of the phase shifts η_ℓ and $\eta_{-\ell-1}$ as shown in equation (3-14),

it is necessary to determine phase shifts by clarifying the relationship with the radial wave function. Various calculation procedures have been developed for the estimation of phase shifts (Bunyan 1963, Bühring 1965, Bunyan and Schonfelder 1965). The present calculation adopts one of the most advantageous procedures which were developed for accurate and fast computer calculation by Yamazaki et al. (1976, 1977a, b)

Introducing the change of variables (Bunyan and Schonfelder 1965),

$$F_\kappa = A_\kappa(r)\cdot\frac{\sin\phi_\kappa(r)}{r} \qquad (3\text{-}18\text{-}a)$$

$$G_\kappa = A_\kappa(r)\cdot\frac{\cos\phi_\kappa(r)}{r} \quad , \qquad (3\text{-}18\text{-}b)$$

equation (3-7) and similar equations for G-ℓ-1 become

$$\frac{d\phi_\kappa}{dr} = \frac{\kappa}{r} + (W-V) - \cos 2\phi_\kappa \quad , \qquad (3\text{-}19\text{-}a)$$

$$\frac{1}{A_\kappa}\cdot\frac{dA_\kappa}{dr} = -\frac{\kappa}{r}\cos 2\phi_\kappa - \sin 2\phi_\kappa \quad , \qquad (3\text{-}19\text{-}b)$$

where

$$\kappa = -(\ell+1), \text{ or } \kappa = \ell \qquad (3\text{-}20)$$

From equation (3-18) and (3-19), we obtain the expression for the phase shifts

$$\tan\eta_\kappa = \frac{K\cdot j_{\ell+1}(Kr) - j_\ell(Kr)\cdot\{(W+1)\tan\phi_\kappa + (1+\ell+\kappa)/r\}}{K\cdot n_{\ell+1}(Kr) - n_\ell(Kr)\cdot\{(W+1)\tan\phi_\kappa + (1+\ell+\kappa)/r\}} \quad , \qquad (3\text{-}21)$$

by taking into account the following relation,

$$\frac{dj_{\ell}(z)}{dz} = \frac{\ell}{z} j_{\ell}(z) - j_{\ell+1}(z) \quad , \qquad (3\text{-}22)$$

and equivalent equation for $n_{\ell}(z)$. The expression on the light in equation (3-21) is evaluated at r=a where a satisfies $V(a) \sim 0$ using only the first order nonlinear differential equation (3-19-a), which simplifies the computer calculation procedure considerably.

As the potential used in these calculations is given by $V(r) = -\frac{Z(r)}{r}$ where Z(r) is the effective nuclear change, numerical calculation of differential equation (3-19-a) can not be made from r=0. Therefore, we expand V(r) and $\phi_{\kappa}(r)$ in a power series in order to derive initial conditions at small r (Bunyan and Schonfelder 1965, Yamazaki 1976, 1977a, b) as,

$$V(r) = -\frac{1}{r}\cdot(Z_0+Z_1r+Z_2r^2+Z_3r^3+ \text{----}) \quad , \qquad (3\text{-}23)$$

$$\phi_{\kappa}(r) = \phi_0+\phi_1r+\phi_2r^2+\phi_3r^3+ \text{----} \qquad (3\text{-}24)$$

By substituting (3-23) and (3-24) into (3-19-a) we obtain

$$\sin 2\phi_0 = -\frac{Z_0}{\kappa} \qquad (3\text{-}25\text{-}a)$$

$$\phi_1 = (W+Z_1-\cos 2\phi_0)/(1-2\kappa\cdot\cos 2\phi_0) \qquad (3\text{-}25\text{-}b)$$

$$\phi_2 = \{2\phi_1\sin 2\phi_0(1-2\kappa\phi_1)+Z_0\}/(2-2\kappa\cos 2\phi_0) \qquad (3\text{-}25\text{-}c)$$

$$\phi_3 = \frac{2\phi_2\cdot\sin 2\phi_0(1-2\kappa\phi_1)+2\phi_1^2\cdot\cos 2\phi_0\cdot(1-\frac{2}{3}\kappa\phi_1)+Z_3}{3-2\cos 2\phi_0} \quad , \qquad (3\text{-}25\text{-}d)$$

with extra conditions

$$0 \leqq 2\phi_0 \leqq \frac{\pi}{2} \qquad (\kappa < 0)$$
$$\pi \leqq 2\phi_0 \leqq \frac{3}{2}\cdot\pi \qquad (\kappa \geqq 0) \qquad (3\text{-}26)$$

in order to keep the wave function finite at r=o. Integration was carried out from r=0.1 by the forth order Lunge-Kutta process which has sufficient accuracy for the present calculations, while the interval in r in the integration was changed as follows:

i) $r_1(=0.1) \leqq r \leqq r_2(=0.1e^5 \simeq 15)$

A change of variable $r=0.1e^t$ is introduced to avoid the use of excessively small intervals. The equation (3-19-a) is then rewritten as

$$\frac{d\phi_\kappa}{dr} = \kappa\sin 2\phi_\kappa + 0.1e^t(W-V-\cos 2\phi_\kappa) \qquad (3\text{-}27)$$

The step was chosen as $\Delta t \sim 0.003$.

ii) $r_2 \leqq r \leqq r_3(=200)$

The ordinary equation (3-19-a) is used with the step $\Delta r \simeq 0.05$.

iii) $r_3 \leqq r \leqq r_4(=518 \simeq 2$ Å)

The equation (3-19-a) is also used with the step of twice as much as that in the region ii), and the integration was stopped at r=518 to reduce computing time. To make this process more appreciable, the charge distribution was reconstructed in this region as a quadratic form taking into account the following conditions.

A) The total charge in the region $r \leq 518$ is made to equal Ze where Z is the atomic number of each element.

B) The charge density and its derivative, also the potential, is made continuous at r=200 to avoid anomalous δ-function type charge distributions (Bühring 1965).

A charge reconstruction of this type in region iii) may have little influence on large angle scattering which is most important in the consideration of backscattered electrons since such scattering occurs for electrons with a small impact parameter, hence for those scattered by an unreconstructed potential. This is ascertained by calculating the scattering cross-section for different r_3 and r_4 values, as shown in Fig. 3-1. The solid line represents the differential scattering cross-sections obtained by the calculation procedure described above and the dotted line obtained using exact analytical expressions of the atomic potential (analytical expressions of Thomas-Fermi potential by Byatt (1956)) up to about 3 Å, while integration was stopped at 4 Å for the latter. It is clear from the figure that the present treatment has enough accuracy in consideration of electron elastic scattering especially in the region of the large scattering angle, which saves the computing time substantially. Elastic scattering cross-sections, then, were calculated according to the procedure described above for a number of elements, while all phase shift was evaluated from $\ell = 0$ to $\ell = \ell'$, where $|\delta_{\ell'}| \leqq 10^{-5}$. It is also ascertained that further calculation corresponding to higher orders of the partial wave hardly affects the scattering cross sections.

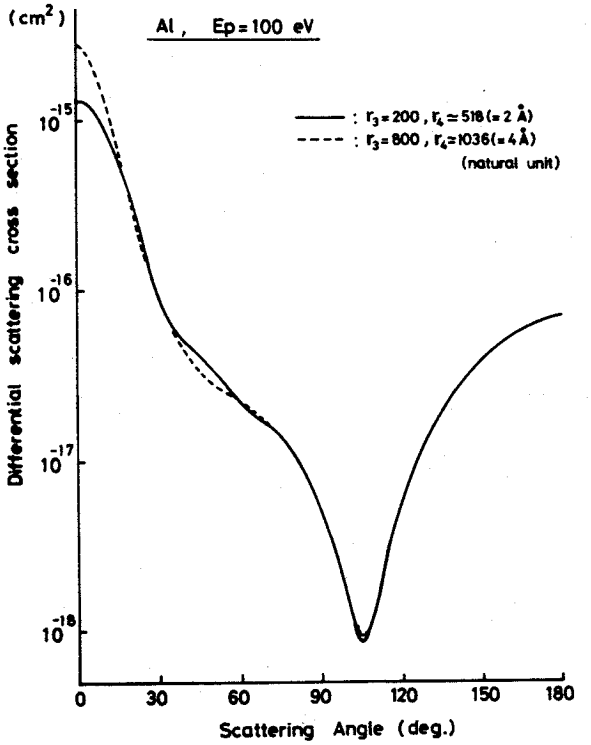

Fig. 3-1 Dependence of the calculation treatment on the differential scattering cross-section:
———; present treatment
------; more exact treatment with long computer time

3-2-3. Calculated results

The atomic potential used in the present calculation for a number of elements was that of Thomas-Fermi-Dirac since its analytical expression is given as a function of Z(atomic number) by Bonham and Strand (1963). That is,

$$V(r) = -\frac{Ze^2}{r}\cdot\sum_{i=1}^{3}\gamma_i e^{-\lambda_i r} \quad , \qquad (3\text{-}28\text{-}a)$$

where

$$\gamma_i = a + b\cdot\ln Z + c(\ln Z)^2 + d(\ln Z)^3 + e(\ln Z)^4 \quad , \qquad (3\text{-}28\text{-}b)$$

and with equivalent expressions for the λ_i's. The values of coefficients a, b, c, d, e are shown in Table 3-1.

Table 3-1 Values of the constants for the determination of γ's and λ's.
(Bonham and Strand)

	a	b	c	d	e
γ_1	0.0126671	-0.0261047	0.0214148	-0.00235658	0.0000210672
λ_1	164.564	-152.192	62.3879	-11.5005	0.808425
γ_2	0.0580612	0.0293077	0.0857135	0.0223342	0.00164675
λ_2	11.3060	-6.31902	2.26025	-0.370738	0.0261151
γ_3	0.927968	-0.00164643	-0.107685	0.0247998	-0.00167822
λ_3	1.48219	-0.0557601	0.0164387	0.00439703	0.000997225

As the analytical expressions for Hartree-Fock potential were given for a number of elements of small atomic number (Strand and Bonham 1964), the scattering cross section was calculated using both atomic potentials for Al to see whether the present potential is adequate to treat elastic scattering processes of light element as Al or not. The result for electrons of 100 eV incident energy is shown in Fig. 3-2, where the solid line represents the differential scattering cross-sections obtained using analytical expressions for Thomas-Fermi-Dirac potential, while the dotted line represents that obtained using analytical expressions for Hartree-Fock potential. Both curves show a quite similar tendency even when the special feature appeared near 90°, and the differential cross-section for light elements does not show such a drastic change as in Fig. 3-2 in the energy region

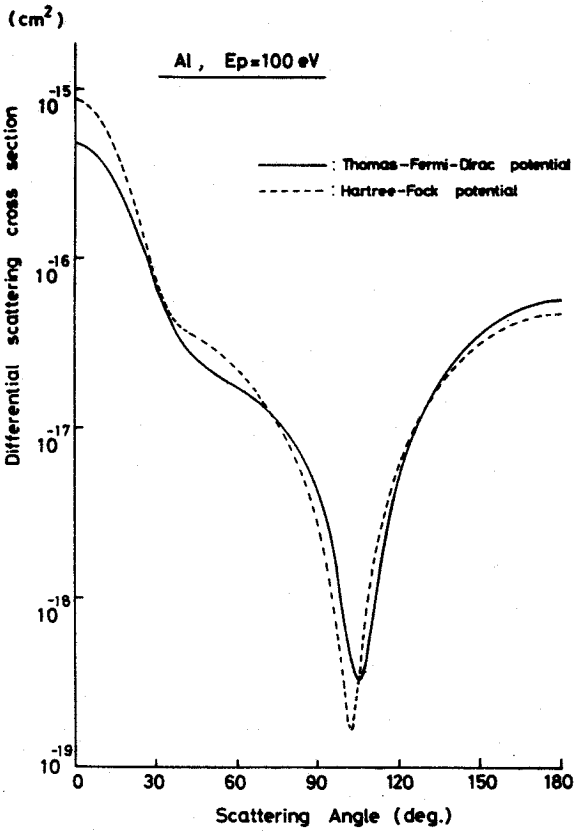

Fig. 3-2 Dependence of the differential scattering cross-section on the type of atomic potential:
——— ; Thomas-Fermi-Dirac potential
------; Hartree-Fock potential

above 500 eV (which is the minimum energy for the present Monte Carlo calculation described in section 3-3), the adopted potential seems to have enough propriety for the present purpose.

The differential scattering cross-sections were calculated for B(Z=5), C(Z=6), N(Z=7), O(Z=8), Al(Z=13), P(Z=15), Ti(Z=22), Cu(Z=29), Ge(Z=32), Zr(Z=40), Ag(Z=47), and Au(Z=79) for primary electron energy from 0.5 keV to 10 keV with energy steps of 0.5 keV (in the energy region between 0.5 keV and 5 keV) and 1.0 keV (between 5.0 keV and 10 keV). Some of the results obtained are shown in Fig. 3-3 for a number of elements described

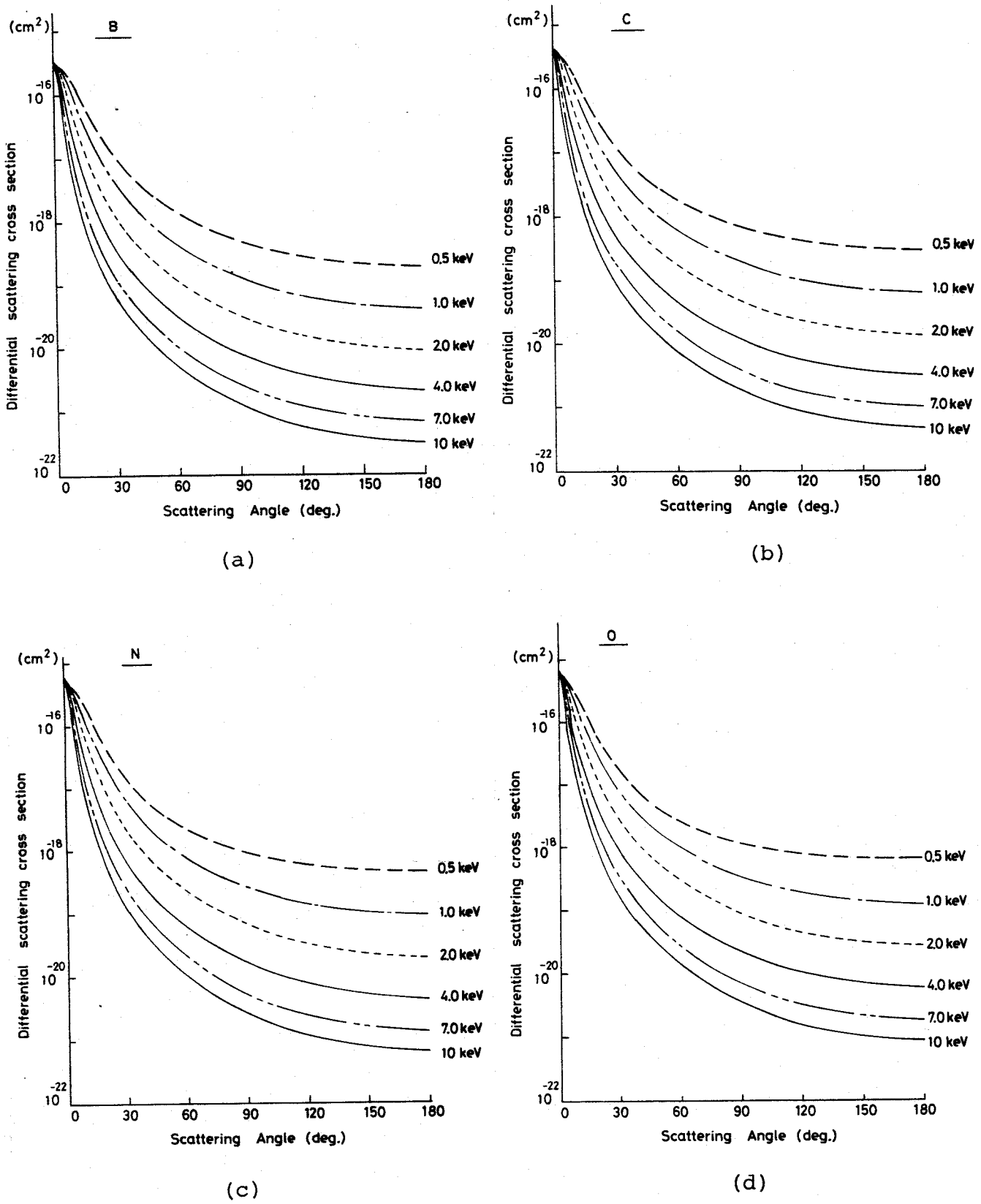

Fig. 3-3 The differential cross-sections for elastic scattering obtained by the partial wave expansion method: (a); B, (b); C, (c); N, (d); O

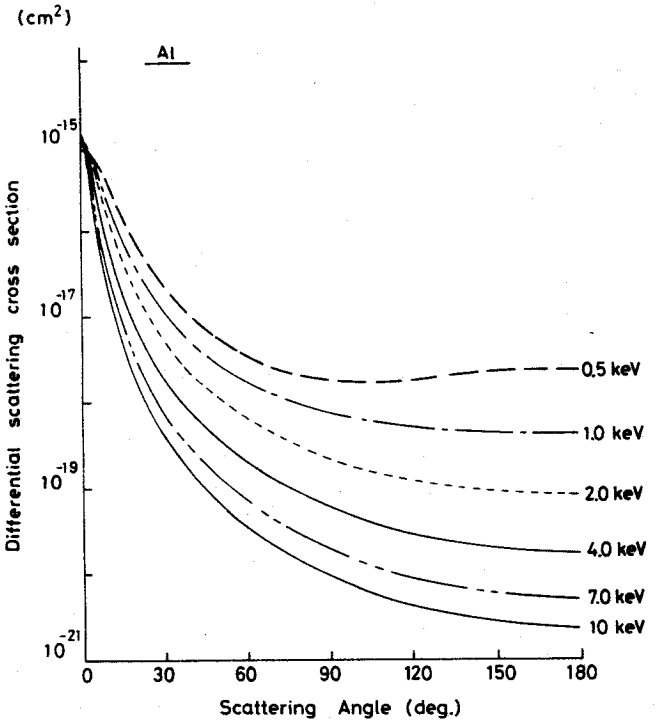

(e)

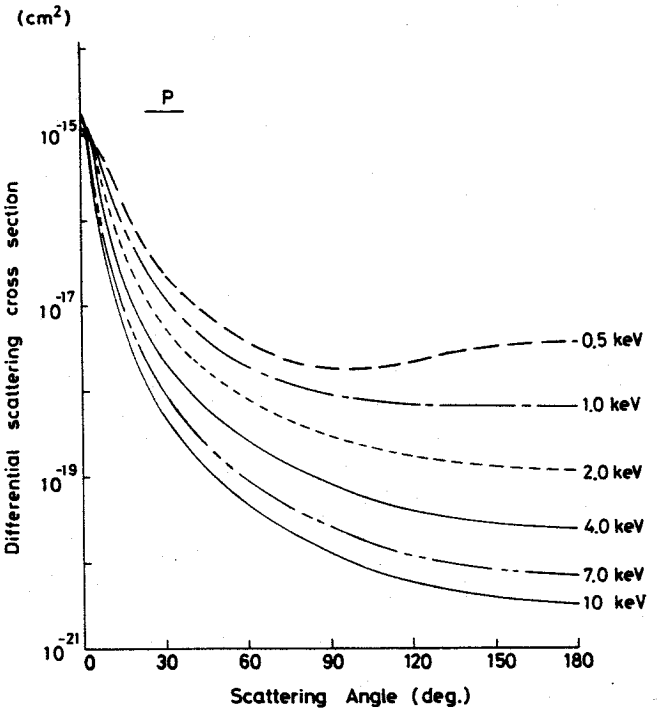

(f)

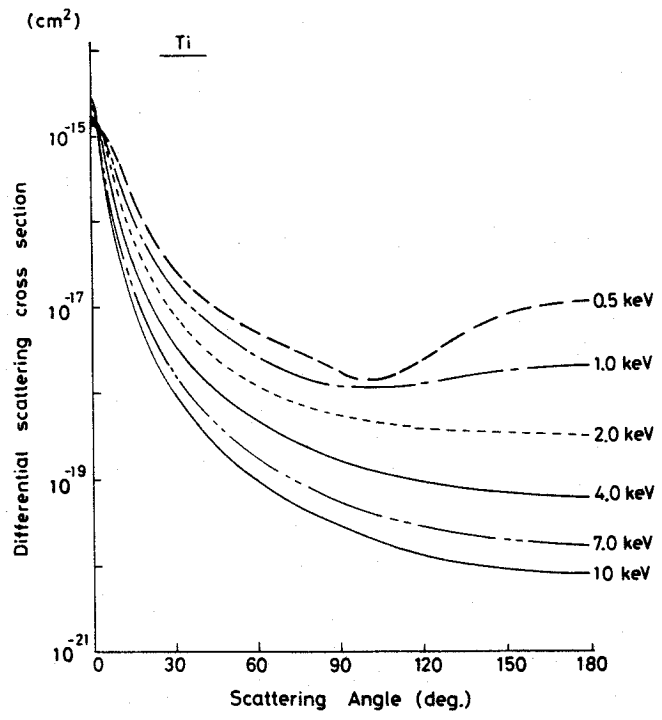

(g)

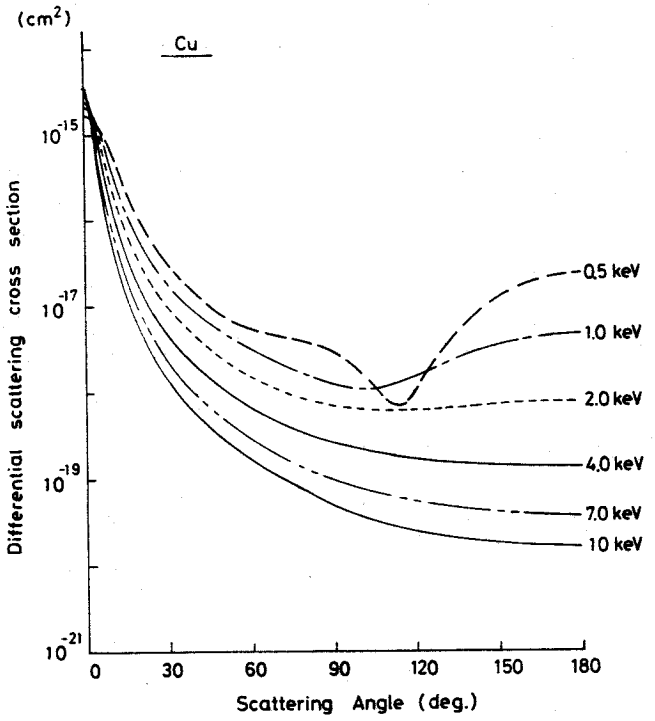

(h)

Fig. 3-3 The differential cross-sections for elastic scattering obtained by the partial wave expansion method: (e); Al, (f); P, (g); Ti, (h); Cu

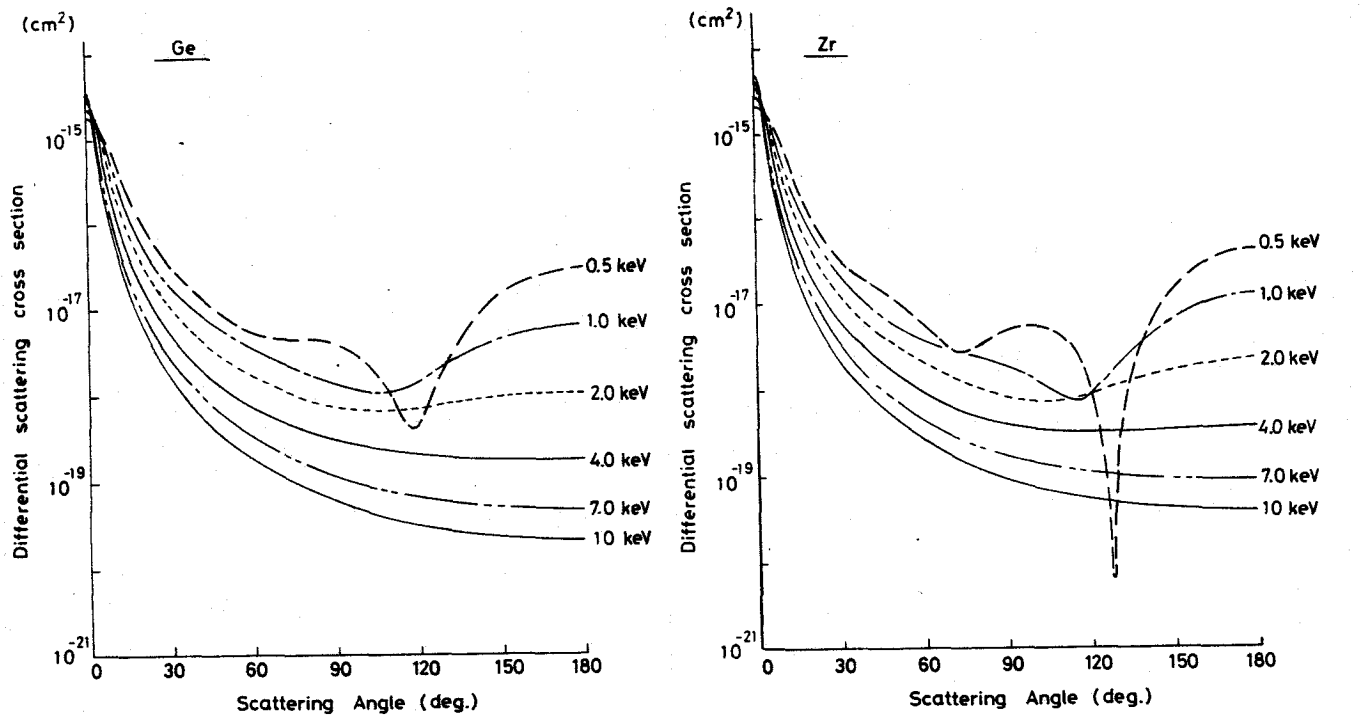

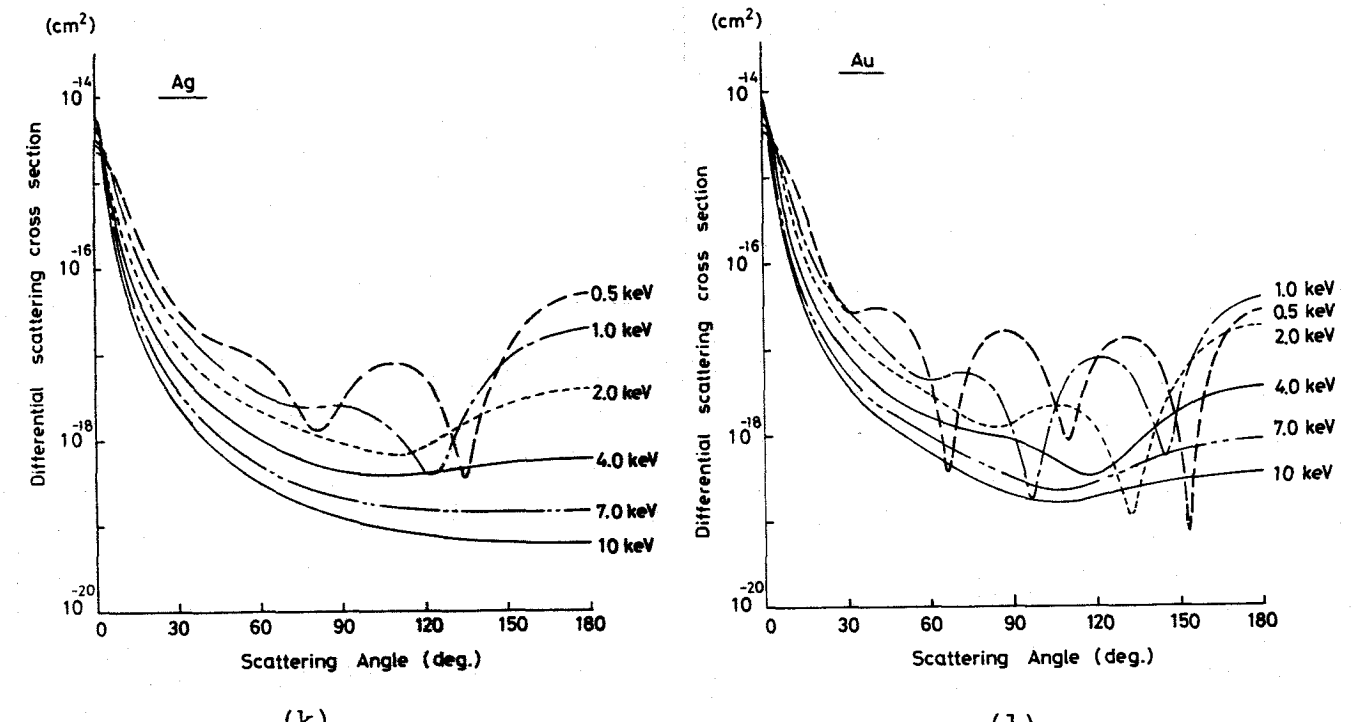

Fig. 3-3 The differential cross-sections for elastic scattering obtained by the partial wave expansion method: (i); Ge, (j); Zr, (k); Ag, (l); Au

above. The results were compared with those published by Fink and Ingram (1972) and showed satisfactory agreement with those in the region from 100 to 1500 eV. As seen in the figure, the differential scattering cross-section comes to show fine features when the atomic number of the atom becomes larger. Such effect was discussed by Yamazaki (1977b).

The differential cross-sections calculated by the present method was compared with those by the screened Rutherford formula (see equation 1-35) with screening parameter of Nigam et al. (1959) for comparison, and the result is shown in Fig. 3-4. In the figure the ratio of these two cross-sections $(\frac{d\sigma}{d\theta})$ p.w.e.m./$(\frac{d\sigma}{d\theta})$ S.R. (Screened Rutherford) is plotted for Al, Cu, Ag, and Au. As seen in Fig. 3-4-(a), the screened Rutherford scattering formula is a good approximation for electrons of energies between several keV and 20 keV for aluminium.

This is probably the main reason why the Monte Carlo calculations based on the screened Rutherford scattering agree so well with the experiment for thin aluminum films (Shimizu et al. 1976), which is the most basic test for theoretical approaches. For the other elements of higher atomic number, the discrepancy between the two cross sections becomes serious as pointed out by Krefting and Reimer (1976).

The total elastic scattering cross-sections for a number of elements described above are shown in Fig. 3-5(a) as a function of electron energy. In Fig. 3-5(b), the comparison of the total elastic scattering cross-section for Al by p.w.e.m. with those by screened Rutherford is shown together with the cross-section by the first Born approximation using the same Thomas-Fermi-Dirac

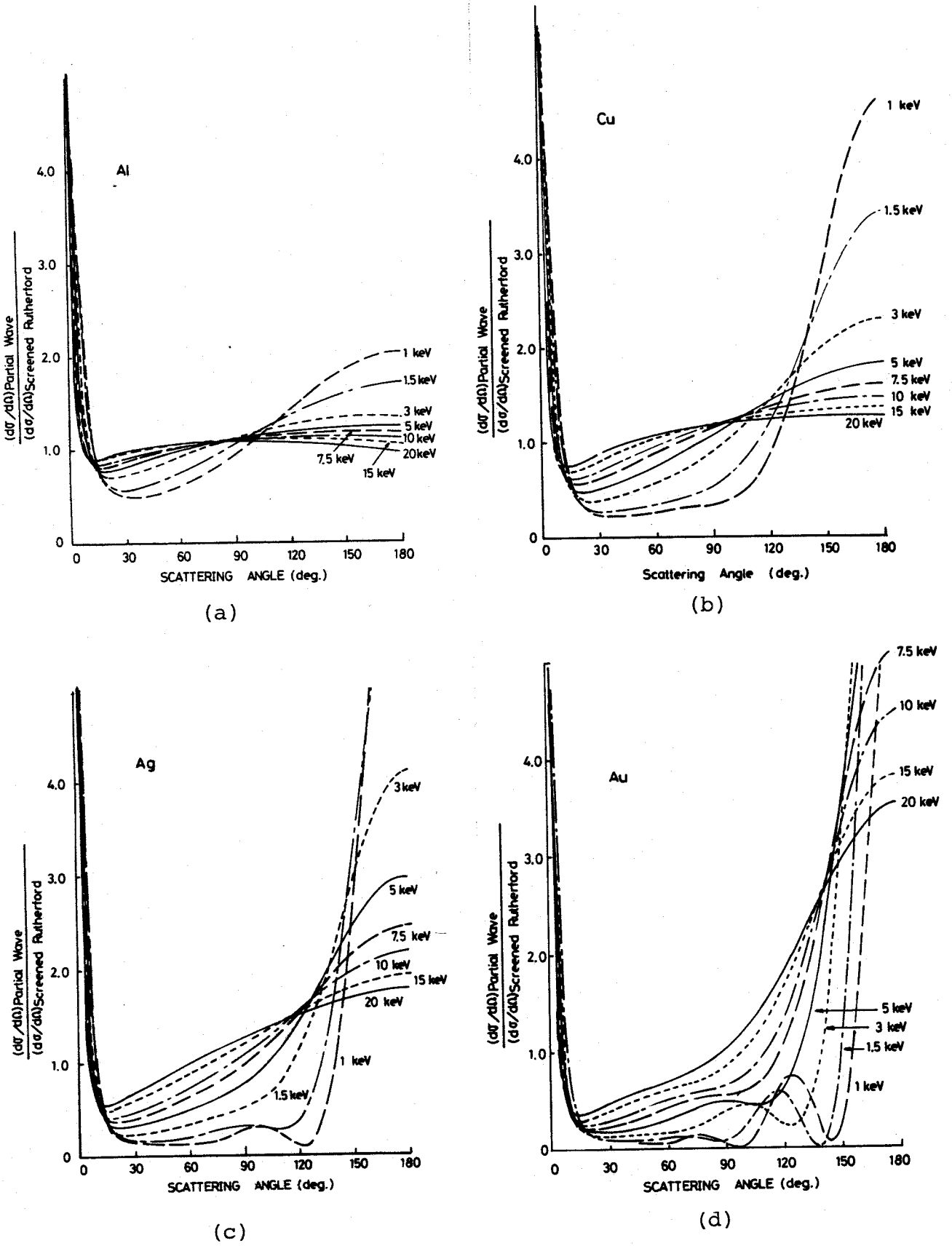

Fig. 3-4 The ratio of the differential cross-sections for elastic scattering obtained by the partial wave expansion method and screened Rutherford formula:
(a); Al, (b); Cu, (c); Ag, (d); Au

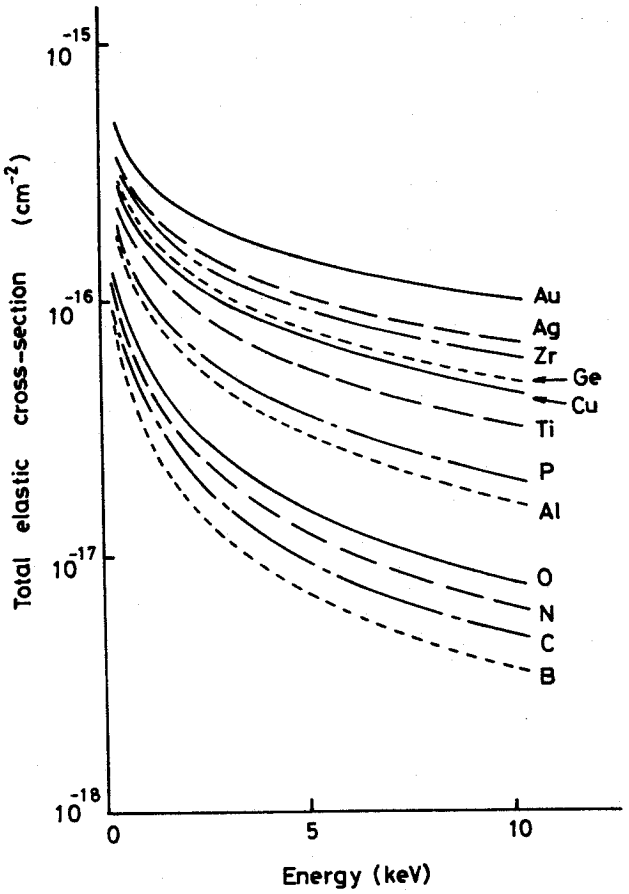

(a)

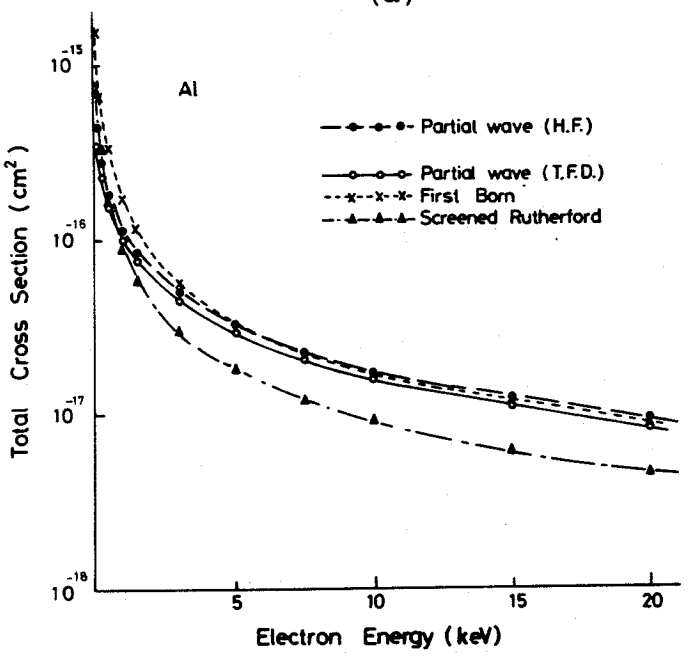

(b)

Fig. 3-5 (a) Total elastic scattering cross-sections as a function of electron energy E for a number of elements.
(b) Comparison of total elastic scattering cross-sections for Al calculated by the partial wave expansion method (with Hartree-Fock and Thomas-Fermi-Dirac potential), the first Born approximation, and Screened Rutherford formula.

potential. As seen in Fig. 3-5(b), so far as the same theoretical representation of atomic potential is used, the first Born approximation gives almost the same result with that by p.w.e.m. at higher energies above ∿10 keV. The cross-section by screened Rutherford formula, on the other hand, gives a little lower value than that by p.w.e.m., though the difference would not have so much of an effect on the simulation of electrons' trajectories by the Monte Carlo method as discussed above.

3-3 Treatment of inelastic scattering

Ritchie et al. (1969) have clearly pointed out that Bethe's stopping power for aluminum mainly consists of those for conduction electron excitation, plasmon, and L-shell excitations. The stopping power obtained as a sum of these three different elementary excitations agrees very well with that of Bethe-Bloch's stopping power which describes the experiment in the high energy region with considerable success and, furthermore, shows quite good agreement even for the lower energy region as Fitting (1974) has recently reported.

Thus, so far as exact knowledge of individual inelastic scattering is given, direct simulation of each individual inelastic scattering process is probably the best way to treat electron penetration though Bethe's stopping power has been widely used for describing the energy loss process of penetrating electrons with considerable success.

This direct simulation approach has been adopted for the electron penetration in aluminum thin films in the papers of Shimizu et al (1976) and of Green and Leckey (1976). Ganachaud and Cailler (1979) have recently reported a Momte Carlo calculation based on a quite similar model, in which they adopted Gryzinski's excitation function for inner-shell electron excitation and dielectric function for the other excitations. These approaches are basically the same in taking into account the elementary excitations for inner-shell electron, conduction electron, and plasmon. However, such a treatment can be applied with accuracy and confidence only to a few materials including aluminum.

Thus, Krefting and Reimer have proposed using Gryzinski's

excitation function (Gryzinski 1965) for inner-shell (core) electron excitation. For the other excitations they used the difference between Bethe's stopping power and that due to core electron excitation i.e.

$$\left(\frac{dE}{dX}\right)_{\text{valence}} = \left(\frac{dE}{dX}\right)_{\text{Bethe}} - \left(\frac{dE}{dX}\right)_{\text{core}} \qquad (3\text{-}29)$$

Another approach has been devised by Shimizu and Everhart (1978b). They have applied Gryzinski's excitation function $d\sigma(E)/dE$ to valence electrons by incorporating an appropriate value of a mean binding energy E_B which satisfies

$$\int_E \left(\frac{d\sigma(E)}{dE}\right)_{E_B} dE = \left(\frac{dE}{dX}\right)_{\text{Bethe}} - \left(\frac{dE}{dX}\right)_{\text{core}} \qquad (3\text{-}30)$$

Although the treatment proposed by Shimizu and Everhart is quite useful for thin films (Adesida et al. 1978) the extension to compound materials, whcih is essential for the present purpose of quantitative AES, is limited because of the complexity in the evaluation of valence electrons in them.

In the treatment of Krefting and Reimer, on the other hand, one can easily extend it to a compound specimen by introducing an extended Bethe's stopping power equation (Philibert and Tixier 1968) for them, which has been widely used in EPMA with considerable success.

Hence the comparison of the result obtained by the direct simulation approach with that of Krefting and Reimer for an aluminum bulk specimen was attempted to see whether the latter approach can be a good approximation of practical use for quantitative AES.

Figure 3-6 shows the energy distributions of backscattered electrons for 10 keV electrons incident on an aluminum bulk specimen, which were calculated by using these two approaches for inelastic scattering process in Monte Carlo calculation.

The result shows good agreement in both approaches while the direct simulation approach has provided a backscattering yield of a few percent higher than that of the other.

This can be understood as follows : In the direct simulation approach all the individual inelastic scattering processes cause

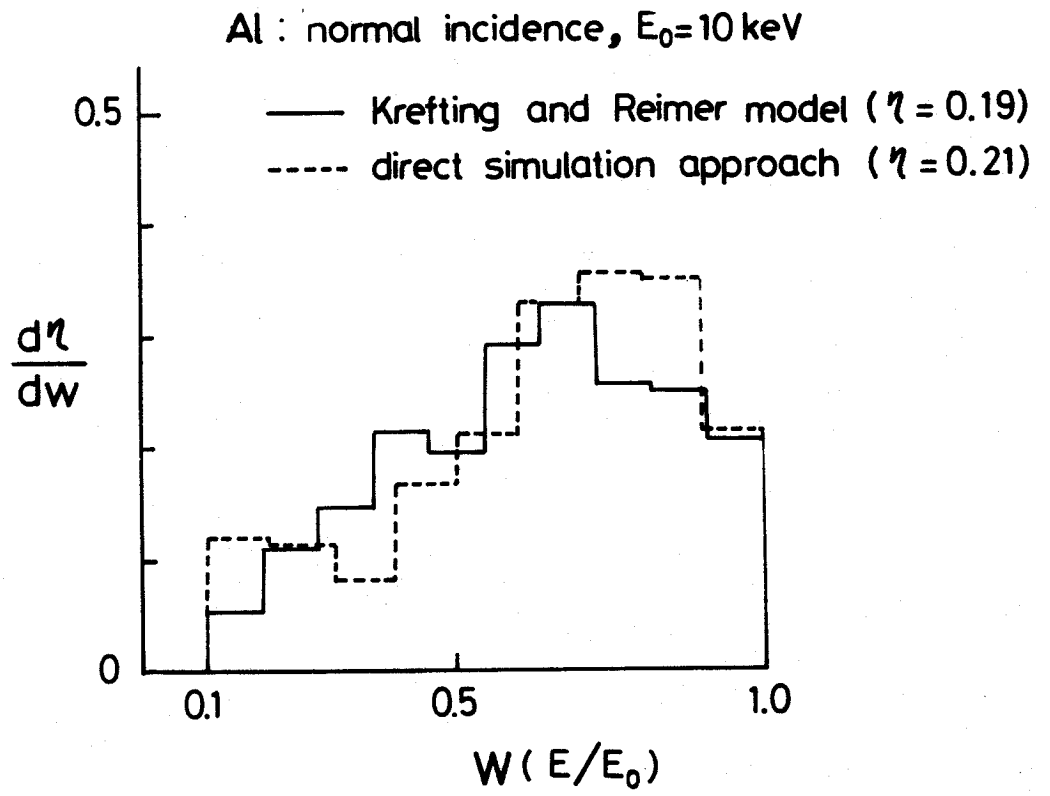

Fig. 3-6 Comparison of the backscattered electron energy distributions for aluminum, based on (a) present model (solid line) and (b) direct simulation approach (dashed line). Incident energy is 10 keV, and the angle of incidence is 45°.

the angular deflection of a primary electron, as described in detail by Shimizu et al. (1976), while only the core-electron excitation causes angular deflection in the other. This results in a higher possibility of backscattering in the direct simulation approach since the single-electron excitation of conduction electrons provides the possibility of large angle deflection of a penetrating electron though it has a small probability. This large deflection results in an increase of backscattered electrons of high energy as seen in Fig. 3-6.

This difference in the backscattered electrons, however, has not resulted in any marked difference in the generation of Auger electrons. Then, a Monte Carlo simulation model based on Krefting and Reimer's treatment was developed. That is, incident electron moves in a material losing its energy partly because of shell electron excitation at some points in the material and partly because of the stopping power of the material which is given by equation (3-29). Here, $(\frac{dE}{dX})_{Bethe}$ is given by the following equation,

$$(\frac{dE}{dX})_{Bethe} = 2\pi e^4 \cdot N_{AV} \cdot \frac{\rho}{A} \cdot Z \cdot \frac{1}{E} \cdot \ln \frac{\gamma E}{J} \quad , \qquad (3\text{-}31)$$

where e is the charge of an electron, ρ is the density of a material and N_{AV}, Z, and A are Avogadro number, atomic number, and atomic weight of the material, respectively. A constant γ was chosen to 1.166[*1)], while for the mean excitation potential either experimentally obtained values (if available) or the value given by the following empirical equation (Berger and Seltzer 1964),

*1) Matsukawa (1973) has investigated the influence of γ -value to the results of Monte Carlo calculations.

$$\frac{J(eV)}{Z} = 9.76 + 58.8\ Z^{-1.19} \qquad (3\text{-}32)$$

was used.

As to $(\frac{dE}{dX})_{core}$, on the other hand, the stopping power formula given by Gryzinski (1965) was used, which is written as

$$(\frac{dE}{dX})_{core} = N_{AV}\frac{\rho}{A}\{\sum_j n_j f(E, E_j)\} \qquad (3\text{-}33\text{-}a)$$

$$f(E, E_j) = \frac{\sigma_0}{E}(\frac{E_j}{E+E_j})^{3/2}[(1-\frac{E_j}{E})\ln(\frac{E}{E_j}) + \frac{4}{3}(1-\frac{E_j}{E})$$

$$\times \ln\{2.7 + (\frac{E}{E_j}-1)^{1/2}\}](1-\frac{E_j}{E})^{1/2} \qquad (3\text{-}33\text{-}b)$$

Here, n_j is the number of j-shell electrons whose binding energy is E_j, and E is the energy of incident electrons. A constant σ_0 is

$$\sigma_0 = 6.56 \times 10^{-14} \quad (eV^2 \cdot cm^2) \qquad (3\text{-}34)$$

If the stopping power given by the equation (3-33) becomes larger than that given by the equation (3-31) at low energy region, then the equation (3-29) is changed to

$$(\frac{dE}{dX})_{Valence} = 0 \qquad (3\text{-}35\text{-}a)$$

that is,

$$(\frac{dE}{dX})_{Total} = (\frac{dE}{dX})_{core} \qquad (3\text{-}35\text{-}b)$$

3-4 Calculation procedure

3-4-1 Determination of free path

In the present calculation, the procedure is based on so-called single scattering model where electrons are scattered either elastically or inelastically by an atom after moving some distance $\lambda(E)$ (free path) which is determined statistically assuming to obey Poisson process by

$$\lambda(E) = - \lambda_m(E) \ln (R) \quad . \tag{3-36}$$

Here, R denotes a uniform random number between 0 to 1, and $\lambda_m(E)$ is the mean free path which is given for polyatomic case by the equation

$$\lambda_m(E) = 1/[N \sum C_\ell^a(\sigma_\ell^e(E) + \sum n_j \sigma_{\ell,j}^i(E, E_j))] \quad , \tag{3-37}$$

where N is the atom density (atoms/cm^3) of the material and C_ℓ^a is an atomic concentration of ℓ-th element of it. $\sigma_\ell^e(E)$ denotes the elastic scattering cross-section which is obtained by p.w.e.m. for 20 different primary energies from 0.5 keV to 10 keV as described in Section 3-2. The cross-section corresponding to any energy E is calculated by linear interporation using these values. $\sigma_{\ell,j}^i$, on the other hand, is the cross-section for inelastic scattering for j-shell (the number of shell electrons is n_j) of that element. Here, a number up to 3 was permitted for ℓ and j to reduce computer time and memories used in the calculation. This restriction, then, requires us to choose the shells to be considered in the calculation and to use mean ionization energy

for those shells especially for heavy elements.

Concerning the ionization cross-section for inner shells, many theoretical and empirical formulae have been proposed by various workers (Worthington and Tomlin 1956, Gryzinski 1965, Rudge and Schwartz 1966, Lotz 1970, Smith and Gallon 1974). Recently, more accurate ionization cross-sections were also calculated (McGuire 1977). In the present calculation Gryzinski's semi-empirical formula by classical treatment is adopted since it gives enough accuracy for the excitation of light atom (Goto et al. 1975, Powell 1976) and that stopping power formula is also given with the same theoretical treatment as described above. The ionization cross-section σ_j^i is written as follows:

$$\sigma_j^i(E, E_j) = \frac{\sigma_0}{E_j^2} \cdot g_j(x) \quad , \tag{3-38-a}$$

$$g_j(x) = \frac{1}{x}\left(\frac{x-1}{x+1}\right)^{3/2}\left\{1 + \frac{2}{3}\left(1-\frac{1}{2x}\right) \ln\left[2.7+(x-1)^{1/2}\right]\right\} \quad , \tag{3-38-b}$$

where by x the overvoltage ratio ($=E/E_j$) is denoted.

3-4-2 Determination of each scattering process

At each scattering point, the element which causes scattering of an electron is first determined statistically taking into account the product of cross-section (both elastic and inelastic) and atomic concentration for each element. Therefore, the scattering by ℓ-th element occurs when the following condition is satisfied. That is,

$$\frac{\sum_{\ell'=1}^{\ell} C_{\ell'}^a (\sigma_{\ell'}^e + \sigma_{\ell'}^i)}{\sum_{\ell} C_{\ell}^a (\sigma_{\ell}^e + \sigma_{\ell}^i)} \leq R < \frac{\sum_{\ell'=1}^{\ell+1} C_{\ell'}^a (\sigma_{\ell'}^e + \sigma_{\ell'}^i)}{\sum_{\ell} C_{\ell}^a (\sigma_{\ell}^e + \sigma_{\ell}^i)} \quad , \tag{3-39-a}$$

where R is a uniform random number and

$$\sigma_{\ell}^{i} = \sum_{j} \sigma_{\ell,j}^{i} \quad . \tag{3-39-b}$$

Next, the type of scattering and also the kind of inner-shell which causes inelastic scattering are determined statistically as follows,

$$R \leq \frac{\sigma_{\ell}^{e}}{\sigma_{\ell}^{e} + \sigma_{\ell}^{i}} \qquad \text{elastic scattering} \tag{3-40-a}$$

$$\frac{\sigma_{\ell}^{e} + \sum_{j'=1}^{j} \sigma_{\ell,j'}^{i}}{\sigma_{\ell}^{e} + \sigma_{\ell}^{i}} \leq R < \frac{\sigma_{\ell}^{e} + \sum_{j'=1}^{j+1} \sigma_{\ell,j'}^{i}}{\sigma_{\ell}^{e} + \sigma_{\ell}^{i}} \qquad \text{inelastic scattering (j-th shell)} \tag{3-40-b}$$

.

The angle of scattering at each scattering point is determined as follows:

i) elastic scattering angle : θ_e

An accumulative function $F(E,\theta)$, which is defined as follows,

$$F(E, \theta) = \frac{\int_0^{\theta} \frac{d\sigma^e}{d\theta} d\theta}{\int_0^{\pi} \frac{d\sigma^e}{d\theta} d\theta} \qquad (0 \leq F(E, \theta) \leq 1) \tag{3-41}$$

is also obtained in the calculation by p.w.e.m. with a step of $\Delta\theta = 2°$. Here $\frac{d\sigma^e}{d\theta}$ denotes the differential scattering cross-section. Therefore, the scattering angle θ_e is determined by the equation

$$F(E, \theta_e) = R \quad , \tag{3-42}$$

where R is a uniform random number.

ii) inelastic scatter angle : θ_i

According to the classical treatment of two-body collision, the angle θ_i is determined by the equation.

$$\sin^2\theta_i = \frac{\Delta E}{E} \quad . \tag{3-43}$$

Here, the loss of energy (ΔE) of an incident electron (energy E) is determined using excitation function $\Phi(E, E_j, \Delta E)$ given by Gryzinski (1965) as follows:

An accumulative function $G(E, E_j, E')$ $(E_j \leqq E' \leqq E)$ is first calculated by the equation,

$$G(E, E_j, E') = \frac{\int_{E_j}^{E'} \Phi(E,E_j,E'')\, dE''}{\int_{E_j}^{E} \Phi(E,E_j,E'')\, dE''} \quad , \qquad (0 \leqq G(E,E_j,E') \leqq 1 \tag{3-44}$$

then it is compared with a uniform random number to decide the loss energy E'. The excitation function given by Gryzinski is,

$$\Phi(E, E_j, \Delta E) = \frac{N\pi e^4}{(\Delta E)^2} \frac{1}{\Delta E} \frac{E_j}{E} \left(\frac{E}{E+E_j}\right)^{3/2} \left(1-\frac{\Delta E}{E}\right)^{\frac{E_j}{E_j+\Delta E}}$$

$$\times \left[\frac{\Delta E}{E_j}\left(1-\frac{E_j}{E}\right) + \frac{4}{3}\ln\left\{2.7 + \left(\frac{E-\Delta E}{E_j}\right)^{1/2}\right\}\right] \quad . \tag{3-45}$$

Practically, the function $G(E, E_j, E')$ is calculated for some values of electron energy E and interpolation procedure is used to determine $G(E, E_j, E)$ for any energy of the incident electron.

An azimuth angle ψ, on the other hand, is determined both for elastic scattering and inelastic scatteirng by the equation,

$$\Delta\psi = 2\pi \cdot R \qquad (0 \leq R \leq 1) \quad . \tag{3-46}$$

As both θ_e (or θ_i) and ψ are determined with respect to the direction of electron incidence, they are related with polar and azimuth angels corresponding to a fixed co-ordinate using Euler relation (Matsukawa 1973).

3-4-3 Energy loss

Thus the path of an incident electron and an excited electron with high energy is determined and pursued till either it is scattered out of the material or it lose its energy below 0.5 keV (stop energy chosen in the present calculation). The energy loss is taken into account in both stopping power and inelastic scattering as discussed in the previous section. Therefore, the energy of an electron E becomes E' after moving free path $\lambda(E)$, where

$$E' = E - \left(\frac{dE}{dX}\right)_{\text{valence}} \cdot \lambda(E) \quad . \tag{3-47}$$

$\left(\frac{dE}{dX}\right)_{\text{valence}}$ is determined by the equation (3-29), (3-21) and (3-33) with a little modification for the case of poly-atomic materials. That is, (3-31) is changed according to Philibert and Tixier (1968) to the following equation,

$$\left(\frac{dE}{dX}\right)_{\text{Bethe}} = 2\pi e^4 \cdot N_{Av} \bar{\rho} \cdot \frac{1}{E} \sum_{\ell} \frac{C_\ell^\omega Z_\ell}{A_\ell} \ln \frac{1.166E}{J_\ell} \quad ,$$

where C_{ℓ}^{ω} is a weight concentration of ℓ-th element. The mean density $\bar{\rho}$, which is given either experimentally (if available) or by the equation

$$\frac{1}{\bar{\rho}} = \sum_i \frac{C_i}{\rho_i} \tag{3-49}$$

is used in the calculation. And for the $(\frac{dE}{dX})_{core}$, (3-33-a) is changed to

$$(\frac{dE}{dx})_{core} = N_{AV} \Sigma C_A^{a\rho} \{\Sigma_j n, f(E,E_j)\}$$

A schema of the treatment of the present calculation is shown in Fig. 3-7, and the flow chart are shown in Appendix II.

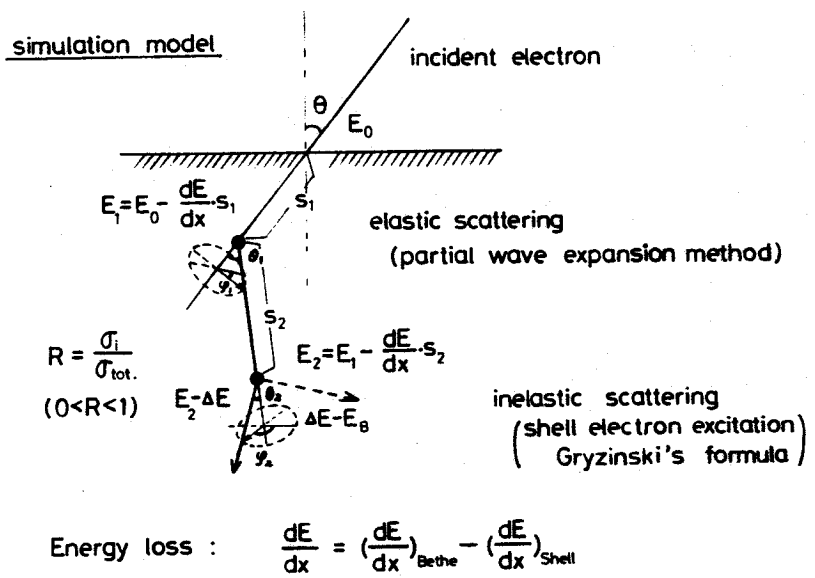

Fig. 3-7 A schema for the present calculation.

3-4-4 Random number

The uniform random number used through the calculation is obtained by the computer with multiplicative congruential method given by Lehmer. That is, the random number is successively calculated by the equation

$$x_{n+1} = \lambda \cdot x_n \pmod{P} \tag{3-51}$$

where λ is chosen to 23 and P, 10^8+1 (Tsuda 1977). Practically, the value x_n is divided by 10^8 and the value (R) between 0 to 1 is obtained and used.

3-5 Results and discussions

3-5-1 Examination of the present Monte Carlo calculations

A) Energy- and angular-distributions of backscattered electrons

Since the energy- and angular-distributions of backscattered electrons play a dominant role in atomic number correction in quantitative AES analysis, the applicability of the present Monte Carlo calculations was first examined through comparison with the experimental results for those distributions for a number of elements of practical interest.

All the results of the Monte Carlo calculation were based on 5000 trajectories

Figure 3-8 shows the comparison between the theoretical results for the energy distributions of backscattered electrons

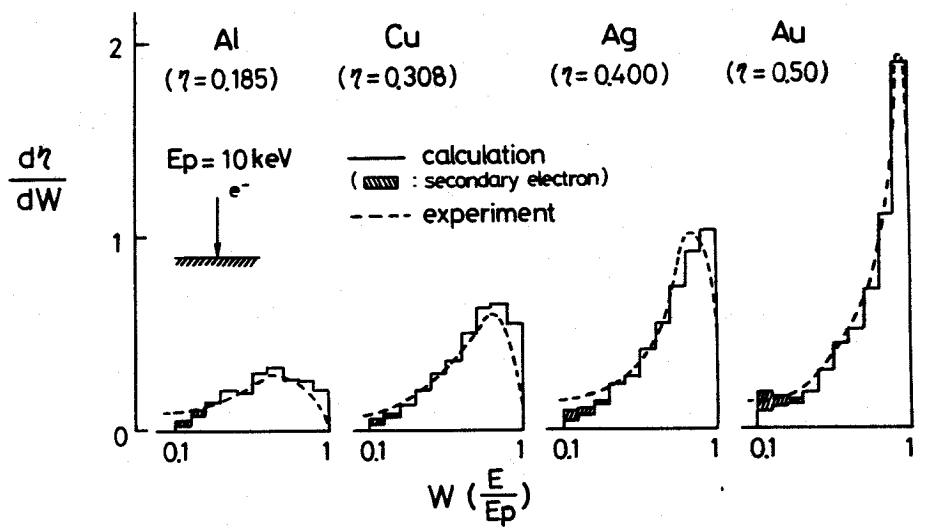

Fig. 3-8 Energy distributions of backscattered electrons for Al, Cu, Ag, and Au at normal incidence. Histograms show the estimated results for 10 keV incident electrons while the dashed lines represent the experimental results by Thomas (1961) (for Al and Ag: 12 keV) and by Matsukawa (1973) (for Cu and Au: 10 keV). Shaded area shows excited secondary electrons and η denotes a backscattering coefficient.

$d\eta/dW$ [$=d\eta/d(E/E_p)$] with the experiemntal ones by Thomas (1961) (for Al and Ag) and by Matsukawa (1973) (for Cu and Au). In these calculations the Auger electrons which arise from the relaxation process of inner-shell excitation was not taken into account to simplify the calculation because the intensity of these Auger electrons is much smaller than that of backscattered electrons.

It has been pointed out that the conventional Monte Carlo calculation , in which the Rutherford scattering formula is used to describe elastic scattering, does not describe the experimental results of backscattered electrons for high Z target like Au as well as for a low Z target (Matsukawa 1973). The present Monte Carlo calculations, on the other hand, describe the energy distributions shown in Fig. 3-8 with considerable success and this suggests that the present approach can be applied to basic study of quantitative AES analysis.

The angular distribution of backscattered electrons obtained from the Monte Carlo calculation is also plotted in Fig. 3-9 only

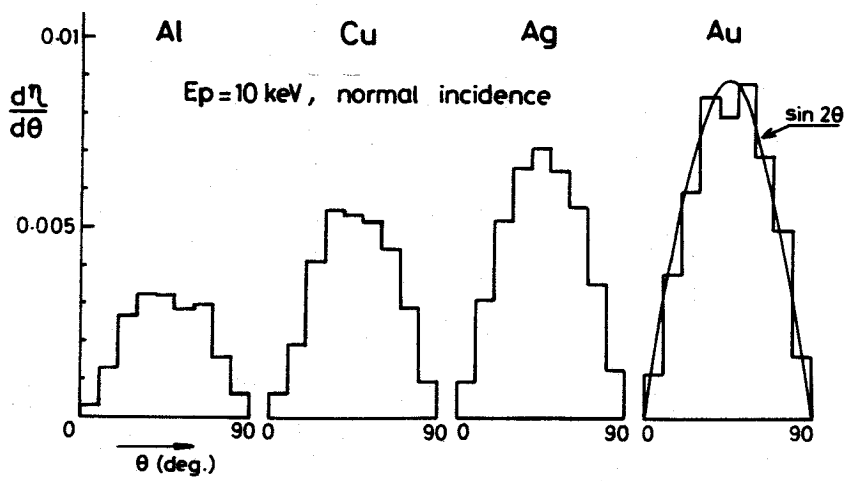

Fig. 3-9 Angular distributions of backscattered electrons for Al, Cu, Ag, and Au at normal incidence of 10 keV electrons. Histograms show the simulation results, and the solid line represents a distribution obeying cosine low.

to confirm that all these distributions follow a cosine law for normal incidence as has been found experimentally by Kanter (1957).

B) Backscattered electron yield and its dependence on the incident angle

A backscattered electron yield η is usually defined as the ratio of the number of secondary electrons which have an energy above 50 eV to the number of incident electrons.

Many experimental values of η obtained with electron microprobe (Kanter 1957, Wittry 1966, Bishop 1966, Colby 1968) are mainly concerned about the value in high energy electron incidence and that they could not get rid of the effect of carbon contaminant. So the value obtained by the present calculation was compared with the experimental one by Koshikawa (1973) which was measured under ultra high vacuum for Al, Cu and Ag at normal incidence of primary electrons.

Solid lines in Fig. 3-10 represent the experimental values by Koshikawa and cross-marks represent the calculated results. It is clear from the figure that the yield by experiment gradually increases as the energy decreases in a region above 1 keV, which is also confirmed by calculation. The calculated results show good coincidence with experimental values for Ag and Al, though a little discrepancy is observed in the case of Cu.

The dependence of the yield on an incident angle of primary electrons is also compared with experimental results by Koshikawa for Cu at 3 keV primary electron energy, which was shown in Fig. 3-11(a). The energy distributions of backsacttered electrons obtained by calculation are also shown in Fig. 3-11(b), and it is clear from these figures that the increase of backsacttered elec-

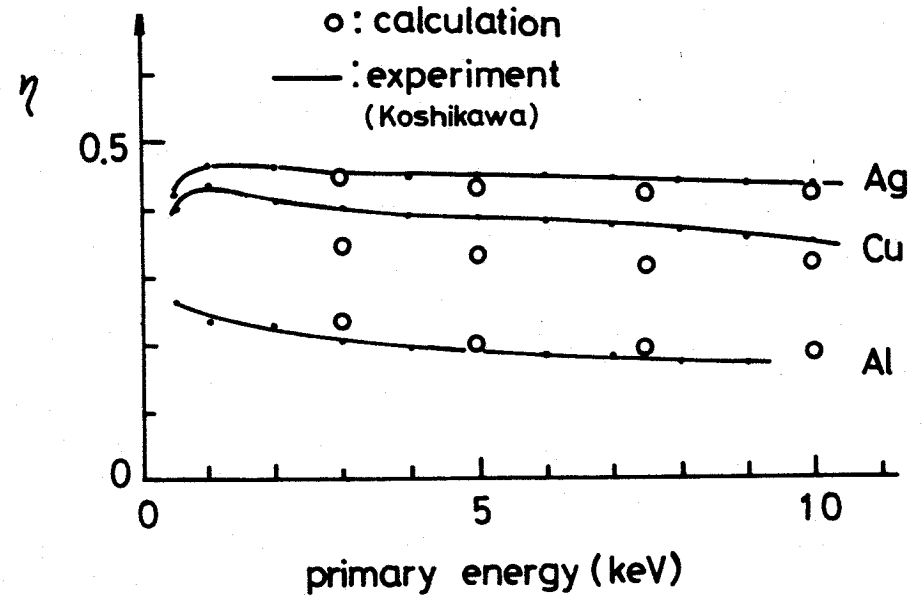

Fig. 3-10 Comparison of the calculated backscattering coefficients with experimental values by Koshikawa (1973) for Al, Cu, and Ag.

trons with high energy mainly contributes to the increase of η at large incident angles (measured from the surface normal). Both the experimental values, shown with a solid line in Fig. 3-11(a), and calculated ones represented by cross marks in the figure show a similar increasing tendency with the angle keeping a certain value of discrepancy which is found in Fig. 3-10. Therefore, this may be attributed to that the experimental values by Koshikawa correspond to the number of secondary electrons with energy above 50 eV while the calculated ones correspond to those with energy above 500 eV as described in the previous section. Reexamination both in experiment and in calculation are necessary for further discussion.

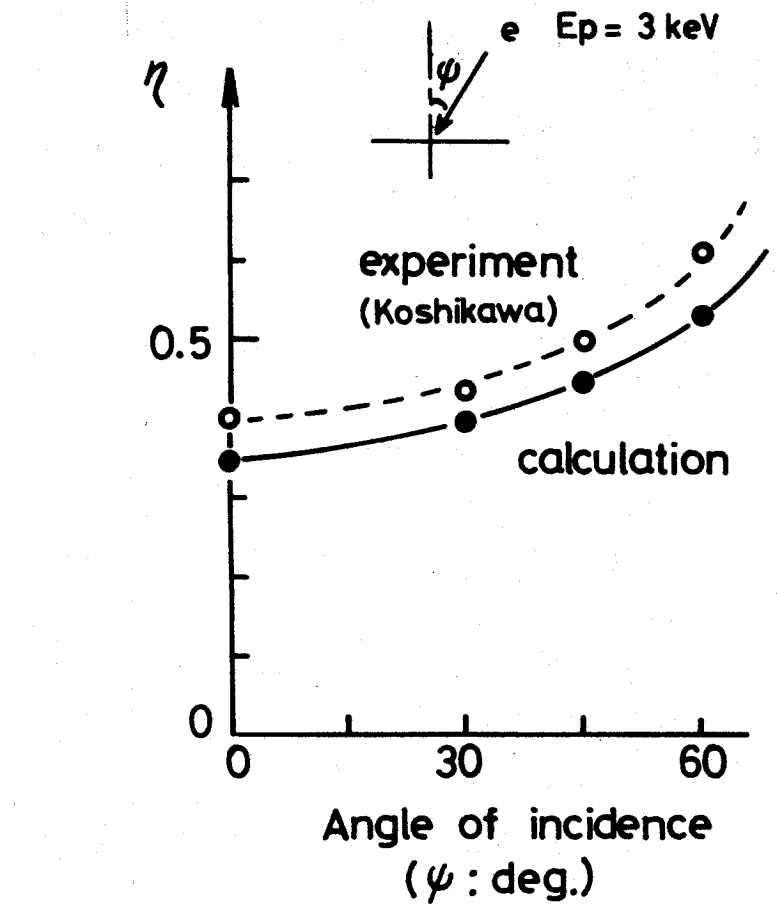

(a)

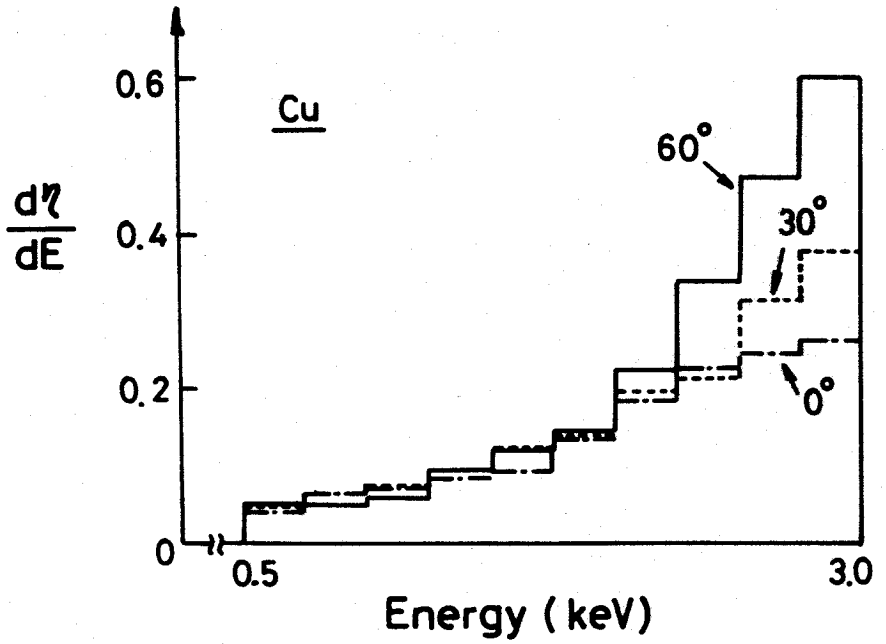

(b)

Fig. 3-11 (a) Dependence of the backscattering coefficient η on the angle of incidence.
(b) Energy distributions of backscattered electrons as a function of the incident angle ψ (calculated by the Monte Carlo method)

3-5-2 Application of the present calculation to quantitative analysis by AES

As discussed in Section 1-3, the contribution of backscattered electrons to Auger signal generation must be well known for the precise quantitaitve analysis by AES. The contribution of backscattered electrons is usually estimated theoretically by the equation,

$$R = 1 + r = 1 + \frac{\int_{E_B}^{E_p} \sigma(E) \frac{d\eta}{dE} dE}{\sigma(E_p) \sec\psi} , \qquad (3\text{-}52\text{-}a)$$

Here σ denotes the ionization cross-section and $\frac{d\eta}{dE}$ is the energy distribution of backscattered electrons. ψ is the angle of incidence for primary electron, while E_p and E_B are primary electron energy and binding energy of an shell being considered, respectively. The second term in equation (3-52-a), therefore, corresponds to the backscattering factor in AES.

To evaluate the Auger-signal generation by the backscattered electrons, in practice, one has to take into account an ejection angle θ (measured from the surface normal) as well as the kinetic energy of a backscattered electron. The probability of Auger signal generation of the backscattered electron penetrating through the surface layer ΔZ is proportional to $\sigma_i(E) \Delta Z \sec\theta$ in which ΔZ should be taken as the same order of magnitude as the mean free path of the Auger electron. Thus, it is much more useful to plot $\int \sec\theta (d^2\eta/dEd\Omega) \times d\Omega$ ($d\Omega$ is the unit solid angle) instead of a simple energy distribution of backscattered electron $d\eta/dE$ [$=\int (d^2\eta/ dEd\Omega)\ d\Omega$]

which is often used in quantitative analysis by AES. In this case, equation (3-52-a) should be changed as follows;

$$R = 1 + r = 1 + \frac{\int_{E_B}^{E_p} \sigma(E) \left(\int_{\Omega} \sec\theta \frac{d^2\eta}{dE\ d\Omega} d\Omega \right) dE}{\sigma(E_p)\ \sec\psi} \quad , \qquad (3\text{-}52\text{-}b)$$

and the backscattering factor was obtained for a number of mono- and poly-atomic materials of practical importance using this equation by the Monte Carlo calculations.

Calculated materials are listed in Table 3-2. Figure 3-12 shows the result of $\int \sec\theta \frac{d^2\eta}{dE\ d\Omega} d\Omega$ distributions

Table 3-2 List of calcualted materials.
(atomic and mean-atomic number of materials are also shown in parentheses)

1) pure element	2) compound & alloy
B (5)	BN (6)
C (6)	Al_2O_3 (10)
Al (13)	SiO_2 (10)
Ti (22)	MgO (10)
Fe (26)	MgF_2 (10)
Cu (29)	KCl (18)
Ge (32)	ZnS (23)
Zr (40)	GaP (23)
Ag (47)	CdS (32)
Au (79)	PbS (49)
	$Au_{0.25}Cu_{0.75}$ (42)
	$Au_{0.5}Cu_{0.5}$ (54)
	$Au_{0.75}Cu_{0.25}$ (67)
	AlAs (23)
	GaAs (32)

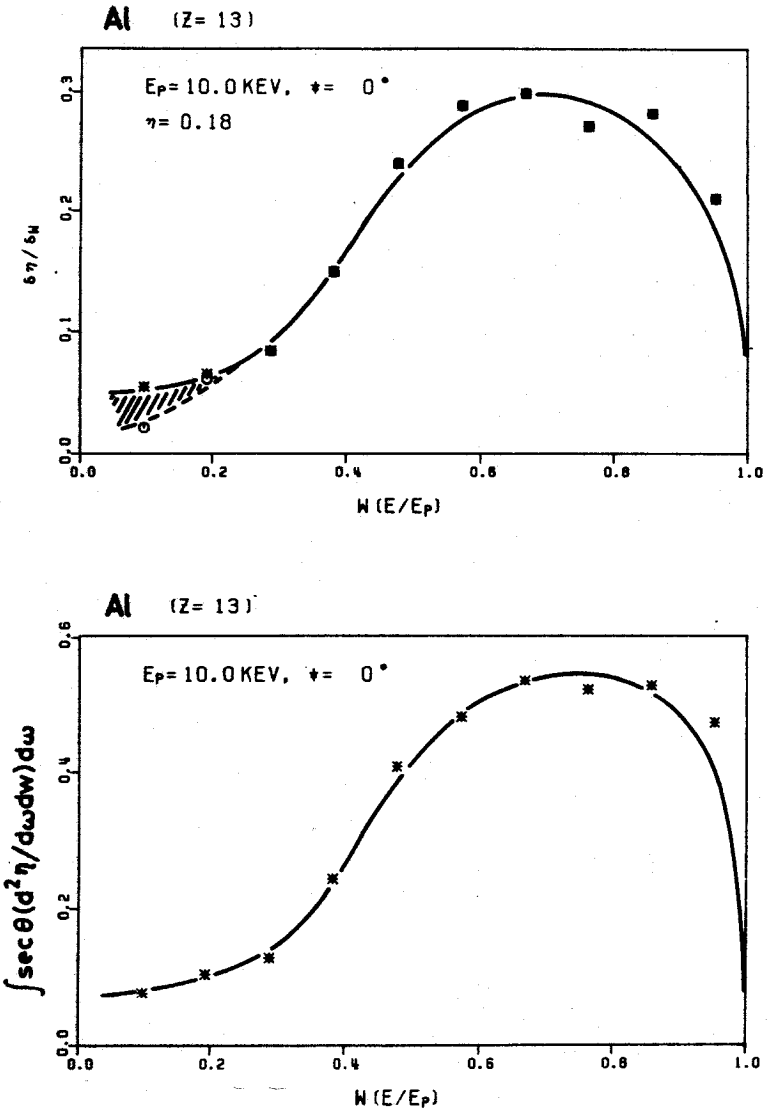

(a)

Fig. 3-12 Energy distributions of backscattered electrons: (a) normal incidence of 10 KV electrons on Al. Lower part shows the distribution weighted by ejection angle of backscattered electrons.

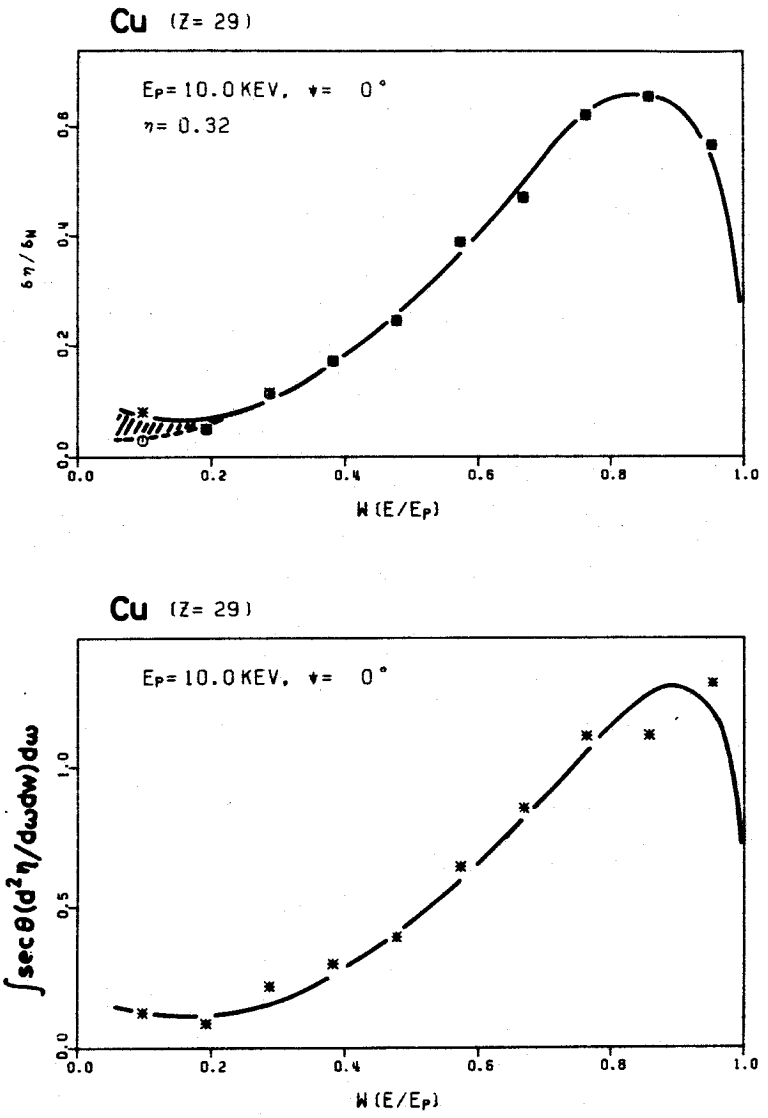

(b)

Fig. 3-12 Energy distributions of backscattered electrons: (b) normal incidence of 10 KV electrons on Cu. Lower part shows the distribution weighted by ejection angle of backscattered electrons.

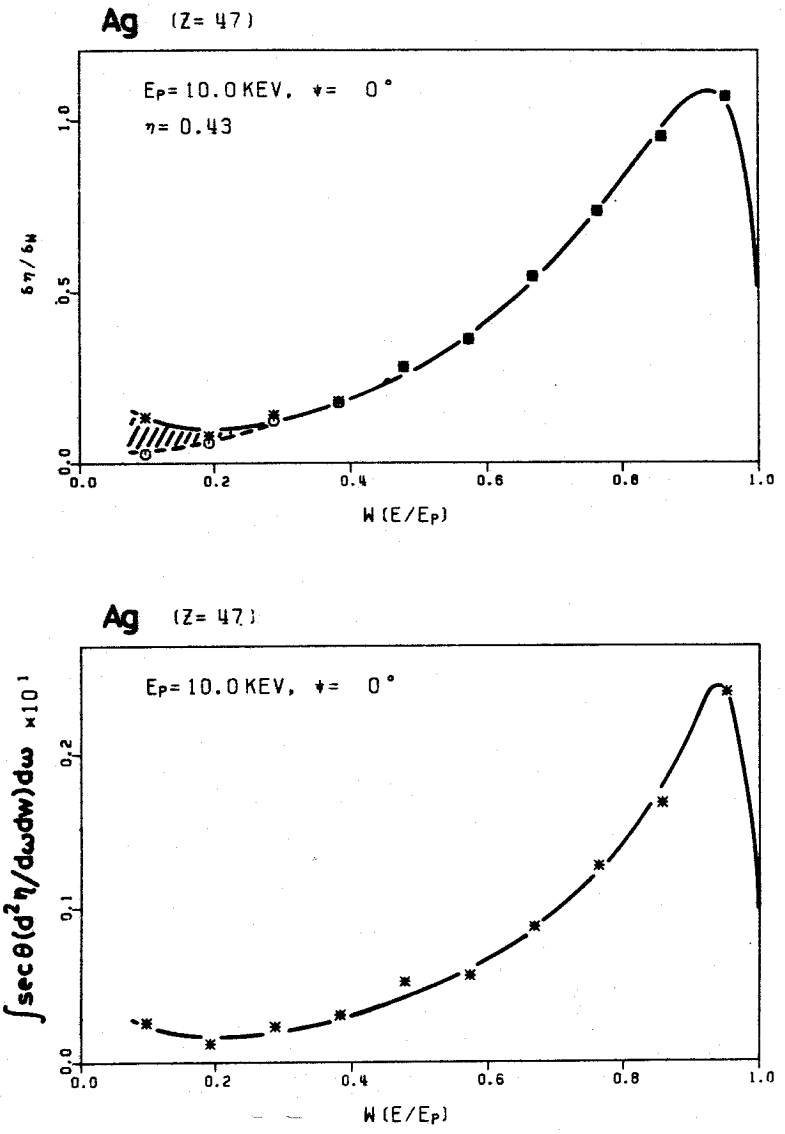

(c)

Fig. 3-12 Energy distributions of backscattered electrons: (c) normal incidence of 10 KV electrons on Ag. Lower part shows the distribution weighted by ejection angle of backscattered electrons.

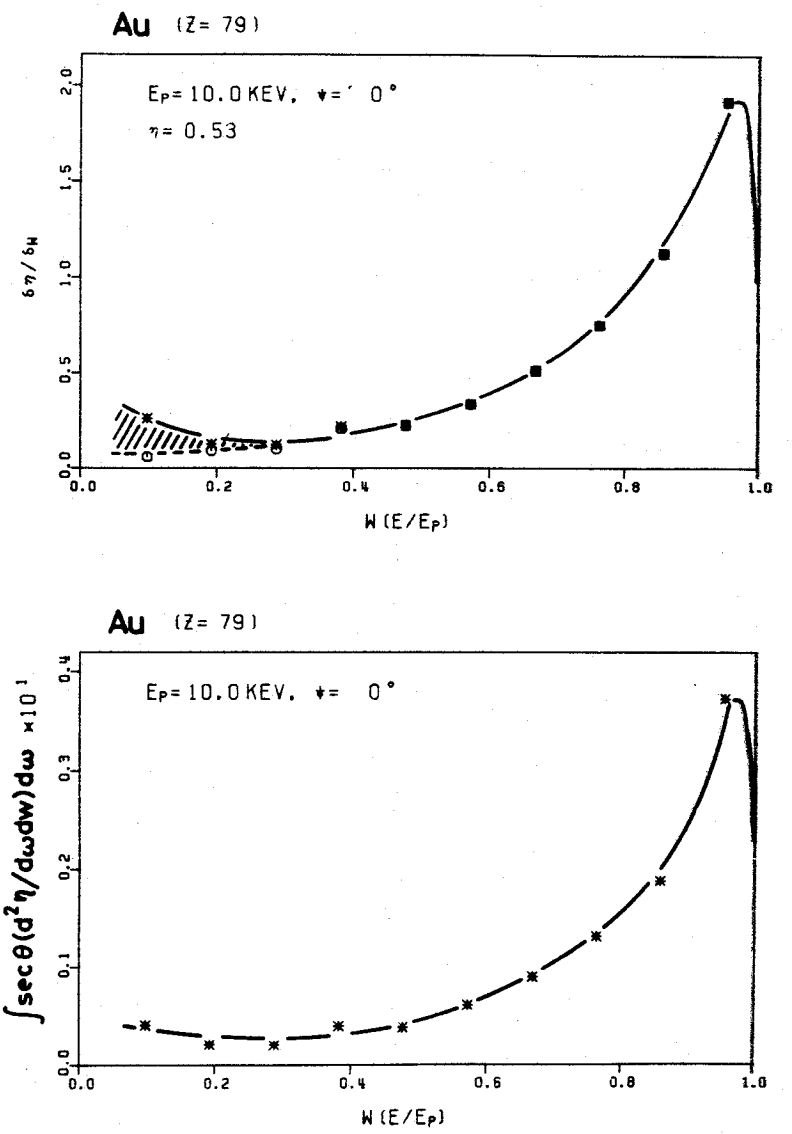

(d)

Fig. 3-12 Energy distributions of backscattered electrons: (d) normal incidence of 10 KV electrons on Au. Lower part shows the distribution weighted by ejection angle of backscattered electrons.

for Al, Cu, Ag, and Au for primary electrons of 10 keV at normal incidence. Comparing the figure with Fig. 3-8, which corresponds to the distribution $\int \frac{d^2\eta}{dE\ d\Omega} d\Omega$, it is found that the distribution in the former is more stressed in the high energy region than the latter probably because backscattered electrons with high energy undergo single scattering and have a higher possibility of ejection near $\theta = 90°$. So the backscattering factor r estimated by the equation (3-52-b) gives higher values than that by (3-52-a) for elements which have high values of E_B since $\sigma(E)$ has its maximum at energy about 3 or 4 times as much as that of E_B.

Some of the calculated results of R(=1+r) are shown in Fig. 3-13 and Fig. 3-14. In the estimation of R, Gryzinski's ionization cross section was used for $\sigma(E)$.

Fig. 3-13 shows the variation of R as a function of binding energy E_B for Al((a)), Cu ((b)), Ag((c)), and Au((d)) at normal incidence of primary electrons. Primary energies of 10 keV, 7.5 keV, 5 keV, and 3 keV which are often used in conventional AES as well as scanning Auger electron microscopy are chosen for calculation, and the difference of R between these energies becomes prominent at high binding energies. The difference of it at low binding energy region (below a few hundred eV) does not have much importance since the distribtuion of backscattered electrons in the equation (3-52-b) is obtained by the Monte Carlo calculation only for those which have an energy above 500 eV.

Figure 3-14, on the other hand, shows the variation of R with atomic number (or mean atomic number for poly-atomic case) for the angle of incidence $\psi=0°$ ((a)$\sim$(d)), $\psi=30°$((e)$\sim$(h)), and $\psi=45°$((i)$\sim$(ℓ)), respectively. Open marks represent the results for

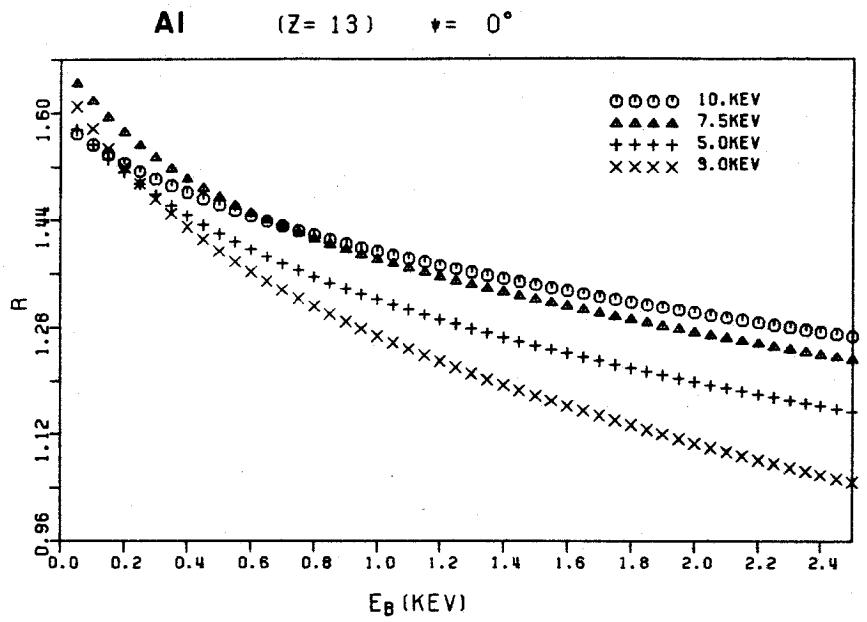

(a)

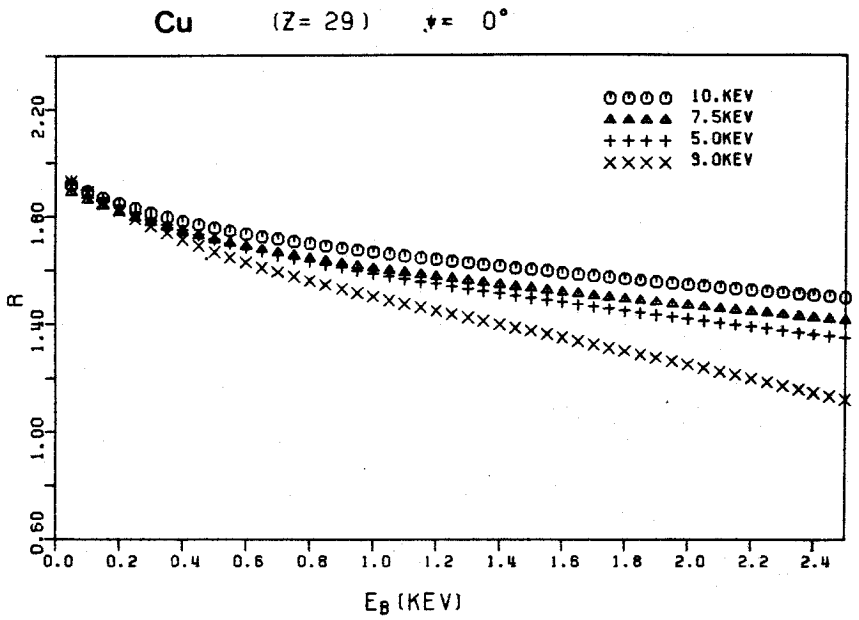

(b)

Fig. 3-13 Variation of R as a function of binding energy E_B: Normal incidence of primary electrons on (a)Al, and (b)Cu.

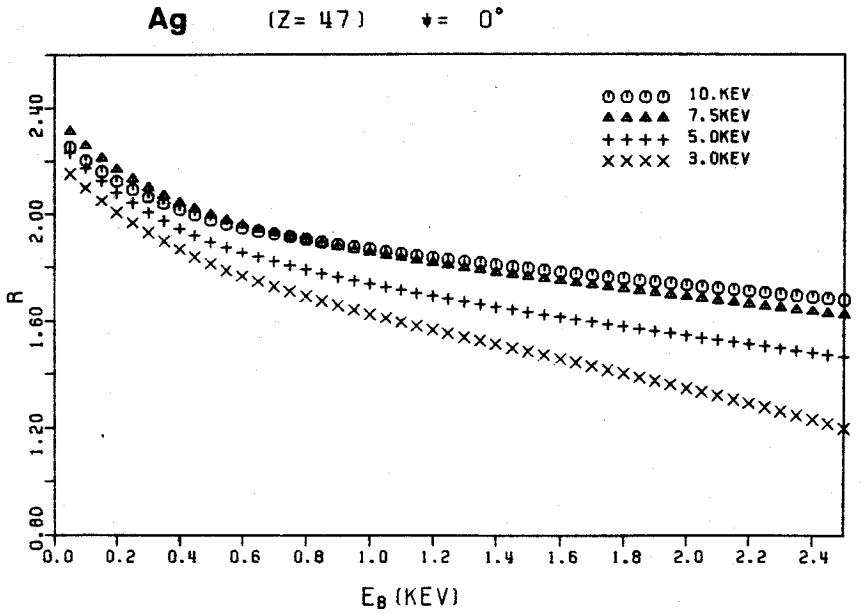

(c)

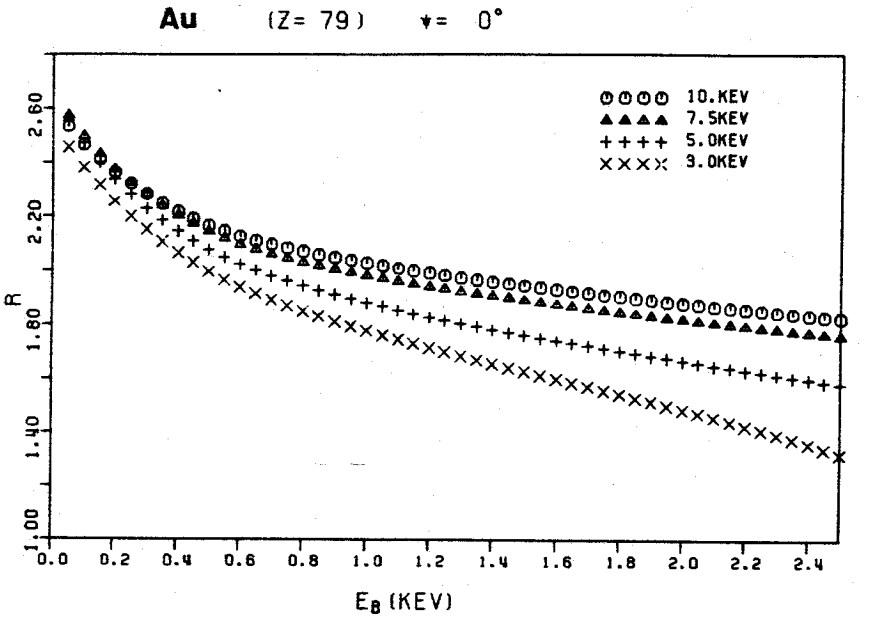

(d)

Fig. 3-13 Variation of R as a function of binding energy E_B: Normal incidence of primary electrons on (c)Ag, and (d)Au.

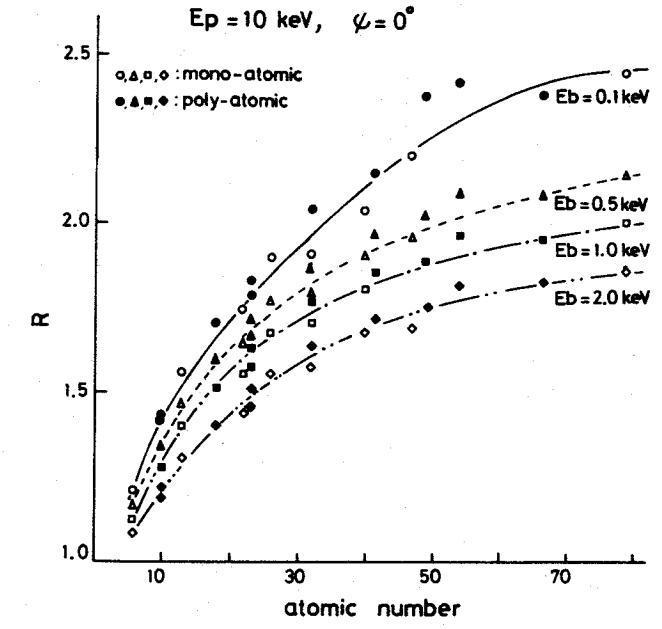

(a)

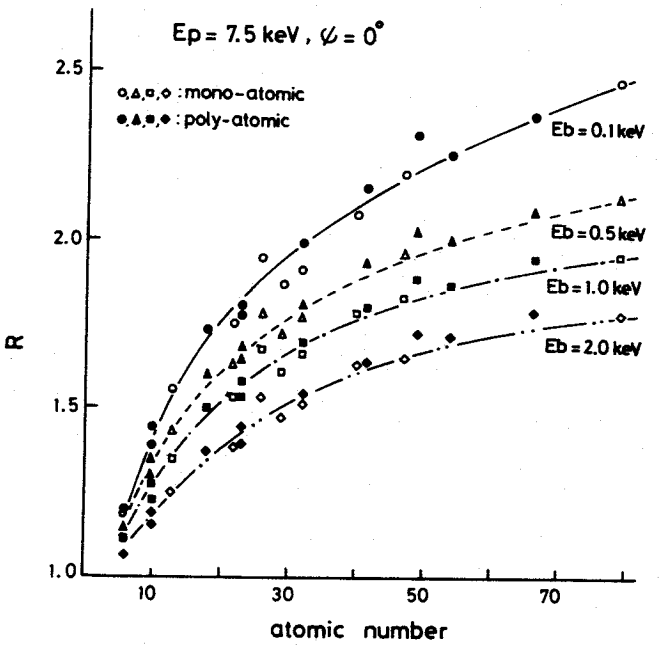

(b)

Fig. 3-14 Variation of the correction factor R with atomic number of materials:
(a); normal incidence of 10 KV electrons.
(b); normal incidence of 7.5 KV electrons.

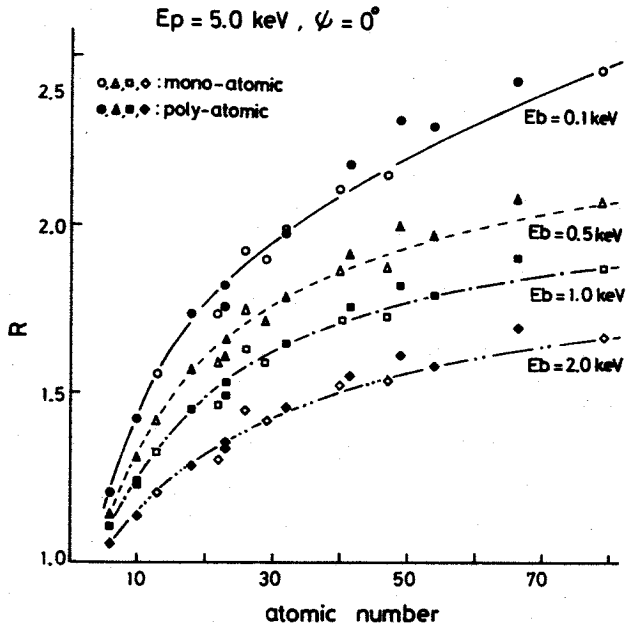

(c)

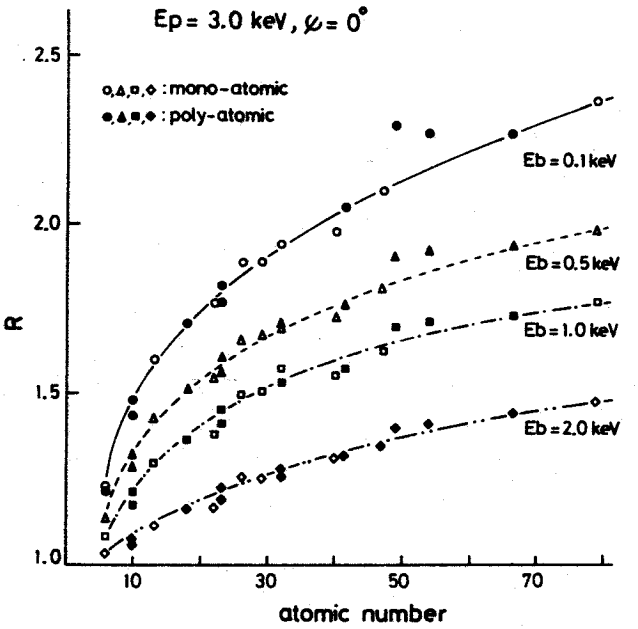

(d)

Fig. 3-14 Variation of the correction factor R with atomic number of materials:
(c); normal incidence of 5 KV electrons.
(d); normal incidence of 3 KV electrons.

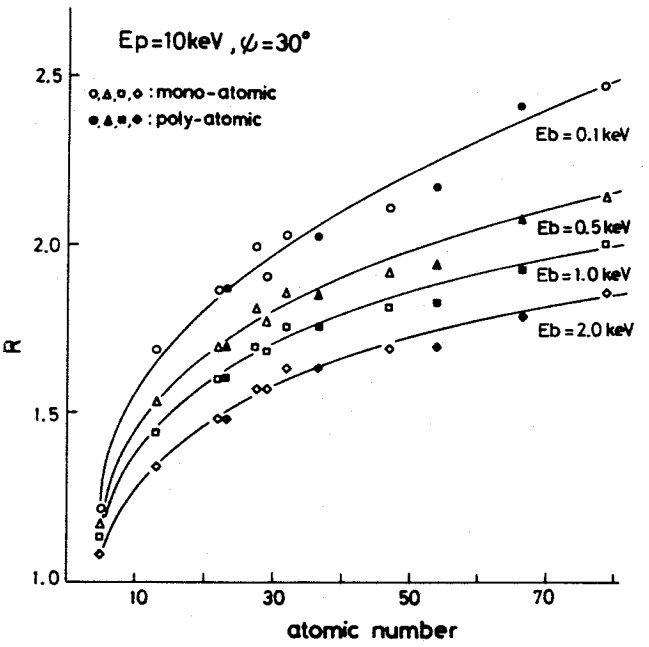

(e)

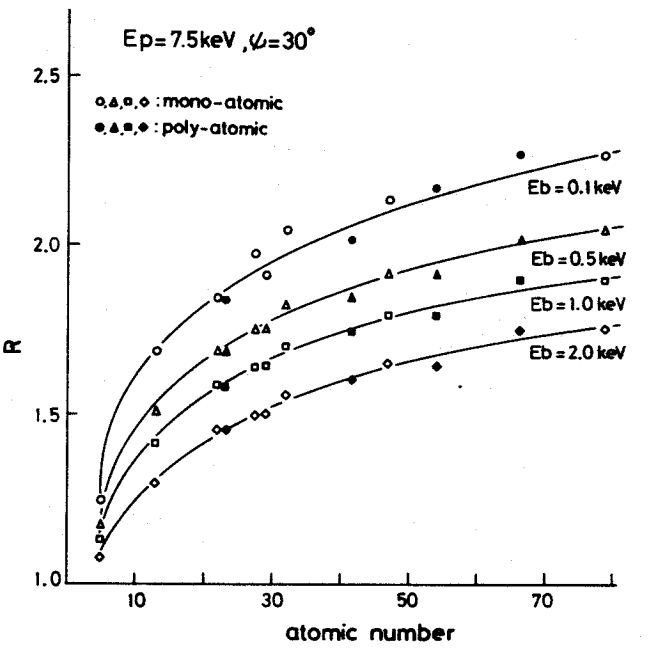

(f)

Fig. 3-14 Variation of the correction factor R with atomic number of materials:
(e); glancing incidence (30°) of 10 KV electrons.
(f); glancing incidence (30°) of 7.5 KV electrons.

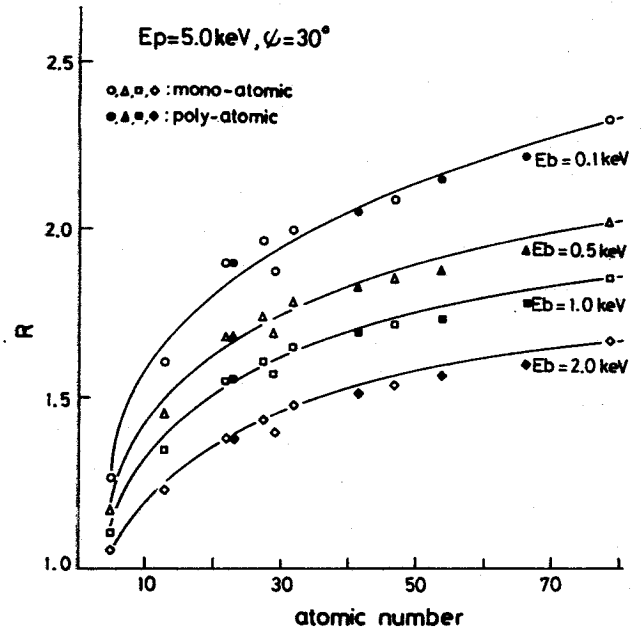

(g)

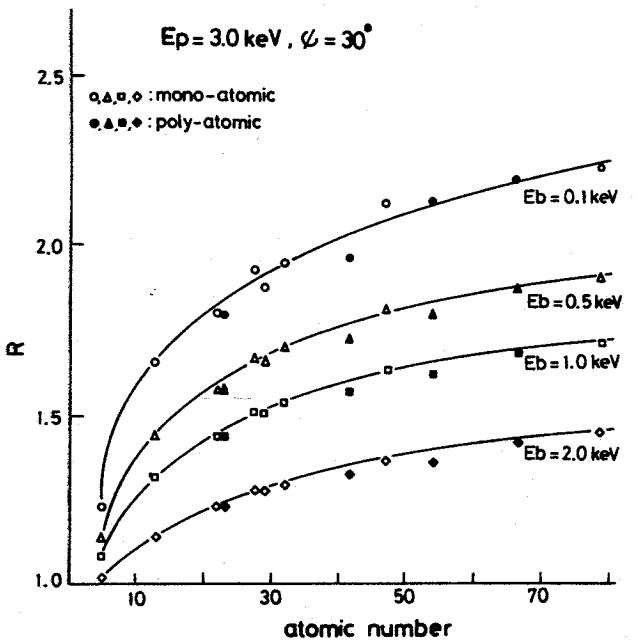

(h)

Fig. 3-14 Variation of the correction factor R with atomic number of materials:
(g); glancing incidence (30°) of 5 KV electrons.
(h); glancing incidence (30°) of 3 KV ekectrons.

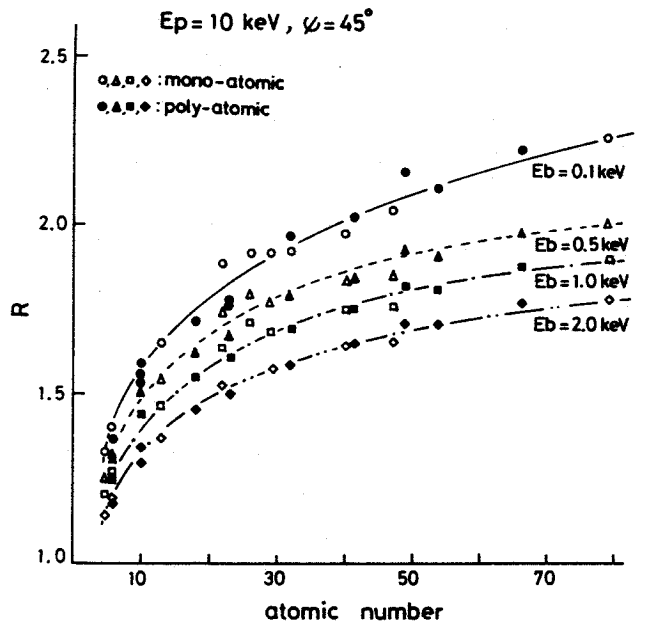

(i)

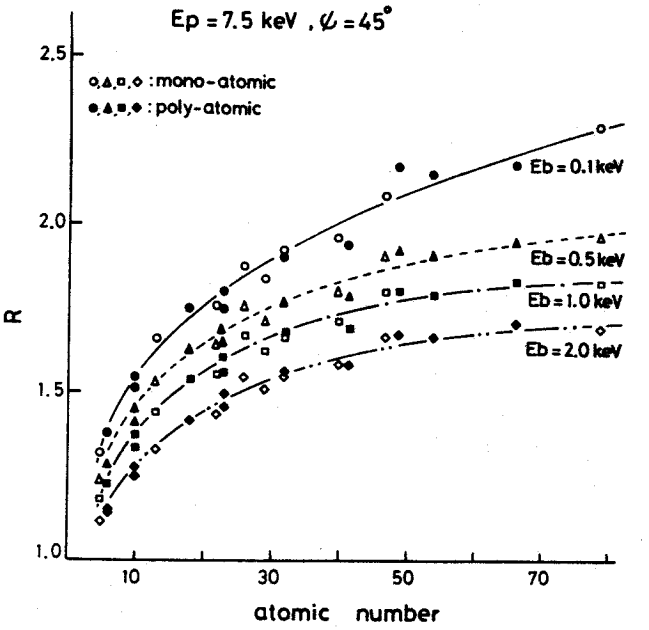

(j)

Fig. 3-14 Variation of the correction factor R with atomic number of materials:
(i); glancing incidence (45°) of 10 KV electrons.
(j); glancing incidence (45°) of 7.5 KV electrons.

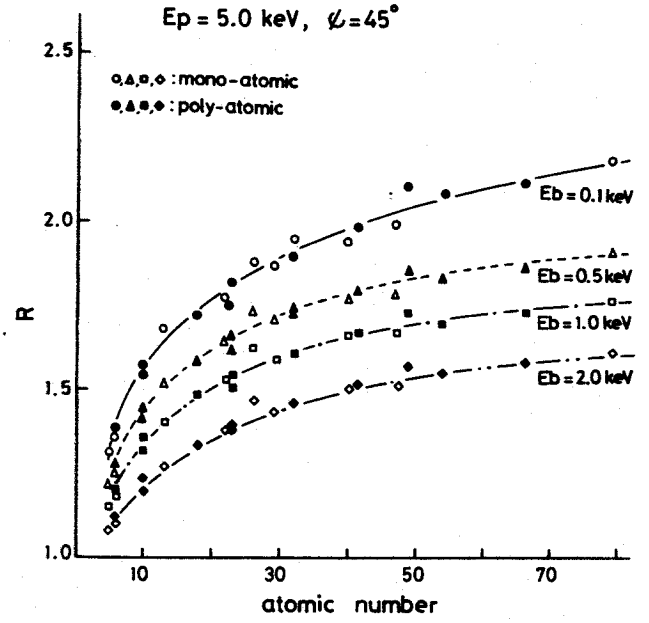

(k)

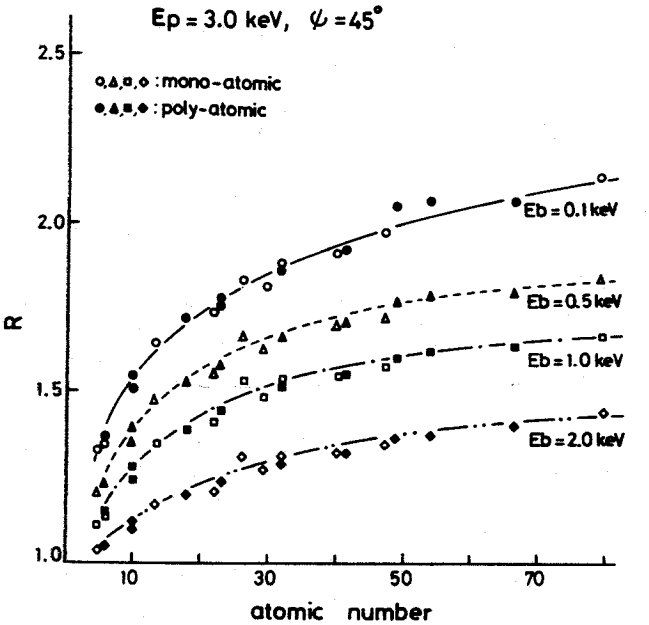

(ℓ)

Fig. 3-14 Variation of the correction factor R with atomic number of materials:
(k); glancing incidence (45°) of 5 KV electrons.
(ℓ); glancing incidence (45°) of 3 KV electrons.

mono-atomic material and solid marks represent the result for poly-atomic material. Since the probability of large angle scattering is higher for high atomic number element, a polyatomic material gives higher R values than monoatomic material with same atomic number, especially for such polyatomic materials with the combination of high- and low-atomic number elements as PbS ($\overline{Z}$ = 49) and Au-Cu alloys ($\overline{Z}$ = 41.5, $\overline{Z}$ = 54, and $\overline{Z}$ = 67.5).

Concerning the dependence of R on the atomic number of the material, Hall and Morabito (1979) used the relation given by Reuter (1972) in the estimation of relative sensitivity factors (see Section 1-3), which is written as

$$R = 1 + 2.8 \cdot (1 - 0.9\, E_b/E_p) \cdot \eta \quad . \qquad (3\text{-}53\text{-}a)$$

Here E_b is the energy to ionize the inner-shell responsible for Auger transition and E_p is the primary energy. η denotes the back-scattering coefficient and its dependence on the atomic number of the matrix was also given by Reuter as follows;

$$\eta = -0.0254 + 0.016Z - 0.000186Z^2 + 8.3 \times 10^{-7} Z^3 \quad . \qquad (3\text{-}53\text{-}b)$$

Using the above two equations, the present results were compared with Reuter's results for two different energies (5 keV and 10 keV) of primary electrons of normal incidence. The results are shown in Fig. 3-15.

The short and long dotted lines in Fig. 3-15(a) and (b) represent the relation of R vs atomic number for binding energies of E_b= 0.5 keV and E_b= 2.0 keV, respectively, while the open and solid

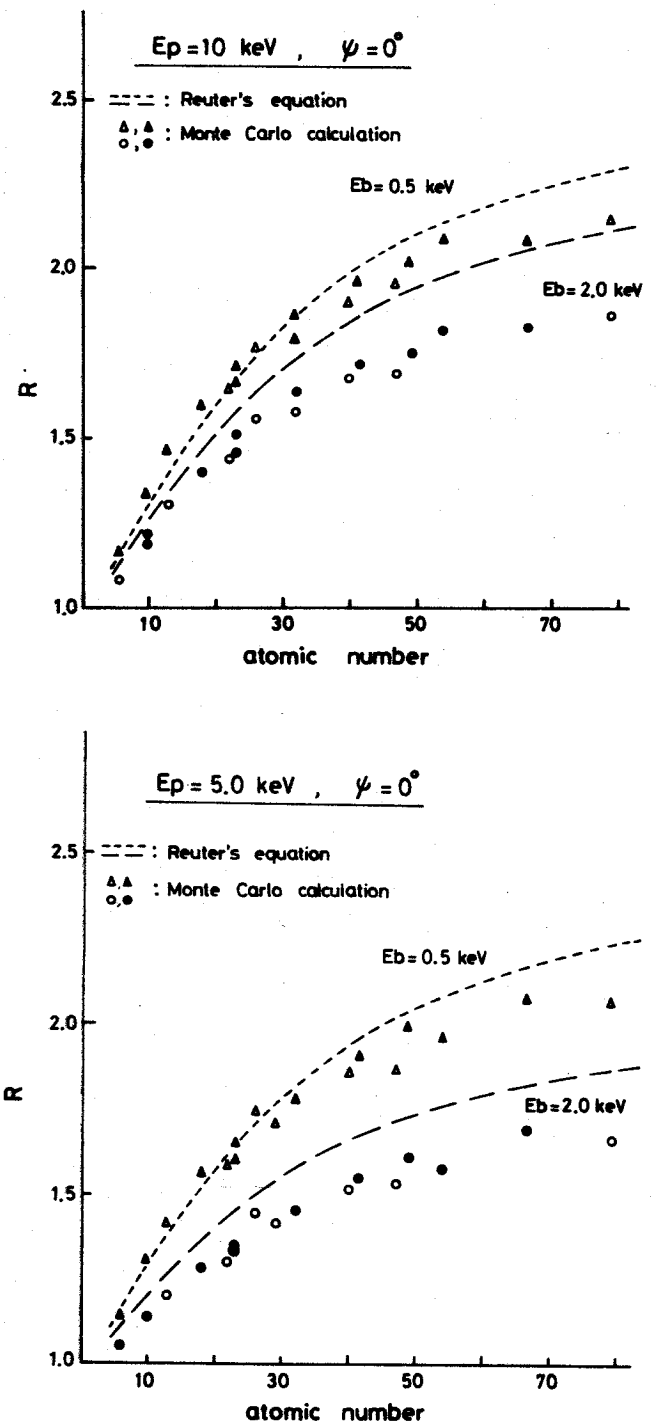

Fig. 3-15 Comparison of the present results with Reuter's equation:
(a); normal incidence of 10 KV electrons.
(b); normal incidence of 5 KV electrons.
Open and solid marks represent the results obtained by the present calculations.

marks represent the results obtained by the present calculation. It is clear from the figures that the results by Reuter give higher values than those by present calculation.

The dependence of η on Z shown in equation (3-53-b) was calculated from polynomial fit to experimental data by Heinrich (1966) at 20 keV, so the difference between both results shown in Fig. 3-15 may be attributed partly to the difference of primary energies. Another possibility of the difference between these results exists in the simple formulation of R as shown in equation (3-53-a). Since the energy distribution of backscattered electrons plays an important role in the estimation of R, other parameters than the backscattering coefficient and over-voltage ratio (i.e., E_p/E_b) have to be taken into account in the equation (3-53-a).

As to the dependence of R on the angle of incidence ψ, the value at glancing incidence gives a little higher value than that at the normal incidence for light elements as Jablonski (1979b) has pointed out, but for heavy elements the former gives a lower value than the latter as seen in Fig. 3-14. This tendency is prominent for low binding energy, therefore, the reason can be considered as follows: As the atomic number of constituent atoms of a material becomes higher, the peak position of the energy distribution of backscattered electrons shifts higher energy region (see Fig. 3-8). Moreover, backscattered electrons with high energy mainly increase as the incident angle of primary electron increases for heavy elements, which can be seen in the Fig. 3-16. This figure shows the change of backscattered electrons with the angle of incidence for Al ((a)) and Au ((b)). The increase of backscattered electrons for Au at a large incident angle ($\psi = 45^\circ$), therefore, does not contribute so much as

that for Al in the case of small binding energy. This, then, leads to the decrease of R for heavy element at large incident angles since the denominator of the equation (3-52-b) becomes large at the large incident angle.

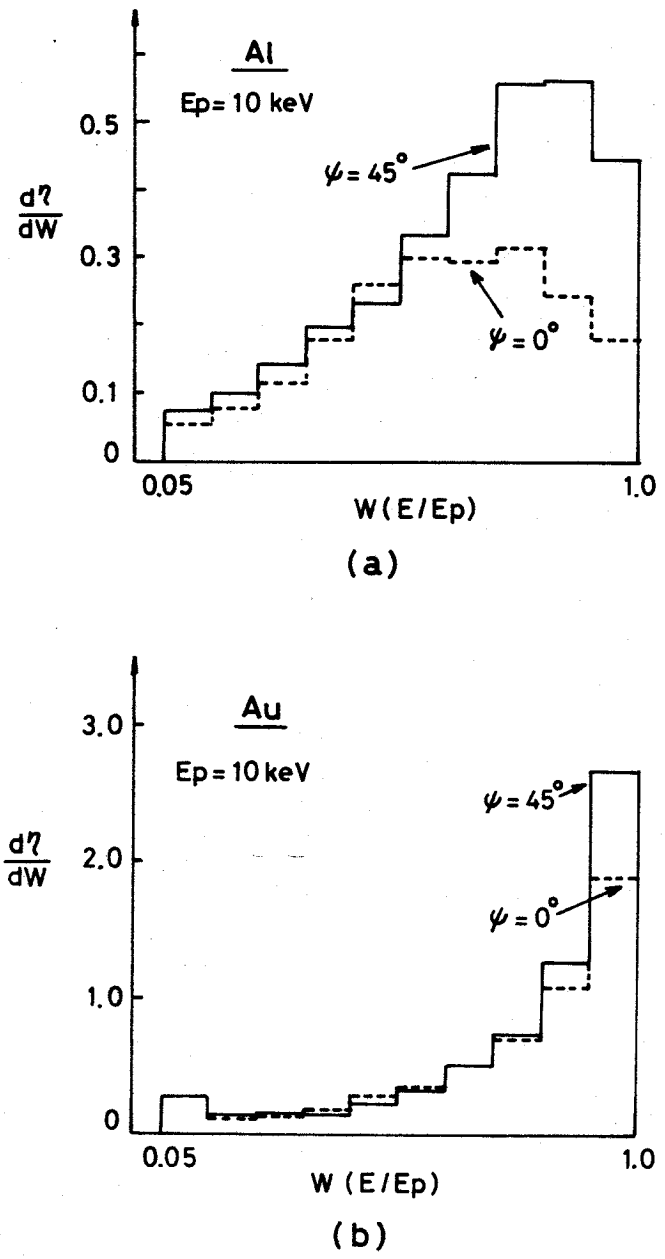

Fig. 3-16 Change of energy distributions of backscattered electrons with angle of incidence:
(a); 10 KV electrons on Al.
(b); 10 KV electrons on Au.

The backscattering factor obtained by the present calculation can be used for the quantitative analysis by AES in the following way.

A) Combination with the relative sensitivity factor

As described in Chapter 1, the sensitivity factor is most commonly used for quantitative analysis by AES, and it is experimentally obtained for pure material and some compounds with known surface compositions (Chang 1975, Davis et al. 1976). Accordingly, the revised sensitivity factor for i element which either exists in a material in a small amount or adsorbs on a material can be obtained by the equation.

$$\alpha_i^m = \alpha_i^o \cdot \frac{\lambda_i^m}{\lambda_i^o} \cdot \frac{(1+r)_i^m}{(1+r)_i^o} \quad . \tag{3-54}$$

Here α_i^o denotes the sensitivity factor for i element at its standard material (i.e., the factor experimentally obtained), while λ_i^o denotes the mean free path of the Auger electrons of i element at that condition. Both the λ_i^o and the mean free path λ_i^m at the material being analyzed are able to be estimated by the equations given by Seah and Dench (1979). Therefore, the revised sensitivity factor α_i^m which takes into account the 'matrix-effect' is calculated using the values $(1+r)_i^m$ and $(1+r)_i^o$ obtained by the present calculation. (The former denotes the backscattering factor in AES for i element in the material and the latter denotes that in standard material). The concentration of i element, then is obtained by a similar equation with (1-25).

$$C_i = \frac{\alpha_i^m I_i}{\sum_j \alpha_j^m I_j} \quad , \tag{3-55}$$

where I_i (and I_j) denotes the measured Auger signal intensity.

B) Determination of the absolute amount of each element.

The Auger signal intensity of a pure element (or standard material of an element) I_i^o can be expressed as,

$$I_i^o = K\, C_i^o\, N_i^o\, \lambda_i^o\, (1+r)_i^o \quad , \tag{3-56}$$

denoting the atom density of the material by N_i^o and its concentration by C_i^o (K is an constant depending on the experimental condition), hence the value

$$S_i^o = \frac{I_i^o}{C_i^o\, N_i^o\, (1+r)_i^o\, \lambda_i^o} \tag{3-57}$$

indicates the Auger signal intensity corresponding to one atom of the element without any contribution of backscattered electrons. The absolute amount of the element in some material, therefore, can be estimated by the equation

$$R_i = \frac{S_i^c}{S_i^o} \quad , \tag{3-58}$$

in which the $S_i^c (=I_i^c/(1+r)_i^c)$ indicates the Auger signal intensity

corresponding to the total number of i element within the detection volume (i.e., escape depth) with no contribution of backscattered electrons. The experimentally dependent constant K can be neglected if I_i^o and I_i^c are obtained under the same experimental conditions. It is, of course, assumed that the energy distribution of backscattered electrons is obtained for the material by the Monte Carlo calculations. The concentration of i element, then, can be estimated by

$$C_i = \frac{R_i}{\sum_j R_j} \qquad \text{(for all elements)} \qquad (3\text{-}59)$$

For the quantitative approach by those two methods, the present results as shown in Fig. 3-13 and Fig. 3-14 would be hoped to contribute substantially.

3-6 Application to SAEM

- Spatial distributions of Auger signal generation -

The present Monte Carlo calculation is very powerful also in the SAEM, because it easily gives the spatial distributions of Auger siganl generation. The profile and the intensity of the Auger signal excited by backscattered electrons have received much attention since they give information about the resolution limit by SAEM. Thus the spatial resolution of KLL- and LVV-Auger signals of Al was calculated. Auger signal intensities were estimated assuming that they are directly related to the ionization probability of the inner shell, K- and L-shell, respectively.

Figure 3-17 shows in-depth distributions of energy dissipation, K- and L-ionizations, in which the contribution of the secondary electrons is shown by the hatched area. These figures seem to be very useful especially in the field of electronprobe microanalysis. The Auger signal distributions, on the other hand, can be calculated using the energy distributions of backscattered eelctrons as mentioned in the above section, and the result is shown in Fig. 3-18.

It is worth noting that almost half of the LVV-Auger electrons and about 30% of the KLL-Auger electrons are produced by the secondary and backscattered electrons. Another point to be noted is that the contribution of secondary electrons to L ionization is remarkable at the vicinity of the incident primary beam impact as is seen in Fig. 3-18 (b). This is quite understandable because the secondary electrons are generated almost normal to the direction of primary electrons of high energies, and

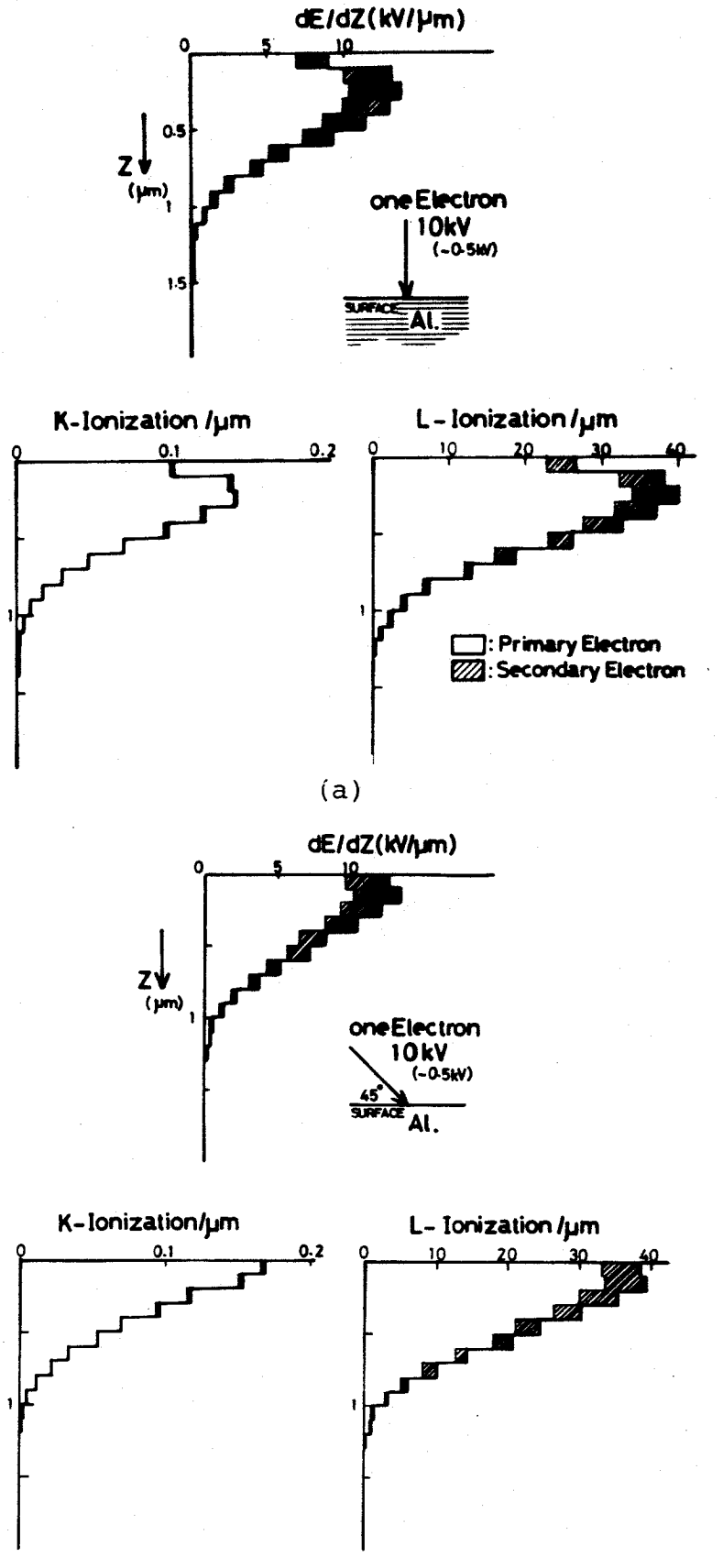

Fig. 3-17 In depth distributions of energy dissipation, K and L ionization in aluminum at (a) normal incidence and (b) glancing (45°) incidence. (Open area: signals generated by primary electrons including backscattered electrons. Hatched area: signals generated by secondary electrons.)

hence, they move parallel with the surface at the vicinity of the incident point leading to a high generation rate of L ionization in the surface layer in question.

Although the spatial distribution of KLL-Auger electrons (Fig. 3-18) extends over a few thousand Å on the surface, the intensity distribution of Auger signals produced by primary electrons is sharp at the point of electron-beam impact and is 100 times more intense than the peak of Fig. 3-18. Hence, the resolution of the scanning Auger electron microscope is mainly determined by the spot size of the primary electron beam. Though above dis-

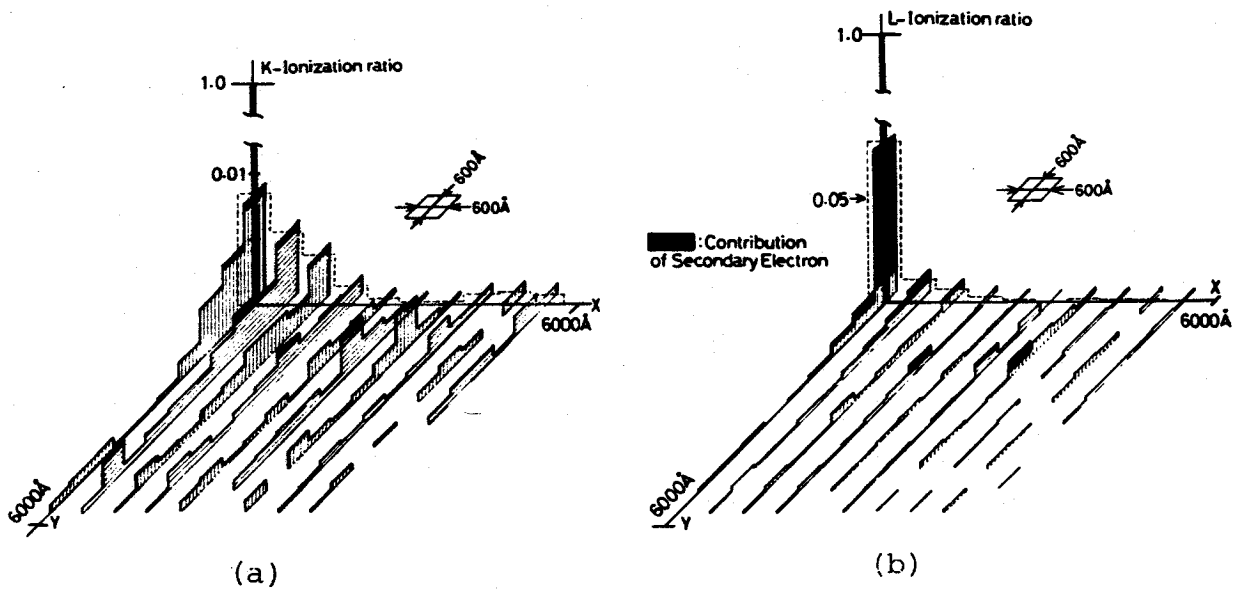

Fig. 3-18 Spatial distributions of K- and L-ionizations generated by 10 keV electrons in surface layer of aluminum. The longitudinal axes indicate K- and L- ionization rate [(ionization by secondary and backscattered electrons)/ (ionization by one primary electron)] in sectional (600 Å) area. (Solid area: signals generated by secondary electrons).

cussion is limited to KLL-and LVV-Auger electrons of Al, it can be applied for other elements since the spatial distributions of backscattered electrons becomes confined near the incident postition of primary electrons as the atomic number of the sample becomes larger. And that the binding energy for inner shell excitation of other elements is higher in general than that for Al L-shell, which also leads to the narrow distribution of Auger electrons excited by backscattered electrons, hence it leads to the conclusion described above.

From this result a rough estimation about the limit of spatial resolution obtainable with SAEM can be made. That is, the resolution limit can be directly deduced from the size of the primary beam which gives a reasonable signal to noise ratio in an Auger image. A schema of output signals of an analyzer in the SAEM is shown in Fig. 3-19. This figure shows the case that the analyzed element exists in a sample point X_n (measuring time

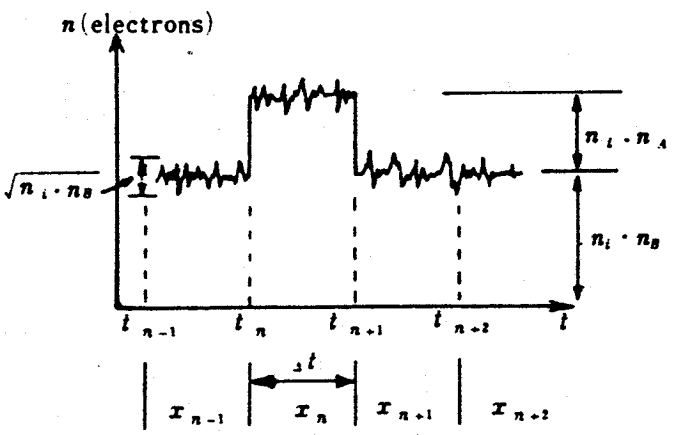

Fig. 3-19 A schema for detected signals in SAEM.

per point is Δt). Here, n_i denotes the number of incident electrons during the time period while n_A and n_B denote the yield of the Auger electron and backscattered electrons at a given energy, respectively. The value n_A and n_B can be evaluated for Al from the results of Monte Carlo calculations described above and they are $\sim 7.7 \times 10^{-6}$ for n_A and $\sim 1.2 \times 10^{-5}$ for n_B (KLL Auger electrons are considered here), respectively, taking into account the detection efficiency for them.

On the condition that the signal to noise ratio is simply decided by the ratio of the Auger signal intensity ($n_i \cdot n_A$) and the background fluctuations ($\sqrt{n_i \cdot n_B}$), the resolution limit can be calculated with further assumptions as follows:

1. To obtain an Auger image of reasonably good contrast the condition $n_i n_A / \sqrt{n_i \cdot n_B} \geq 10$ is necessary.
2. It takes 400 sec. to take one Auger map (which is an ordinary used condition in a SAEM) and sampling points (picture elements) are 256 x 256.

Using these values the least value of primary beam current, $I_p \geq 5.0 \times 10^{-9}$ (A), is obtained. This current gives the probe diameter of ~ 100 Å for field emission source, which indicated that a little higher spatial resoltuion than that obtained up to this time would be expectable, although this discussion neglects other problems which cause reduction of signal to noise ratio.

3-7 Conclusions

The application of the Monte Carlo calculation procedure to quantitative analysis by AES is described in this chapter, and the results are concluded as follows:

(1) The numerical calculation procedure by partial wave expansion method was applied to the calculation of elastic scattering cross-section for electron-atom scattering in the energy region between 0.5 keV to 10 keV, which should be taken into account in AES. The results were compared with the cross-sections by Rutherford-type scattering formula which is often used in conventional Monte Carlo calculations of electron penetration in solids and confirmed the necessity of the former treatment especially in low energy electron scattering with heavy atoms.

(2) The Monte Carlo simulation procedure for the quantitative analysis by AES was newly developed using the elastic cross-section obtained by the partial wave method and the treatment for inelastic scattering proposed by Krefting and Reimer with some modification for it.

(3) The energy distribution of backscattered electrons which was weighted by the ejection angle of those electrons was obtained and used for the estimation of the contributions of them to Auger signal generation, i.e., the backscattering factor in AES.

(4) The quantitative analystical procedure by AES using the back-scattering factor obtained by the calculation was proposed for two cases.

and finally,

(5) The present Monte Carlo calculation was applied to the Scan-

ning Auger electron microscopy, and the spatial resolution limit for AES analysis was estimated. It was shown that the spatial resolution was mainly determined by the probe size of primary electrons which gives enough signal to noise ratio, and the limit of spatial resolution expectable in a scanning Auger electron iamge was also evaluated.

Chap. 4 Estimation of contributions of backscattered electrons in AES -- Comparison of calculated results with experiment --

4-1 Introduction

This chapter describes the comparison of experimental results with calculated ones which are obtained by the Monte Carlo simulation described in the previous chapter.

The validity of the simulation model in quantitative analysis by AES can be examined if it describes accurately the increase of Auger signal intensity due to the contribution of backscattered electrons. The contribution, however, cannot be simply estimated in experiment as discussed in Chap. 1. As for the dependence of Auger signal intensity on primary electron energy we can easily measure it, and it can be expected that the dependency reflects contributions of backscattered electrons leading to a different tendency from that expected by the consideration of only primary electrons (i.e., the dependency of ionization probabilities on primary energy). So, the dependence of Auger signal intensity on primary electron energy was measured for a number of pure elements and a binary alloy, which is described in detail in Section 4-2. This experimental investigation has another merit in that variation of the signal intensity can be directly estimated from the measured Auger peak heights since other terms affecting the signal intensity such as mean free path, Auger transition probability, Auger peak shape and so on, do not need to be taken into account.

In section 4-3, the quantitative interpretation of AES analysis of $Al_xGa_{1-x}As$ by Arthur and LePore (1977) is described. They have pointed out that the intensity ratios of Al/As and Ga/As show a linear change with x in spite of the fact that the mean atomic number and so the backscattering factor considerably changes with x. Therefore, the Auger signal intensity was calculated by Monte Carlo simulation, and the calculation has explained well the linear functioning of intensity ratios of Arthur and LePore.

4-2 Dependence of Auger signal generation on primary electron energy

4-2-1 Experimental

In order to examine the usefulness of the Monte Carlo calculation approach to the quantitative AES analysis mentioned in the previous chapter, the experimental study on the dependence of Auger signals on primary electron energy was performed. (Ichimura et al. 1980a)

The schematic diagram of the SAEM, JEOL JAMP-3, used in the present study is shown in Fig. 4-1(a). The apparatus is evacuated by rotary pump and oil diffusion pump roughly, and then by ion pump and Ti-sublimation pump to high vacuum. The base pressure after baking is in the order of 10^{-10} Torr.

The electron beam can be focused on a sample surface by two stage-condenser lenses and an objective lens up to about a few hundred Å in diameter, and it impinges on the sample at an incident angle of 45°. The energy of primary electrons can be changed from 1 keV to 30 keV continuously. Auger electrons ejected from the sample are measured by CMA either in the dN/dE mode spectra (energy modulation) or in the N(E) mode spectra (beam brightness modulation) using beam blanking coil which is discussed in detail in a later chapter. Modulation frequency is chosen to ∿3 kHz considering the frequency characteristics of the pre-amplifier. The outer-view of the JAMP-3 is also shown in Fig. 4-1(b).

In the present experiment, the measurement of Auger signal intensity was performed, first, for a number of pure elements of practical interest such as aluminum, copper, silver, and gold.

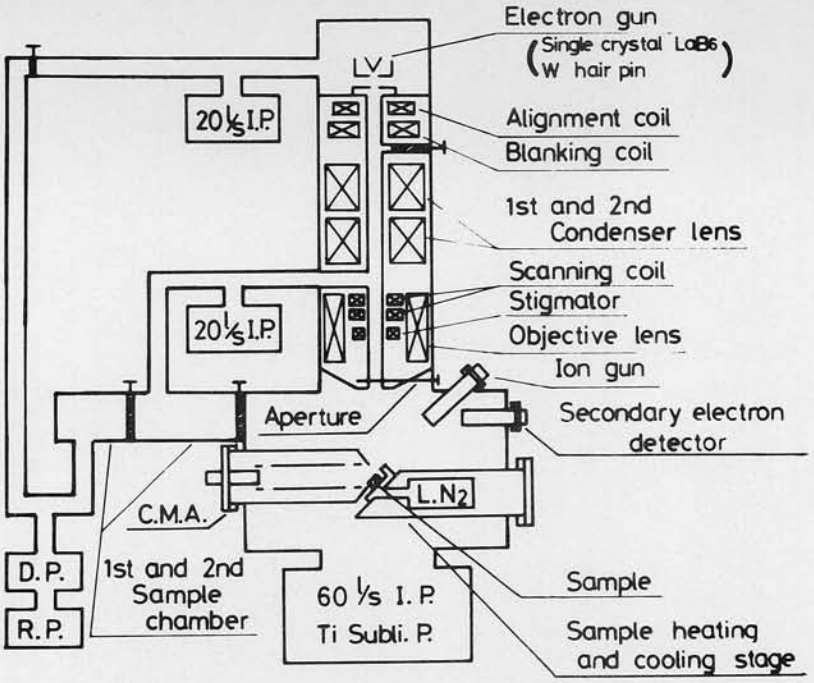

(a)

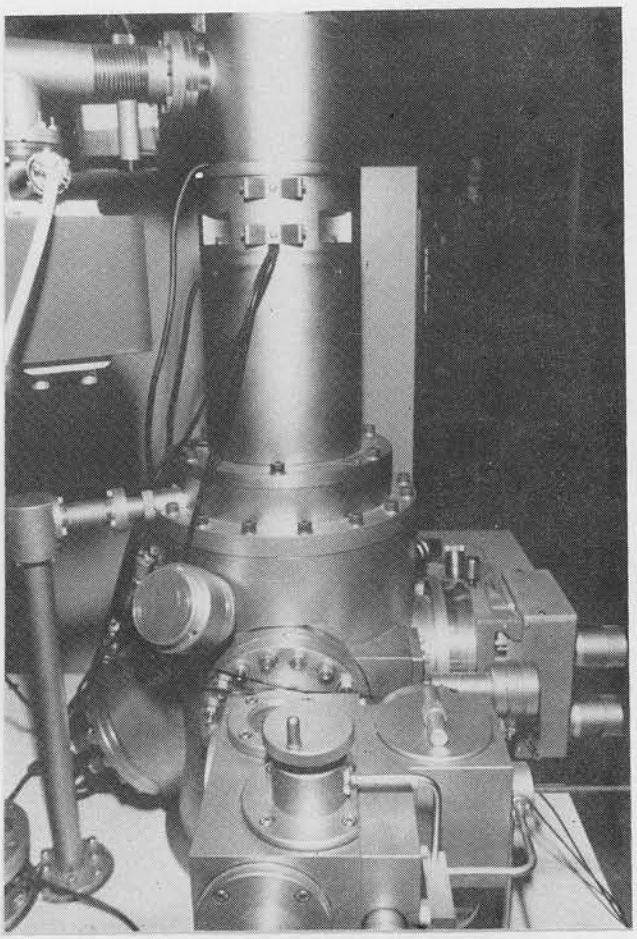

(b)

Fig. 4-1 A schematic diagram of the SAEM (JAMP-3) ((a)) and an outer view of it ((b)).

The intensity of Auger signals was obtained by measuring peak to peak heights in the dN(E)/dE mode spectra with modulation voltages of 5 eV_{p-p} for low-energy signals and 10 eV_{p-p} for high-energy signals. The primary beam current was about 0.2 ∿ 0.5 μA for all measurements and the angle of incidence was 45°. The measurement was repeated by changing the primary energy from low (about 3 keV) to high (about 15 keV) and then decreasing it from high to low and vice versa. The primary electron energy was measured by using a calibration curve between the reference and output voltages, which was checked before and after the measurement. Another check of the primary electron energy was also carried out by measuring the elastic peak at low primary energies with the CMA.

Polycrystalline samples of Al, Cu, Ag, and Au were mechanically and electrolytically etched to a mirror surface finish and then sputter cleaned by Ar ions in the apparatus. Though the ambient pressure during the experiment was less than 5.0×10^{-9} Torr, these samples, particularly aluminum, were so sensitive as to be easily oxidized, resulting in large experimental errors. Hence the sputter-cleaning procedure was repeated before each measurement. Moreover, to avoid electron-beam damage (electron-beam-enhanced absorption) the incident beam was scanned in the region of about 100 μm square during the measurement. This also has the merit of averaging the influence of surface topography. One example of the measured topography is shown in Fig. 4-2.

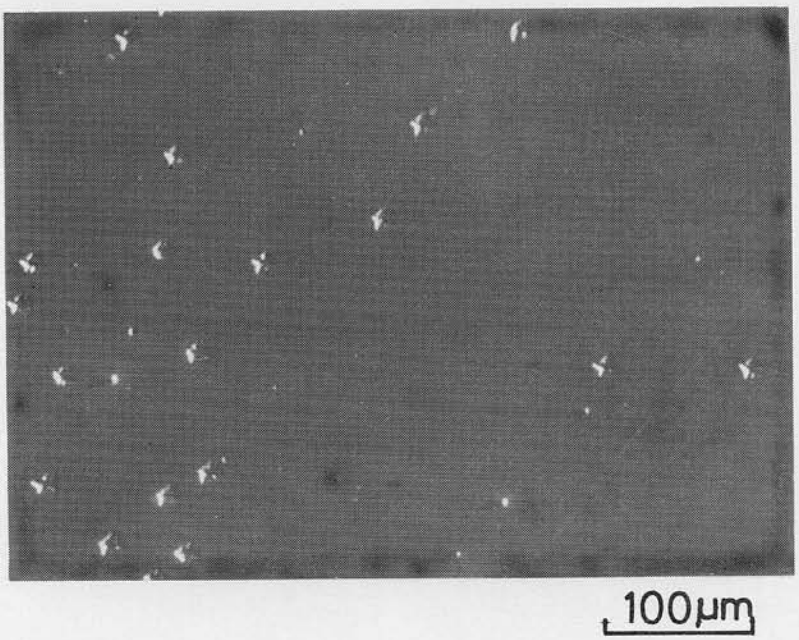

Fig. 4-2 Measured topograph of a sample (Al) after electrolytic polishing. (etch pits are observed)

4-2-2 Results and discussions

Both the experimental and theoretical results are plotted for aluminum, copper, silver, and gold in Fig. 4-3(a), (b), (c), and (d), respectively. Measured Auger signals were KLL transition (∿1400 eV) and LVV transition (∿70 eV) for Al, LMM transition (∿920 eV) and MVV transition (∿60 eV) for Cu, MVV transition (∿350 eV) for Ag, and MNN transition (∿2030 eV) and NVV transition (∿70 eV) for Au. In Figs. 4-3(a)-(d), the excitation probability of the shell responsible for the Auger transition is plotted as a theoretical value and compared with the experimental value. The probability was calculated assuming that all electrons in each shell, i.e., K, L, M, etc., have the same ionization energy, and the result is shown in Figs. 4-3(a)-(d). The results in Figs. 4-3(a)-(d) are normalized at 7.5, 6, 7.5 and 10 keV for Al, Cu, Ag, and Au, respectively, for convenience of comparison.

The solid line represents the total intensity of Auger signals while the broken line represents the intensity of Auger signals generated by only the primary electrons. So the difference between the two lines in Fig. 4-3 shows the contribution of backscattered electrons and secodnary electron with high energy. All the results in Figs. 4-3(a)-(d) were obtained by using Krefting and Reimer's treatment for inelastic scattering, which was described in the previous chapter.

Using the other two treatments mentioned in the previous chapter, we have also performed similar calculations for Al to confirm that no marked difference can be found among these results. This suggests, as a practical approach, the present Monte Carlo calculation approach based on Krefting and Reimer's treatment can be extended to other materials, for which precise knowledge on individual inelastic scattering has not been provided.

As seen in Figs. 4-3(a)-(d), the present calculation describes the experimental result with considerable accuracy for Al, Cu, and Ag, while slight discrepancies can be seen to occur in the case of Au. The origin of this difference, however, may be assumed to not arise from inaccuracy in the basic simulation of electron scattering in materials of high atomic number but from estimation of the ionization at the surface. That is, the ionization probability was calculated using the equation (3-52-b) in which Gryzinski's ionization formula with mean sub-shell ionization energies instead of individual sub-shell ionization energies is used for $\sigma(E)$. The relative error of this, i.e., the difference between the lowest and highest ionization energies of

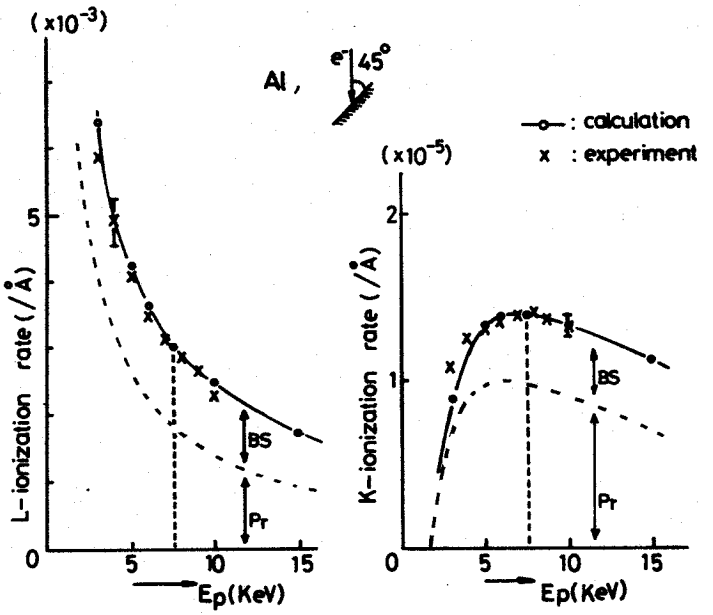

(a)

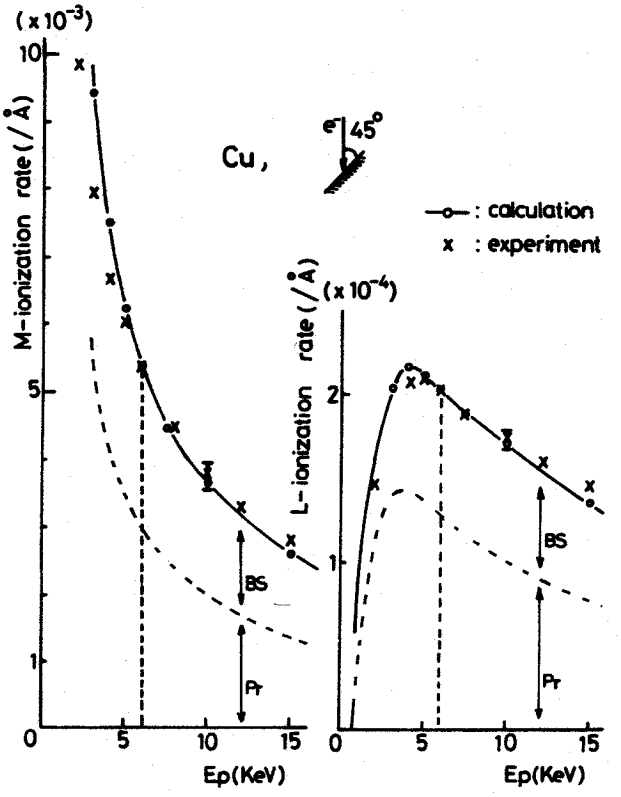

(b)

Fig. 4-3 The dependence of Auger signal intensities on primary electron energy for (a) Al KLL and LVV, and (b) Cu LMM and MVV at angle of incidence 45°.
X : experimental result, o : calculated result.
——:total intensity of Auger electrons (calculated),
----:intensity of Auger electrons generated by only primary electrons (calculated).

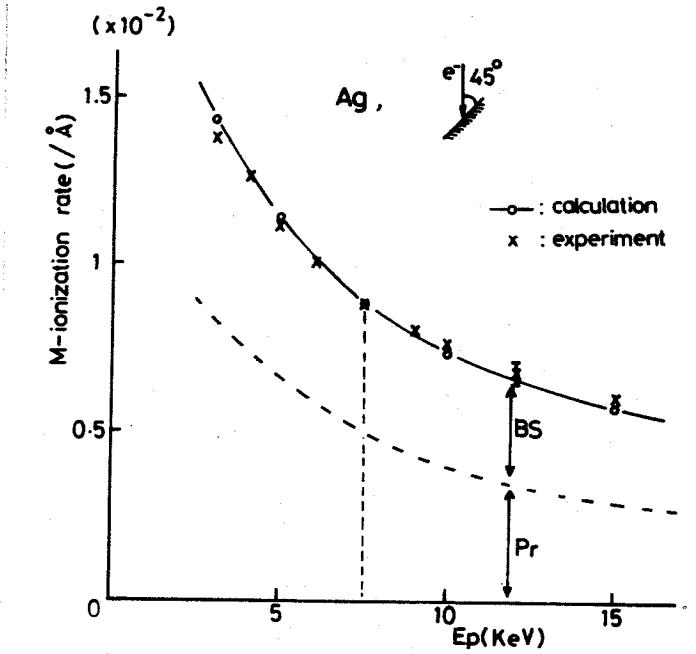

(c)

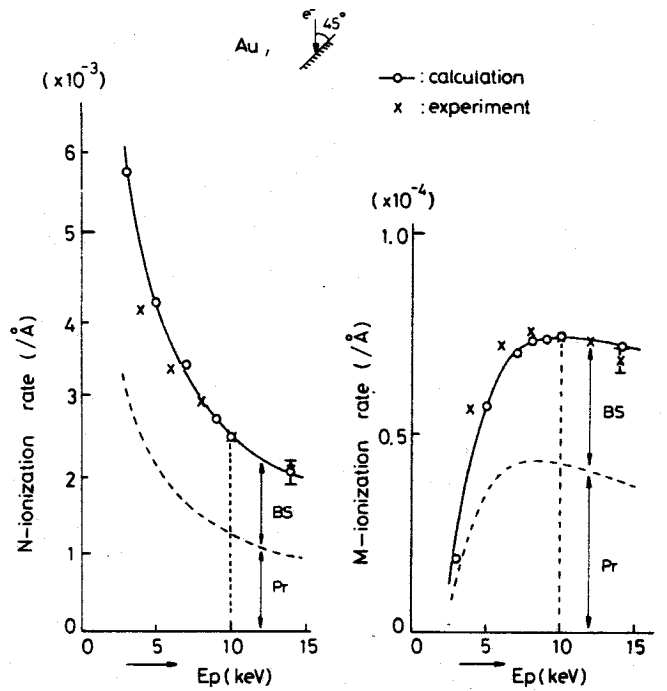

(d)

Fig. 4-3 The dependence of Auger signal intensities on primary electron energy for (c) Ag MVV, and (d) Au MNN and NVV at angle of incidence 45°.

X : experimental result, o: calculated result.

——:total intensity of Auger electrons (calculated)

----:intensity of Auger electrons generated by only primary electrons (calculated).

sub-shells divided by the mean ionization energy, becomes large for outer shell electrons and hence for Auger signals from high Z elements such as Au. The variation of signal intensity, then, was calculated for three different binding energies (E_B), i.e., 2550 eV (mean value of M-shell binding energy), 2200 eV (its minimum binding energy), and 1900 eV for comparison. The result, which is shown in Fig. 4-4, shows the best coincidence in the case of the latter. Therefore another possibility for this discrepancy must be considered since the energy of measured Auger signals is ∿2030 eV.

Another possible factor resulting in the discrepancy for Au is due to the inappropriateness of extending the Gryzinski cross

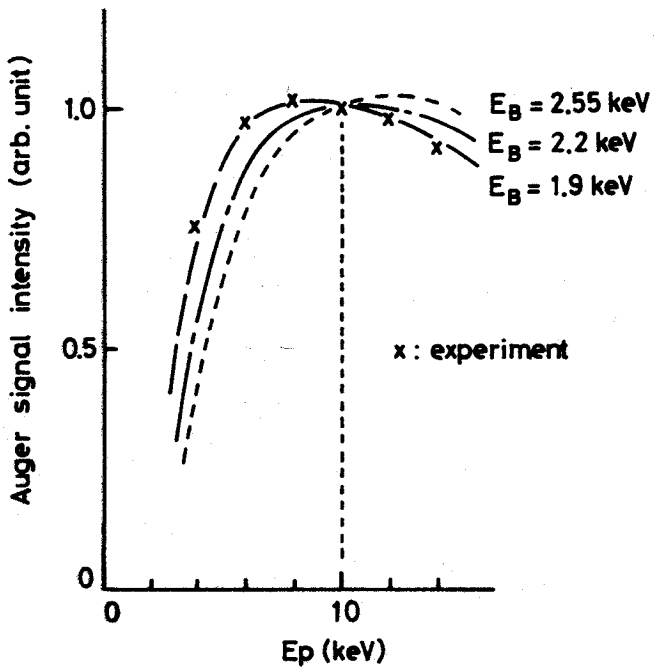

Fig. 4-4 The variation of Auger siganl intensity as a function of primary energy for different binding energies of E_B = 2.55 keV (-----), E_B = 2.2 keV (—•—•—), and E_B = 1.9 keV(— — —). All the results (including experimental ones) are normalized at 10 keV.

section formula to outer-shell electrons such as M and N shells. The Gryzinski cross-section has been widely used and it has described a number of experimental results, particularly for light elements, with considerable success (Leapman and Cosslett 1976, Powell 1976). Its applicability for outer-shell electrons in heavy elements, however, is still open to criticism and further verification (Vriens 1969).

To study this question in more detail, we measured Cu-Auger signal intensities in Au-Cu alloy. The results are shown in Fig. 4-5(a), where the calculated results are compared with the experimental ones for a sample of $Au_{0.8}Cu_{0.2}$, corresponding to 43 at.% of Cu. In the calculation, the energy distribution of backscattered electrons in Au-Cu alloy was first obtained by the Monte Carlo calculation, and then the Auger signal generation by backscattered electrons was estimated by the equation

$$I_A^B = \int_{E_B}^{E_p} \sigma_i(E) \left(\frac{d\eta}{dE}\right)_w dE \quad , \qquad (4\text{-}1)$$

where

$$\left(\frac{d\eta}{dE}\right)_w = \int_{\Omega} \sec\theta \cdot \frac{d^2\eta}{dE d\omega} \cdot d\omega \qquad (4\text{-}2)$$

was defined in Section 3-5.

In Fig. 4-5(a), both the results are normalized at 5 keV. Agreement between both results is satisfactory and this suggests that the present model describes the scattering process of penetrating electrons in the sample with considerable accuracy.

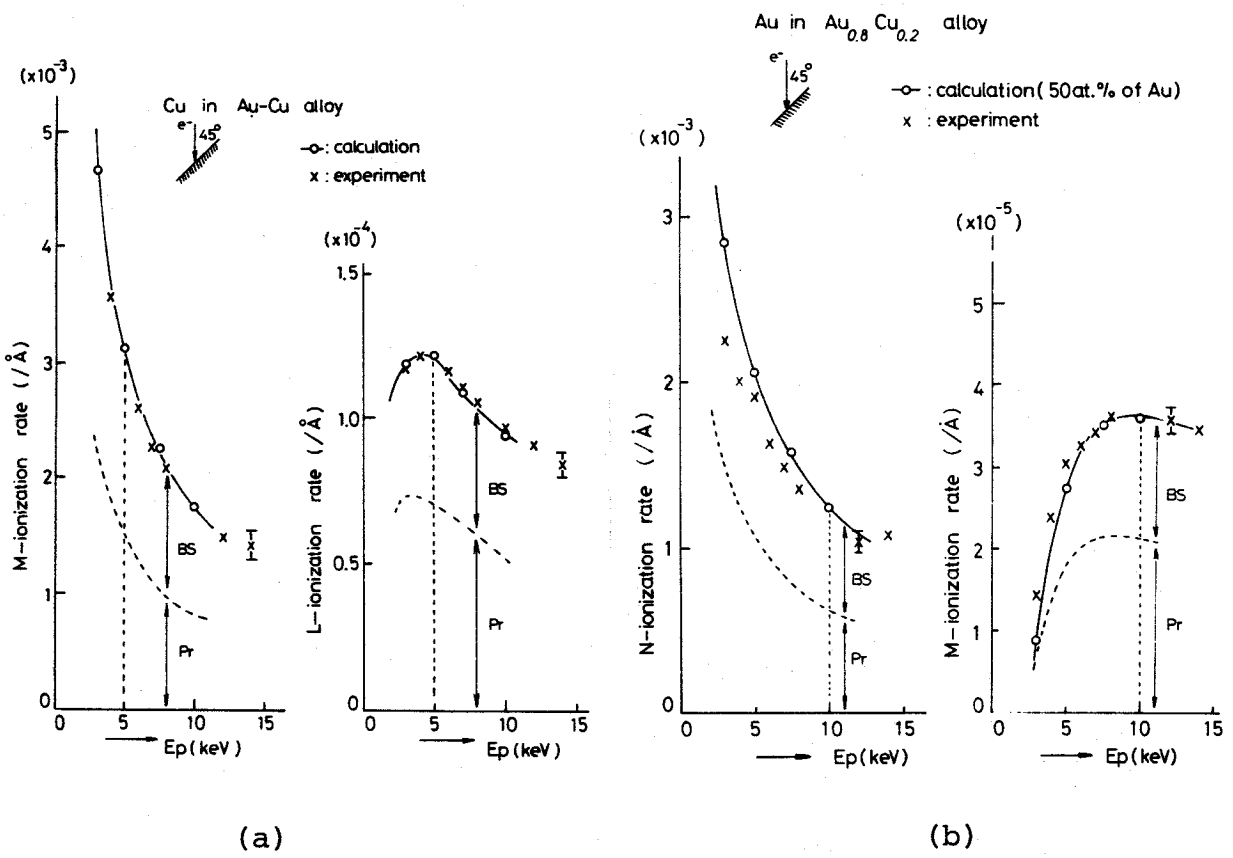

Fig. 4-5 The dependence of Auger signal intensity on primary electron energy in Au-Cu alloy.
(a)Cu LMM and MVV and (b)Au MNN and NVV Auger electron intensity at angle of incidence 45°. x: experimental result for $Au_{0.8}Cu_{0.2}$ alloy (nearly 57 at.% of Au). o: calculated result for 50 at.% of Au and Cu sample. ——: total intensity (calculated). ---: signals generated by only primary electrons (calculated).

The Auger signal for Au in the Au-Cu alloy shown in Fig. 4-5(b), on the other hand, has shown the same discrepancy as that in Fig. 4-3(d).

These two results seem to indicate that the $\int \sec\theta \times (d^2\eta/dE\, d\omega)d\omega$ distribution calculated by the present model is appropriate for Au-Cu alloy samples while $\sigma_i(E)$ is appropriate only for σ_L and σ_M of Cu so long as we use the formula given by Gryzinski. Since the Gryzinski excitation function was used to describe the scattering in Au-Cu alloy materials, inappropriateness in the use of Gryzinski's formula may, of course, affect the distribution of backscattered electrons for Au. This effect, however, seems to be very slight judging from the result of Cu-Auger signals probably because of the rather low possibility of exciting inner-shell electrons of Au-atoms.

Thus, the present model allows us to evaluate the contribution of backscattered electrons to the Auger signal generation with considerable accuracy provided that the ionization cross section for shell electrons in question is precise enough.

Concerning Auger electron excitation by a primary electron, the ionization cross-section suggests that the intensity of Auger electrons has as the maximum at the primary energy nearly three times as much as relevant shell-ionization energy. These can be seen in the broken lines for Al K ionization, Cu L ionization, and Au M ionization.

The contribution of backscattered electrons (the secondary electron with high energy hardly contribute to such high energy excitation) results in a shift of this maximum towards higher primary energy, i.e., nearly five times of the shell-ionization

energy obviously seen in the result of Al K and Cu L ionizations.

This has already been pointed out empirically by Palmberg for conventional AES in which the primary electron is usually lower than 5 keV (Palmberg 1972). Concerning Al-KLL Auger electrons MacDonald also proposed operating a scanning Auger electron microscope at a primary energy of five times the K-ionization energy, i.e., around 7.5 keV, for AES analysis of Al and Si in integrated circuit devices (MacDonald 1976).

The present Monte Carlo calculation has also provided the number of backscattered electrons having the same kinetic energy as that of Auger electrons for a given energy window of CMA, which forms the background in the Auger electron spectra. This allows us a more detailed argument on the signal-to-noise ratio in the AES study. For the Al-KLL Auger electrons, for instance, the calculation suggests that the signal-to-noise ratio increases slowly as the primary energy increases for an angle of incidence of 45°. This has often been pointed out empirically for AES analysis with JAMP-3 (Mogami 1978a).

Since the dependence of both the Auger signal intensity and signal-to-noise ratio on primary electron energy, in principle, determines optimum operating condition, the present calculation provides us with practical knowledge on that condition.

4-3 Quantitative interpretation of AES analysis of $Al_xGa_{1-x}As$ by Arthur and LePore

Further verification of the model can be achieved by comparing the calculation with the quantitative analysis of such materials of practical interest as semi-conductor compounds. Arthur and LePore have reported a systematic study of quantitative analysis of $Al_xGa_{1-x}As$ using AES (Arthur and LePore 1977). They have pointed out that the ratios of Auger intensities of Ga to As and Al to As, respectively, are linear functions of Al-concentration whcih is estimated by the direct measurement of band gap in $Al_xGa_{1-x}As$. Their results are shown in Figure 4-6, in which the mean atomic number changes from 23 to 32 as the concentration (x) changes from 1 to 0, and this leads to ~20% change in backscattering coefficeint.

In the present study, therefore, the Motne Carlo simulation approach is applied to see whether or not the present approach describes such a straight-line relationship in spite of the rather great variation of backscattering coefficient as mentioned above, leading to more comprehensive understanding of backscattering matrix effect. (Ichimura et al. 1981)

Figure 4-7 shows the change of intensity ratios of those Auger signals, Al(1396 eV)/As(1228 eV) and Ga(1070 eV)/As(1228 eV) for different concentrations of Al. The results were obtained from Monte Carlo calculations for five different values of x (x=0, 0.3, 0.5, 0.7 and 1.0) for 3 keV electrons at angle of incidence 30°, which are the same as the experimental condition of Arthur and LePore. The intensities of Auger signals were estimated from ionization probabilities of inner shells for genera-

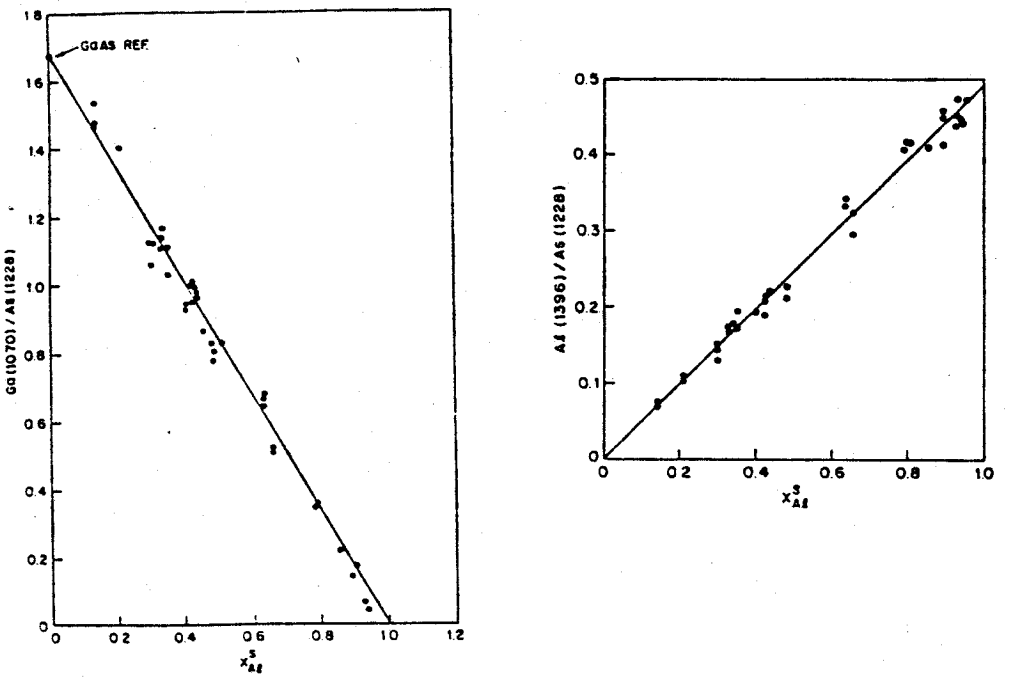

Fig. 4-6 Relationship between Al-concentration and Auger peak-height ratios, Ga(1070 eV)/As(1228 eV)(a) and Al(1396 eV)/As(1228 eV)(b). Primary electron energy E_p = 3 keV, and the angle of incidence ψ = 30° (measured from the surface normal). (Arthur and LePore 1977)

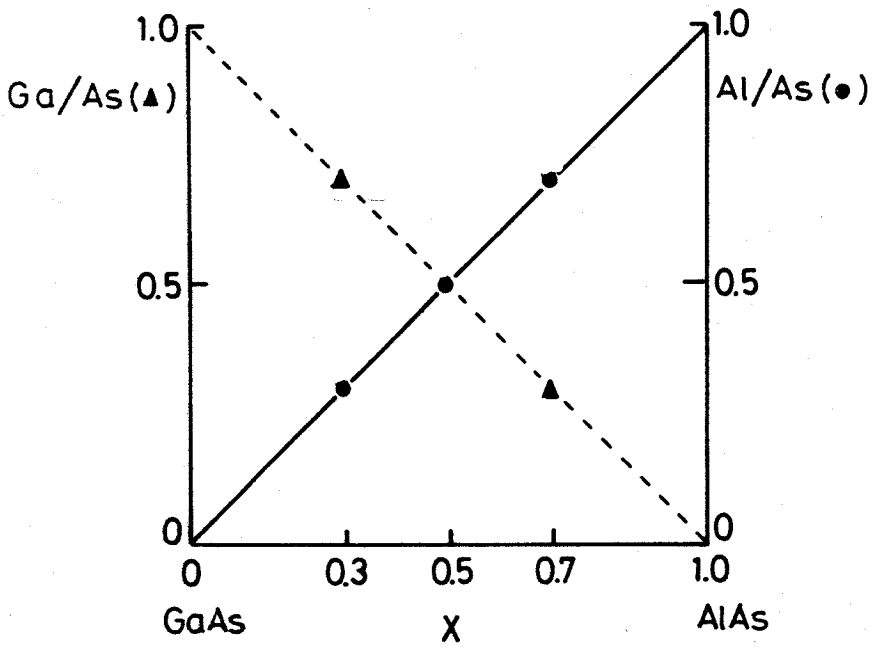

Fig. 4-7 Changes of intensity ratios of Auger signals with Al concentration. Solid marks denote the ratios of Ga- and Al-Auger signals to As-Auger signal at each composition.

tion of the Auger signals in question. Both the energies at the surface region and the ejection angles of backscattered electrons were taken into account in the assessment of their contribution to Auger signal generation as described in detail in the previous chapter.

To understand this linear functioning of Ga- and Al-concentration, we plotted the energy distributions of backscattered electrons from $Al_xGa_{1-x}As$ for three different compositions in Fig. 4-8.

Note that changing composition of the sample from AlAs to the GaAs hardly affects the profile of energy distributions

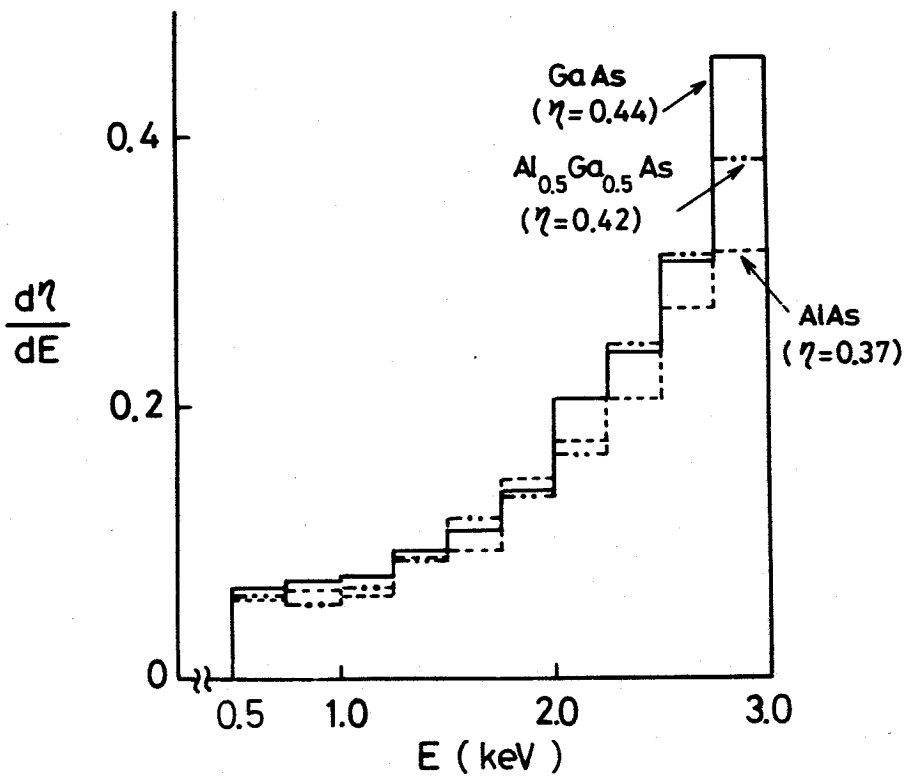

Fig. 4-8 Energy distributions of backscattered electrons for $Al_xGa_{1-x}As$ with x = 0, 0.5, and 1.0. Incident energy of primary electrons is 3 keV and an angle of incidence 30°. η denotes a backscattering coefficient at that condition.

which leads to the apparent cancellation of matrix effect when the Auger signal intensity ratio is considered, whereas the backscattering coefficeint, η, gradually decreases for higher values of x.

The backscattering matrix effect has been treated as a function of mean atomic numebr for keV electrons with considerable success (Poole and Thomas 1962) and the experimental results (Darlington 1971) for those electrons suggest, e.g., an increase more than 10 % in mean fractional energy of backscattered electrons, $\int_0^E p_E \frac{d\eta}{dE} dE / \int_0^E p \frac{d\eta}{dE} dE$, for the increase of mean atomic number from 23 (AlAs) to 32 (GaAs). Thus, the backscattering matrix effect for electrons of energy region below a few keV is quite different from that for keV electrons.

This is mainly due to the fact that, according to the calculations of elastic scattering by partial wave expansion method the probability of large angle scattering becomes much larger for atoms of higher atomic number as the energy of incident electrons decreases as shown in Fig. 4-9. Figure 4-9(a) shows the comparison of total elastic scattering cross sections between atomic number Z = 13(Al) and Z = 32(nearly corresponds to Ga and As) in the energy region below 10 keV, while (b) shows the comparison of differential scattering cross section between them at 3 keV, and both of them clearly indicate the higher probability of large angle scattering in Ga- and As-atoms than Al-atom. This makes the contribution of an element of higher atomic number to the electron backscattering much larger than that estimated from conventional calculation in the Born approximation, which has widely been used for KV electrons. (Heinrich et al. 1976). Since the sum of concentra-

tions of Ga and As is always more than 50 at.% in the region of the ternary system considered here, backscattered electrons are mainly affected by scattering processes with the Ga- and As-atoms resulting in similar energy distributions of backscattered electrons as shown in Fig. 4-8. Al-atoms turned out to have rather little affect on the energy distributions of backscattered electrons while η is affected by Al-concentration.

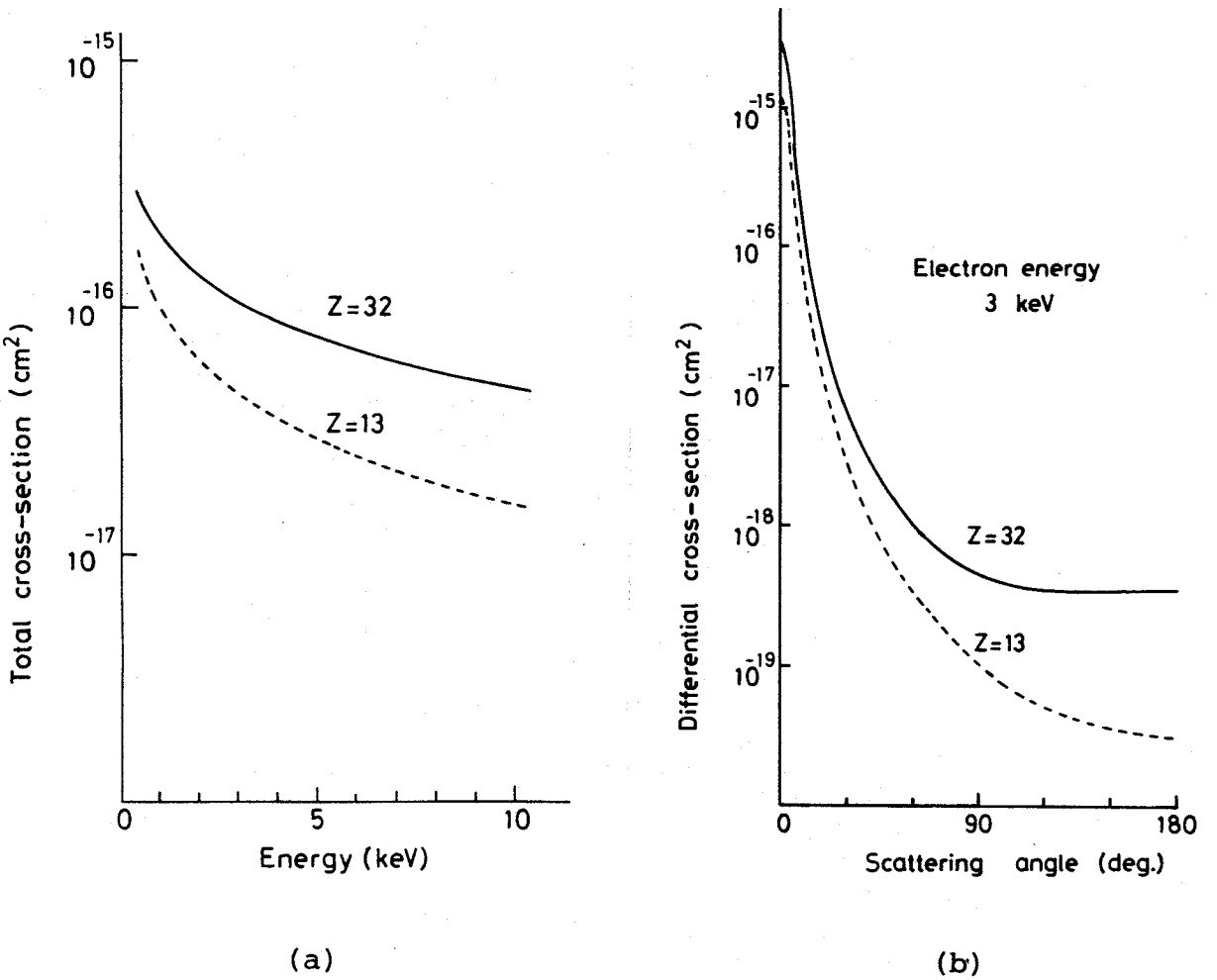

Fig. 4-9 Comparison of elastic scattering cross-sections for Z = 32 (corresponding to Ga and As) and Z = 13 (Al) :
(a) total scatteirng cross-sections;
(b) differential scattering cross-sections for 3 kV electrons.

Consequently the similarity in energy distribution for different concentration in Fig. 4-8 and the fact that all of the elements in the compound have nearly the same ionization energies for Auger electron generation cause Auger signal sensitivities of the three elements to change similarly with x. This leads to the straight-line relationship in Fig. 4-7 which agrees very well with the experimental results obtained by Arthur and LePore.

This straight-line relationship for Al-concentration of Auger peak height ratios (Al/As and Ga/As) was also confirmed by the calculation for the experimental conditions of 10 keV primary electrons at normal incidence, as shown in Fig. 4-10. Though the shape of energy distributions of backscattered electrons (Fig. 4-10(a)) is a little different from that shown in Fig. 4-8, the similarity of the energy distributions for three different compositions shown in Fig. 4-10(a) also leads to the straight-line relationship for Al-concentration as shown in Fig. 4-10(b).

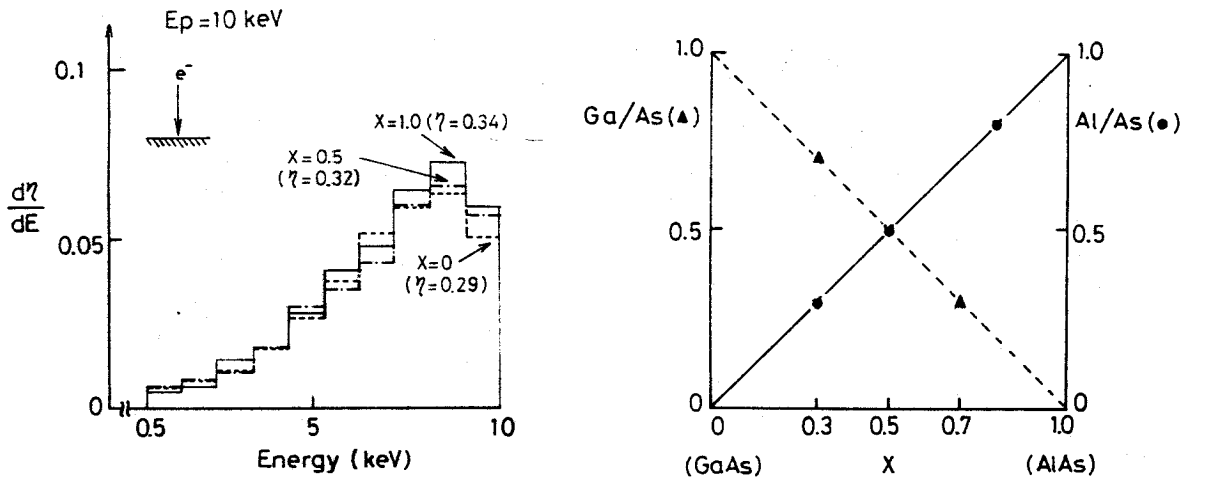

Fig. 4-10 Energy distributions of backscattered electrons ((a)), and changes of intensity ratios of Auger signals as a function of Al-concentration ((b)) for $Al_xGa_{1-x}As$ at normal incidence of 10 kV electrons.

4-4 Conclusions

The verification of this Monte Carlo calculation has been done by comparison with the experimental results of the dependence of Auger signals on primary electron energy, which was performed with scanning Auger electron microscope JAMP-3. Theory has described the experiment very well for results of Al, Cu, and Ag, though we need a more accurate shell-excitation function to attain better agreement for such a high Z element as Au.

Further verification has also been performed by comparison with experimental results for such semi-conductor compounds as $Al_xGa_{1-x}As$. The calculation explained the observed tendency (linear relationship of Auger peak height ratio with Al-concentration) satisfactory, and it was found that the exact elastic scattering corss sections which are calculated by p.w.e.m. have great importance in the treatment of scattering processes especially in the low energy region of below a few keV considered here.

Chap. 5 Application of SAEM for surface analysis

5-1 Introduction

The SAEM which has been improved to obtain spatial resolutions of submicrons as mentioned in the previous chapters will be expected to provide detailed information on surface properties and elemental analysis of local area on a surface. One of the applications of the most practical importance in material science is probably to study the surface segregation and the grain boundary diffusion (Seah and Hondros 1973). Quite a few investigations about diffusion mechanism (Janssen et al. 1977b) and more practical problems (i.e., device failure caused by grain boundary and surface diffusion (Inoue et al. 1976)) have already been reported using SAEM, which allows local analysis of micron area.

This chapter, first, describes the study of surface segregation at elevated temperature in Cu-Ni alloys (section 5-2). Segregation of sulphur atoms to the surface at a high temperature, which was observed by Inui and Shimizu (1979) using conventional AES was clearly observed under the SAEM. This has revealed that the S-Auger and Cu-Auger images are complimentary in contrast, leading to another confirmation of Inui and Shimizu's work that surface segregation of Cu and S are competitive and S at the outermost atom layer tends to supress the surface segregation of Cu.

Other fundamental problems observed using the SAEM are also described in the paragraphs that follows. In section 5-3, a characteristic hump which is observed in energy distributions of backscattered electrons on Si is examined. The structures which

appear in the background region in N(E) mode Auger spectrum are required to be well studied, since the background subtraction is one of the most important problems to be solved for quantitative analysis by AES. The hump which appears in the background region of Si LVV-Auger spectrum was assumed to be due to excitation of the inner shell (L-shell) by backscattered electrons and a theoretical interpretation based on a simple model was proposed as a speculation.

Finally, in Section 5-4, a fundamental study of electron beam damage under such a high current density as the SAEM is described. Electron beam damage has attracted much attention particularly in AES and in SAEM, though the compositional change during analysis was the main objective. Both the compositional and topographical changes, then, in thin film SiO_2 on Si due to electron beam irradiation were investigated and the damage dependence on the energy dissipation in thin film was made clear. Some practical methods for reducing the beam damage, i.e., sample cooling and primary beam chopping were also examined.

5-2 Observation of surface segregation of sulphur in Cu-Ni alloys at elevated temperature

Surface segregation at an elevated temperature in Cu-Ni alloys has attained considerable attention as a typical phenomena of surface segregation associated with practical importance for understanding surface properties of metals in wide use (Langeron 1979) and it has been extensively studied both in theory (Williams and Nason 1974, Burton et al. 1975) and experiment (Brongersma et al. 1978, Ling et al. 1978, Ng et al. 1979). It has already been reported by Inui and Shimizu (1979) that sulphur segregated to the surface when Cu-Ni alloys were heated and that this surface segregation of sulphur had marked effect on the surface composition of Cu and Ni as shown in Fig. 5-1. They have also revealed that the existence of sulphur supresses the surface segregation of copper leading to a considerable reduction of evaporation rate of copper atoms at an elevated temperature.

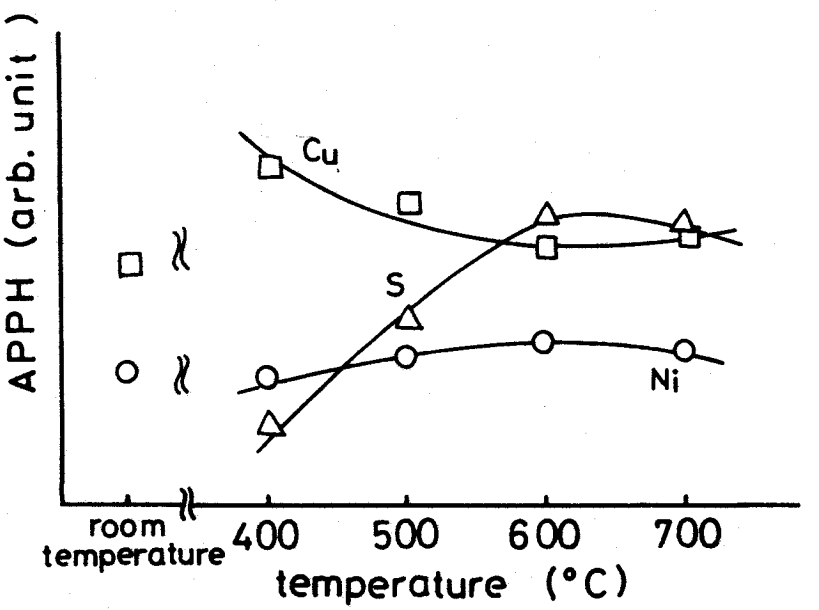

Fig. 5-1 Variation of Auger-peak height of Ni, Cu and S in Cu-Ni (50 wt%) alloy as sample temperature was elevated from room temperature to 700°C. (Inui and Shimizu 1979).

Since a conventional Auger electron detection system was used in their study with a primary electron beam size of a few mm, it was expected that a detailed information especially as to the spatial distributions of sulphur and copper on Cu-Ni alloy surface would be obtained with an SAEM which allows for surface analysis of a local area below microns in diameter.

To observe the surface segregation in Cu-Ni alloys at an elevated temperature under the same experimental conditions as that in Inui and Shimizu, a specific sample heater was devised which is demountable in a specimen stage of the JAMP-3.

A schematic diagram of the sample holder is shown in Fig. 5-2(a), in which a commercial type indirect sample heater assembly of Varian Associates is mounted, and its outerview is given in Fig. 5-2(b). This holder allows us to heat the sample up to $\sim$1000°C with ease without any disturbance by electron emission for heating and the sample temperature was measured with a chromel alumel thermo-couple which was welded at the sample.

After ion bombardment with 1.5 keV Ar^+ ions for surface cleaning, the sample was heated from room temperature to $\sim$600°C in 15 min, and kept at $\sim$600°C for 10 min. Then the power supply for heating was switched off and the sample surface was observed under the JAMP-3 after the sample was cooled down below 50°C. This procedure was the same as that in the work of Inui and Shimizu (1979).

All the measurements were done under experimental conditions; primary beam current $\sim 3 \times 10^{-7}$ A at 10 kV, modulation amplitude is $30eV_{p-p}$ and scanning speed 800 sec/frame for 256 x 256 picutre elements. The results are shown in Fig. 5-3. An

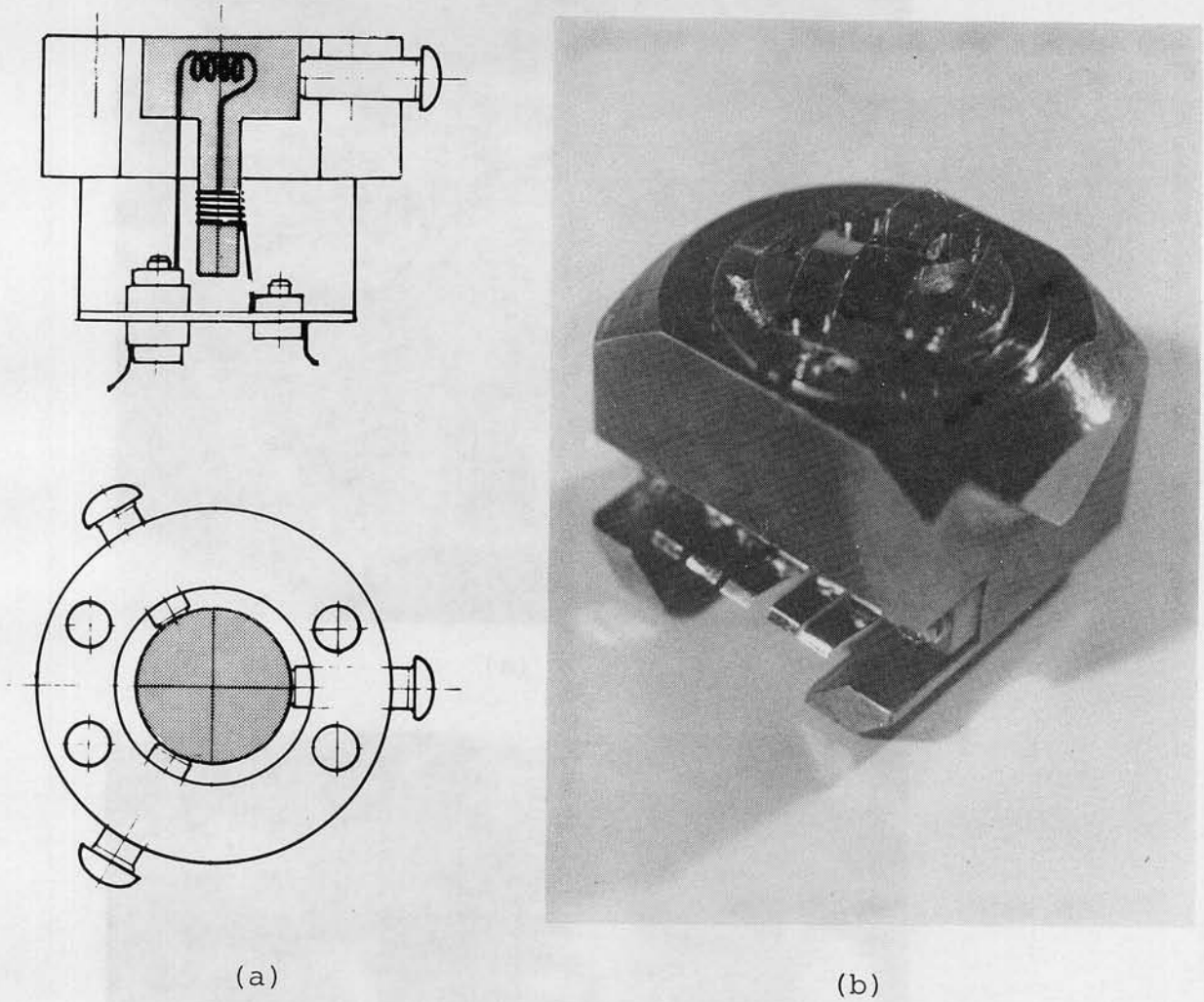

(a) (b)

Fig. 5-2 Sample stage with a sample heater for JAMP-3: (a) schematic diagram and (b) outer view.

absorbed current (specimen current) image of the Cu-Ni (50 wt%) alloy is shown in Fig. 5-3(a) and Auger-electron images for S LVV-, Cu LVV-, and Ni LVV-transitions in Figs. 5-3(b),(c) and (d), respectively. Comparing Fig. 5-3(a) with Fig. 5-3(b), it was found that the contrasts of these two images are complementary, i.e., very dark areas in the absorbed current image (Fig. 5-3(a)) correspond well to brighter areas in the Cu-Auger electron image (Fig. 5-3(c)) and vice versa.

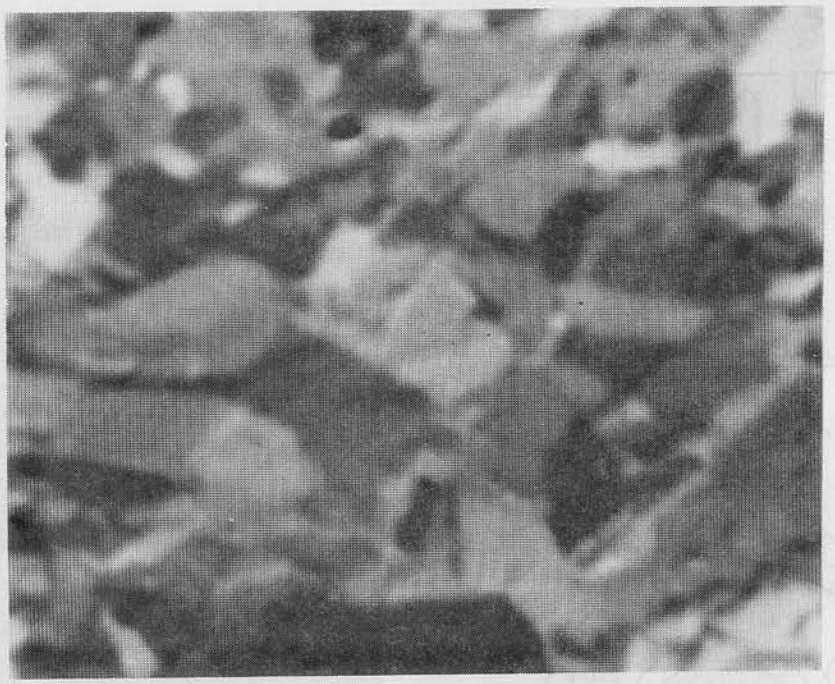

(a)

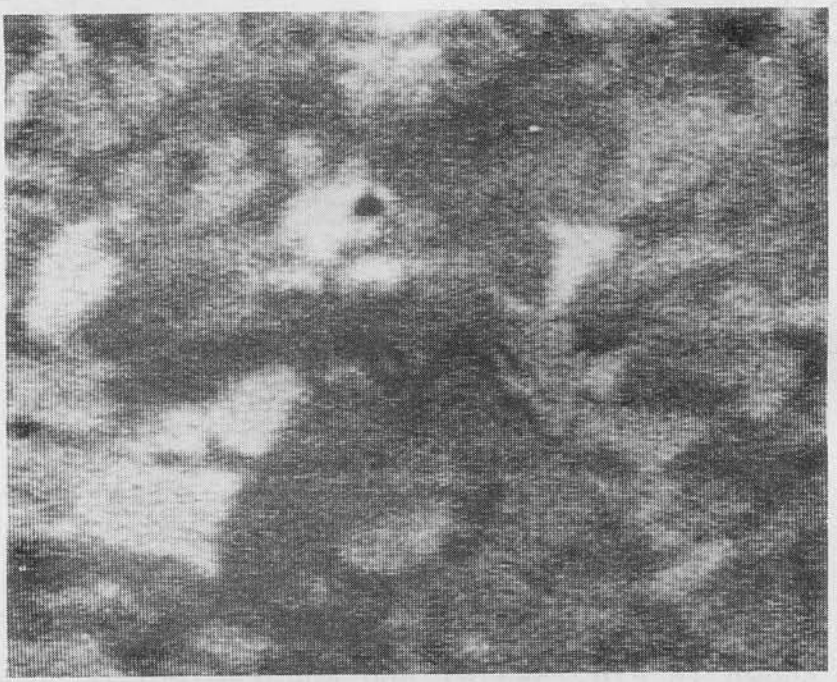

(b)

Fig. 5-3. Various scanning electron images of Cu-Ni alloy .
(a); Absorbed current image.
(b); S-Auger electron (LVV-transition) image .
(30 eV_{p-p} modulation, 800 sec./frame)
Both were taken under conditions of Ep= 10 keV, and Ip $\simeq 3 \times 10^{-7}$ A. The sample was heated at 600 °C after ion bombardment with 1.5 keV Ar^{+} ions.

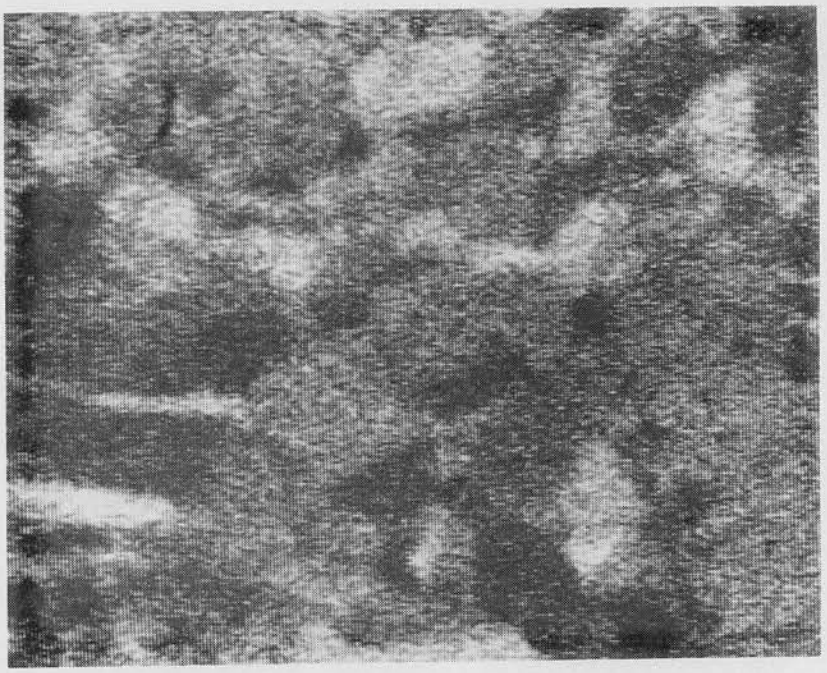

(c)

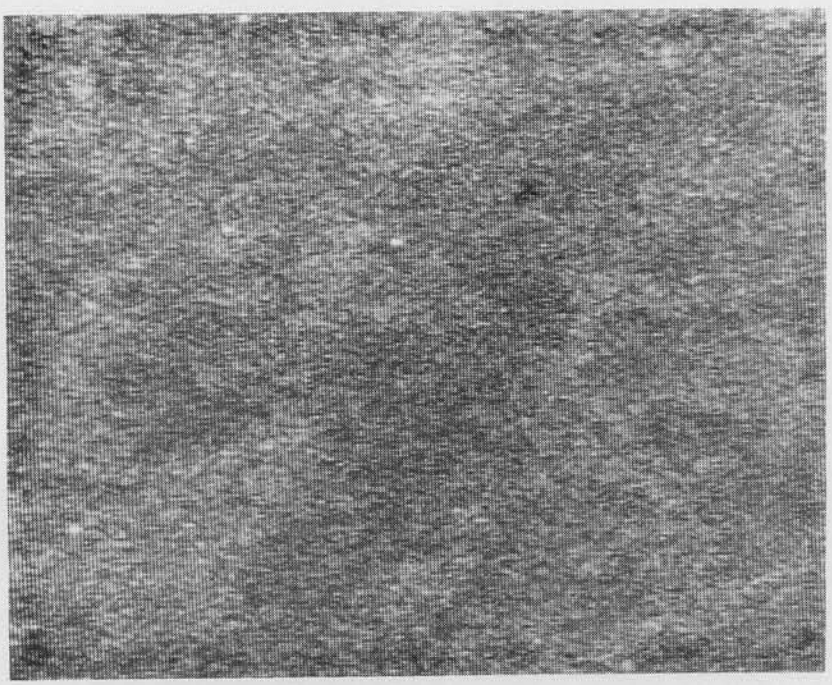

(d)

50 μm

Fig. 5-3. Various scanning electron images of Cu-Ni alloy.
(c); Cu-Auger electron (LVV-transition) image.
(d); Ni-Auger electron (LVV-transition) image.
Both were taken under conditions of Ep= 10 keV, Ip $\simeq 3 \times 10^{-7}$ A, 30 eV_{p-p} modulation, and 800 sec./frame. The sample was heated at 600 °C after ion bombardment with 1.5 keV Ar^{+} ions.

Note that Cu-Auger electron intensity becomes weak in an S-rich area, and these areas correspond to grains which are more clearly seen in Fig. 5-3(a). The contrasts of Ni-Auger electron image shown in Fig. 5-3(d), on the other hand, looks quite similar to S-Auger electron image (Fig. 5-3(b)) though the Ni-Auger electron image shows a rather poor contrast.

According to the ISS-study of Brongersma et al. (1978) the outermost atom layer is covered in a major part by Cu-atoms at such high sample temperatures as $\sim$600°C. Hence the surface compositions tends to be more Cu-rich as the sample temperature elevates. However, the surface segregation of sulphur, which covers some of grains preferentially, suppresses the surface segregation of copper. As seen in Fig. 5-1 this results in a decrease of Auger intensity of Cu-atoms as the surface concentration of sulphur becomes larger. Furthermore, since the outermost atom layer was almost covered by either Cu- or S-atoms, the Auger signal intensity of Ni-atoms was hardly changed for elevation of the sample temperature. This feature can also be seen in the results shown in Figs. 5-3(b), (c) and (d). These images clearly indicate that Auger signals of Cu are very weak at areas where S-Auger signals are strong, probably due to the fact that the existence of sulphur supressed the surface segregation of copper.

Since the atom size of S is smaller than that of Cu and this leads to a smaller attenuation of Ni-Auger signals due to the S-surface coverage, one may, according to Seah and Dench (1979), assume that attenuation of Ni-Auger signals due to the coverage of Cu-atoms on the top layer is larger than that due to S-atoms provided that both atomic densities of S- and Cu-atoms in these surface coverages are the same. This has resulted in the contrast

of Ni-Auger electron image that shows a rather weak signal intensity at S-rich area whereas the signals are very weak at Cu-rich area as seen in Fig. 5-3(d).

Normally the Auger-signal intensity of pure nickel (the lowest energy peak of LVV-transitions, 718 eV) is roughly half of that of pure copper (at the highest energy peak of LVV-transitions, 929 eV), the low Auger signal intensity of nickel in Fig. 5-3(d), therefore, suggests that the outermost atom layer is covered in major part by other atoms, i.e., in this case, either Cu or S. It should also be noted that another sufficient ion sputtering of the Cu-Ni alloys after the above observation hardly revealed any marked contrast in both the Auger electron images of copper and nickel except for a few local areas which were bright in both the images, probably due to surface topograph.

The interesting findings of this study include the following :

(1) The surface segregation of sulphur takes place in grains preferentially.

(2) The outermost atom layer of Cu-Ni alloys at elevated temperatures covered in major part by either Cu or S and those coverages are different from grain to grain.

(3) The existence of sulphur at the outermost atom layer tends to suppress the surface segregation of copper.

(4) Surface analysis of the local area with a scanning Auger electron microscope is becoming a powerful tool leading to more comprehensive understanding of the surface segregation.

5-3 Study on a characteristic hump in energy distributions of Si

Measurement of Auger-signal intensity in N(E)-mode is, in principle, more desirable for quantitative argument in Auger electron spectroscopy (AES) though dN(E)/dE-mode has been widely used. This approach, however, requires precise knowledge of background, i.e. energy distribution of backscattered electrons since one has to subtract the background to assess the signal intensities. Several workers (Sickafus 1971, Grant et al. 1973, 1974a, b, c, Houston 1974, Staib and Kirschner 1974, Bindell and Colby, 1975) have proposed approaches for the subtraction of the background and applied them to some practical AES with success. (see Section 1-2) The background, however, often looks so complicated that those approaches cannot fully solve the difficulties. Even in energy regions where the distribution of backscattered electrons is considered to be of a smooth curve or straight line for the measurement with cylindrical mirror analyzer (CMA), recent investigation (Le Gressus et al. 1979) has revealed that the backgrounds of actual N(E)-curves do not form such a simple smooth curve as assumed so far. Thus, basic studies of the background as well as Auger signal are of most necessity for precise analysis by AES.

The N(E) mode spectra can be obtained either by direct recording of the output signals of a CMA or by modulating the primary beam current intensity to utilize phase sensitive detection systems. To obtain N(E) mode spectrum by the latter method, an electron beam chopping circuit was designed and constructed. This is one type of beam brightness modulation (BBM) system which

was devised by Mogami and Sekine (1976). The schematic diagram of the circuit is shown in Fig. 5-4(a) and the characteristic of electron beam chopped at 3 kHz was in Fig. 5-4(b). It is clear from Fig. 5-4(b) that the circuit has enough features (duty ratio, rising up and falling down characteristics, etc.) to use N(E) mode detection of Auger signals.

A measured Auger spectrum of Si in N(E) mode after Ar^+ ion sputtering (E_p = 1.5 keV, I_p = 10 μA/cm^2, ∿2 hours) is shown in Fig. 5-5. This was obtained under the high energy resolution of CMA ($\Delta E/E \leq 0.5\%$) and vacuum pressure of less than ∿1 x 10^{-9} Torr, while the primary beam energy (E_p) is 5 keV and the current is ∿0.2 μA. Two Auger peaks of Si due to LVV- and KLL-transitions are clearly in the figure in the low and high energy region, respectively, and moreover a small hump can be detected at about 200 eV. The peak position of the hump seems to be closely related to the excitation energy of Si L-shell. To examine the origin of the hump a calculation based on a simple model was achieved as follows. (Ichimura et al. 1980b)

The probability that backscattered electrons of kinetic energy E excite inner shell electrons during path length S is simply proportional to $\sigma(E)\cdot S$ in which $\sigma(E)$ is total ionization cross-section for the inner-shell electrons of binding energy Ec. We can write the total cross section according to Gryzinski (1965) in the form

$$\sigma(E) = \frac{\pi e^4 Z_i N}{E_c}\cdot\frac{1}{E}\cdot\left(\frac{E-E_c}{E+E_c}\right)^{3/2}\cdot\left[1+\frac{2}{3}\left(1-\frac{E_c}{E}\right)\cdot\ln\left\{2.7+\left(\frac{E-E_c}{E_c}\right)^{1/2}\right\}\right] \quad (5\text{-}1)$$

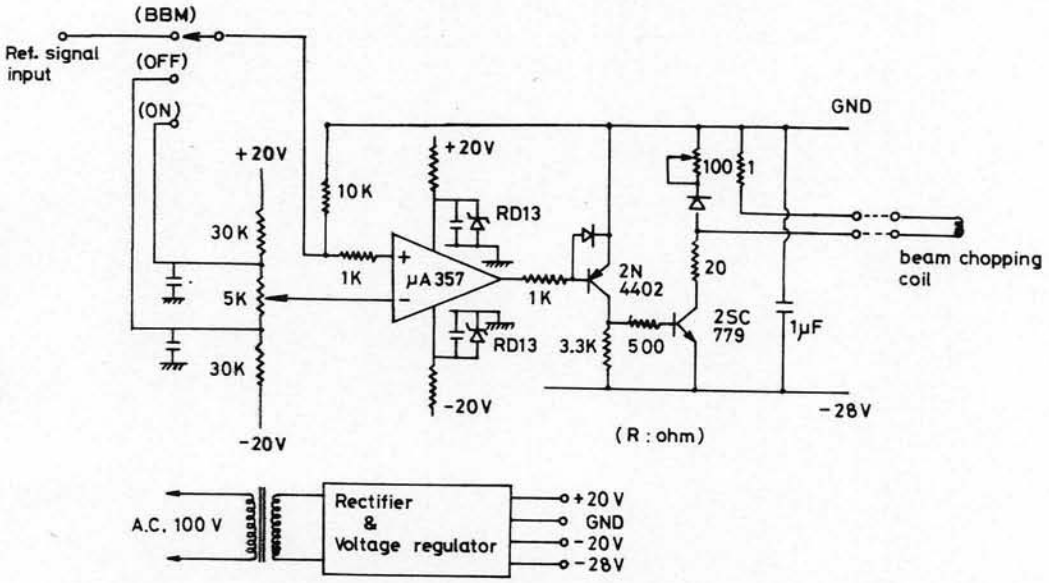

(a)

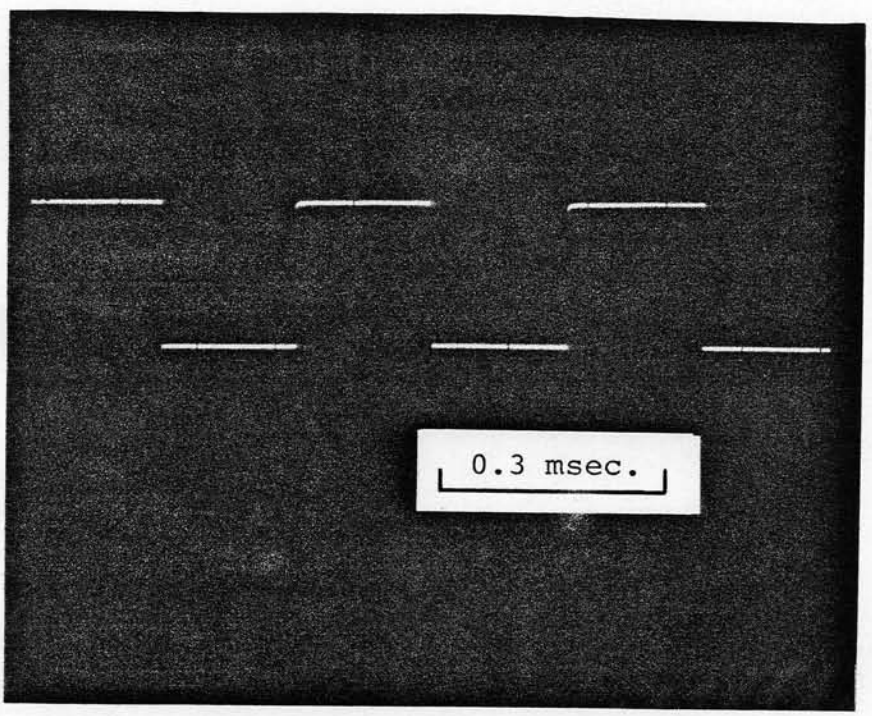

(b)

Fig. 5-4 Schematic diagram of electron beam chopping circuit ((a)) and the characteristic of chopped electron beam at 3 kHz ((b)).

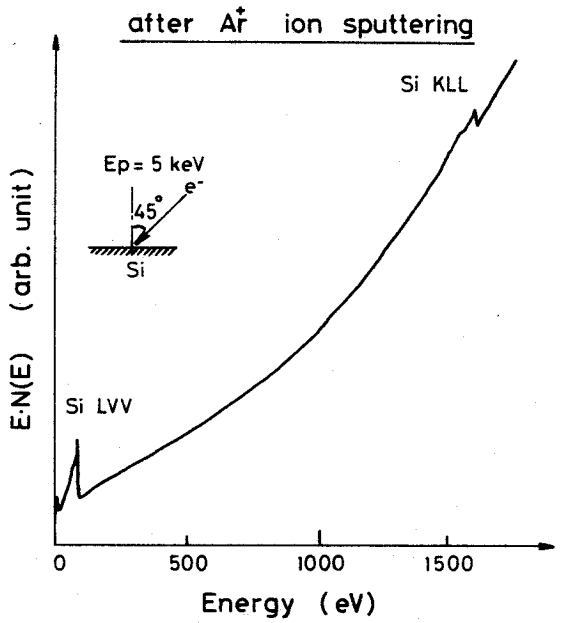

Fig. 5-5 Auger electron spectrum from Si after Ar^+ ion sputtering. Primary energy is 5 keV and the angle of incidence 45°.

where Z_i and N are number of inner shell electrons in question and atomic density, respectively. We may take S equal to $\ell(E)$, the mean free path of an electron of kinetic energy E, for the convenience of further discussion. These backscattered electrons lose a certain amount of kinetic energy due to inner-shell electron excitation and we can obtain estimation of this energy loss E from Gryzinski's excitation function by writing

$$\gamma(\Delta E) = \frac{\pi e^4 Z_i N}{\Delta E^3} \cdot \frac{E_c}{E} \cdot \left(\frac{E}{E+E_c}\right)^{3/2} \cdot \left(1-\frac{\Delta E}{E}\right)^{\frac{E_c}{E_c+E}}$$

$$\times \left[\frac{\Delta E}{E_c} \cdot \left(1-\frac{E_c}{E}\right) + \frac{4}{3}\left\{\ln 2.7 + \left(\frac{E-\Delta E}{E_c}\right)^{1/2}\right\}\right] \qquad (5\text{-}2)$$

This $\gamma(\Delta E)$ gives the probability that a backscattered electron of kinetic energy E will have the kinetic energy $E' = E-\Delta E$

after the inner-shell electron excitation. Thus, the inner-shell electron excitation results in a decrease in the number of backscattered electrons of E and an increase in that of backscattered electron of E'. Denoting the intensity of backscattered electrons with kinetic energy E measured by CMA in N(E)-mode as Bo(E), we can obtain estimates of the decrease of backscattered electrons of energy E due to the inner-shell electron excitation by writing

$$\sigma(E)\cdot B_0(E)\cdot \ell(E)$$

This excitation, then, results in an increase of backscattered electrons of E' by

$$\gamma(E-E')\cdot B_0(E)\cdot \ell(E)$$

Since backscattered electrons in the energy range between Ec and E_p (primary energy) have probabilities to excite inner-shell electrons, this leads to an increase of backscattered electrons of energy E' which is given by

$$B_1(E') = \int_{E_c+E'}^{E_p} \gamma(E-E')\ B_0(E)\cdot \ell(E)\cdot dE \qquad (5\text{-}3)$$

Thus, the resultant N(E)-curve is written by

$$N(E) = B_0(E) + \int_{E_c+E}^{E_p} \gamma(E'-E)\cdot B_0(E')\cdot \ell(E')\cdot dE'$$

$$-\{\sigma(E)\cdot B_0(E)\cdot \ell(E)\} \qquad (5\text{-}4)$$

In Eq. 5-4 Bo(E) can be estimated from the measurement and $\ell(E)$, from empirical formula as follows,

$$\ell(E) \propto \sqrt{E} \cdot 10^{-8} \quad \text{(cm)} \qquad (5\text{-}5)$$

Hence substituting Eq. (5-5) to Eq. (5-4), we can proceed with the calculation of equation 5-4, and the result is shown in Fig. 5-6. The solid line in the figure was obtained experimentally and the dotted line was obtained by the calculation, in which 112 eV was used for E_c as the average energy of Si-L shell excitation energy and linear background (AE + B) was assumed for Bo(E) where A and B were assessed from the solid surve. Both of the curves are fitted at two points (100 eV and 1000 eV) indicated

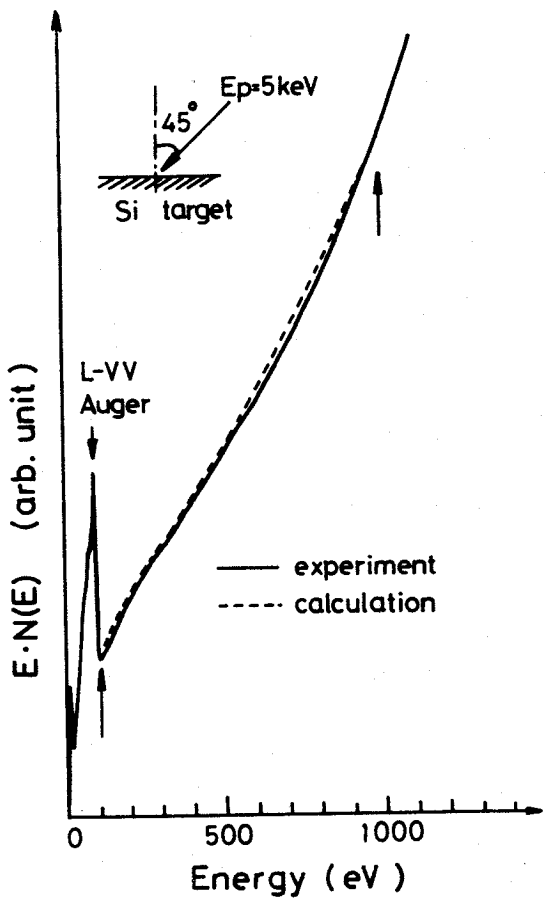

Fig. 5-6
Comparison of the theoretical calculation with experiment. Both results are fitted at two points indicated by arrows.

by arrows for convenience of comparison.

Although we assumed a straight line for N(E)-curve, the calculation shows that the L-shell excitation of backscattered electrons at the surface layer causes visible change for N(E)-curve to have a small hump about 200 eV and the curve is no longer a straight line as that of the experimental result shown by the solid line in Fig. 5-6, and these two curves show a reasonably good resemblance indicating the possibility of excitation mechanism considered here. The present model also suggests that L-shell excitation results in a more marked change in the N(E)-curve for Al since the probability of L-shell excitations becomes higher owing to a lower excitation energy Ec in Eq. (5-1). This agrees quite well with the experimental results obtained by Mogami (1978b).

In conclusion, the characteristic hump which appeared in the background region of N(E) spectrum was observed and can be well explained by a simple model. Of course, other mechanisms leading to the features in N(E) mode spectra should be fully studied.

5-4 Observation of electron beam damage in thin-film SiO_2 on Si

5-4-1 Damage measurement in thin-film SiO_2 on Si

Electron beam damage has attracted much attention and well studied especially for the past several years, because detailed knowledge of the damage is indispensable for the interpretation of experimental results by AES. Up to now, however, the damage under such high current densities as those in an SAEM, together with the relation between the surface compositional and topographical changes, have not yet been well studied, although a sample would seem to be in danger of undergoing other types of severe damage during analysis under SAEM.

Thus the electron beam damage under various experimental conditions with the SAEM is examined using thin film SiO_2 on Si as a sample (Ichimura and Shimizu 1979). Electron beam damage to SiO_2 material widely used in semiconductor devices has been investigated from various points of view, and some aspects of them (volume changes (O'Keefe and Handy 1968), enhancement of chemical etch rate (O'Keefe and Handy 1968), charge trapping (Szedon and Sandor 1965, Simons et al. 1968), etc.) have already been reported. The dissociation of SiO_2 into elemental silicon and oxygen and its dependence on incident electron conditions have also been well investigated. (Thomas 1974, Johannessen et al. 1976, Carriere and Lang 1977)

The SiO_2 film used in the present experiment was thermally grown on silicon substrate at $\sim$950°C, and the tickness of the SiO_2 film which has a step-like shape are about 4300 Å, 1700 Å, 850 Å, 450 Å, respectively. All measurements have been achieved

under the vacuum condition of less than $\sim 1 \times 10^{-9}$ Torr.

First, the film of ~4300 Å was bombarded by primary electrons (E_p = 10 keV, I_p = 0.5 A) in order to observe beam damage by scanning electron image, while the compositional change of the surface was measured by AES. Immediately after the electron beam irradiation of the sample as received, Auger peaks of Si in SiO_2 were found in low and high energy region, which correspond LVV- and KLL-transitions, respectively, while strong oxygen-peak and weak carbon-peak which is due to surface contamination were also detected as shown in Fig. 5-7. The appearance of silicon Auger signal at 92 eV, which is characteristic of an electron bombarded surface (Thomas 1974), was clearly seen after a certain degree (about 250 min.) of electron beam exposure. This corresponds to an electron beam charge of $\sim 2 \times 10^{-4}$ C/cm^2. In this case the carbon contaminant is desorbed from the surface as also shown in Fig. 5-7.

Figure 5-8(a) shows the observed topography of the film after the beam exposure. The depression of the irradiated surface area can be seen, while moreover, a peak has appeared at the center of it. Figure 5-8(b) shows the changes of oxygen and silicon Auger signal intensities measured at the dotted points in the x and y directions in Fig. 5-8(a) with ~0.5 μm spot size. From these results, it may be seen that there was a decrease of oxygen atoms in the surface area under irradiation accompanied by an increase of silicon at its center.

O'Keefe and Handy (1968) have also reported a decrease in the thickness of the oxide layer by bombardment with keV electrons, but of no more than 2 % even under saturation condi-

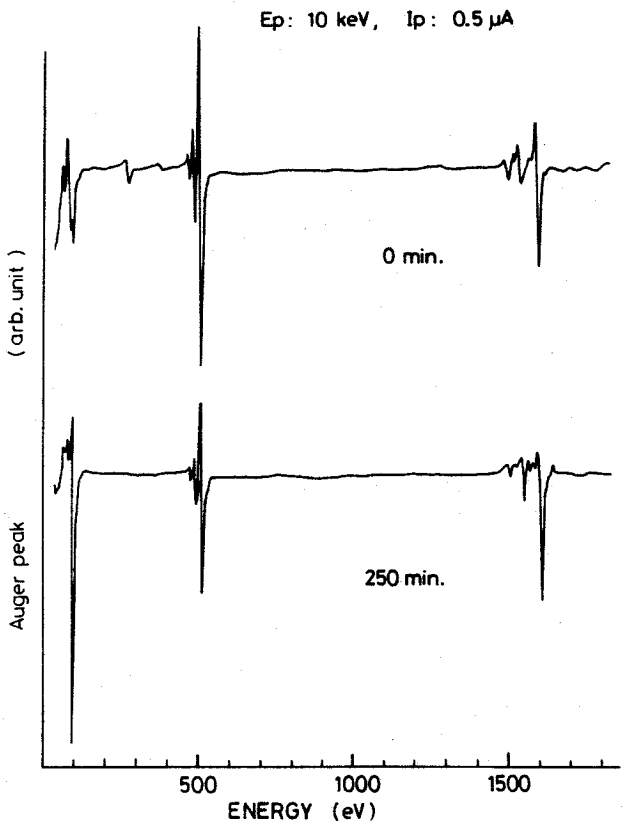

Fig. 5-7 Auger electron sepctra from SiO_2 on Si
(a) Immediately after the electron beam irradiation
(b) after 250 min. exposure of electron beam.

tions. Under such a high current density of the primary beam as that of the present experiment, it is clear from the figures that the decrease in the oxide layer thickness is considerable, as a result of the desorption of oxygen dissociated from SiO_2. Furthermore, these results clearly show the concentration of silicon in the center of the beam under these conditions.

Second, we investigated how damage progressed with different doses of the electron beam using primary electrons of 10 keV and 1 μA. Observations were made as follows: one area of the sample was irradiated for a fixed time period, after which Auger analysis of the damaged surface area was performed; next, another area

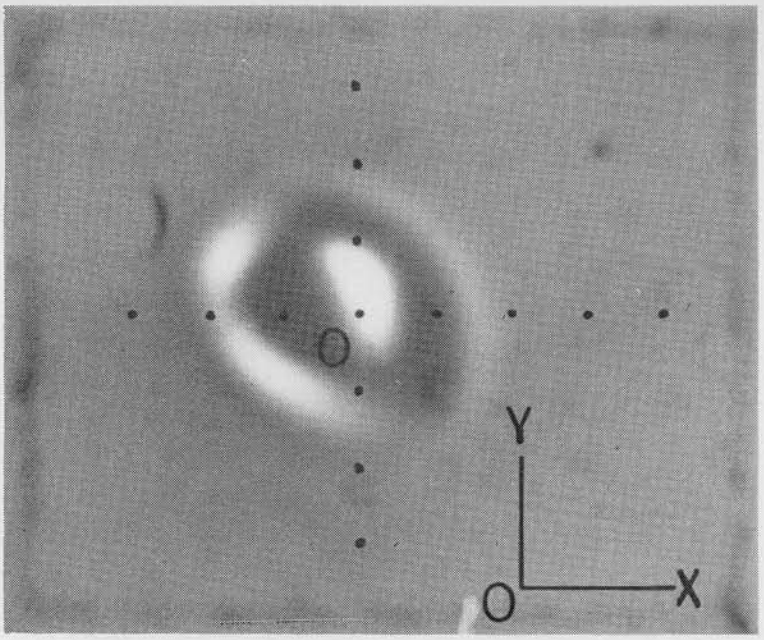

(a)

5 μm

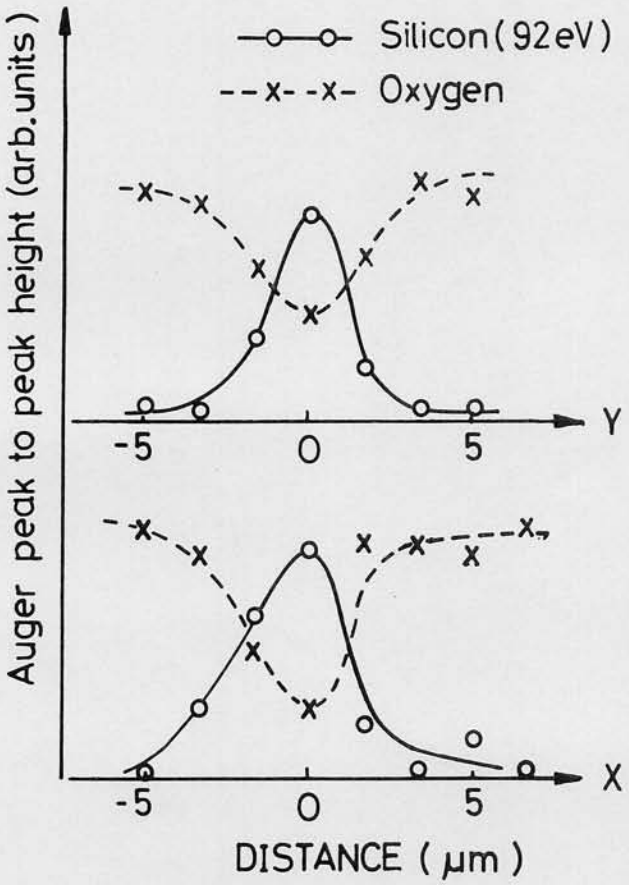

(b)

Fig. 5-8 Topography and Auger signal changes after electron beam exposure (E_p= 10 keV, I_p= 0.5 μA, 250 min.) on SiO_2 film: (a) backscattered electron image of the SiO_2 film; (b) oxygen and silicon (92 eV) Auger signal intensities at dotted points in (a).

was irradiated for a longer time period and reanalyzed; and so forth. Some of the obtained results are shown in Fig. 5-9.

After about 50 min. of exposure, corresponding to an electron beam charge of $\sim 5 \times 10^{-3}$ C/cm^2, the SiO_2 surface underwent a fairly larger depression, but no discernible peak appeared at the center. Observation after about 70 min. of exposure, however, revealed a distinctly visible peak at the center of the irradiated area. The results of the Auger analysis in each case are also shown in Fig. 5-9, indicating that the topographical changes at the center of the depressing area were associated with the concentration of silicon there. As a result of observation after even longer irradiation is not different from that shown in Fig. 5-9(b), it would seem that these concentrated silicon atoms act as a cover on the SiO_2 film, preventing further dissociation of the SiO_2 beneath.

To study the energy dependence of the damage of thin-film SiO_2, we performed the same experiment using other primary energies, 7 and 15 keV, respectively.

Figure 5-10(a) shows the result obtained by bombardment with 7 keV primary electrons, and Fig. 5-10(b) shows that obtained with 15 keV primary electrons, each with about 50 min. of exposure. We can distinctly observe a peak in Fig. 5-10(a), but not in Fig. 5-10(b) or Fig. 5-9(a). Comparing these results, we can conclude that the incidence of electron of 7 keV caused severer damage on the thin film than that of 10 and 15 keV electrons.

On the other hand, when Thomas (1974) measured the damage dependence of SiO_2 on incident energies using AES, he found lower surface damage for lower incident energies.

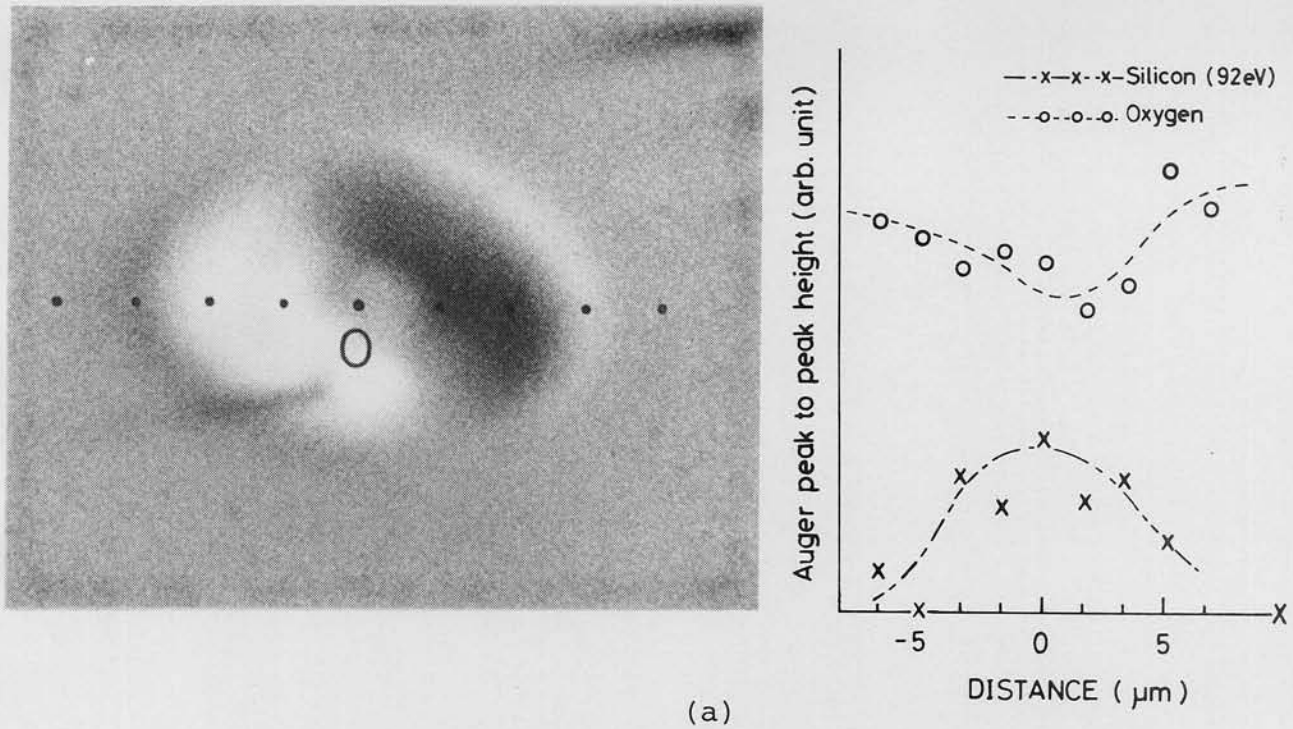

(a)

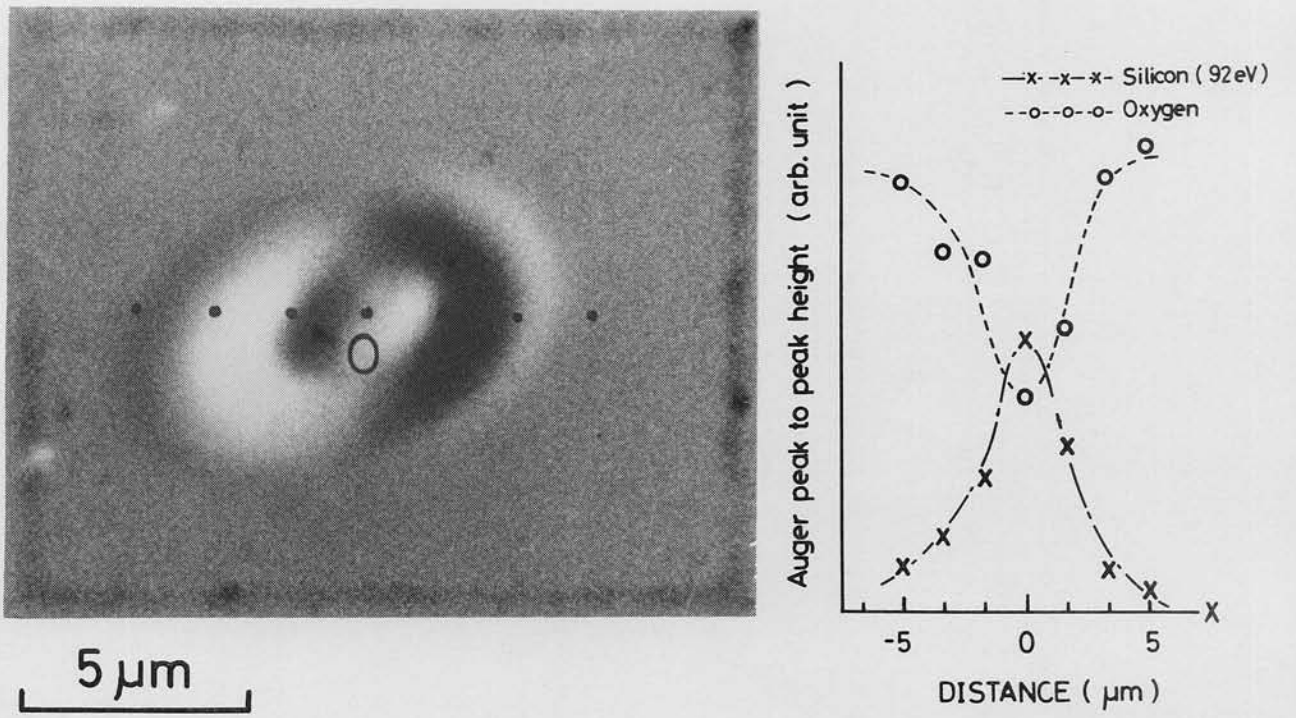

(b)

Fig. 5-9 Processes of the damage on SiO_2 with dose of electron beam: backscattered electron images and Auger signal variations of oxygen and silicon after about a 50-min. (a) and a 70-min. (b) exposure of electron beam (E_p= 10 keV, I_p= 1 μA).

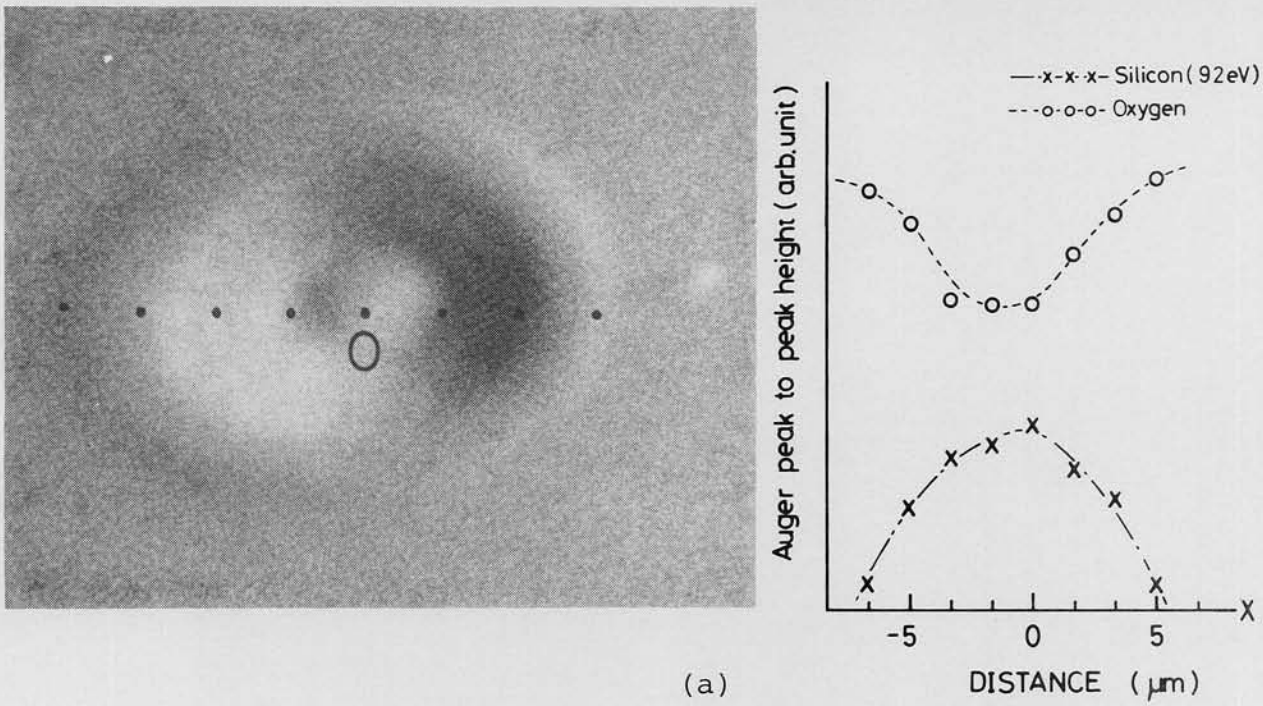

(a)

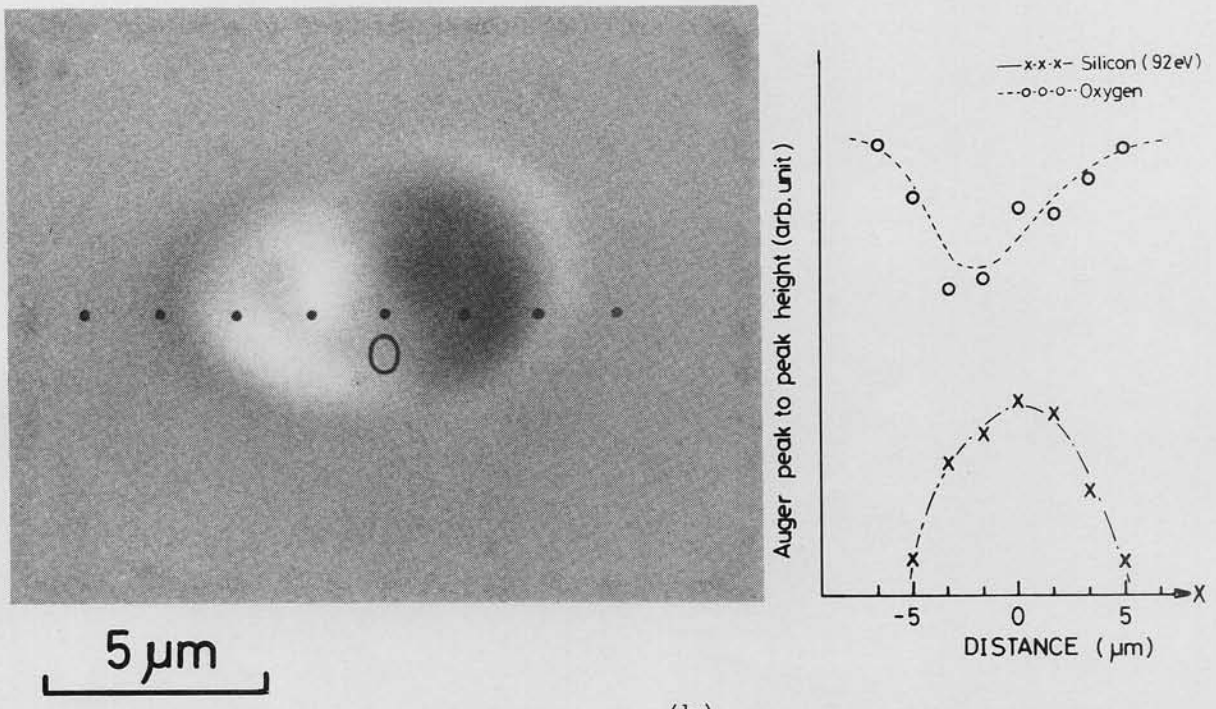

(b)

Fig. 5-10 Incident energy dependence of the damage: backscattered electron images and Auger signal variations of oxygen and silicon after about 50-min. exposure of 7 keV (a) and 15 keV (b) electrons; primary current is 1 μA.

To seek to understand this difference, the energy dissipation in the thin film was calculated. According to Everhart and Hoff, the energy dissipation E_d in thin SiO_2 film can be calculated using

$$E_d = fE_p \int_0^t \lambda(y)dy \qquad (5\text{-}6)$$

where

$$\lambda(y) = 0.60 + 6.21y - 12.40y^2 + 5.69y^3 \qquad (5\text{-}7)$$

and f denotes the effective energy incidence considering the backscattering effect, E_p is the incident energy, and t is the thickness of SiO_2 film normalized to the electron range R_g. For the case SiO_2, R_g is given by

$$R_G(\mu m) = 0.0181 \cdot E_p^{1.75}(keV) \qquad (5\text{-}8)$$

From these equations, the dissipation of incident energy in a film ~4300Å thick can be calculated. Taking the same f value for these three incident energies, the relative value E_d was thus estimated. Table 5-1 shows the resultant value normalized to 10 keV. As the range is longer for higher incident electrons, it is found that the energy dissipation in the film is much higher for 7 keV and lower for 15 keV. From this finding, the observed difference between our result and that of Thomas can be explained as follows: the thickness of Thomas's SiO_2 sample compared with

Table 5-1 Relative values of energy dissipation in thin SiO_2 film (normalized to 10 keV).

E_p	7 (keV)	10 (keV)	15 (keV)
E_d	1.2	1.0	0.6

ours was such that all the energies of the incident electrons, except those of the backscattered electrons were dissipated in SiO_2 and hence the beam damage to SiO_2 was proportional to the primary electron energy.

As is well known, electron beam irradiation of thin-film SiO_2 on Si yields charge trapping at the Si-SiO_2 interface under biased conditions (Szedon and Sandor 1965, Simons et al. 1968). The amount of trapped charge strongly depends on the energy dissipated at the Si-SiO_2 interface (Simons et al. 1968), probably because ionizations occurring in the oxide adjacent to the silicon interface are the most effective in introducing it. The observed tendency concerning the energy dependence of the desorption of oxygen and the concentration of silicon in this experiment seems to indicate that these phenomena, which have their origin in the dissociation of SiO_2, occur in the whole mass of SiO_2 under irradiation. It further indicates that dissociated oxygen can easily move to the SiO_2-vacuum interface and desorb from it.

Other three SiO_2 films with different thickness, $\sim$450 Å, $\sim$850 Å, and $\sim$1700 Å, respectively, were also irradiated using

primary electrons of 10 keV and 1 μA to see the damage dependence on oxide thickness. Figure 5-11 shows the observed topography and Auger signal intensity variations on the irradiated area after a certain degree (∿70 min.) of electron beam exposure, which is the same condition with Fig. 5-9(b). All of the observed topography show no noticeable feature at the center of the depressing area and that the flat area at the center becomes greater as the SiO_2 thickness is thinner. These results, together with strong Si (92 eV) peaks at the center which are also shown in the figure, seem to indicate that in the case of thin oxide films silicon atoms cannot concentrate enough to prevent further dissociation of SiO_2 and Si-substrate becomes visible. The electron beam damage, therefore, is so severe that it changes the SiO_2 film more than ∿2000 Å. Damage was also observed during the point analysis of the irradiated area, so some practical technique to reduce the electron beam damage by AES analysis must be researched.

5-4-2 Some trials for damage reduction

Considering the fact that the electron beam damage is closely related with the energy dissipation in the film, it was supposed that some thermal effect concerns the beam damage. To make this point clear, and to test the possibility of reducing electron beam damage, a sample cooling stage was devised. The schema is shown in Fig. 5-12(a), and its characteristics are shown in Fig. 5-12(b). The sample holder is attached to the stage and is cooled down by liquid N_2 which flows through the stage. It takes about an hour for a sample to be cooled down below - 100°C.

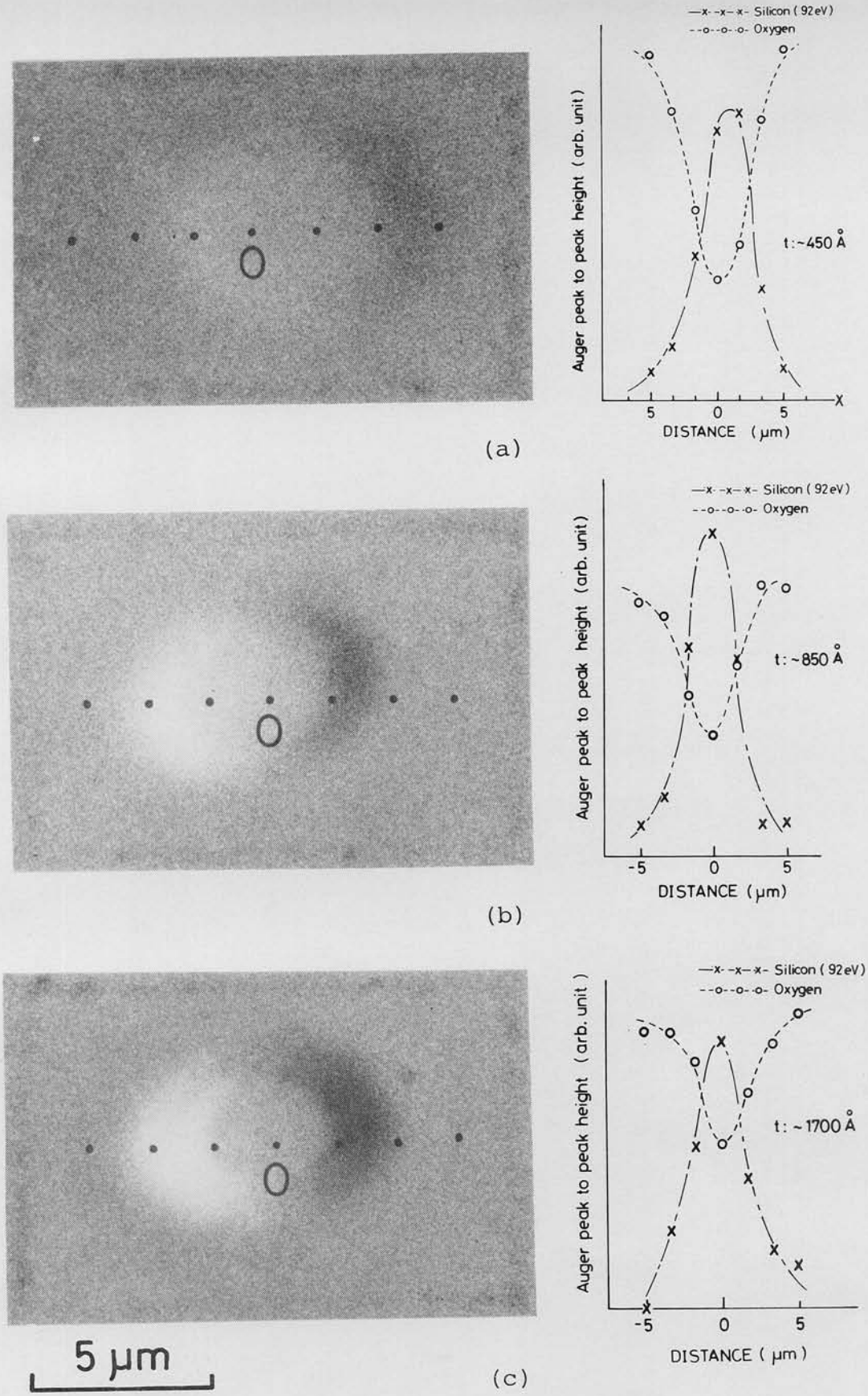

Fig. 5-11 Thickness dependence of the damage on SiO_2 after 70-min. exposure of electron beam (E_p= 10 keV, I_p= 1 μA): backscattered electron images and Auger signal variations on the film of (a)~450 Å, (b)~850 Å, and (c)~1700 Å.

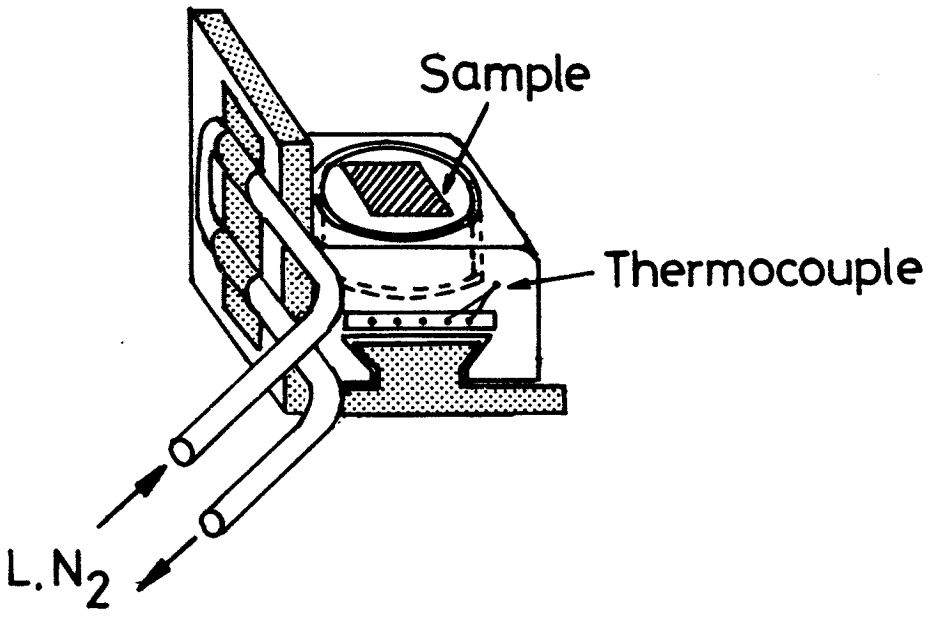

(a)

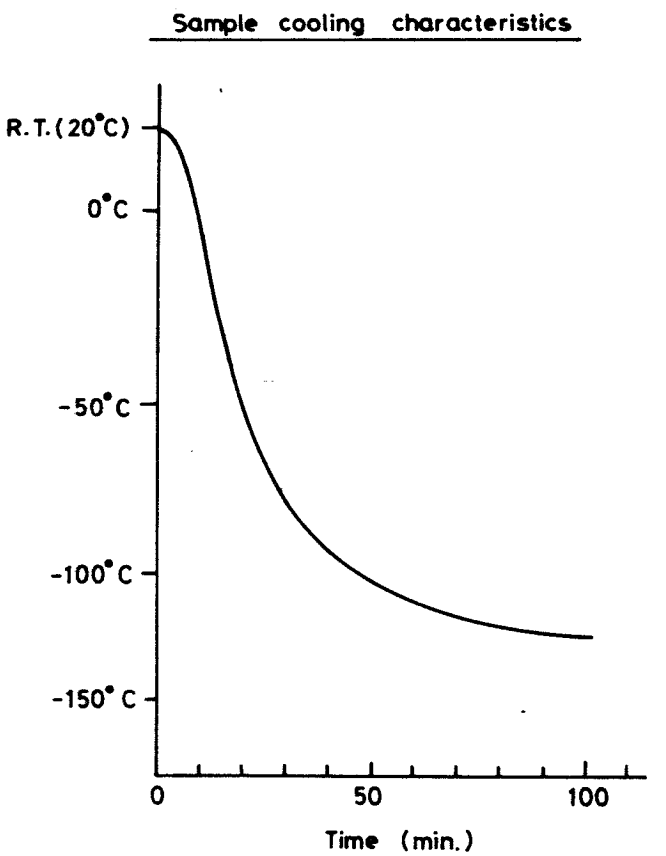

(b)

Fig. 5-12 A schema of the sample cooling stage ((a)) and its cooling characteristic ((b)).

The temperature was measured by a chromel-alumel thermocouple welded to the sample stage.

Using the sample cooling stage, the electron beam damage in thin film SiO_2 at low temperautre ($\sim$-100°C) was observed. Figure 5-13(a) shows the Auger signal intensity variations during electron beam irradiation and Fig. 5-13(b) shows observed topography after a certain degree ($\sim$180 min.) of electron beam exposure. The primary electron beam of 10 keV and 1 μA is also used in the experiment and the oxide thickness is $\sim$4300 Å. Although the increase of Si (92 eV)-Auger signals and decrease of O-Auger signals show a rather repressed tendency at low temperature (-90°C) than at room temperature, which is also shown in Fig. 5-13(a), the observed topography reveals that this is mainly due to the sample movement during cooling. Therefore, the cooling of the sample does not have a marked effect on the reduction of electron beam damage.

Another possible method to reduce the electron beam damage during AES analysis is to use a chopped electron beam. The N(E)-mode detection of Auger signals using a chopped electron beam which was first proposed by Mogami and Sekine (1976) is called the BBM technique as is mentioned in the previous section. They suggested that the technique permits attenuating the probe current necessary for obtaining Auger spectra to one-hundredth that of the conventional method, which greatly contributes to decrease specimen damage. The usefulness of BBM technique, then, for the damage reduction was confirmed using the electron-beam chopping circuit which is described in the previous section.

Figure 5-14(a) shows the observed topography on SiO_2 thin

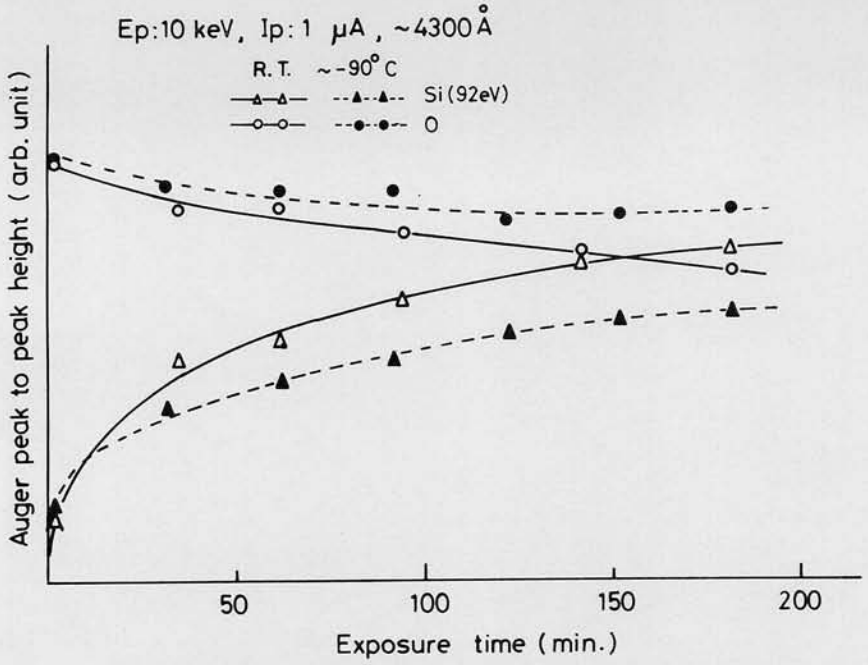

(a)

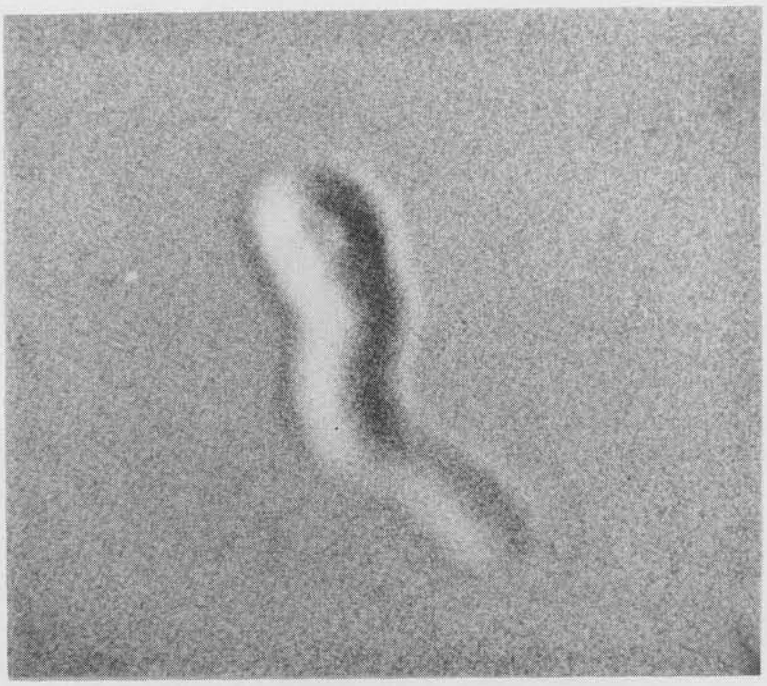

(b)

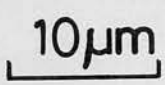

Fig. 5-13 Temperature dependence of the damage.
(a) comparison of Auger signal intensity change with exposure time of electron beam; open marks at room temerature, solid marks at ~-100°C.
(b) observed topography after 180-min. exposure of electron beam at ~-100°C.

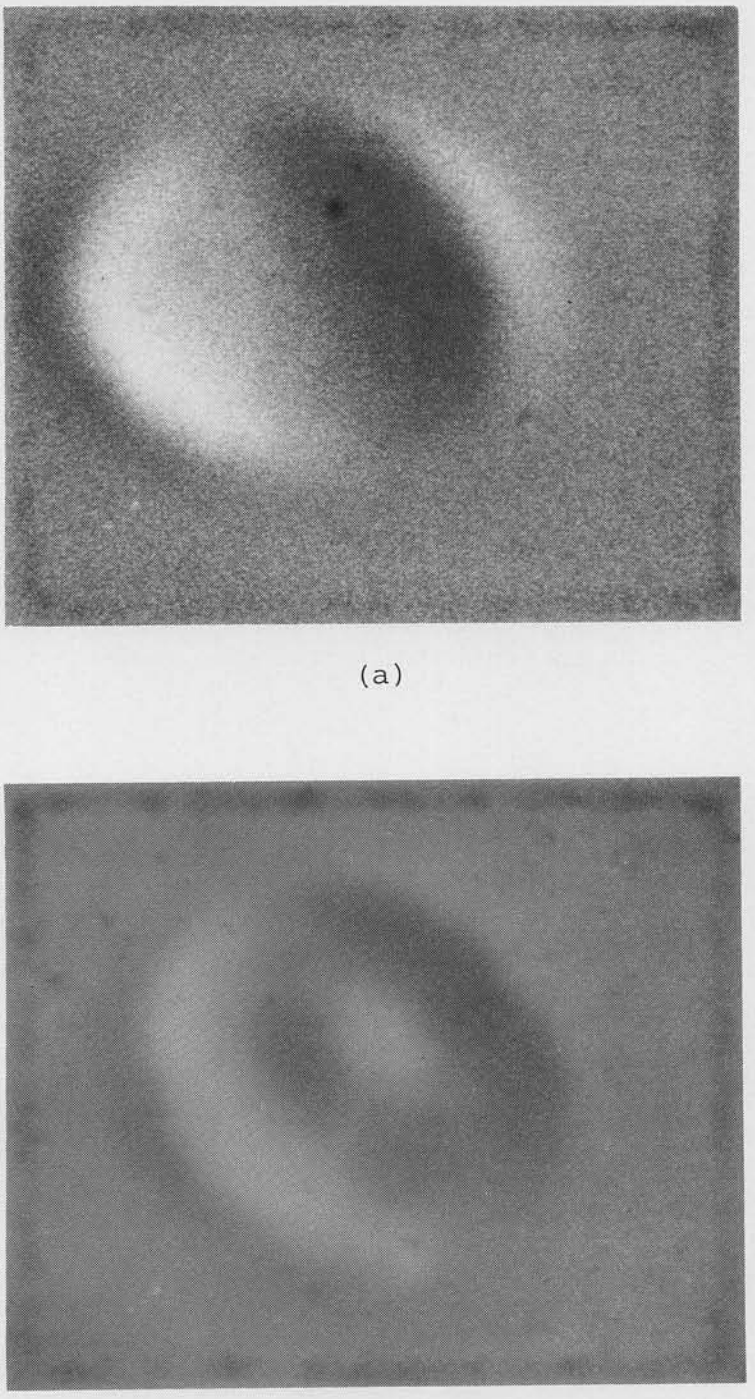

Fig. 5-14 Comparison of observed topography after electron beam exposure for Auger signal detection by (a) BBM method (modulation frequency 3 kHz) and (b) ordinary method.

film after a certain degree (∿120 min.) of chopped electron beam exposure. Comparing it with the topography shown in Fig. 5-14(b) which is observed after the same exposure conditions (E_p = 10 keV I_p = 1 μA, ∿120 min.) except for the beam continuity, it is clear that the BBM technique is very effective to decrease the electron beam damage even under the same current intensity which is used in the conventional technique. This is probably due to the fact that the beam damage strongly depends on the total dose to the sample.

5-5 Conclusions

Some applications of SAEM to fundamental probelms of the material surface were described in this chapter. Observation of sulphur segregation to Cu-Ni alloys surface in the Auger images clearly idnicates the suppression of Cu segregation to the surface due to the existence of sulphur. The devised sample heater was also ascertained to be very useful for observation of surface diffusion which often occurs preferentially in some grains.

The detection of Auger spectra in N(E) mode spectra was achieved using specially made electron beam chopping circuit, and the observed hump in the N(E) mode spectra on Si can be well explained by a proposed simple model based on inner-shell excitation by backscattered electrons.

The electron beam damage, which is one of the most important problems in AES, is also well examined using thin film SiO_2 on Si as a sample and it was found that the beam damage causes not only compositional but also topographical changes of the material. It is clear that these damages depend on the energy dissipation in the oxide film and BBM technique is very useful reducing the beam damage, although the sample cooling does not have any marked effect on it.

Summary

The present work consists of five chapters, which describe the basic studies on scanning Auger electron microscopy relating to the high spatial resolution measurement with the SAEM and the quantitative analysis by AES. The results obtained in the present study are summarized chapter by chapter as follows.

Chapter 1 ; Present status of surface analysis by scanning Auger electron microscopy

1) Principle and the features of surface analysis by AES are briefly descirbed.
2) A historical view and the development of SAEM are given together with the problem associated with the application of SAEM to surface analysis.
3) The present status of quantitative analysis by AES is described. It is pointed out that the main factor for quantification by AES is the correction of backscattering factor in AES.

Chapter 2 ; Approaches to high spatial resolution measurement with SAEM

1) Square wave modulation technique for effective Auger signal detection in SAEM are newly applied improving signal to noise ratio in an Auger image.
2) The signal modulation is synchronized with electron beam scanning, which improves the degradation of the Auger image by moire.
3) Digital system for 'real time' signal processing is devised to improve the spatial resolution in an Auger image.
4) A micro-computer is introduced to the SAEM, JAMP-3, to achieve high accuracy and high energy-resolution measurement.

5) Single crystal LaB_6 cathode is applied to JAMP-3, to achieve high accuracy and high energy-resolution measurement in scanning Auger electron mciroscopy.

Chapter 3 ; Application of Monte Carlo calculation to AES --- Approach to quantitative analysis

1) Elastic scattering cross-sections are numerically calculated by partial wave expansion method to treat electron-specimen interaction in energy region interested in AES and scanning Auger electron microscopy.

2) Treatment of inelastic scattering processes in a specimen is considered. Bethe's continuous slowing down approximation and the inner-shell excitations are combined to simulate electron-specimen interaction in mono- and poly-atomic materials.

3) A Monte Carlo simulation program for the quantitative analysis by AES is developed.

4) Present Monte Carlo calculation model is examined through comparison with experimental results for i)angular- and energy- distributions of backscattered electrons, and ii) energy- and incident angle-dependence of backscattering coefficient.

5) Energy distributions of backscattered electrons which are weighted by the ejection angle of backscattered electrons are calculated. Using the distribution, correction factors for the contribution of backscattered electrons are obtained for a number of materials of practical interest.

6) Two quantitative approaches using the present results are proposed.

7) The present Monte Carlo calculation approach is applied to the calculation of spatial distribution of Auger signal generation in Al. The results are further applied to the estimation of spatial-resolution limit in scanning Auger electron microscopy and the resolution of ~100 Å is estimated.

Chapter 4 ; Estimation of contribution of backscattered electrons --- Comparison of calculated result with experiment

1) The dependence of Auger signal generation on primary electron energy is examined for a number of elements (Al, Cu, Ag, and Au). The experimental results coincide well with calculation by the Monte Carlo method for Al, Cu, and Ag, but a little discrepancy is seen for Au. The reason is considered through the same experiment for Au-Cu alloy.

2) Quantitative analysis by AES for semiconductor-compound ($Al_xGa_{1-x}As$) is theoretically interpreted by the present Monte Carlo calculation.

Chapter 5 ; Application of SAEM for surface analysis

1) Surface segregation of sulphur on Cu-Ni alloy at elevated temperature is observed using devised sample heating stage. It is ascertained in Auger images that the existence of sulphur suppresses the Cu-segregation to the surface.

2) N(E) mode detection of Auger signals is achieved and the hump at background region is observed for Si-specimen. A qualitative interpretation of the hump is also proposed.

3) Electron beam damage under such high energy and high current intensity as the SAEM is investigated using thin film SiO_2 on Si as a sample. Both the topographical- and compositional-changes of the sample due to the damage are observed.

The dependence of the damage on the energy dissipated in the film is also ascertained.

4) The possibility of the damage reduction by applications of i) devised specimen cold stage and ii) introduction of Beam Brightness Modulation method are tested.

Appendix I Functions of the interface to JAMP-3

Figure A-1 shows the electronic circuit of the interface which has been constructed in the present study, and the block diagram and pin assignment of the MCS 6522 is shown in Fig. A-2.

The MCS6522 has 16 registers which are connected to processor address lines through the decorder (SN7400, SN7404, and SN7408) and the chip access control.

Two 8-bit output registers (ORA and ORB) can be used as bi-directional ports, and each of these lines can be programmed to act as either an input or an output by the use of data direction registers (DDRA and DDRB). Hence, it can be easily connected to the 12-bit D/A converter (DAC-80). Output signals of the DAC-80 are fed to X-Y recorder and/or KEPCO 2000B and/or brightness modulation ciucuit of the CRT of the JAMP-3 through analog switches (TL185 and TL191). These switches are controlled by pins (CA2 and CB 2) of the MCS 6522, which are directed to manual output mode by the aid of a peripheral control register (PCR). For the control of CRT brightness, a monostable multivibrator SN74LS122 is also used.

Two timers (Timer 1 and Timer 2) of the MCS 6522 are used for the signal detection. The Timer 2 is able to count negative-going pulses on PB6, to which the output signal of the V/F is transferred through a positive-nand gate (SN7400). Another input of the SN7400 is connected to the PB7 of the MCS6522 (No.1) through an inverter (SN7404). The PB7 can be programmed to produce pulses while the Timer 1 decrements the contents of the counter at system clock (1 MHz) rate. Therefore, the time for signal acquisition at an energy step is determined by the number

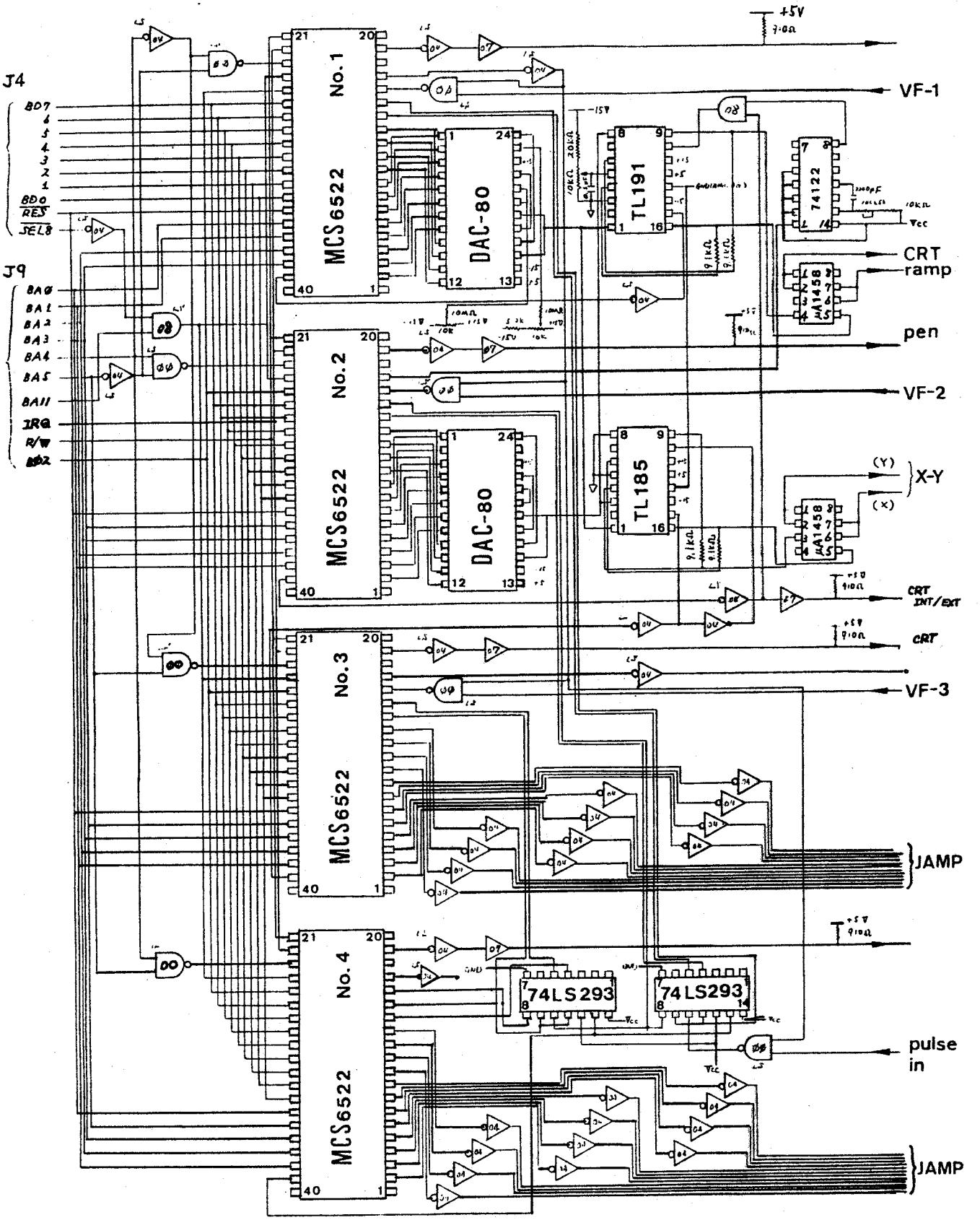

Fig. A-1 Electronic circuit of the interface

loaded to the Timer 1, and the maximum time at one step is about 65 msec. (The maximum number which can be loaded to the counter is 256 x 256 (2 byte).) For the detection of signals with high frequency, two counter (SN74LS293) are used together with the Timer 2 of the MCS6522.

The scanning of primary eelctrons is also controlled by the use of two MCS6522, and 12 lines of output registers (ORA and ORB) are connected to 12 bit D/A of the JAMP-3.

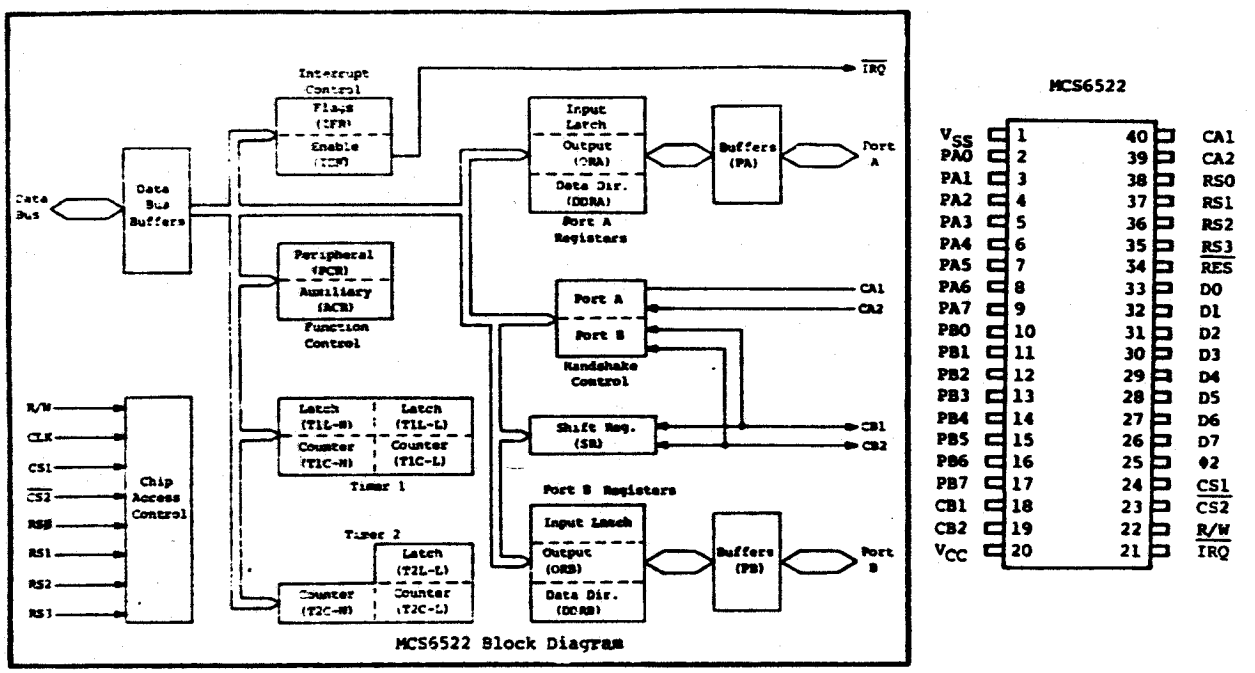

Fig. A-2 Block diagram and pin assignment of the MCS6522 (from the data-sheet of the MCS6522)

Appendix II. Flow chart of the Monte Carlo calculation program

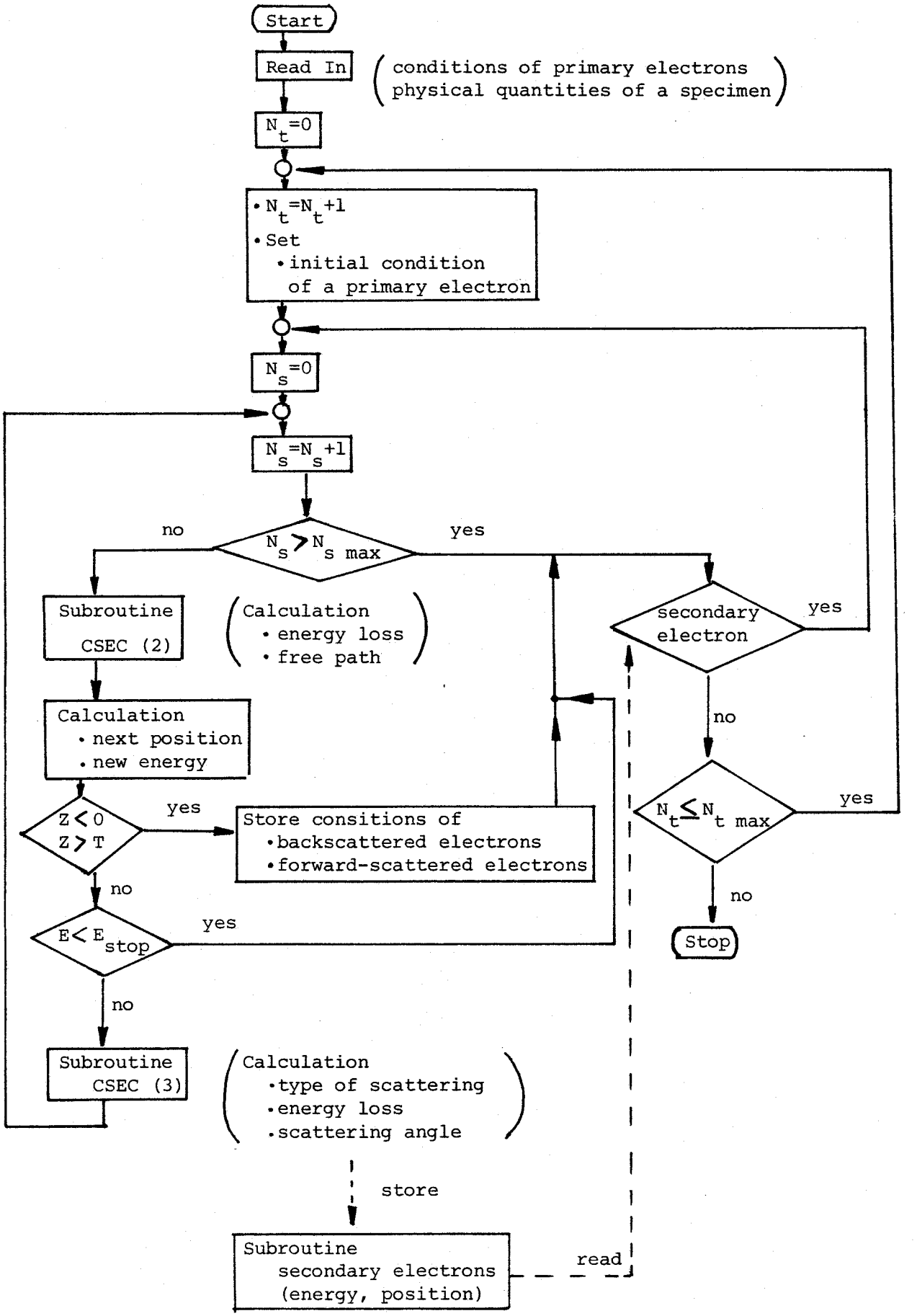

REFERENCES

Adesida I., Shimizu R. and Everhart T.E., 1978, Appl. Phys. Lett., 33, 849.

Arthur J.R. and LePore J.J., 1977, J. Vac. Sci. Technol., 14, 979.

Auger P., 1925, Comp, Rend., 180, 65.

Bambynek et al., 1972, Rev. Mod. Phys., 44, 716.

Berger M.J. and Seltzer S.M., 1964, Nuclear Science Report, No. 39, NAS-NRC, 205.

Bethe H., 1930, Ann. Physik., 5, 325.

Bindell J.B. and Colby J.W., 1975, Proc. 10-th Annual Conf. on Microbeam Analysis Society, August 11-15, MGM Hotel, Las Vegas, Nevada.

Biship H.E., 1966, X-ray Optics and Microanalysis, Eds. R. Castaing, P. Deschamps and J. Philibert, (Hermann, Paris), 112.

Biship H.E. and Riviere J.C., 1969, J. Appl. Phys., 40, 1740.

Bonham R.A. and Strand T.G., 1963, J. Chem. Phys., 39, 2200.

Booker G.R., 1970, in : Modern Diffraction and Imaging Techniques in Materials Science, Eds. S. Amelinckx, R. Gevers, G. Remaut and J. Van Landuyt (North-Holland, Amsterdam), 553.

Borom M.P. and Hanneman R.E., 1967, J. Appl. Phys. 38, 2406.

Broers A.N., 1969, Rev. Sci. Instrum., 40, 1040.

Brongersma H.H., Sparnaay M.J. and Buck T.M., 1978, Surf. Sci., 71, 657.

Browning R., Bassett P.J., El Gomati M.M. and Prutton M., 1977a, Proc. Roy. Soc., London, A357, 213.

Browning R., El Gomati M.M. and Prutton M., 1977b, Surf. Sci., 68, 328.

Bühring W., 1965, Nuclear Phys., 61, 110.

Bunyan P.J., 1963, Proc. Phys. Soc., 81, 816.

Bunyan P.J. and Schonfelder J.L., 1965, Proc. Phys. Soc., 85, 455.

Burhop E.H.S., 1952, The Auger Effect and Other Radiationless Transitions (Cambridge U.P., London).

Burton J.G., Hyman E. and Fedak F.G., 1975, J. Catalysis, 37, 106.

Byatt W.J., 1956, Phys. Rev., 104, 1298.

Callan E.J., 1961, Phys. Rev. 124, 793.
Carrière B. and Lang B., 1977, Surf. Sci., 64, 209.
Chang C.C., 1974, in : Characterization of Solid Surfaces, Eds. P.F. Kane and G.B. Larrabee (Plenum, New York, 1974) ch. 20.
Chang C.C., 1975, Surf. Sci., 48, 9.
Chattarji D., 1976, The Theory of Auger Transitions (Academic London).
Christou A., 1976, J. Appl. Phys., 47, 5464.
Chen M.H., Crasemann B. and Mark H., 1980, Phys. Rev. A21, 436.
Colby J.W., 1968, Advan. X-ray Anal., 11, 287.
Coster D. and Kronig R. de L., 1935, Physika, 2, 13.

Darlington E.F.H. St. G., 1971, Ph. D thesis, University of Cambridge (unpublished).
Darwin C.G., 1928, Proc. Roy. Soc., A118, 654.
Davis L.E., MacDonald N.C., Palmberg P.W., Riach G.E. and Weber R.E., 1976, Handbook of Auger Electron Spectroscopy, Physical Electronics Industries, Minnesota.
El Gomati M.M. and Prutton M., 1978, Surf. Sci., 72, 485.
Everhart T.E. and Hoff P.H., 1971, J. Appl. Phys., 42, 5837.

Fabre M. and Ripelle de la., 1949, J. Phys. (Paris), 10, 319.
Feibelman P.J., McGuire E.J. and Pandey K.C., 1976, Phys. Rev. Lett., 36, 1154.
Feibelman P.J. and McGuire E.J., 1977, Phys. Rev., B15, 3375.
Fink M. and Yates A.C., 1970a, Tech. Rept. No. 88, Electronic Research Center, The University of Texas.
Fink M. and Yates A.C., 1970b, Atomic Data, 1, 385.
Fink M. and Ingram J., 1972, Atomic Data, 4, 129.
Fitting H.J., 1974, Phys. Status Solidi, A26, 525.

Ganachaud J.P. and Cailler M., 1979, Surf. Sci., 83, 498.
Gerlach R.L. and DuCharme A.R., 1972, Surf. Sci., 32, 329.
Gerlach R.L. and MacDonald N.C., 1976, Scanning Electron Microscopy, Eds. O. Johari and I. Corvin (IITRI, Chicago, 1976), 200.
Goto K., Ishikawa K., Koshikawa T. and Shimizu R., 1975, Surf. Sci., 47, 477.

Goto K., Ichimura S., and Shimizu R., 1979, Rev. Sci. Insturm., 50, 46.
Goto K., Ichimura S. and Shimizu R., 1980, Rev. Sci. Instrum., 51, 95.
Grant J.T., Haas T.W. and Houston J.E., 1973, Phys. Letters, 45A, 309.
Grant J.T., Haas T.W. and Houston J.E., 1974a, Proc. 2nd Intern. Conf. on Solid Surfaces, Japan J. Appl. Phys., Suppl. 2, Pt 2, 811.
Grant J.T., Hooker M.P. and Haas T.W., 1974b, Surface Sci. 46, 672.
Grant J.T., Haas T.W. and Houston J.E., 1974c, J. Vac. Sci. Technol. 11, 672.
Grant J.T., Hooker M.P., Springer R.W. and Haas T.W., 1976, Surf. Sci., 60, 1.
Green A.J. and Leckey R.C.G., 1976, J. Phys. D; Appl. Phys. 9, 2123.

Haak H.W., Sawatzky G.A. and Thomas T.D., 1978, Phys. Rev. Lett., 41, 1825.
Hall P.M., Morabito J.M. and Conley D.K., 1977a, Surf. Sci., 62, 1.
Hall P.M. and Morabito J.M., 1977b, Surf. Sci., 67, 373.
Hall P.M. and Morabito J.M., 1979, Surf. Sci., 83, 391.
Harris L.A., 1968, J. Appl. Phys., 39, 1419.
Heinrich K.F.J., 1966, X-ray Optics and Microanalysis (Hermann, Paris), 159.
Heinrich K.F.J., Newbury D. and Yakowitz H. (Eds.), 1976, Use of Monte Carlo Calculations in Electron Probe Microanalysis and Scanning Electron Microscopy NBS-special publication 460.
Hollway P.H., 1977, Surf. Sci., 66, 479.
Houston J.E., 1974a, Appl. Phys. Lett., 24, 42.
Houston J.E., 1974b, Rev. Sci. Instrum. 45, 897.
Houston J.E., Moore G. and Lagally M.G., 1977, Solid State Commun., 21, 879.

Ichimura S. and Shimizu R., 1979, J. Appl. Phys., 50, 6020.
Ichimura S., Aratama M. and Shimizu R., 1980a, J. Appl. Phys., 51, 2853.

Ichimura S., Aratama M. and Shimizu R., 1981, J. Vac. Sci. Technol. (in press)
Ichimura S., LeGressus C., Shimizu R., Goto K. and Massignon D., 1980b, Comp. Rend., B291, 67.
Inoue T, Horiuchi S., Iwai H., Shimizu H. and Ishida T., 1976, Proc. 7th Conf. on Solid State Devices (Tokyo, 1975), Suppl. of Japan. J. Appl. Phys., 15, 63.
Inui T. and Shimizu R., 1979, Technol. Repts. Osaka Univ., 29, 373.
Ishida T., Uchiyama M., Oda Z. and Hashimoto H., 1976, J. Vac. Sci. Technol., 13, 711.
Ishida Y., Iida F., Koyama N. and Shimizu H., 1976, Scripta Metallurgica, 10, 1021.

Jablonski A., 1979a, Surf. Interface Anal., 1, 122.
Jablonski A., 1979b, Surf. Sci. 87, 539.
Janssen A.P., Harland C.J. and Venables J.A., 1977a, Surf. Sci., 62, 277.
Janssen A.P., Venables J.A., Hwang J.C.M. and Balluffi R.W., 1977b, Phil. Mag., 36, 1537.
Janssen A.P. and Venables J.A., 1978, Surf. Sci., 77, 351.
Johannessen J.S., Spicer W.E. and Strausser Y.E., 1976, J. Appl. Phys., 47, 3028.
Kanter H., 1957, Ann. Phys. (Leipzig), 20, 144.
Kessler J., 1976, Polarized Electrons (Springer, Berlin).
Kirschner J., 1977, Appl. Phys., 14, 351.
Koshikawa T., 1973, Ph. D Thesis, Osaka Univ. (unpublihsed).
Krefting E.J. and Reimer L., 1976, NBS Spec. Pub. 460, 45.

Lafferty J.M., 1951, J. Appl. Phys., 22, 299.
Lander J.J., 1953, Phys. Rev., 91, 1382.
Langeron J.P. (Ed.), 1979, Le Vide les Couches Minces-Spectrometree Auger.
Leapman R.D. and Cosslett V.E., 1976, Phil. Mag. 33, 1.
Le Gressus C., Pellerin F., Balnchard B. and Okuzumi H., 1977, Proc. 7th Intern. Vac. Congr. & 3rd Intern. Conf. Solid Surfaces, Eds. R. Dobrozemsky, F. Rüdenauer, F.P. Viehböck and A. Breth (Berger & Söhne, Vienna, 1977), 2323.
Le Gressus C., Massingnon D., Mogami A. and Okuzumi H., 1979,

Proc. Washington Scanning Electron Microscopy Annual Symp. 1, Ed. O. Johari, 161.

Ling D.T., Miller J.N., Lindau I., Spicer W.E. and Stefan P.M., 1978, Surf. Sci., 74, 612.

Lotz W., 1970, Z. Physik, 232, 101.

MacDonald N.C., 1970, Appl. Phys. Lett., 16, 76.

MacDonald N.C. and Waldrop J.R., 1971, Appl. Phys. Lett., 19, 315.

MacDonald N.C., 1976, (private communication).

MacDonald N.C., Hovland C.T. and Gerlach R.L., 1977, Scanning Electron Microscopy (vol. 1), Proceedings of the Workshop on SEM Applications to Semiconductors (IITRI, Chicago), 201.

Madden H.H. and Houston J.E., 1977, Solid State Commun. 21, 1081.

Matsukawa T., 1973, Ph. D thesis, Osaka Univ. (unpublished).

Martin A.D., 1975, J. Phys. D ; Appl. Phys., 8, 2074.

McGuire E.J., 1977, Phys. Rev. A16, 62.

Menyhard M. and Gergely G., 1977, Proc. 7th Intern. Vac. Congr. & 3rd Intern. Conf. Solid Surfaces, Eds. R. Dobrozemsky, F. Rüdenauer, R.P. Viehböck, and A. Breth (Berger & Söhne, Vienna, 1977), 2165.

Mogami A. and Sekine T., 1976, Proc. 6th European Congr. on Electron Microscopy (Jerusalem, Aug. 1976), 422.

Mogami A., 1978a, JEOL (Jpn. Electron Opt. Lab.) News, 16E, 14.

Mogami A., 1978b, private communication

Mogami A. and Sekine T., 1978 , Proc. 9th Intern. Congr. on Electro-Microscopy. (in press)

Mott N.F. and Massey H.S.W., 1965, The Theory of Atomic Collisions (Oxford, London).

Ng Yee S., Tsong T.T. and McLane S.B., Jr., 1979, Phys. Rev. Lett., 42, 588.

Nigam B.P., Sundaresan M.K. and Wu Ta-You, 1959, Phys. Rev., 115, 491.

O'Keeffe T.W. and Handy R.M., 1968, Solid-State Electron, 11, 261.

Palmberg P.W., 1972, in : Electron Spectroscopy, Ed. D.A. Shirley (North-Holland, Amsterdam), 835.
Palmberg P.W., 1973, Anal. Chem., 45, 549A.
Palmberg P.W., 1976, J. Vac. Sci. Technol., 13, 214.
Penn E.R., 1976, Phys. Rev., B13, 5248.
Philibert J. and Tixier R., 1968, in : Nat. Bur. Stand. (U.S.) Spec. Publ. 298, Ed. K.F.J. Heinrich, 13.
Pocker D.J. and Haas T.W., 1975, J. Vac. Sci. Technol., 12, 370.
Poole D.M. and Thomas P.M., 1962, J. Inst. Met., 90, 228.
Powell C.J., 1973, Phys. Rev. Lett., 30, 1179.
Powell C.J., 1976, Rev. Mod. Phys., 26, 33.
Powell C.J., 1977, Proc. 7th Intern. Vac. Congr. & 3rd Intern. Conf. Solid Surfaces, Eds. R. Dobrozemsky, F. Rüdenauer, F.P. Vieböck, and A. Breth (Berger & Söhne, Vienna, 1977), 2319.

Renter W., 1972, Proc. 6th. Intern. Conf. on X-ray Optics and Microanalysis Eds. G. Shinoda, K. Kohra and T. Ichinokawa (Univ. of Tokyo Press, Tokyo), 121.
Ritchie R.H., Garber F.W., Nakai M.Y. and Birkhoff R.D., 1969, Adv. Radiat. Biol., 3, 1.
Rudge M.R.H. and Schwartz S.B., 1966, Proc. Phys. Soc. (London) 88, 563.

Savitzky A. and Golay M.J.E., 1964, Anal. Chem., 36, 1627.
Schockley W. and Pierce J.R., 1938, Proc. Inst. Radio Engrs. N.T., 26, 321.
Schwidtal K., 1978, Surf. Sci., 77, 523.
Seah M.P., 1972, Surf. Sci., 32, 703.
Seah M.P. and Hondros E.D., 1973, Proc. R. Soc. Lond., A335, 191.
Seah M.P. and Dench W.A., 1979, Surf. Interface Anal., 1, 2.
Shimizu R., Kataoka Y., Tanaka T. and Kawai S., 1975a, Jpn. J. Appl. Phys., 14, 1089.
Shimizu R., Kataoka Y., Kawai S. and Tanaka T., 1975b, Appl. Phys. Lett., 27, 113.
Shimizu R., Kataoka Y., Ikuta T., Koshikawa T. and Hashimoto H., 1976, J. Phys. D ; Appl. Phys., 9, 101.
Shimizu R., Aratama M., Ichimura S., Yamazaki, Y. and Ikuta T.,

1977a, Appl. Phys. Lett., 31, 692.
Shimizu R., Shinike T., Kawai S. and Tanaka T., 1977b, Jpn. J. Appl. Phys., 16, 669.
Shimizu R., Everhart T.E., MacDonald N.C. and Hovland C.T., 1978a, Appl. Phys. Lett., 33, 549.
Shimizu R. and Everhart T.E., 1978b, Appl. Phys. Lett., 33, 784.
Sickafus E.N., 1971, Rev. Sci. Instrum., 42, 933.
Sigsbee R.A. and Wilson R.H., 1973, Appl. Phys. Lett. 23, 541
Simons M. Jr., Monteith L.K. and Hauser J.R., 1968, IEEE Trans. Electron Devices, ED-15, 966.
Smith D.M. and Gallon T.E., 1974, J. Phys. D : Appl. Phys., 7, 151.
Smith M.A. and Levenson L.L., 1977, Phys. Rev., B16, 2973.
Springer R.W., Pocker D.J. and Haas T.E., 1975, Appl. Phys. Lett. 27, 368.
Springer R.W. and Pocker D.J., 1977, Rev. Sci. Instrum. 48, 74.
Staib P. and Kirschner J., 1974, Appl. Phys., 3, 421.
Sternglass E.J., 1954, Phys. Rev., 95, 345.
Strand T.G. and Bonham R.A., 1964, J. Chem. Phys., 40, 1686.
Sze S.M., Moll, J.L. and Sugano T., 1964, Solid-State Electron, 7, 509.
Szedon J.R. and Sandor J.E., 1965, Appl. Phys. Lett., 6, 181.

Taylor N.J., 1969, Rev. Sci. Insturm., 40, 792.
Thoams R.N., 1961, Ph. D thesis, Univ. of Cambridge, (unpublished).
Thomas S., 1974, J. Appl. Phys., 45, 161.
Todd G., Poppa H., Moorhead D. and Bales M., 1975, J. Vac. Sci. Technol., 12, 953.
Tsuda T., 1977, "*Monte Carlo ho to simulation*" (Baifukan, Tokyo) (in Japanese).
Venables J.A., Janssen A.P., Harland C.J. and Joyce B.A., 1976, Phil. Mag., 34, 495.

Vogel S.F., 1970, Rev. Sci. Insturm., 41, 585.
Vriens L., 1969, in : Case Studies in Atomic Collisions Physics 1, Eds. MacDaniel E.W. and MaxDowell M.R.C. (North-Holland, Amsterdam), 337.

Weber R.E. and Peria W.T., 1967, J. Appl. Phys., 38, 4355.
Williams F.L. and Nason D., 1974, Surf. Sci., 45, 377.
Wittry D.B., 1966, X-ray Optics and Microanalysis, Eds. R. Castaing, P. Deschamps, and J. Philibert (Hermann, Paris), 168.
Worthington C.R. and Tomlin S.G., 1956, Proc. Phys. Soc., A69, 401.

Yamazaki Y., Shimizu R. and Hashimoto H., 1976, J. Phys. Soc. Japan, 41, 721.
Yamazaki Y., Shimizu R. and Hashimoto H., 1977a, Technol. Rep. Osaka Univ., 27, 317.
Yamazaki Y., 1977b, Ph. D thesis, Osaka Univ. (unpublished).

両　　親　　へ

List of publications

1. "Application of Monte Carlo Calcu;ation to Fundamentals of Scanning Auger Electron Microscopy"
   R. Shimizu, M. Aratama, S. Ichimura, Y. Yamazaki, and T. Ikuta
   Appl. Phys. Lett. 31, 692 (1977)

2. "An Application of Square Wave Modulation Techinque to Scanning Auger Electron Microscopy"
   K. Goto, S. Ichimura, and R. Shimizu
   Japan J. Appl. Phys. 16, 2087 (1977)

3. "Highly Stable Single-crystal LaB_6 Cathode for Conventional Electron Microprobe Instrument"
   R. Shimizu, T. Shinike, S. Ichimura, S. Kawaii and T. Tanaka
   J. Vac. Sci. Technol. 15, 922 (1978)

4. "Synchronous Modulation in Scanning Auger Electron Microscopy"
   K. Goto, S. Ichimura, and R. Shimizu
   Rev. Sci. Instrum. 50, 46 (1979)

5. "Observation of Electron-beam Damage in Thin Film SiO_2 on Si with Scanning Auger Electron Microscope"
   S. Ichimura and R. Shimizu
   J. Appl. Phys. 50, 6020 (1979)

6. "Application of Monte Carlo Calculation Technique to Quantitative Analysis by Auger Electron Spectroscopy"
   R. Shimizu, S. Ichimura, and M. Aratama
   Proc. 14th Conf. Microbeam Analysis, San Antonio, Texas, 12-17 August, 1979, Ed. D.E.Newbury (San Francisco press Inc.,1979) pp30-34 (invited paper)

7. "Monte Carlo Calculation Approach to Quantitative Auger Electron Spectroscopy"
   S. Ichimura, M. Aratama, and R. Shimizu
   J. Appl. Phys. 51, 2853 (1980)

8. "Digital Integration in Scanning Auger Electron Microscopy"
   K. Goto, S. Ichimura, and R. Shimizu
   Rev. Sci. Instrum. 51, 95 (1980)

9. "Angular Distribution of Si Atoms Sputtered by keV Ar^+ Ions"
T. Okutani, M. Shikata, S. Ichimura, and R. Shimizu
J. Appl. Phys. 51, 2884 (1980)

10. "Etude du fond continu associe a l'emission d'electrons Auger"
S. Ichimura, C. LeGressus, R. Shimizu, K. Goto, and D. Massignon
Compt. Rend. B291, 67 (1980)

11. "An Interpretation of Quantitative Analysis of Arthur and LePore for $Al_xGa_{1-x}As$ using AES"
S. Ichimura, M. Aratama, and R. Shimizu
J. Vac. Sci. Technol. (in ptrss)

(in Japanese)

1. "Auger Electron Spectroscopy with High Spatial Resolution"
S. Ichimura, R. Shimizu, and K. Goto
High Accuracy 9, No. 2, 1 (1979)

2. "Monte Carlo Calculation Technique as Applied to Quantitative Analysis by AES"
S. Ichimura and R. Shimizu
JSPS Technol Committee 141 Report, No. 267, 1 (1980)